AIX-MARSEILLE UNIVERSITÉ

ECOLE DOCTORALE DE PHYSIQUE ET SCIENCES DE LA MATIERE

UMR 7326 - Laboratoire d'Astrophysique de Marseille

Thèse présentée pour obtenir le grade universitaire de Docteur

Discipline : Sciences de la Terre et de l'Univers
Spécialité : Astrophysique et Cosmologie

Olivier Benjamin KAUFFMANN

Les premières galaxies réionisant l'Univers vues par le JWST et COSMOS

The first galaxies reionizing the Universe
as seen with JWST and COSMOS

Sous la direction de Olivier ILBERT et Olivier LE FEVRE

Soutenance le 08/01/2021 devant le jury composé de :

Stéphane CHARLOT	Rapporteur
Johan RICHARD	Rapporteur
Véronique BUAT	Examinatrice
Roser PELLO	Examinatrice
Karina CAPUTI	Examinatrice
Olivier ILBERT	Directeur de thèse

Résumé

L'observation de l'Univers distant, c'est-à-dire de l'Univers jeune, est d'une importance majeure pour comprendre la formation des galaxies et des grandes structures. Environ 370 000 ans après le Big Bang, l'Univers est principalement constitué d'un gaz diffus d'hydrogène neutre. L'époque durant laquelle l'hydrogène dans le milieu intergalactique devient progressivement ionisé est appelée la réionisation. L'observation des spectres de quasars lointains suggère que la réionisation se termine à un décalage vers le rouge (redshift) de $z \sim 6$, environ un millard d'années après le Big Bang. Cependant, l'évolution temporelle et spatiale de cette transition de phase demeure peu connue, de même que la nature des objets contribuant à ce processus. Il est attendu que les premières galaxies soient une des principales sources de photons ionisants, en particulier les galaxies peu brillantes.

L'observation des galaxies pendant la réionisation est délicate pour de multiples raisons, ce qui implique que le nombre de détections reste limité à ce jour. En effet, la visibilité de ces objets distants dépend de leurs propriétés intrinsèques, mais également de la distribution et de l'état d'ionisation de l'hydrogène le long de la ligne de visée. L'expansion de l'Univers provoque le décalage vers le rouge du spectre de ces galaxies, qui deviennent indétectables dans le domaine visible. De ce fait, il devient nécessaire de réaliser des observations profondes dans l'infrarouge proche. Ce champ de recherche va grandement bénéficier des prochaines missions spatiales telles *James Webb* et *Euclid*. Le télescope spatial *James Webb* (*JWST*) fournira des images haute résolution dans l'infrarouge proche et moyen, et se concentrera sur des champs profonds de quelques arcminutes carrées. Le télescope *Euclid*, quant à lui, observera 15 000 deg^2 du ciel dans le visible et l'infrarouge proche, avec les champs profonds *Euclid* couvrant 40 deg^2. Ainsi, ces missions permettront l'étude des galaxies, faibles d'une part, et brillantes mais rares d'autre part, pendant l'époque de la réionisation.

Cette thèse est centrée sur l'étude statistique des galaxies lointaines durant la réionisation de l'Univers, à partir de sondages photométriques. L'objectif est de fournir de nouvelles contraintes sur la chronologie de la réionisation, ainsi que de préparer les sondages profonds avec la prochaine génération de télescopes. Pour ce faire, cette thèse s'articule autour de deux axes principaux, la simulation des premières observations du télescope *JWST* d'une part, afin de fournir des prédictions quant aux galaxies à grand redshift, et le traitement et l'analyse des données photométriques dans le champ COSMOS d'autre part, en préparation des champs profonds *Euclid*.

Introduction à la réionisation

Dans le chapitre 1, je présente les modèles théoriques et les contraintes observationnelles actuelles sur l'époque de la réionisation. En premier lieu, je rappelle les principes du modèle standard de la cosmologie. Les premières étapes de l'histoire de l'Univers, comprenant la recombinasion cosmique, les âges sombres et l'époque de la réionisation, sont introduites. Je présente ensuite une description analytique de la première phase de la réionisation, dite pré-recouvrement (Gnedin 2000). Durant cette phase, les premières galaxies, situées aux pics du champ de densité de masse, émettent des photons énergétiques ionisant l'hydrogène neutre dans leur environnement proche (Barkana et al. 2001). Il se forme alors des bulles d'hydrogène ionisé dans le milieu inter-galactique, qui grandissent avec le temps. Les bulles des galaxies peu éloignées finissent par se recouvrir, alors que d'autres bulles se forment. Ce phénomène se poursuit jusqu'à l'ionisation quasi-totale du milieu inter-galactique.

Il existe plusieurs sondes observationnelles permettant de contraindre cette époque de l'Univers. Les spectres d'absorption des quasars à $z > 6$ ont permis de placer la fin de la réionisation à redshift $z \sim 6$ via l'effet Gunn-Peterson (Fan et al. 2006). D'autre part, le télescope Planck a fourni une mesure de l'effet cumulé de la réionisation sur le rayonnement fossile (Planck Collaboration et al. 2018). L'observation directe des sources contribuant à la réionisation reste une des méthodes les plus utiles pour comprendre l'évolution temporelle et spatiale de l'Univers à cette époque. Bien qu'il y ait encore des incertitudes, ce sont les galaxies qui semblent conduire la réionisation, en particulier les galaxies de faibles masses (Finkelstein et al. 2019). Pour que l'Univers soit entièrement ionisé à $z > 6$, il est nécessaire qu'un certain nombre de photons ionisants aient été émis, et de ce fait qu'un certain nombre de galaxies se soient formées. La chronologie de la réionisation peut ainsi être contrainte par le comptage des galaxies à grands redshifts, quantifié par la fonction de luminosité dans l'ultraviolet (UV).

La détection des galaxies à grands redshifts ($z > 6$) se base essentiellement sur la photométrie profonde dans l'infrarouge proche. En effet, ces galaxies restent indétectables dans le domaine visible à cause de l'absorption par le milieu inter-galactique entourant ces sources. Les images astronomiques permettent de sonder une portion complète du ciel, et ainsi d'observer un grand nombre de sources simultanément. Afin d'identifier les galaxies à grand redshift, des observations dans plusieurs bandes spectrales sont nécessaires afin de mesurer les couleurs de ces sources. En comparant les couleurs observées à celles provenant de modèles de galaxies, la nature et les paramètres physiques des sources peuvent être estimés. Cependant, les échantillons de galaxies à grands redshifts peuvent être contaminés par des sources possédant des propriétés spectrales (couleurs) similaires. Ceci concerne principalement des galaxies à bas redshifts ($z \sim 1 - 2$), qui sont bien plus nombreuses que celles à grands redshifts, et des naines brunes.

Simulation des observations du télescope spatial *James Webb*

Dans le chapitre 2, je présente une analyse prospective des images du télescope spatial *James Webb* (*JWST*). Le lancement de ce télescope de 6 m de diamètre est prévu pour octobre 2021 (octobre 2018 en début de thèse). Les instruments à bord du *JWST* comprennent une caméra infrarouge proche (NIRCam) et une caméra infrarouge moyen (MIRI), couvrant ensemble les longueurs d'onde de 0.6 à 28 microns. Avec une résolution spatiale sous la seconde d'arc (une première au-delà de 3 microns), le *JWST* aura un champ de vue de quelques arcminutes carrées et une sensibilité sans précédent dans l'infrarouge. Ces caractéristiques rendent ce télescope particulièrement adapté à l'étude des galaxies lointaines (à des décalages vers le rouge $z > 6$), qui restent indétectables dans le domaine du visible.

Afin d'évaluer les performances du *JWST*, j'ai mené des simulations d'images astronomiques reproduisant les premiers programmes d'observation du *JWST*. L'objectif est de produire des prédictions réalistes par rapport aux galaxies lointaines, de quantifier le nombre de détections attendues et la fraction de contaminants. Cela implique également l'évaluation des méthodes d'extraction de source et d'estimation des paramètres physiques. La simulation d'image est nécessaire afin de reproduire les limites de détection pour les sources étendues, ainsi que les effets de confusion, c'est-à-dire la superposition de sources se trouvant sur des lignes de visée proches. De telles sources peuvent être difficiles à séparer et à caractériser, en particulier avec des sondages toujours plus profonds dans lesquels ces effets se manifestent de plus en plus (Dawson et al. 2016). Les programmes simulés comprennent CEERS (Cosmic Evolution Early Release Science) dans le champ EGS (Extended Groth Strip), et les programmes des équipes GTO (Guaranteed Time Observations) des instruments NIRCam et MIRI dans le HUDF (*Hubble* Ultra-Deep Field). L'étude des galaxies réionisant l'Univers fait partie des applications scientifiques de ces programmes. Les deux champs concernés profitent d'ores et déjà d'une couverture spectrale importante, notamment avec les observations profondes avec le télescope spatial *Hubble* (*HST*).

Pour réaliser ces simulations, j'ai utilisé le catalogue JAGUAR (Williams et al. 2018) comprenant un ensemble complet de galaxies simulées, allant de l'Univers proche à l'Univers lointain. Ce catalogue a été affiné en incluant l'émission de la poussière aux spectres des galaxies (Schreiber et al. 2018), et en ajoutant des galaxies dans l'Univers proche. De plus, j'ai produit un ensemble d'étoiles et de naines brunes, à partir des contraintes actuelles sur ces objets (e.g., Caballero et al. 2008 ; Pecaut et al. 2013 ; Baraffe et al. 2015). Les naines brunes, en particulier, peuvent contaminer les échantillons de galaxies lointaines car elles possèdent des couleurs similaires. Ces sources sont injectées dans des images générées à l'aide du logiciel `SkyMaker` (Bertin 2009), simulant les futures observations avec le *JWST* et les données *HST* existantes. Les images se basent sur les connaissances actuelles de ces instruments, comme les fonctions d'étalement de point (point spread function ou PSF) et les niveaux de bruit attendus. La détection des sources et la photométrie sont réalisées en utilisant les mêmes méthodes que pour de vraies images astronomiques, avec le programme `SExtractor` notamment. Les propriétés physiques des galaxies sont mesurées avec `LePhare` (Arnouts et al. 2002 ; Ilbert et al. 2006), un outil d'ajustement de distributions spectrales d'énergie (SED-fitting).

Les paramètres physiques ainsi déterminés, notamment le redshift, la masse stellaire, le taux de formation d'étoiles et la magnitude absolue UV, sont comparés aux vrais paramètres des galaxies simulées. Les redshifts photométriques sont globalement en accord avec les redshifts d'entrée, mais sont sujets à plusieurs limitations. Les sondages simulés utilisent principalement des bandes larges, qui ne permettent pas de profiter pleinement des raies d'émission pour estimer le redshift. De plus, le break de Balmer d'une galaxie proche, situé à 4000 Å lors de l'émission, peut se confondre avec le break de Lyman d'une galaxie plus lointaine, situé à 912 Å à l'émission. Une autre contrainte est le manque de données dans les longueurs d'onde bleues, ce qui limite la précision du redshift pour les galaxies à $z < 2$, qui peuvent de ce fait contaminer les échantillons de galaxies à $z > 5$. Avec les simulations d'images, il est possible d'estimer l'impact de la confusion de sources sur la fraction de redshifts catastrophiques. Ainsi, à la limite de détection, jusqu'à 20% des sources catastrophiques sont provoquées par la contamination de sources voisines dans le champ EGS, et jusqu'à 40% dans le HUDF. Les paramètres physiques restants sont essentiellement en accord avec les paramètres d'entrée. La dispersion se limite à 0.25 dex pour les masses stellaires et 0.3 dex pour les taux de formation d'étoiles. Une large fraction des mesures catastrophiques proviennent de redshifts photométriques erronés, en particulier pour les galaxies peu massives.

En utilisant la photométrie, la morphologie et les redshifts photométriques, il est possible de définir des critères de sélection pour les galaxies à $z \geq 5$. L'objectif est de rejeter un maximum de contaminants, typiquement des galaxies à bas redshift et des naines brunes, sans pour autant rejeter les vraies galaxies à haut redshift. En premier lieu, je démontre que les naines brunes peuvent être efficacement rejetées, jusqu'à atteindre une densité de surface inférieure à 0.01 arcmin^{-2}, tout en n'affectant que peu la complétude des galaxies. Ensuite, je compare plusieurs approches de sélections, utilisant soit des coupures couleur-couleur adaptées à chaque redshift, soit les distributions de probabilité des redshifts. Les galaxies à $z \geq 5$ pouvant être correctement identifiées sont quantifiées, ainsi que leur complétude et leur pureté. La fonction de luminosité (LF) UV des galaxies, c'est-à-dire la densité comobile de galaxies par unité de luminosité intrinsèque, est calculée en fonction du redshift, puis comparée avec le catalogue d'entrée. Les sondages profonds du *JWST* permettent bien d'apporter des contraintes fortes sur les galaxies faibles (avec magnitudes absolutes $M_{\mathrm{UV}} > -20$ mag). La pente faible de la LF peut être récupérée avec une erreur de $0.1 - 0.25$. Cependant, le nombre de galaxies brillantes à $z > 7$ reste limité dans les champs *JWST*, à cause de la surface des sondages. Pour contraindre la partie brillante de la LF, il est nécessaire d'utiliser des sondages couvrant de plus grandes surfaces, comme avec la mission spatiale *Euclid*.

Réduction et analyse des données photométriques dans le champ COSMOS

Dans le chapitre 3, je présente les données photométriques dans le champ COSMOS. Ce champ de 2 deg^2 jouit d'une grande couverture en longueur d'onde qui s'étend des rayons X aux ondes radio. En particulier, les observations haute résolution dans le visible et l'infrarouge proche figurent parmi les plus grands sondages profonds jamais réalisés (Scoville et al. 2007). Le dernier catalogue photométrique dans le champ COSMOS en date, nommé COSMOS2015 (Laigle et al. 2016), a été grandement utilisé par la communauté scientifique et fait office de référence. Ce catalogue inclut notamment les données dans l'infrarouge proche du programme UltraVISTA (McCracken et al. 2012), celles de Suprime-Cam dans le visible (Taniguchi et al. 2007 ; Taniguchi et al. 2015) et les images SPLASH dans l'infrarouge moyen (Steinhardt et al. 2014). En rassemblant les sondages profonds dans le champ COSMOS depuis 2015, l'objectif est de fournir un nouveau catalogue photométrique de référence, appelé COSMOS2020. La réduction des données du champ COSMOS est d'une importance capitale pour le bon déroulement de la future mission spatiale *Euclid*, qui utilisera COSMOS comme champ de calibration. De plus, les méthodes appliquées à COSMOS2020 seront directement transférées au sondage Cosmic Dawn, qui comprend la couverture visible, avec la caméra Hyper Suprime-Cam (HSC) du télescope Subaru, et infrarouge moyen, avec le télescope spatial *Spitzer*, des champs profonds et de calibration *Euclid*.

Les nouvelles données photométriques dans le champ COSMOS comprennent les images UltraVISTA dans l'infrarouge proche, plus précisément de la quatrième publication de données (DR4). Ces images dans les bandes Y, J, H, K_s sont jusqu'à une magnitude plus profondes que dans COSMOS2015. Dans le visible, les images de la caméra Hyper Suprime-Cam du télescope Subaru couvrent le champ COSMOS dans les bandes g, r, i, z, y. Le Subaru Strategic Program (SSP) avec HSC atteint $27-28$ mag de profondeur (Aihara et al. 2019), dépassant les limites des données Suprime-Cam. Dans l'infrarouge moyen, les images finales du télescope spatial *Spitzer*, produites en combinant toutes les images existantes pour le sondage Cosmic Dawn (Moneti et al. in prep.), incluent le champ COSMOS. Les images dans la bande U du sondage CLAUDS (CFHT Large Area U-band Deep Survey) du télescope Canada-France-Hawaï (CFHT) sont également incluses (Sawicki et al. 2019). Toutes ces données photométriques (incluant les anciennes données) sont (re)calibrées à l'aide de la référence astrométrique *Gaia*, permettant une meilleure précision de bande à bande.

Pour la réduction des données COSMOS, la stratégie adoptée comprend deux approches distinctes, produisant deux catalogues photométriques. La première approche, dite "classique", est équivalente à celle utilisée par Laigle et al. 2016 pour COSMOS2015. La détection et la photométrie des images haute résolution sont réalisées avec le logiciel `SExtractor`. La photométrie d'ouverture est extraite des images dont les PSFs ont été homogénéisées, ce qui permet une meilleure mesure des couleurs. Les images basse résolution du télescope *Spitzer* sont traitées avec le programme IRACLEAN, utilisant les images hautes résolutions comme information préalable pour déterminer la photométrie des sources confondues. Dans la seconde approche, avec le logiciel the Farmer, la photométrie est mesurée avec le logiciel the Tractor en se basant sur l'ajustement de modèles de brillance de surface. Ceci permet de traiter de manière équivalente les images haute et basse résolution, de mesurer directement le flux total des galaxies, ainsi que de mieux séparer les galaxies confondues. Cette seconde approche bénéficie des résultats de la première approche pour sa validation.

Ce catalogue photométrique est issu d'un travail collaboratif au sein de la collaboration COSMOS. Dans cet effort commun, j'ai produit la photométrie haute résolution (visible et infrarouge proche) du catalogue classique, comprenant l'homogénéisation des PSFs, la détection et la photométrie. J'ai également participé à la création des masques et au calcul des cartes de profondeur. Les masques permettent notamment d'identifier les halos autour des étoiles brillantes, qui contaminent les sources proches. Les cartes de profondeur indiquent la profondeur en fonction des coordonnées célestes, ce qui est utile pour la visualisation et la validation des données. La profondeur est mesurée dans des ouvertures vides de diamètre fixé, identiques aux ouvertures utilisées pour la photométrie des sources détectées. Pour ce faire, il est nécessaire d'identifier les régions vides de sources, sélectionner des coordonnées aléatoires dans ces régions, puis mesurer le flux dans ces ouvertures. La déviation standard de ces flux donne une mesure de profondeur.

Pour réaliser le catalogue classique, les étapes sont les suivantes. La détection des sources est réalisée sur une image combinée dans les bandes $izYJHK_s$, permettant l'identification de sources faibles. La sélection est ainsi orientée vers les galaxies à grand redshift notamment, et risque de ne pas inclure les sources les plus bleues. L'homogénéisation des PSFs est réalisée avec le programme PSFEx, en sélectionnant un échantillon de sources ponctuelles dans chaque image. Ces sources, principalement des étoiles, sont identifiées via leurs profils de brillance de surface, leurs magnitudes et leurs positions. La PSF de chaque image est ainsi modélisée, et un noyau de convolution est produit pour transformer la PSF observée en une PSF cible, définie par un profil de Moffat (Moffat 1969). La photométrie est extraite de ces images dans des ouvertures de $2''$ et $3''$ de diamètre avec SExtractor. Les erreurs sur les magnitudes sont amplifiées pour prendre en compte le bruit corrélé de chaque image, et les magnitudes d'ouverture sont transformées en magnitudes totales via une correction moyenne appliquée à toutes les bandes. Les paramètres physiques sont ensuite déterminés avec les programmes LePhare et EAZY (Brammer et al. 2008), en utilisant les deux catalogues photométriques séparément. Les photométries et paramètres physiques obtenus à partir des deux catalogues sont en excellent accord, mis à part à la limite de détection. Je me suis également très impliqué dans la comparaison des deux catalogues photométriques, dans la validation de l'ensemble des catalogues produits par COSMOS2020 (catalogues photométriques, redshifts photométriques, paramètres physiques), ainsi que dans l'écriture de l'article présentant COSMOS2020, inclus dans le chapitre 3.

Recherche des galaxies à grand décalage vers le rouge dans COSMOS

Dans le chapitre 4, je présente la recherche de galaxies pendant la réionisation de l'Univers dans le champ COSMOS. L'accent est porté sur les galaxies les plus lointaines qu'il est possible d'observer, en utilisant les deux catalogues COSMOS2020. Les galaxies à $z > 7.5$ sont sélectionnées en se basant sur les redshifts photométriques estimés avec `LePhare`. Ceci permet d'identifier les galaxies présentant un break de Lyman dans les bandes Y ou J, comme ces sources sont indétectables dans le domaine visible. Il est donc nécessaire que les galaxies soient détectées dans les bandes H et K_s de UltraVISTA, et potentiellement dans l'infrarouge moyen avec les canaux 1 et 2 de IRAC. De plus, la sélection se limite au domaine UltraVISTA ne présentant pas de sources brillantes ayant été masquées. Comme deux catalogues photométriques sont à notre disposition, les critères de sélection peuvent être appliqués séparément aux deux catalogues, puis les résultats peuvent être comparés pour une sélection plus robuste.

J'ai identifié une ensemble de 36 candidats de galaxies à $z > 7.5$ dans le champ COSMOS, incluant 21 nouveaux candidats ne figurant pas dans la littérature. Certains nouveaux candidats de galaxies font l'objet de propositions d'observations spectroscopiques, afin de confirmer le redshift de ces sources. Le cas des galaxies confondues avec des sources voisines est particulièrement intéressant avec le catalogue de `the Farmer`. Dans de tels cas, la photométrie d'ouverture se retrouve contaminée par les proches voisins, qui n'ont statistiquement pas les mêmes couleurs. Avec l'approche de `the Tractor`, les flux des sources confondues peuvent être séparés, offrant ainsi une mesure plus exacte que pour la photométrie d'ouverture. Je présente ainsi 3 nouveaux candidats de galaxies à $z > 7.5$ identifiées dans le catalogue `the Farmer`, dont la photométrie d'ouverture est visiblement contaminée dans le visible. Ceci est une démonstration que le model-fitting comme celui de `the Tractor` offre de nouvelles possibilités dans l'analyse des images hautes résolutions, en plus des images basses résolutions. Lors de l'analyse des données dans les champs profonds *Euclid*, il sera de ce fait important d'utiliser une méthode comme celle de `the Farmer`.

Les données infrarouge du champ COSMOS ont été utilisées précédemment pour la recherche de galaxies pendant la réionisation de l'Univers (e.g., Bowler et al. 2015). En particulier, Stefanon et al. 2019 et Bowler et al. 2020 ont présenté un total de 25 candidats distincts à $z > 7.5$ en utilisant les DR3 et DR4 de UltraVISTA, respectivement. Je retrouve 15 de ces candidats comme étant à grand décalage vers le rouge, alors que 4 possèdent des importantes solutions secondaires à bas redshift. Les 6 candidats non détectés avec l'image de détection $izYJHK_s$ de COSMOS2020 sont tout juste distinguables dans certaines des bandes J, K_s, ch1 et ch2. De ce fait, la détermination de redshifts photométriques à partir de ces objets reste incertaine.

L'effet de lentille gravitationnelle par des galaxies d'avant-plan, en particulier l'effet de magnification gravitationnelle, est mesuré pour toutes les galaxies sélectionnées. Les galaxies massives à bas redshift, situées à une courte distance angulaire d'une source d'arrière-plan, peuvent en effet augmenter la luminosité observée de cette source. Cet effet dépend de la masse de la lentille et des distances respectives avec la lentille et la source. Bien qu'aucun candidat ne présente de lentille forte, la magnification cumulée de plusieurs lentilles faibles se révèle importante pour au moins un candidat.

En utilisant cette nouvelle sélection de galaxies à $z > 7.5$, j'ai estimé la fonction de luminosité UV des galaxies à $z = 8, 9, 10$. Commes les candidats sont intrinsèquement brillants, l'extrémité brillante de la LF est contrainte à $M_{\mathrm{UV}} < -21.5\,\mathrm{mag}$. Les mesures sont en accord avec les résultats de la littérature, notamment ceux de Bowler et al. 2020. Ceci indique la faible incomplétude de l'échantillon de galaxies, en particulier pour les plus brillantes. La forme de la LF observée est sujet à plusieurs biais observationels et de sélection, notamment la contamination par les noyaux actifs de galaxies, le biais de magnification et le biais d'Eddington. Ces différents biais ainsi que leurs effets sur la densité de galaxies sont discutés.

Conclusions

Au cours de cette thèse, j'ai conduit une étude statistique des galaxies pendant l'époque de la réionisation de l'Univers. Pour ce faire, j'ai utilisé des images astronomiques simulées et réelles, en contribuant à la préparation des futurs sondages avec les télescopes *JWST* et *Euclid*. En premier lieu, j'ai produit une analyse prospective des galaxies qui seront observées lors des premiers sondages profonds du télescope *James Webb*. J'ai réalisé des simulations de bout en bout, de l'extraction des sources dans des images simulées, jusqu'au calcul des fonctions de luminosité. Dans un second temps, j'ai participé à la réduction et au traitement des données dans le champ COSMOS, dans le but de produire un nouveau catalogue photométrique de référence, COSMOS2020. Ce champ servira de calibration pour *Euclid* et nos méthodes seront transposées aux données HSC et *Spitzer* dans les champs profonds *Euclid*. Cette décennie profitera d'une nouvelle génération de sondages profonds, dans l'infrarouge avec *JWST* et *Euclid*, dans les ondes radio avec SKA, donnant de nouvelles sondes pour étudier la réionisation.

Mots clés : réionisation - galaxies à grands décalages vers le rouge - données photométriques

Abstract

The epoch of cosmic reionization is one major step in the evolution of the Universe, driven by the formation of the first stars and galaxies. Energetic photons emitted from these objects progressively ionize the neutral hydrogen in the inter-galactic medium. Hence, the degree of hydrogen ionization impacts the observed evolution of the high-redshift galaxy population. The main topic of this PhD is the statistical description of high-redshift galaxies during the reionization of the Universe, through deep imaging surveys. The detection and identification of these rare, faint galaxies essentially rely on multi-wavelength photometry, in particular in the near-infrared as these sources remain invisible in the optical. This field will benefit from the next generation of telescopes like the *James Webb* space telescope (*JWST*) and *Euclid*. In preparation for these missions, I treated mock and real astronomical images, including in the cosmic evolution survey (COSMOS) field.

In preparation for the future *JWST* imaging programs, I firstly produced a prospective analysis of the high-redshift galaxies to be detected. I performed extensive image simulations of the first accepted *JWST* programs in extragalactic fields, in complement to the existing data from the *Hubble* space telescope (*HST*). In these end-to-end simulations, galaxies and stars are injected into realistic mock images, extracted, then the physical parameters and the galaxy ultra-violet (UV) luminosity function are computed. The statistical description of the galaxy population at high-redshift requires robust completeness and purity estimates, provided in this analysis.

In parallel, I processed the deep imaging data in the 2 deg^2 of the COSMOS field. With the COSMOS team, we provided a new reference multi-wavelength catalog, named COSMOS2020, including the new near-infrared UltraVISTA images and the optical data from Hyper Suprime-Cam (HSC). In this joint effort, I produced the aperture photometry catalog using the high-resolution images. This work is of major importance notably for the *Euclid* mission, as COSMOS will be one of the *Euclid* calibration fields. Moreover, the methods tested for COSMOS will be directly applied to the Cosmic Dawn survey, i.e. the HSC and *Spitzer* coverage of the Euclid Deep Fields. Finally, I searched for galaxies at $z > 7.5$ using the COSMOS2020 catalog. Multiple new high-redshift candidates were identified, in particular using the deblended photometry. With this updated sample of candidates, I computed the galaxy UV luminosity function at $z \geq 8$, which is consistent with the literature, and discussed the observed shape of the bright end.

Keywords: reionization - galaxies: high-redshift - photometric data

Acknowledgments

Contents

List of Figures

List of Tables

List of acronyms

ACS Advanced Camera for Surveys, on-board *HST*.
ADU analog digital unit.
AGN active galactic nucleus.

BAO baryon acoustic oscillations.

CCD charge-coupled device.
CDFS Chandra Deep Field South.
CDM cold dark matter.
CEERS Cosmic Evolution Early Release Science.
CFHT Canada-France-Hawaii telescope.
CLAUDS CFHT large area U-band deep survey.
CMB cosmic microwave background.

DPL double power law.
DR data release.

EDFF Euclid Deep Field Fornax.
EDFN Euclid Deep Field North.
EDFS Euclid Deep Field South.
EDGES Experiment to Detect the Global Epoch of reionization Signature.
EGS Extended Groth Strip (field).
ERS early release science.
ETC exposure time calculator.

FLRW Friedmann-Lemaître-Robertson-Walker (metric).
FWHM full width at half maximum.

GOODS Great Observatories Origins Deep Survey.
GOODS-N GOODS-North (field).
GOODS-S GOODS-South (field).
GRB gamma-ray burst.

GTO guaranteed time observations.

H hydrogen (atom).
H20 Hawaii-Two-0 (survey).
HDFN *Hubble* deep field North.
He helium (atom).
HFF *Hubble* Frontier Fields.
HII hydrogen (ionized).
HSC Hyper Suprime-Cam.
HSC-SSP Hyper Suprime-Cam Subaru strategic program.
HST *Hubble* space telescope.
HUDF *Hubble* ultra-deep field.

IFU integral field unit.
IGM inter-galactic medium.
IMF initial mass function.
IR infrared.
IRAC Infrared Array Camera, on-board *Spitzer*.
IRX infrared excess.
ISM inter-stellar medium.

JADES *JWST* Advanced Deep Extragalactic Survey.
JAGUAR JADES extraGalactic Ultradeep Artificial Realizations.
JWST *James Webb* space telescope.

LAE Lyman alpha emitter.
LBG Lyman break galaxy.
LF luminosity function.

MCMC Markov chain Monte Carlo.
MIRI Mid-Infrared Instrument, on-board *JWST*.

NEP North Ecliptic Pole (field).
NIRCam Near-Infrared Camera, on-board *JWST*.
NIRISS Near-Infrared Imager and Slitless Spectrograph, on-board *JWST*.
NIRSpec Near-Infrared Spectrograph, on-board *JWST*.
NISP Near-Infrared Spectrometer and Photometer, on-board *Euclid*.
NMAD normalized median absolute deviation.

PAH polycyclic aromatic hydrocarbon.

PDFz redshift probability distribution function.

PSF point spread function.

SED spectral energy distribution.

SEP South Ecliptic Pole (field).

SFH star formation history.

SFR star formation rate.

SFRD star formation rate density.

SKA Square Kilometer Array.

SMF stellar mass function.

SMUVS *Spitzer* matching survey of the UltraVISTA ultra-deep stripes survey.

SN supernova.

SNe supernovae.

SPLASH *Spitzer* Large Area Survey with Hyper Suprime-Cam.

SXDF Subaru-XMM Deep Field.

UDS Ultra-deep Survey (field).

UKIDSS UKIRT Infrared Deep Sky Survey.

UKIRT United Kingdom Infra-Red Telescope.

UV ultraviolet.

UVLF ultraviolet luminosity function.

VIMOS Visible Multi-object Spectrograph.

VIS Visible Imager, on-board *Euclid*.

VLT Very Large Telescope.

VUDS VIMOS Ultra Deep Survey.

VVDS VIMOS VLT Deep Survey.

WFC3 Wide Field Camera 3, on-board *HST*.

XDF *Hubble* extreme deep field.

XMM-Newton X-ray Multi-Mirror telescope.

Introduction

Cosmology is the science of the origin, content and evolution of the Universe. The description of the Universe on multiple temporal and spatial scales, from local stars to galaxies and large-scale structures, almost entirely relies on light as direct source of information. Our understanding of the astrophysical phenomena therefore depends on the development of high-performance instruments.

Observing the distant, or equivalently, the early Universe, is of major importance to understand structure and galaxy formation. The hydrogen atoms formed $370,000$ years after the Big Bang remain mostly neutral, until the first stars form and start emitting ionizing photons with energies greater than 13.6 eV. The epoch where the neutral hydrogen in the inter-galactic medium progressively becomes ionized is called cosmic reionization. The temporal and spatial evolution of this major gas-phase transition is still to be determined, as well as the nature of the sources driving this process. Observations suggest that reionization ended at redshift $z \sim 6$, however the number of sources detected before this epoch remains limited. The visibility of distant objects depends on the ionization state of the hydrogen along the line of sight. Galaxies are expected to be one of the main sources of ionizing photons, particularly faint galaxies. Therefore, the census of galaxies during cosmic reionization contains information about the degree of ionization of the inter-galactic medium. In addition, the observed properties of the cosmic microwave background are also modified by the reionization history, bringing complementary constraints.

The goal of this thesis is the discovery and the statistical description of high-redshift galaxies during cosmic reionization, in order to impose new constraints on the timeline of this process. The detection and characterization of high-redshift sources mostly relies on multi-wavelength imaging from large and deep surveys. In this context, my work is centered on the future observations with the *James Webb* space telescope (*JWST*), and the the latest results in the cosmic evolution survey (COSMOS) field.

This thesis is organized as follows.

Chapter 1

The first chapter reviews the theoretical and observational background of this thesis. The standard cosmological model, the history of the Universe and the physics of reionization are introduced. The main reionization probes are discussed, with an emphasis on the direct observation of high-redshift galaxies. Optical and near-infrared imaging surveys with a major impact on this science field are presented, in addition to the standard galaxy selection techniques.

Chapter 2

In the second chapter, the prospective analysis of the future *JWST* observations is presented. The *JWST* mission and the first observing imaging programs are introduced. On this basis, the image simulations used to make predictions about the high-redshift galaxies to be observed are described. These forecasts include the high-redshift galaxy selection, with the resulting completeness and purity, and the estimated UV luminosity function.

Chapter 3

The third chapter describes the COSMOS field and its deep imaging data set. On this basis, all the data processing leading to the COSMOS2020 photometric catalog is detailed. This includes the data reduction, source extraction, photometry and the estimation of physical parameters. In addition, the importance of these results regarding the *Euclid* space mission is presented.

Chapter 4

In the fourth chapter, the search for galaxies at $z > 8$ in the COSMOS field is described. The details of the selection and the identified galaxy candidates are presented. Ultimately, the bright end of the galaxy UV luminosity function is constrained.

Finally, the conclusions and perspectives of this work are presented.

1. Introduction to reionization

1.1. Cosmological model

Modern cosmology made huge improvements during the 20$^{\text{th}}$ century. Einstein's theory of general relativity, introduced in a series of papers in 1915 (Einstein 1915), provided a new description of gravity, space and time. This new approach managed to explain the anomaly of the perihelion advance of Mercury, and the deflection of the light around the Sun, which was observed during a solar eclipse in 1919 by Eddington (Dyson et al. 1920). The expansion of the Universe was measured from the observation of Cepheids (Hubble 1929), and the model of the Big Bang was introduced based on this study (Lemaître 1931). In addition, the cosmic microwave background was discovered by accident (Penzias et al. 1965). All these discoveries and developments led to the present, standard cosmological model, namely the mathematical description of the Universe and its time evolution.

The standard model of cosmology remarkably manages to describe many observational phenomena in the Universe, including the large-scale structure of the Universe, the distribution of galaxies, the abundance of light elements (hydrogen, helium) from the primordial nucleosynthesis, and the accelerated expansion of the Universe. In this section, the basic principles of the cosmological model are introduced, including a mathematical description of the space-time geometry and the content of the Universe.

1.1.1. Cosmological parameters

The geometry of the Universe may be modelled using the cosmological principle, implying that the spatial distribution of matter is homogeneous (symmetric under translation) and isotropic (symmetric under rotation) at large scales. The mathematical description of the space-time geometry resides in the metric tensor, from which lengths and times can be measured. The metric of an isotropic and homogeneous curved Universe is the Friedmann-Lemaître-Robertson-Walker (FLRW) metric. The space-time interval ds can be written as a function of time t and space (r, θ, ϕ) using spherical coordinates:

$$ds^2 = c^2dt^2 - a^2(t)\left[\frac{dr^2}{1-kr^2} + r^2d\theta^2 + r^2\sin^2\theta d\phi^2\right], \tag{1.1}$$

where c is the speed of light, k the space curvature and $a(t)$ the scale factor. The space curvature is set to 0 for a flat space, +1 for a closed (spherical) space and −1 for an open (hyperbolic) space. The scale factor describes the size of the Universe and its evolution with time. It is arbitrarily normalized to one at the present time in a flat space. By construction, the spatial coordinates (r, θ, ϕ) are comoving, namely independent of the expansion of the Universe.

The dynamics of the Universe may be derived using the FLRW metric with the Einstein's equation, relating the space-time geometry to the energy content. This leads to the Friedmann equations, assuming a perfect fluid (with zero viscosity) at rest, with density ρ and pressure p:

$$\left(\frac{\dot{a}}{a}\right)^2 = \frac{8\pi G\rho}{3} - \frac{kc^2}{a^2} + \frac{\Lambda c^2}{3}, \tag{1.2}$$

$$\frac{k}{a^2} + \frac{\dot{a}^2}{c^2 a^2} + \frac{2\ddot{a}}{ac^2} = -\frac{8\pi G p}{c^4} + \Lambda, \tag{1.3}$$

where $\dot{a}$ is the time derivative of the scale factor, and G is the gravitational constant. These equations are coupled with the equations of state of each component, namely the relation between density ρ and pressure p:

$$p = w\rho c^2, \tag{1.4}$$

where w is the equation of state parameter, which depends on the nature of the content. The Universe contains non-relativistic matter, grouping baryonic and dark matter, and radiation including relativistic matter. Friedmann equations involve a cosmological constant Λ appearing as an integration constant in Einstein's equation. This additional term, called dark energy, behaves like a fluid of density ρ_Λ constant over time:

$$\rho_\Lambda \equiv \frac{\Lambda c^2}{8\pi G}. \tag{1.5}$$

The pressure of dark energy is negative, which is required for the expansion of the Universe to be accelerated. In the ΛCDM standard model of cosmology, the content of the Universe is dominated by dark energy and non-relativistic, cold dark matter (CDM). Using the model of the cosmological constant, the dark energy equation of state parameter equals $w = -1$. Multiple alternative models of dark energy exist and have different values of w, which may also vary with time. One possible time parametrization is the following:

$$w(a) = w_0 + (1 - a)w_a, \tag{1.6}$$

where w_0 and w_a are assumed to be constant. In the ΛCDM model, these parameters are $w_0 = -1$ and $w_a = 0$.

The rate of expansion of the Universe is characterized by the Hubble parameter defined as:

$$H(t) \equiv \frac{\dot{a}}{a}. \tag{1.7}$$

At the present time, the Hubble parameter is noted $H_0 = 100h\,\mathrm{km\,s^{-1}\,Mpc^{-1}}$ where h is a dimensionless parameter.

The critical density of the Universe ρ_{crit} can be obtained by solving Eq. 1.2 for a flat space-time without dark energy:

$$\rho_{\mathrm{crit}} \equiv \frac{3H^2(t)}{8\pi G}. \tag{1.8}$$

The abundance parameters Ω_i (dimensionless) are defined as the ratio of the densities ρ_i to the critical density of the Universe:

$$\Omega_i \equiv \frac{\rho_i}{\rho_{\mathrm{crit}}}. \tag{1.9}$$

The curvature abundance parameter Ω_k can be analogously defined as:

$$\Omega_k \equiv \frac{-kc^2}{a^2(t)H^2(t)}, \tag{1.10}$$

and the Friedmann equation Eq. 1.2 becomes:

$$\Omega_m + \Omega_\gamma + \Omega_\Lambda + \Omega_k = 1, \tag{1.11}$$

where Ω_m, Ω_γ and Ω_Λ are non-relativistic matter, radiation and dark energy abundance parameter, respectively. This relation is true at any time, although abundance parameters are by convention defined at present time. Introducing the equations of state for each component of the Universe, the Hubble constant evolves with redshift as:

$$H(a) = H_0\sqrt{\Omega_m a^{-3} + \Omega_\gamma a^{-4} + \Omega_k a^{-2} + \Omega_\Lambda a^{-3(1+w)}}, \tag{1.12}$$

where the Ω_i are the present abundances and w is the (a priori unknown) dark energy equation of state parameter.

1.1.2. Cosmological times

The motion of galaxies with respect to a terrestrial observer, including the expansion of the Universe and the peculiar motion, leads to the shift and stretch of the emitted spectrum because of the Doppler effect. Hence, a photon emitted at a wavelength λ_e will be observed at a wavelength λ_o. The redshift z is then defined as the relative spectral shift (to the red for positive values):

$$z \equiv \frac{\lambda_o - \lambda_e}{\lambda_e}. \tag{1.13}$$

The wavelength of a photon moving at the speed of light inside a space-time described by the FLRW metric is redshifted by

$$z = \frac{1}{a(t)} - 1, \tag{1.14}$$

because of the expansion of the Universe. As a consequence, the redshift z, which is a measurable quantity, is a proxy for time t.

1.1.3. Cosmological distances

Cosmological distances between observable space-time events become challenging to estimate in a curved Universe in expansion. Multiple distance measures exist depending on the available information, such as redshift, apparent angular size or luminosity. Note that all the definitions of cosmological distances coincide at sufficiently low redshift, where the expansion of the Universe remains negligible.

The comoving distance D_c is the line-of-sight distance between two events at redshifts 0 and z respectively, excluding the expansion of the Universe:

$$D_c(z) = c \int_0^z \frac{dz'}{H(z')}. \tag{1.15}$$

The physical distance D_p is the comoving distance scaled by the expansion of the Universe, as $D_p(z) = a(z)D_c(z)$

The comoving distance between two events at the same redshift z and separated on the sky by an angle $\delta\theta$ is $D_M(z)\delta\theta$, where the transverse comoving distance D_M is defined as follows:

$$D_M(z) = \begin{cases} \frac{c}{H_0\sqrt{-\Omega_k}} \sin\left(H_0\sqrt{-\Omega_k} D_c(z)\right) & k > 0 \\ D_c(z) & k = 0 \\ \frac{c}{H_0\sqrt{\Omega_k}} \sinh\left(H_0\sqrt{\Omega_k} D_c(z)\right) & k < 0 \end{cases}. \tag{1.16}$$

The angular diameter distance D_A is defined as the ratio between the physical size l of the object and its angular size $\delta\theta$ in the sky:

$$D_A = \frac{l}{\delta\theta}. \tag{1.17}$$

It corresponds to the physical distance to the object in a flat and static Universe.

In a general FLRW Universe, it is related to the transverse comoving distance as:

$$D_A(z) = \frac{D_M(z)}{1+z}. \tag{1.18}$$

The luminosity distance D_L relates the bolometric luminosity L (integrated over wavelength) of an object and the observed bolometric flux f as:

$$D_L^2 = \frac{L}{4\pi f}. \tag{1.19}$$

In a flat Universe, the energy spreads over a sphere of radius D_L. It also corresponds to the physical distance to the object in a flat and static Universe. It is related to the transverse comoving distance as:

$$D_L(z) = (1+z)D_M(z). \tag{1.20}$$

1.1.4. Observational constraints on the cosmological model

The cosmic microwave background (CMB), in particular the temperature and polarization anisotropies, provides one of the strongest constraints on the cosmological parameters. Complementary probes include the baryon acoustic oscillations (BAO), namely the fluctuations in the density of the baryonic matter in the Universe, and supernovae (SNe). The BAO provide a standard ruler, a fixed scale length in cosmology. Similarly, the supernovae are standard(izable) candles, from the fact that the intrinsic luminosity of these events are (essentially) identical.

The latest CMB constraints from the Planck satellite on the cosmological parameters (Planck Collaboration et al. 2018) are listed in Table 1.1. Both the results from the analysis of the CMB alone, and the combined analysis of the CMB and BAO, are given. The parameter Ω_b represents the abundance of baryonic matter. The spatial curvature parameter Ω_k is in agreement with a flat Universe. The mid-point reionization redshift z_{re} and the Thomson optical depth τ are discussed in the next section. The dark energy equation of state parameter w_0, computed assuming $w_a = 0$ and combining the constraints from the CMB, BAO and SNe, is consistent with the simple cosmological constant model, with $w_0 = -1.028 \pm 0.032$. The current constraints on w_a remain relatively broad.

Note that for the cosmological parameters which explicitly depend on the Hubble constant, it is common to remove this dependence before estimating the parameters. In the case of the abundance parameters, this is performed by estimating $\Omega_i h^2$ instead of Ω_i. The reason for this comes from the historical discrepancy between the multiple estimations of the Hubble constant, different probes being subject to different biases.

Table 1.1. – Estimation of the cosmological parameters with the 68% confidence intervals from Planck Collaboration et al. 2018. The second column gives the constraints from the CMB analysis alone, the third column from the combined analysis of the CMB and BAO.

Parameter	Value	
	Planck	Planck+BAO
h	0.674 ± 0.005	0.677 ± 0.004
Ω_m	0.315 ± 0.007	0.311 ± 0.006
$\Omega_b h^2$	0.0224 ± 0.0002	0.0224 ± 0.0001
Ω_Λ	0.685 ± 0.007	0.689 ± 0.006
Ω_k	-0.0106 ± 0.0065	0.0007 ± 0.0019
z_{re}	7.67 ± 0.73	7.82 ± 0.71
τ	0.054 ± 0.007	0.056 ± 0.007

1.2. History of the Universe

1.2.1. Primordial Universe

The main steps of the evolution of the Universe are summarized in Fig. 1.1. After the Big Bang, the Universe is entirely ionized and mostly contains photons, electrons, hydrogen and helium nuclei produced in the primordial nucleosynthesis, in addition to few heavier elements. The temperature decreases because of the expansion of the Universe, until atomic nuclei and electrons recombine, so that the massive particles have no electric charge. The medium becomes transparent to light, as photons cannot interact with charged particles. This instant is called the cosmic "recombination" and happened 370 000 years after the Big Bang. The cosmic background radiation, emitted at this time of the Universe, has a blackbody spectrum at a temperature of $T \sim 3000\,\mathrm{K}$, peaking at a wavelength of one micron. Because of the expansion of the Universe, this radiation cooled to the present temperature of $T = 2.73\,\mathrm{K}$ (Planck Collaboration et al. 2018), peaking at the wavelength of one millimeter. This is called the cosmic microwave background (CMB). The isotropy of this radiation, and especially the correlation between the temperature fluctuations at large celestial distances, is one of the main argument in favor of the inflation theory. These temperature fluctuations, of the order of $\Delta T/T \sim 10^{-5}$, directly reflect the primordial matter density field.

1.2.2. Dark ages

After recombination, the Universe mainly contains a diffuse gas of neutral atoms. This period of the Universe is called the "dark ages" as no light is emitted. Despite the expansion of the Universe, structures start to grow through gravity from the

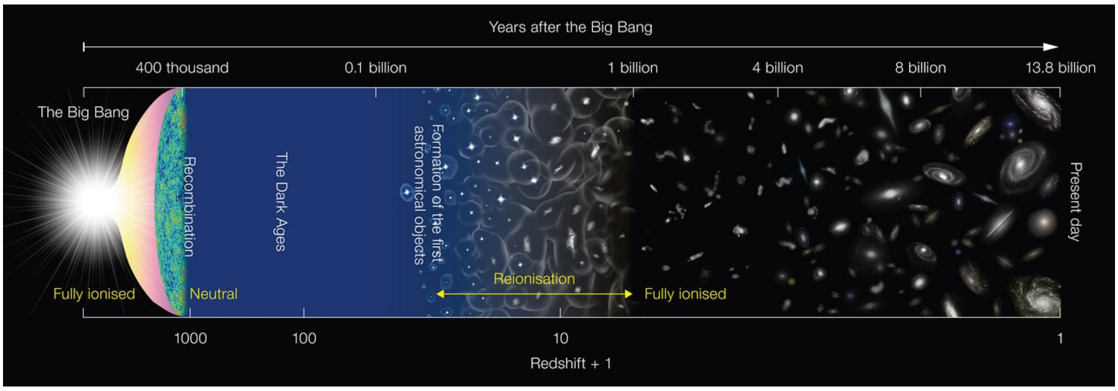

Figure 1.1. – Schematic diagram of the history of the Universe. Credit: NAOJ.

primordial fluctuations in the mass density field. In the regions with a density higher than the mean density of the Universe, the diffuse gas concentrates and becomes denser and hotter. This process persists until the first stars form, and the nuclear fusion of the hydrogen starts in the core of these stars.

1.2.3. Cosmic reionization

The first massive stars emit photons, the first light emitted in the Universe since cosmic recombination (apart from thermal emission). Photons with an energy $E > 13.6\,\mathrm{eV}$ (with a wavelength shorter than $912\,\mathrm{\AA}$), which are called ionizing or Lyman continuum photons, can ionize neutral hydrogen. Therefore, the diffuse neutral hydrogen in the vicinity of the stars progressively becomes ionized (Barkana et al. 2001). This ionized hydrogen nuclei may recombine after collisions with free electrons. If the transition occurs from the ionized to the ground state ($\mathrm{H}^+ + e^- \rightarrow \mathrm{H(1s)} + \gamma$), another ionizing photon is emitted and may ionize another hydrogen atom. In this case, there is no net recombination. For this reason, the notion of "case B" recombination is introduced, including all the transitions from the ionized state to an atomic state of hydrogen, except the one to the ground state. In contrast, the "case A" recombination includes all the transitions from the ionized to the atomic state (Osterbrock 1989).

Consequently, both ionization and recombination affect the ionized region around an emitting source, increasing and decreasing its volume, respectively. In the case of the first galaxies, the ionizing radiation is expected to be isotropic, forming bubbles of ionized hydrogen. The configuration with a balance between ionization and recombination is called a Strömgren sphere. The transition between the inner, fully ionized hydrogen and the outer, mostly neutral IGM is called the ionizing front. The ionization rate of galaxies remains low as few ionizing photons are emitted, and the ionization front remains thin. In contrast, quasars have harder spectra (namely emitting more energetic photons), leading to higher ionization rates and a thicker ionization front (Kramer et al. 2008), because of the increased mean free path of the ionizing photons.

Isolated ionized bubbles form in the high-density regions, which is called the *pre-overlap* stage of reionization (Gnedin 2000). More and more stars and galaxies form in the high-density regions, and so do the ionized bubbles. Nearby bubbles start to overlap, which corresponds to the *overlap* stage of reionization. The surface of the total ionizing front decreases, the total recombination rate decreases as well and the expansion of the bubbles accelerates. This process is called percolation. The neutral hydrogen in the low-density regions rapidly becomes ionized. Eventually, the diffuse hydrogen in the inter-galactic medium becomes almost entirely ionized. In this *post-overlap* stage, the Universe becomes transparent to ionizing light. The remaining neutral hydrogen reservoirs are high-density regions containing no ionizing source, which are called Lyman limit systems (McQuinn et al. 2011).

1.3. Reionization : theory

1.3.1. Reionization timeline

The reionization timeline, basically the time evolution of the cosmic hydrogen density in the inter-galactic medium, can be analytically modelled using simple assumptions (Madau et al. 1999; Barkana et al. 2001). We assume that the sources driving reionization are high-redshift star-forming galaxies. In the whole section, the indexes p and c indicate physical and comoving units, for clarity.

We first consider a single galaxy as ionizing source, emitting N_γ ionizing photons into a volume V_p. We assume a spherical ionized volume with a sharp ionization front. In the hypothetical case with no hydrogen recombination or cosmic expansion, the mean hydrogen number density $\langle n_\mathrm{H} \rangle$ can be expressed as:

$$\langle n_\mathrm{H} \rangle_p V_p = N_\gamma. \tag{1.21}$$

The steady state where the radius of the ionized volume remains constant over time is called a Strömgren sphere. In this case, ionization and recombination balance each other. This can be expressed as:

$$\alpha_\mathrm{B} \langle n_e n_\mathrm{H} \rangle_p V_p = \frac{dN_\gamma}{dt}. \tag{1.22}$$

where n_e is the electron number density and α_B is the case B recombination coefficient. This collision rate coefficient scales with temperature T as (Osterbrock 1989):

$$\alpha_\mathrm{B}(T) = 2.60 \times 10^{-19} \left(\frac{T}{10^4}\right)^{-0.76} \mathrm{m}^3\,\mathrm{s}^{-1}. \tag{1.23}$$

In the inter-galactic medium mostly containing hydrogen and helium, the mean electron density can be expressed as a function of the mean hydrogen density as

(Kuhlen et al. 2012):

$$\langle n_e \rangle = f_e(z) \langle n_{\rm H} \rangle \tag{1.24}$$

with

$$f_e(z) = 1 + \eta(z) \frac{Y_p}{4X_p}, \quad \eta(z) = \begin{cases} 1 & \text{singly ionized He} \quad (z > 4) \\ 2 & \text{doubly ionized He} \quad (z \leq 4) \end{cases}, \tag{1.25}$$

where X_p and Y_p are the cosmic hydrogen (H) and helium (He) mass fractions. In the primordial Universe, the heavy elements mass fraction Z_p remains negligible compared to $X_p \sim 0.75$ and $Y_p \sim 0.25$ (Steigman 2007). By definition, the mass fractions of all the elements sum to one, hence we assume that $X_p = 1 - Y_p$. Note that the hydrogen is fully ionized in the considered volume.

The time derivative of the physical volume includes both cosmic and peculiar expansions, as it can be observed from the relation with the time derivative of the physical volume:

$$\frac{dV_p}{dt} = \frac{d}{dt}(a^3 V_c) = a^3 \frac{dV_c}{dt} + 3HV_p, \tag{1.26}$$

where the last term on the right represents cosmic expansion.

The time evolution of the ionized volume (in physical units) therefore equals the difference from the recombination and ionization equilibrium:

$$\langle n_{\rm H} \rangle_p \left(\frac{dV_p}{dt} - 3HV_p \right) = \frac{dN_\gamma}{dt} - \alpha_{\rm B} f_e C_{\rm clump} \langle n_{\rm H} \rangle_p^2 V_p, \tag{1.27}$$

where $C_{\rm clump}$ is the volume-averaged clumping factor of ionized hydrogen, which is defined as:

$$C_{\rm clump} = \frac{\langle n_{\rm H}^2 \rangle}{\langle n_{\rm H} \rangle^2}. \tag{1.28}$$

The clumping factor is a measure of non-uniformity of the medium and the importance of recombination. Hence, no recombination implies that $C_{\rm clump} = 0$, low-density regions with negligible recombination have $C_{\rm clump} \sim 1$ and high-density regions have $C_{\rm clump} \sim 100$.

Once expressed in comoving units, Eq. 1.27 becomes:

$$\frac{dV_c}{dt} = \frac{1}{\langle n_{\rm H} \rangle_c} \frac{dN_\gamma}{dt} - \frac{\alpha_{\rm B}}{a^3} f_e C_{\rm clump} \langle n_{\rm H} \rangle_c V_c, \tag{1.29}$$

with $\alpha_{\rm B}/a^3$ the recombination coefficient in comoving units. This result is valid for a single ionizing source. We then take the sum over all the bubbles in a cosmological volume and divide by this volume. The ionized volume V_c becomes the (comoving) volume-averaged hydrogen ionized fraction $Q_{\rm HII}$, and the number of ionizing photons N_γ becomes the mean ionizing photon (comoving) number density $\langle n_{\rm ion} \rangle$. In addition, we need to assume a common clumping factor for the whole cosmological volume. Equation 1.29 finally becomes:

$$\frac{dQ_{\rm HII}}{dt} = \frac{\langle \dot{n}_{\rm ion} \rangle}{\langle n_{\rm H} \rangle} - \frac{Q_{\rm HII}}{t_{\rm rec}}, \tag{1.30}$$

where the mean recombination time in the IGM is defined as (Madau et al. 1999; Kuhlen et al. 2012):

$$t_{\rm rec} = \frac{1}{\alpha_{\rm B}(T_{\rm IGM}) f_e(z) C_{\rm clump} \langle n_{\rm H} \rangle (1+z)^3}, \tag{1.31}$$

with $T_{\rm IGM}$ the IGM temperature at mean density. The mean hydrogen number density (comoving) can be expressed as:

$$\langle n_{\rm H} \rangle = X_p \Omega_b \rho_c / m_p \tag{1.32}$$

with Ω_b the baryon abundance parameter, ρ_c critical mass density of the Universe (comoving, or physical at present time), and m_p the proton mass. The cosmic ionization rate, which is time-dependent, can be expressed as:

$$\langle \dot{n}_{\rm ion} \rangle = f_{\rm esc} \xi_{\rm ion} \rho_{\rm SFR}, \tag{1.33}$$

where $f_{\rm esc}$ is the escape fraction of Lyman continuum (ionizing) photons, $\xi_{\rm ion}$ is the ionizing photon production efficiency (production rate per unit star-formation rate), and $\rho_{\rm SFR}$ is the (comoving) star formation rate density (SFRD).

The list of parameters required to estimate the ionized fraction $Q_{\rm HII}$ from Eq. 1.30 are listed in Table 1.2 with their fiducial values. These parameters are usually assumed to be fixed for simplicity, although they may be time-dependent, spatial-dependent, and variable with the galaxy physical properties. Nevertheless, some of these parameters have a similar impact on reionization history, or can compensate for each other. As a consequence, reionization occurs more rapidly if the escape fraction, the star formation rate density or the IGM temperature are larger, or if the clumping factor is smaller. The most uncertain parameter remains the escape fraction.

1.3.2. Thomson optical depth

The scattering between photons and free charged particles is called Thomson scattering. In the context of cosmic reionization, photons from the cosmic microwave background may interact with free electrons in the inter-galactic medium, which are tracers of ionized hydrogen. The time-integrated impact on CMB photons is quantified with the Thomson optical depth τ, which can be predicted from reionization theory. The time evolution of this single parameter describes the progress of the reionization process.

Optical depth is a measure of the extinction of a flux of particles through a

Table 1.2. – Summary of the reionization parameters

Parameter	Unit	Fiducial value	Source
$f_{\rm esc}$		0.2	[1,2]
$\xi_{\rm ion}$	$\mathrm{s}^{-1}\,M_\odot^{-1}\,\mathrm{yr}$	$10^{53.14}$	[2]
$C_{\rm clump}$		3	[3,4]
$T_{\rm IGM}$	K	10^4	[5,6]
Y_p		0.245 ± 0.003	[7,8]

[1] Ouchi et al. 2009, [2] Robertson et al. 2015, [3] Pawlik et al. 2009, [4] Shull et al. 2012, [5] Becker et al. 2011, [6] Bolton et al. 2012, [7] Steigman 2007, [8] Peimbert et al. 2016

specific medium. It depends on the cross section σ and the density n of the medium (in physical units) as:

$$\tau = \int_0^l \sigma n \; dl' = \int_0^t v\sigma n \; dt' = \int_0^z v\sigma n \frac{dz'}{H(z')(1+z')}, \tag{1.34}$$

where l is the (physical) length crossed by the particles of velocity v. In the case of CMB photons interacting with free electrons in the ionized inter-galactic medium, the Thomson optical depth can be written as:

$$\tau = \int_0^z c\sigma_{\rm T} \langle n_e \rangle (z') H^{-1}(z')(1+z')^2 \; dz', \tag{1.35}$$

where $\sigma_{\rm T} = 6.6524587 \times 10^{-29}\,\mathrm{m}^2$ is the Thomson scattering cross section. The comoving, volume-averaged electron number density $\langle n_e \rangle$ is related to the hydrogen ionized fraction $Q_{\rm HII}$ as:

$$\langle n_e \rangle (z) = f_e(z) Q_{\rm HII}(z) \langle n_{\rm H} \rangle, \tag{1.36}$$

where $\langle n_{\rm H} \rangle$ is the total hydrogen density (including both neutral and ionized hydrogen). The Thomson optical depth, integrated from $z = 0$ to any given redshift, finally becomes:

$$\tau(z) = c \langle n_{\rm H} \rangle \sigma_{\rm T} \int_0^z f_e(z') Q_{\rm HII}(z') H^{-1}(z')(1+z')^2 \; dz' \tag{1.37}$$

1.4. Reionization: observational probes

There are multiple observational probes which may be used to constrain reionization history. Most of these methods indirectly describe the state of the IGM at high redshift, through the interaction of the neutral hydrogen or free electrons with background light. In this section, I present a list of probes and introduce the physical objects and processes involved. Figure 1.2 summarizes a few recent

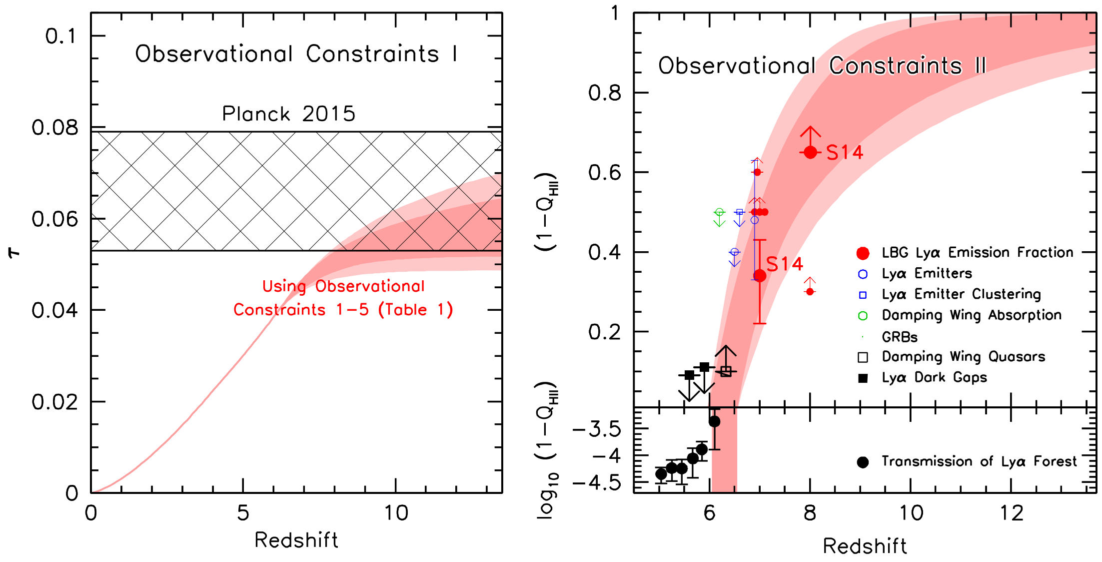

Figure 1.2. – Evolution of the integrated Thomson optical depth (*left*) and the hydrogen neutral fraction (*right*) with redshift. The red shaded area illustrate the reionization history models from Bouwens et al. 2015a. The markers and the checkered area indicate observational constraints from multiple probes introduced in Sect. 1.4. Credit: Bouwens et al. 2015a

constraints from these probes.

1.4.1. Quasars

Quasars are the brightest objects in the Universe. The spectral energy distribution of these objects present a featureless power-law continuum with strong emission lines, in particular the Lyman alpha line (at a wavelength of $\lambda_{\mathrm{Ly}\alpha} = 1216\,\text{Å}$ and an energy of $E = 10.2\,\mathrm{eV}$). The clouds of neutral hydrogen atoms, in the foreground of the quasar, may absorb the Lyα photons at the redshift of clouds, namely at a wavelength of $\lambda_{\mathrm{Ly}\alpha}(1+z)$. The width of the absorption line depends on the size and temperature of the cloud. The multiple absorption lines integrated along the line-of-sight of the quasars lead to the so called Lyman alpha forest. The ionization of the IGM can therefore be assessed measuring the redshift and the optical depth of each of these neutral hydrogen clouds. Before the end of reionization, neutral hydrogen is so abundant in the IGM that all the photons are absorbed. In the spectrum of the quasar at $z > 6$, this leads to a strong absorption feature with no flux blueward of Lyman alpha. This is called the Gunn-Perterson effect, which has been observed for the first time in the spectrum of quasars at $z > 6$ (Becker et al. 2001). In contrast, the spectrum of quasars at $z < 6$ do not present this effect, indicating a low neutral hydrogen fraction ($< 10^{-3}$). Using a sample of 19

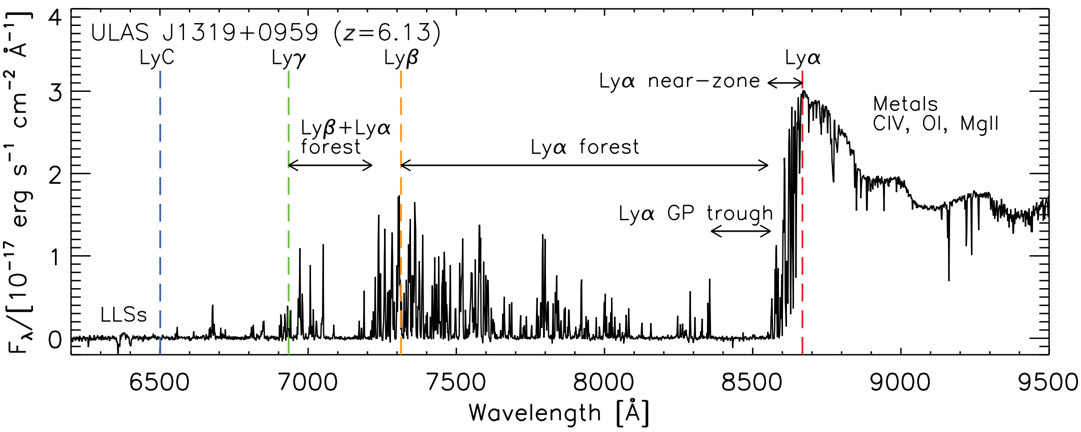

Figure 1.3. – Spectrum of the quasar ULAS J1319+0959 at redshift $z = 6.13$, presenting some of the key spectral features mentioned in Sect 1.4.1. Credit: Becker et al. 2015.

quasars at redshift $z \sim 6$, Fan et al. 2006 constrained the ionization state of the IGM and concluded that cosmic reionization is complete at $z \sim 6$. More recent studies confirmed this statement using larger samples of quasars (Bolton et al. 2011; McGreer et al. 2015). Figure 1.3 represents a quasar spectrum and illustrates the multiple absorption features that can be used to constrain reionization.

1.4.2. Lyman alpha emitters

Lyman alpha emitters (LAEs) are galaxies presenting a strong Lyman alpha emission line. These galaxies can be observed even if the continuum emission remains undetected. These sources are typically identified using narrow-band photometry, and characterized with spectroscopy.

The LAE fraction is the ratio between the number of LAEs and the total number of galaxies, typically UV-bright starburst galaxies, at a given redshift. For the galaxy sample at the denominator, Lyman break galaxies (LBG) can be used, which are selected using the Lyman break in the rest-frame UV with broad-band imaging (see Sect. 1.6.2). As redshift increases, galaxies have younger stellar populations and the dust content decreases. More Lyman alpha photons are emitted per galaxy and less are absorbed by dust, so the LAE fraction increases (Stark et al. 2010; Stark et al. 2011). At the epoch of reionization, the absorption of Lyman alpha photons by the neutral hydrogen in the IGM drastically increases. In addition, the fraction of the baryonic matter inside the IGM increases with increasing redshift. The LAE fraction is expected to decrease with increasing redshift at $z > 6$, so that a turn-over in the evolution of the LAE fraction with redshift may reflect the end of reionization (Fontana et al. 2010; Pentericci et al. 2011; Pentericci et al. 2014; Schenker et al. 2014). However, the Lyman alpha visibility depends also on the physical properties of the galaxy population, the dust content, and the distribution and kinematics of neutral hydrogen (Verhamme et al. 2006; Verhamme et al. 2008; Hayes et al. 2014). In the case of saturated absorption, photons redward of the Lyman alpha resonance may be affected, leading to the red damping wing feature.

The observed luminosity function of LAEs provides additional constraints on the evolution of galaxies and the IGM. The shape and amplitude of the LAE luminosity function remain constant over redshift for $3 < z < 6$, meaning that the Lyα emission increases with redshift, in the same time as the IGM opacity, the two effects cancelling out (Ouchi et al. 2008). Furthermore, the attenuation of LAEs is stronger if they are closer to neutral hydrogen clouds. As a consequence, the spatial distribution of the neutral hydrogen clouds impacts the apparent distribution of galaxies, and so the clustering of LAEs (e.g., Ouchi et al. 2010).

1.4.3. Gamma-ray bursts

The gamma-ray bursts (GRB) are the brightest electromagnetic events in the Universe. These events may result from the collision of compact objects (black holes, neutral stars) or the collapse of massive stars. The light curve (emission as a function of time) consists of a short flash followed by a longer afterglow. The time scales may vary a lot among events. The long-duration GRBs, with a flash longer than two seconds, lead to bright and long (weeks) afterglows.

The smooth spectrum of the GRB afterglow is subject to the Gunn-Peterson effect, similarly to quasars. In addition, the neutral hydrogen gas in the host galaxy produces a damping of the Lyman alpha line at redder wavelengths, called the damping wing. The modelling of this damping wing enables the ionization state of the medium to be estimated (e.g., Totani et al. 2006; Chornock et al. 2013). As an example, Patel et al. 2010 inferred that $Q_{\mathrm{HII}} \geq 0.27$ (with 95% confidence) using a GRB at $z = 6.7$. Regarding the study of reionization, GRBs have two advantages compared to quasars. Firstly, GRBs are widely distributed among low-mass galaxies at high redshift, whereas quasars are only located in high-density regions likely to be ionized. Secondly, GRBs can be observed at very high redshift (see Cucchiara et al. 2011 for a tentative event at $z = 9.4$). However, these events are extremely rare. With the space-based multi-band astronomical variable objects monitor (SVOM), to be launched in 2022, the detection of GRBs at high redshift will be possible through optical and infrared observations (Wei et al. 2016).

1.4.4. Hydrogen 21-cm line

The transition between two hyperfine energetic levels of the hydrogen atom in its ground state emits (or absorbs) a 21 cm photon. In the configuration where the spins of the proton and the electron are anti-parallel, the energy of the hydrogen atom is slightly lower than where the spins are parallel (e.g., Pritchard et al. 2012). The 21-cm line, in emission or in absorption, is therefore a *direct* tracer of neutral hydrogen, which can be used to characterize the Universe from the dark ages till the end of cosmic reionization. The measurement of the photons emitted through this transition is challenging for multiple reasons. Firstly, the transition timescale is of the order of 1 Myr, meaning that only a significant amount of neutral hydrogen may produce a strong 21-cm feature. Secondly, the 21-cm photons emitted during the epoch of reionization are redshifted to wavelengths contaminated by foreground astrophysical and terrestrial sources.

Recently, the Experiment to Detect the Global Epoch of reionization Signature (EDGES; Bowman et al. 2008) claimed a detection with an unexpectedly strong and wide absorption feature (Bowman et al. 2018). It is still not clear what physical processes could produce such feature. These results will need to be confirmed with the Square Kilometer Array (SKA [1]). With its collecting area of $0.4\,\mathrm{km}^2$, SKA will notably measure the 21-cm anisotropy power spectrum over $1000\,\mathrm{deg}^2$ at $z \sim 6$, and over $10\,\mathrm{deg}^2$ to $z \sim 27$ (Koopmans et al. 2015). This will give the first constraints on the state of the Universe at this time of its evolution.

1.4.5. Cosmic microwave background

The photons from the cosmic microwave background may interact with free electrons through Thomson scattering. The scattered CMB photons become polarized, leading to a damping in the anisotropy power spectrum, measurable from the CMB analysis. The integrated effect of Thomson scattering from recombination to the present day, which is related to the total column density of free electrons, is quantified by the Thomson optical depth τ. The latest results from the Planck satellite (Planck Collaboration et al. 2018) give the reionization redshift mid-point $z_{\mathrm{re}} = 7.67 \pm 0.73$ and the optical depth $\tau = 0.054 \pm 0.007$ (68% confidence intervals).

1.5. Sources of the reionization

Star-forming galaxies are presumably the major contributors to the reionization process over cosmic time (e.g., Finkelstein et al. 2019). Blue massive stars formed within galaxies therefore emitted most of the Lyman continuum photons necessary to ionize the inter-galactic medium, which also managed to escape from galaxies. In addition, binary stars produce more Lyman continuum photons than single stars, and the interactions between stars increase the effective escape fraction of the host galaxies (e.g., Secunda et al. 2020). The census of star-forming galaxies at high-redshift, quantified using the UV luminosity function (LF), gives an estimate the amount of star-formation in the Universe (see Sect. 1.3) which is related to the number of emitted ionizing photons. The evolution of the observed UVLF with redshift represents the evolution of galaxy populations with time, as well as the state of the IGM. Contrarily to quasars, galaxies are more numerous at

1. https://www.skatelescope.org/

very high redshift. As an illustration, the most distant galaxy ever observed is at $z = 11.1$ (Oesch et al. 2016) and the most distant quasar is at $z = 7.5$ (Bañados et al. 2018). For these reasons, the search for star-forming galaxies at $z > 6$ is of major importance to constrain the reionization timeline, under the assumption that star-forming galaxies dominated the ionizing photon budget.

Active galactic nuclei (AGN) may also contribute to the total ionizing photon budget in high-mass galaxies. The accretion of matter by a supermassive black hole in the center of the galaxy produces a specific radiation spectrum with strong emission lines, notably at short wavelengths. The importance of the AGN contribution to the reionization process is still unclear (e.g., Laporte et al. 2017).

1.5.1. Galaxy UV luminosity function

The galaxy luminosity function $\phi(L, z)$, at a given redshift z, is the number of galaxies N per comoving volume V per interval of intrinsic luminosity L. In this case, the luminosity is monochromatic and expressed in frequency units (in erg/s/Hz). This may be written as:

$$\phi(L, z) = \frac{d^2N}{dV dL}(L, z). \tag{1.38}$$

The differential comoving volume dV depends on the surveyed area and the assumed cosmology as:

$$dV = \frac{c}{H(z)} D_M^2(z) d\Omega dz, \tag{1.39}$$

where $d\Omega$ is the solid angle element. The luminosity function in the rest-frame UV is computed from the observed galaxy luminosities, uncorrected for dust attenuation. The observed UV luminosity function (UVLF) of galaxies may be fitted with a Schechter function (Schechter 1976), parametrized as:

$$\phi(L)dL = \frac{\phi^*}{L^*} \left(\frac{L}{L^*}\right)^\alpha \exp\left(-\frac{L}{L^*}\right) dL, \tag{1.40}$$

where L^* is the turn-over luminosity, ϕ^* the normalization density, in Mpc^{-3}, and α the faint-end slope. The Schechter function, expressed as a function of absolute magnitude M (see Sect. 1.6.4), becomes:

$$\phi(M)dM = 0.4 \ln(10)\, \phi^*\, 10^{-0.4(\alpha+1)(M-M^*)} \exp(-10^{-0.4(M-M^*)}) dM, \tag{1.41}$$

where M^* is the turn-over magnitude. The UV luminosity density can be estimated by integrating the UVLF over luminosity to a given lower limit $L_{\rm min}$ as:

$$\rho_{\rm UV}(z) = \int_{L_{\rm min}}^{\infty} L\phi(L, z) dL. \tag{1.42}$$

In the case of a Schechter luminosity function, the luminosity density can be expressed analytically:

$$\rho_{\mathrm{UV}} = \Gamma\left(\alpha + 2, \frac{L_{\mathrm{min}}}{L^*}\right) \phi^* L^*, \tag{1.43}$$

where Γ is the upper incomplete gamma function. It is required to set a lower integration limit if $\alpha \leq -2$, as the luminosity density would diverge otherwise. This result is only true assuming the slope remains the same to $L_{\mathrm{min}} = 0$. However, below a given mass (as an example, the mass of the Sun), a source cannot be considered as a galaxy anymore. Therefore, one expects a turn-over at the very faint end of the luminosity function. The exact magnitude of this turn-over at high-redshift is still under debate (Livermore et al. 2017; Bouwens et al. 2017), and has significant implications on the resulting UV luminosity density.

The UVLF measurement may be subject to several biases, such as contaminants artificially increasing the observed number counts, and incompleteness leading to the contrary. Gravitational lensing, in particular in the strong lensing regime, leads to the magnification of a fraction of the galaxies of interest. Magnification increases the apparent surface of a source while maintaining surface brightness, so that the total flux of the source increases. This leads to the so called magnification bias, distorting especially the very bright end of the luminosity function (Mason et al. 2015). The uncertainties affecting the LF measurement are Poisson errors, from the counting of rare objects, and cosmic variance. Poisson errors increase as the square root of the number of objects, so that the main limitations are the size and the depth of the surveys. Cosmic variance is the uncertainty in the observational estimate of the galaxy number density from the underlying large-scale structure fluctuations (Trenti et al. 2008). For a given survey, cosmic variance is related to the typical clustering scale. Therefore, cosmic variance decreases if the size of the survey increases, if the mean redshift increases, or if the mean stellar mass decreases (Moster et al. 2011).

The recent LF measurements from Bouwens et al. 2015b, for $z \geq 4$ and at the rest-frame wavelength of 1600 Å, are illustrated in Fig. 1.4. The LFs effectively present a rapid drop at bright magnitudes and a linear trend at the faint end, with a transition situated at $M^* \sim 21$ mag. The faint-end slope typically decreases with increasing redshift, reaching $\alpha \sim -2$ at $z > 7$.

1.5.2. Cosmic star formation rate density

The rest-frame UV luminosity of a galaxy is dominated by the emission from young blue massive stars. Since these stars have a short lifetimes (the order of millions of years), the UV luminosity is an indicator of the recent star formation within the galaxy, in particular at 1500 Å. The relation between the two physical

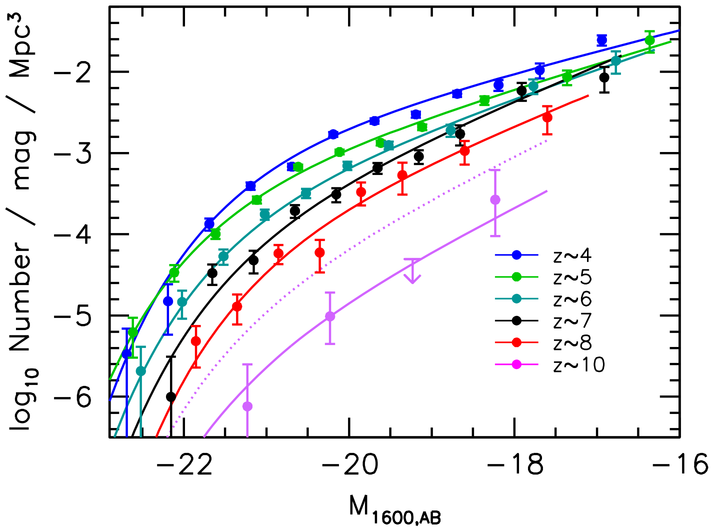

Figure 1.4. – UV luminosity function measured from $z \sim 4$ to $z \sim 10$. The markers are non-parametric (binned) estimates of the UVLF. The solid lines are parametric estimates. The dashed line is an extrapolation of the $z \sim 4-8$ LF to $z = 10$. Source: Bouwens et al. 2015b

quantities can be written as:

$$\mathrm{SFR} = \kappa_{\mathrm{UV}} \times L_{\mathrm{UV}}. \tag{1.44}$$

The parameter κ_{UV} depends on the wavelength of interest, the initial mass function (IMF), the star formation history (SFH) and the metallicity enrichment history. The initial mass function describes the mass distribution of newly formed stars in a galaxy. Assuming a Salpeter IMF (Salpeter 1955) within the $0.1 - 100\,M_\odot$ mass range and a constant SFR over time, the conversion factor remains roughly constant with redshift (within 20%) and can be set to (Madau et al. 2014):

$$\kappa_{\mathrm{UV}} = 1.15 \times 10^{-28}\,M_\odot \mathrm{yr}^{-1}(\mathrm{erg/s/Hz})^{-1}. \tag{1.45}$$

This conversion factor tends to increase as redshift or metallicity increases, nevertheless these two effects compensate each other, as younger high-redshift galaxies mostly have lower metallicities. Using Eq. 1.44, the luminosity density ρ_{UV} can be converted to the star formation rate density (SFRD), noted ρ_{SFR}, which can be used to constrain cosmic reionization.

Dust attenuation

The attenuation by interstellar dust may severely impact the UV light emitted by young massive stars, which is absorbed and re-emitted in the far-infrared. By definition, attenuation includes both extinction, namely the absorption of photons directly emitted towards the observer, and the scattering of photons into the observer line-of-sight. This process depends on both the dust grain characteristics and the geometry of stars and dust within galaxies. The resulting attenuation is a function of wavelength, which is described by the attenuation law. Attenuation is globally increasing with decreasing wavelengths, so that the rest-frame UV emission from bright stars may be strongly attenuated, in comparison with the optical or infrared emission. The attenuation in the rest-frame UV is defined as the ratio between the observed $f_{\mathrm{UV},o}$ and emitted $f_{\mathrm{UV},e}$ fluxes, or expressed in magnitude units:

$$A_{\mathrm{UV}} = -2.5 \log_{10} \left(\frac{f_{\mathrm{UV},o}}{f_{\mathrm{UV},e}} \right). \tag{1.46}$$

As a consequence, the observed SFRD computed from the UVLF uncorrected for dust attenuation does not represent the total star formation. Dust attenuation may be estimated from the observed UV spectral slopes β. Using a sample of UV-selected starburst galaxies, Meurer et al. 1999 measured the relation between β and the infrared excess IRX, defined as:

$$\mathrm{IRX} = \frac{L_{\mathrm{IR}}}{L_{\mathrm{UV}}}, \tag{1.47}$$

where L_{IR} is the bolometric luminosity of the galaxy (integrated over wavelength), with a dominant component in the far-infrared. In Eq. 1.47, the UV luminosity in erg/s is computed as νL_ν, where ν is the frequency and L_ν the monochromatic luminosity per unit frequency. The infrared luminosity is a measure of the energy absorbed by dust, mostly in the UV, and re-emitted as a thermal radiation. Hence, the sum of the UV and infrared luminosities is a proxy for the total SFR of the galaxy. After calibrating the IRX with dust attenuation, the relation between attenuation and the UV slope becomes: (Meurer et al. 1999):

$$A_{\mathrm{UV}} = 4.43 + 1.99\beta \,\mathrm{mag}. \tag{1.48}$$

With this equation, the mean attenuation of a galaxy sample with a given distribution of UV slopes can be estimated (e.g., Bouwens et al. 2015b). However, this relation assumes an intrinsic UV spectral slope of $\beta_0 = -2.23$, which may not be adequate for very high-redshift galaxies with low metallicity stellar populations (Wilkins et al. 2013; Reddy et al. 2018).

Cosmology dependence

The cosmological parameters assumed in the computation of the UV luminosity functions may vary among studies. Nevertheless, observable quantities, such as flux, target redshift, survey area and number counts, are independent of the cosmology. Constructed from these quantities, the observed monochromatic flux f_{UV} (in the rest-frame UV), per redshift bin dz per solid angle $d\Omega$ (Maniyar et al. 2018):

$$\frac{d\,f_{\mathrm{UV}}}{dzd\Omega} = \frac{(1+z)}{4\pi D_L^2}\frac{\rho_{\mathrm{SFR}}}{\kappa_{\mathrm{UV}}}\frac{dV}{dzd\Omega}, \tag{1.49}$$

may be used to modify the SFRD measurement from one cosmology to another. The $(1+z)$ factor comes from the conversion from observed to emitted frequency units, which is not impacted by the assumed cosmology. Similarly, the assumed IMF (involved in the conversion factor κ_{UV}) may be modified through a multiplicative correction (Madau et al. 2014).

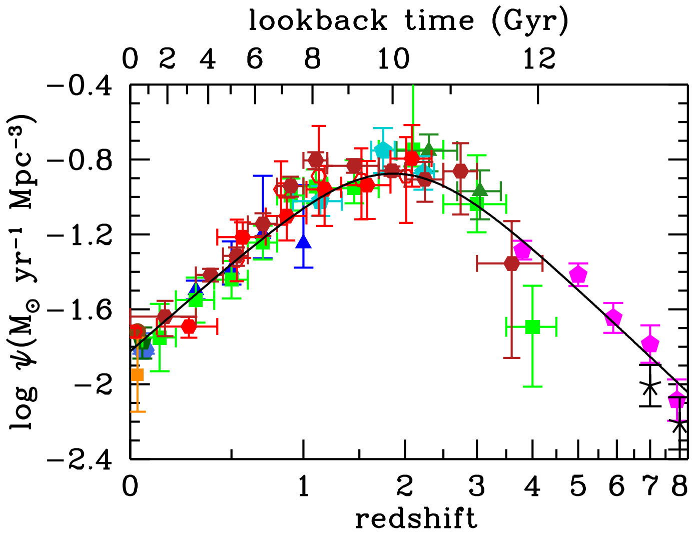

Figure 1.5. – Cosmic star formation rate density as a function of redshift, as compiled by Madau et al. 2014. The green, blue, black and pinks markers indicate SFRDs from UVLFs corrected for dust attenuation. The red points are SFRDs computed from infrared LFs.

Observational constraints

Figure 1.5 represents the SFRD measurements compiled by Madau et al. 2014, using galaxy luminosity functions in the rest-frame UV and in the infrared. The UV estimates are corrected for dust attenuation. The redshift evolution of the SFRD is parametrized as:

$$\rho_{\mathrm{SFR}}(z) = a\frac{(1+z)^b}{1+[(1+z)/c]^d}\,M_\odot\,\mathrm{yr}^{-1}\,\mathrm{Mpc}^{-3}, \tag{1.50}$$

with $a = 0.015$, $b = 2.7$, $c = 2.9$ and $d = 5.6$ (Madau et al. 2014). Starting from the present time, the SFRD increases with redshift up to a peak $z \sim 2$, referred as “cosmic noon”, then decreases up to cosmic reionization. The shape of the SFRD at $z > 8$ is still under debate in the literature (McLeod et al. 2016), because of the limited number of galaxies identified at this epoch. The most recent results indicate that the main contribution to the SFRD at high-redshift comes from low-mass galaxies, which have larger escape fraction than high-mass galaxies (Finkelstein et al. 2019).

1.6. Finding the first galaxies

The discovery of high-redshift galaxies remains driven by broad-band photometry. Astronomical images have the advantage to simultaneously observe a large number of sources over large areas, and to reach improved depths compared to spectroscopy. Broad-band filters are generally sufficient to capture the main spectral features in the emission spectra of galaxies. Nevertheless, spectroscopic observations can be useful to confirm the redshift of selected galaxy candidates. In this section, I present existing large imaging surveys, from both space and ground-based observatories. Then, I discuss the commonly used techniques to identify and characterize high-redshift galaxies from photometric data, focusing on optical and near-infrared broad-band imaging.

1.6.1. Imaging surveys

We live in an era where we benefit from space telescopes in addition to ground-based observatories. Observing from space overcomes many ground-based telescope limitations, including the atmospheric distortions, limiting the resolution, and the background emission (especially in the infrared), limiting the depth of the image. In addition, space observations overcome the issue of atmospheric transmission. In contrast, the technical restrictions from the space launch and the space environment make these missions more expensive to build and maintain, and limit the size of the primary mirror. Space and ground-based telescopes are therefore complementary. The deepest observations of the Universe were taken from space, with the *Hubble* space telescope (*HST*) and its on-board Advanced Camera for Surveys (ACS) in the optical and the Wide-Field Camera 3 (WFC3) in the near-infrared. In addition, the mid-infrared images from the *Spitzer* space telescope, with the Infrared Array Camera (IRAC), provided complementary information to characterize high-redshift objects. In the future, the *James Webb* space telescope (*JWST*) will revolutionize near-infrared astronomy with high-resolution near- and mid-infrared imaging and spectroscopy (see chapter 2).

The complete description of the galaxy population at high redshift requires galaxies to be identified over a large range of intrinsic brightnesses, to properly constrain the galaxy luminosity function. For this reason, extragalactic imaging surveys typically have a “wedding-cake” structure, with deep pencil-beam regions to detect faint galaxies, and shallow wide-field regions to observe rare bright galaxies.

One of the major surveys in the context of galaxy evolution is the Cosmic Assembly Near-infrared Deep Extragalactic Legacy Survey (CANDELS; Grogin et al. 2011; Koekemoer et al. 2011), covering a total of 750 arcmin^2 with deep *HST* imaging. The CANDELS fields include the Great Observatories Origins Deep Survey (GOODS; Giavalisco et al. 2004) with two fields, COSMOS (Scoville et al. 2007), the Extended Groth Strip (EGS; Davis et al. 2007), and the United Kingdom infrared telescope (UKIRT) Infrared Deep Sky Survey (UKIDSS; Lawrence et al. 2007) Ultra-deep Survey field (UDS; Cirasuolo et al. 2007). Furthermore, the *Hubble* Ultra-Deep Field (HUDF) covering 4.7 arcmin^2 (e.g., Illingworth et al. 2013) benefits from the deepest astronomical images ever taken, reaching depths of 30 mag in the optical and the near-infrared. Alternatively, the *Hubble* Frontier Fields (HFF; Lotz et al. 2017) include deep imaging of six massive galaxy clusters, to observe background galaxies magnified through gravitational lensing. With this set of observations, thousands of galaxies at $z \geq 4$ were identified and the galaxy UV luminosity function was estimated up to $z \sim 10$ (e.g., Bouwens et al. 2015b; Finkelstein et al. 2015; McLeod et al. 2016; Oesch et al. 2018).

Deep imaging from ground-based telescopes also enabled the analysis of the high-redshift galaxy population. The COSMOS field (Scoville et al. 2007, see chapter 3), with the Suprime-Cam optical images from the Subaru telescope (Miyazaki 2015) and the UltraVISTA near-infrared images from the VISTA telescope (McCracken et al. 2012), led to the discovery of particularly rare and bright galaxies at $z > 6$ (e.g., Bowler et al. 2015). Using a set of imaging data from the COSMOS field, in addition to images from the Canada-France-Hawaii telescope (CFHT), thousands of galaxies at $2 < z < 6$ were selected and observed with multi-slit spectroscopy in the Visible Multi-object Spectrograph (VIMOS) Ultra Deep Survey (VUDS; Le Fèvre et al. 2015) on the very large telescope (VLT). In preparation for the deep fields covered with the future *Euclid* mission, the on-going Cosmic Dawn Survey assembles multi-wavelength data from the optical to the mid-infrared (see Sect. 3.2), to provide stellar mass measurements for $3 < z < 12$ galaxies. With the Hyper Suprime-Cam (HSC) from the Subaru telescope, and in particular the on-going Subaru Strategic Program (SSP; Aihara et al. 2018), about 1400 deg^2 of the sky will be observed in multiple optical broad bands. Using the first 100 deg^2 of this survey, Ono et al. 2018 selected more than 600 galaxies at $6 < z < 7$.

1.6.2. Selecting high-redshift galaxies

In order to have a realistic view of the distant Universe, one needs to find samples of high-redshift galaxies which are representative of the real galaxy population. This requires the galaxy samples to be complete, including as many real high-redshift galaxies as possible, and pure, without containing contaminants such as low-redshift galaxies, stars or artifacts. The selection of high-redshift galaxies from broad-band imaging may be challenging, since the observed colors can be caused by distinct spectral features.

Lyman break galaxies

Star-forming galaxies at high-redshift typically present a strong drop in the observed emission blueward of the Lyman limit at 912 Å, with respect to the smooth rest-frame UV emission redward of Lyman alpha at 1216 Å. This drop, caused by the absorption of the emitted UV photons by the inter-stellar medium, is called the Lyman break. The galaxies presenting this spectral feature are named Lyman break galaxies (LBG). During the epoch of reionization at $z > 6$, the neutral hydrogen in the inter-galactic medium absorbs the flux blueward of Lyman alpha, leading to an even stronger drop in the galaxy spectrum.

The Lyman break in the galaxy spectrum may be identified using the observed magnitudes in three bands, or equivalently, two colors. This is mainly performed with broad-band imaging (e.g., Steidel et al. 1996). The first band must be blueward of the break, the second one right redward of the break, and the third one at even redder wavelengths. The color computed from the first two adjacent bands describes the amplitude of the break, and the color from the two bands redward of the break constrains the rest-frame UV slope, which depends on the galaxy physical properties, mostly the star formation rate and the dust content. The flux blueward of the break, especially blueward of the first band, is expected to be zero (e.g., Bouwens et al. 2015a). These features are illustrated in Fig. 1.6, where star-forming galaxies at different redshifts are observed through broad-band filters. As the Lyman break shifts to the red, the observed flux in the blue bands drops and the Lyman break color becomes redder. In the color-color plot, this leads to the tracks moving vertically since the rest-frame UV color remains stable.

This technique has the advantage of only relying on galaxy photometry. It showed to be particularly efficient and provided star-forming galaxy samples with relatively homogeneous properties (e.g., Giavalisco 2002). Nonetheless, the Lyman break criteria are based on a priori knowledge of mean integrated IGM transmission, the Lyman break intrinsic to the galaxies, and the Lyman continuum escape fraction (Thomas et al. 2017).

Spectral energy distribution fitting

An alternative approach relies on spectral energy distribution (SED) templates of galaxies, constructed from spectroscopic observations or stellar population synthesis models (e.g., Bruzual et al. 2003). Using these templates with known physical properties, the expected magnitudes in the considered photometric bands are computed using the filter transmission curves. The colors of each template are compared to the observed magnitudes of the detected source, and the template presenting the best fit is expected to correctly describe the source. The physical parameters of this source, such as the redshift and stellar mass, can therefore be estimated. Instead of using the best-fit template, these physical parameters may be estimated from the median of the physical parameter distribution, computed using all the fitted templates.

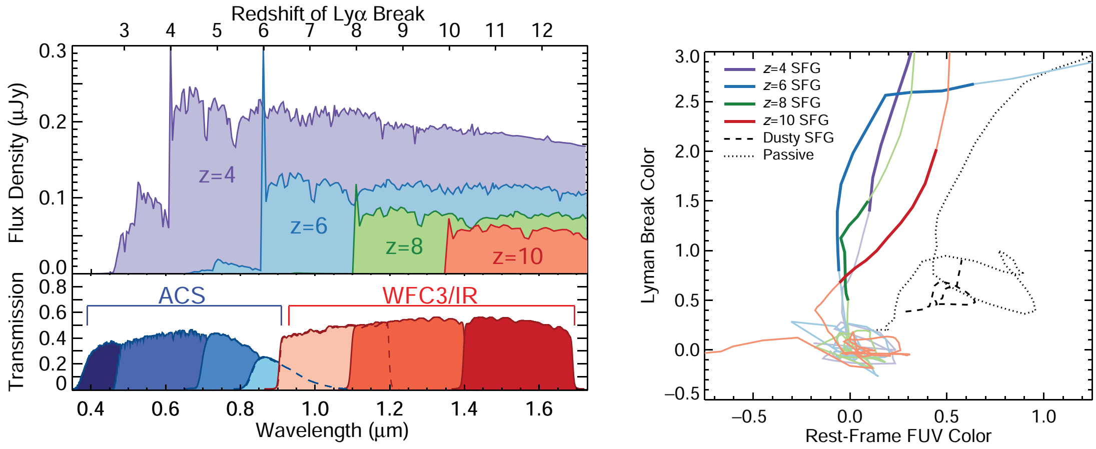

Figure 1.6. – *Left panel:* Spectral flux density (in frequency units) of a star-forming galaxy at four different redshifts. The transmission curves of the *HST* optical ACS/B, V, i', z' bands and near-infrared WFC3/Y, J, H bands are also indicated (in increasing wavelengths). *Right panel:* Color-color plot showing the tracks of the star-forming galaxy with redshift. The rest-frame FUV colors are $V - i'$, $z' - Y$, $J - H$ and $H - [3.6]$ for redshifts $z = 4, 6, 8, 10$, where [3.6] is the *Spitzer*/IRAC channel 1 band. The Lyman break colors are $B - V$, $i' - z'$, $Y - J$ and $J - H$, respectively. Source: Finkelstein 2016

One advantage of the SED-fitting approach is that it uses all the available colors of the sources. Specific spectral features in addition to the Lyman break, such as the Balmer break, may provide key information to describe the detected sources. Le Fèvre et al. 2015 showed that a large fraction of high-redshift galaxies may be missed using the two-color Lyman break criteria, in comparison to SED-fitting. However, the results depends on the assumptions involved in the fitted galaxy templates, as well as the mean IGM properties (Thomas et al. 2017).

In this thesis, I mainly used the software `LePhare` (Arnouts et al. 2002; Ilbert et al. 2006) to perform SED-fitting. This program is based on a χ^2 fitting method between the theoretical and observed fluxes. At a redshift z and for a template T, the χ^2 is computed as:

$$\chi^2(z, T) = \sum_i \frac{(F_{\mathrm{obs},i} - \alpha F_{\mathrm{tem},i}(z, T))^2}{\sigma^2_{\mathrm{obs},i}}, \tag{1.51}$$

where i represents one filter, $F_{\mathrm{obs},i}$ is the observed flux in this filter, $\sigma_{\mathrm{obs},i}$ is the observed flux uncertainty, and $F_{\mathrm{tem},i}$ is the predicted flux using this template at this redshift. The normalization factor α can be computed analytically by solving

$\partial\chi^2/\partial\alpha = 0$, giving (Arnouts et al. 1999):

$$\alpha = \sum_i \left(\frac{F_{\mathrm{obs},i} F_{\mathrm{tem},i}}{\sigma^2_{\mathrm{obs},i}} \right) \Big/ \sum_i \left(\frac{F^2_{\mathrm{tem},i}}{\sigma^2_{\mathrm{obs},i}} \right). \tag{1.52}$$

The χ^2 value can be converted into a probability $p = \exp\left(-\chi^2/2\right)$. The redshift probability distribution function of one detected source is then computed with a Bayesian approach, using the probability of all the templates at a given redshift.

1.6.3. Contaminants

As discussed in the previous section, the selection of high-redshift galaxies mostly relies on the observed colors of these sources. However, there are other astrophysical objects presenting similar colors, which may contaminate the selected galaxy samples. Figure 1.7 illustrates the similarity between the SED of a high-redshift galaxy and its potential contaminants. In addition, the transmission curves of the *HST* bands are indicated. Since high-redshift galaxies are only detected in the near-infrared, only few bands can be typically used to perform SED-fitting. At the wavelength of the expected Lyman break, contaminants also present red near-infrared colors in the observed frame, especially $(z - J)$ in this case. Hence, it may be difficult to discriminate contaminants from the observed colors around the Lyman break.

Low-redshift galaxies

Galaxies at low redshift ($z \sim 1 - 2$) are the main contaminants to the high-redshift ($z > 5$) galaxy samples. Even though deep multi-wavelength imaging may be sufficient to separate these two galaxy populations, the number density of low-redshift galaxies is few orders of magnitude higher. As a consequence, more low-redshift galaxies may be assigned a high photometric redshift than the contrary. Red dusty galaxies at low redshift presents a red optical continuum which may be mistaken for a Lyman break (Tilvi et al. 2013). These galaxies may be rejected using a strong selection on the UV slope of the desired galaxy sample. However, this would bias the sample towards blue, unattenuated star-forming galaxies at high redshift. In addition, blue low-redshift galaxies with a strong Balmer break, at 4000 Å in the emission frame, may be confused with a high-redshift galaxy with a Lyman break (Le Fèvre et al. 2015). This degeneracy may have a strong impact if the set of imaging bands do not cover the Lyman break at low redshift.

Brown dwarfs

Stars from the Milky Way are also an important source of contamination, in particular cold brown dwarfs. Brown dwarfs are stars which did not start hydrogen fusion in the core, and have typical masses of $M < 0.5 M_\odot$ and effective temperatures

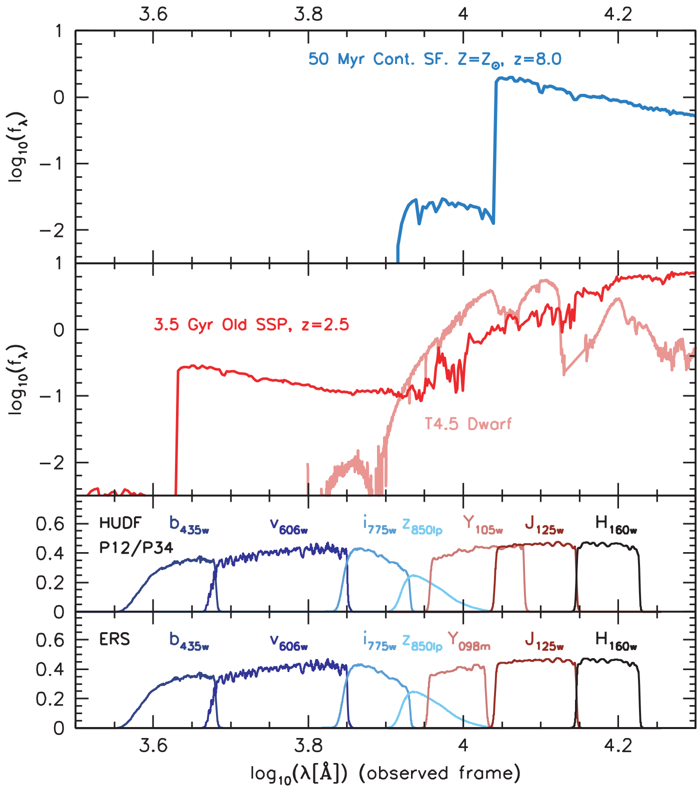

Figure 1.7. – Spectral flux density (in wavelength units) of a high-redshift galaxy and its potential contaminants. *Top panel:* Model SED of a high-redshift $z = 8$ star-forming galaxy. *Middle panel:* Observed SED of a low-mass star (class T) and model SED of a low-redshift $z = 2.5$ galaxy. *Bottom panels:* Transmission curves of the *HST* bands available in the HUDF and the ERS fields. Source: Lorenzoni et al. 2011

of $T_{\rm eff} < 4\,000\,{\rm K}$ (Pecaut et al. 2013). The spectrum of a stellar object typically consists of blackbody thermal emission, in addition to spectral lines from the surface or the atmosphere of the star. In the case of brown dwarfs, the spectral lines dominate the emission in the optical. However, the absorption by water, methane, ammonia and/or metals impacts the optical part of the spectrum, so that these objects are only detectable in the near-infrared. Figure 1.8 illustrates the spectrum of multiple brown dwarf models, and presents the comparison with the blackbody radiation at similar effective temperatures. Stellar objects are classified by spectral types according to their spectral features. The types of brown dwarfs include the M, L, T and Y types, ordered in decreasing temperatures. The type Y of brown dwarfs is defined by the strong absorption feature at $1.5\,\mu$m, presumably caused by ammonia (Cushing et al. 2011; Kirkpatrick et al. 2012). The properties of the coolest brown dwarfs remain poorly constrained. Contrarily to low-redshift

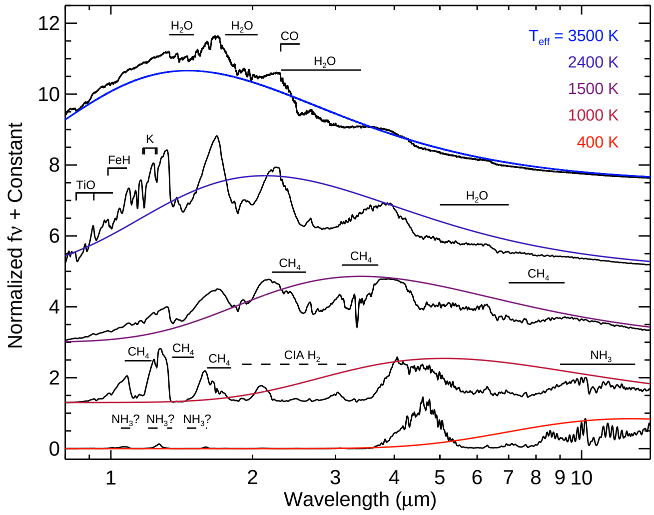

Figure 1.8. – Spectral flux density (in frequency units) of brown dwarfs model templates. The black lines indicate the models and the colored lines represent blackbody radiations at the corresponding temperatures. The molecules responsible for the strong absorption features are also indicated. Credit: M. C. Cushing

galaxies, the surface density of brown dwarfs remains limited (Caballero et al. 2008), especially at high galactic latitudes where deep extra-galactic surveys are located. Although, high-redshift galaxies are rare and so are brown dwarfs.

Stellar objects appear point-like in astronomical images, whereas galaxies may present extended surface brightness profiles in high-resolution images with narrow point spread functions (PSF). This means that stars and galaxies may be separated based on morphology (Leauthaud et al. 2007). However, brown dwarfs and high-redshift galaxies are more challenging to classify, because faint galaxies typically appear point-like. In addition, the emission spectrum of brown dwarfs peaks in the near-infrared, meaning that high-resolution space-based imaging is required in the infrared. This will be permitted with the future deep *JWST* images.

1.6.4. Determining the physical parameters of galaxies

In this section, I describe the main physical parameters of galaxies, which can be estimated from broad-band imaging. Apart from redshift, this includes stellar mass, star formation rate and absolute magnitudes. These parameters all affect the observed magnitudes and colors of galaxies in specific ways.

Stellar mass

Stellar mass is the summed baryonic mass of the stars within a galaxy. It is distinct from the total mass of the galaxy, which includes the additional gas, dust and dark matter. The main contribution to the stellar mass comes from low-mass stars. The strong continuum emission in the optical spectrum of galaxies is caused by the cumulated blackbody radiations from stars with various temperatures. This continuum presents a break at 4000 Å because of the limited number of hot blue stars and the absorption by dust, primarily affecting short wavelengths. In addition, the emission blueward of the 4000 Å break is more affected by the recent star formation than the optical blackbody continuum. Consequently, the amplitude of the rest-frame optical continuum is the main tracer of stellar mass. The inferred stellar masses are sensitive to the assumed initial mass function (IMF), namely the mass distribution of stars formed from the gravitational collapse of molecular gas. At the high-mass end, the IMF describes a power law with a logarithmic slope of $\alpha = -2.35$ (Salpeter 1955), whereas the low-mass end is less constrained. In addition, it is not clear whether the IMF is universal or sensitive to the initial conditions of star formation.

Star formation rate

Star formation rate (SFR) describes the mass of stars formed in a galaxy in a given time interval. Stars are formed in galaxies over cosmological timescales, and the star formation history (SFH), namely the SFR as a function of time, induces the shape of the observable galaxy emission. Nonetheless, the blackbody emission from newly formed, hot massive stars produces a continuum of UV photons. Since these stars have short lifetimes (a few million of years), the slope of the rest-frame UV continuum is a tracer of recent star formation. Unfortunately, dust attenuation also affects the shape of the UV continuum, with a stronger effect on bluer photons. This leads to a strong degeneracy between SFR and dust attenuation, explaining the difficulty to estimate the SFR of individual galaxies from broad-band imaging. Alternative tracers of star formation include the Hα line, which can be identified through narrow-band imaging (in a specific redshift range) or spectroscopy.

Absolute magnitudes

Absolute magnitudes describe the intrinsic luminosity of celestial objects, at a given wavelength or in a given passband. It is computed as the apparent magnitude of the object placed at a 10 parsec distance from the observer (basically at $z = 0$). The apparent magnitude m expressed in the AB system (Oke 1974) is defined as:

$$m(f_\nu) = -2.5 \log_{10}(f_\nu) - 48.6, \tag{1.53}$$

where f_ν is the flux density in frequency units (expressed in erg/s/cm^2/Hz). The absolute magnitude M is defined as:

$$M(L_\nu) = m\left(\frac{L_{\frac{\nu}{1+z}}}{4\pi(10\,\mathrm{pc})^2}\right), \tag{1.54}$$

where L_ν is the luminosity density (expressed in erg/s/Hz). The distance between the observer and the celestial object affects the relation between apparent and absolute magnitudes in multiple ways. Firstly, the observed flux (energy per unit area) decreases as the luminosity distance from the object increases (see Sect. 1.1.3). This effect is quantified with the distance modulus μ and depends on the assumed cosmology:

$$\mu = 5\log_{10}\left(\frac{D_L}{10\,\mathrm{pc}}\right). \tag{1.55}$$

Secondly, the emission spectrum is redshifted because of the expansion of the Universe. This results in the shift and the stretch of the bandpass in the observed frame compared to the rest frame, both impacting absolute magnitudes. The K-correction (Oke et al. 1968) is then introduced to compensate for these two effects. Consequently, the absolute magnitude in the rest-frame UV, estimated from the observed apparent magnitude in a bandpass S, is expressed as:

$$M_{\mathrm{UV}} = m_S - \mu - K, \tag{1.56}$$

where K is the K-correction (Hogg et al. 2002). In practice, absolute UV magnitudes are computed using the apparent magnitudes in the band whose observed-frame wavelength is the close to the rest-frame UV, at the given redshift, in order to limit the K-correction (e.g., Ilbert et al. 2005). In `LePhare`, absolute magnitudes are computed using observed apparent magnitudes and K-corrections estimated from the best-fit galaxy template. This is less template-dependent than directly using the absolute magnitude of the templates.

1.7. Summary

In this chapter, I presented both the theoretical and experimental aspects to constrain cosmic reionization based on the observation of high-redshift galaxies. The main steps are summarized here. Deep near-infrared imaging is required to detect these faint and rare sources. It is not possible to detect them in the optical, because of the absorption blueward of the rest-frame Lyman alpha line by the neutral hydrogen in the IGM. Hence, complementary optical imaging is required to identify the Lyman break in the observed emission of the galaxies. The addition of mid-infrared imaging can be helpful to reject low-redshift contaminants. Galaxies can then be counted per absolute magnitude in the rest-frame UV, leading to the galaxy UV luminosity function. In order to describe the entire galaxy population at high redshift, both intrinsically faint and bright galaxies need to be identified, from deep pencil-beam surveys and wide-field imaging respectively. With the combined analysis of wide and deep fields, the shape of the UVLF can be constrained to both ends. From there, the integrated UV luminosity density describes the number of UV photons emitted from galaxies in a cosmic volume. Since the galaxy UV emission is related to the star-formation rate, the star-formation rate density can be obtained. The cosmic SFRD, and in particular its evolution with redshift, can be related to the fraction of neutral hydrogen in the IGM through the theoretical models of reionization. Finally, the integrated effect of reionization on the cosmic microwave background can be computed through the Thomson optical depth τ, and compared with the independent results from the Planck mission.

In this framework, my contribution consisted of the analysis of present and future imaging surveys, to search for high-redshift galaxies during cosmic reionization. With the deep pencil-beam surveys of the *James Webb* space telescope, a large number of galaxies at $z > 9$ will be detected, giving new constraints on the faint-end of the galaxy UV luminosity function. These scientific analyses will strongly benefit from prospective studies to select both pure and complete samples of galaxies. For this purpose, I conducted end-to-end simulations of accepted *JWST* programs, in which I predicted the future constraints on cosmic reionization, from the detection of high-redshift galaxies to the computation of star-formation rate density. In parallel, deep imaging surveys are on-going in the COSMOS field, in particular UltraVISTA in the near-infrared. This multi-wavelength data set can be used to identify rare, bright galaxies at high redshift. Hence, I have been involved in the processing of the latest images in the COSMOS field, giving me the opportunity to study the high-redshift Universe. Furthermore, the COSMOS photometry has been (and will be) used in a variety of scientific subjects, including for the future *Euclid* space mission. This highlights the importance of the work I have undertaken within the COSMOS collaboration.

2. Simulating the James Webb space telescope imaging surveys

2.1. Introduction

The *James Webb* space telescope (*JWST*; Gardner et al. 2006) is a forthcoming infrared telescope, and the worthy successor of the *Hubble* space telescope (*HST*) and the *Spitzer* space telescope. *JWST* will provide sub-arcsecond, high-sensitivity images at wavelengths above 3 microns, for the first time ever. With its unprecedented capabilities, the *JWST* will be well-suited for the analysis of high-redshift galaxies during the epoch of reionization. In preparation for the future observations with *JWST*, I designed and implemented extensive simulations of the first accepted observing programs. Galaxies and stars are injected into realistic mock images, considering the future *JWST* images in addition to existing ancillary data. The detectable sources are then extracted, the physical parameters are estimated and the galaxy UV luminosity function is computed. These end-to-end simulations are necessary to predict the performance of the survey, and validate the scientific methods used for the analysis. In the context of cosmic reionization, the statistical properties of the recovered high-redshift galaxy population can be evaluated, and compared to the input population. The computation of the UVLF at high redshift, as well as the consequences on reionization history, are highly sensible to incompleteness and contamination by foreground objects, which are both quantified with these simulations.

2.2. Description of the telescope

The actual launch date is set to October 2021, bearing in mind this used to be October 2018 at the beginning of this thesis. The primary mirror consists of 18 hexagons for a total collecting area of $25\,\mathrm{m}^2$ and a diameter of 6.5 m, in comparison with the 2.4 m diameter primary mirror on-board *HST*. The telescope is protected with a sun shield to limit the thermal self-emission, which dominates the background at wavelengths larger than $15\,\mu$m. The telescope will be orbiting the Earth-Sun Lagrangian point L2. The mission duration will be at least 5 years and is expected to extend beyond 10 years. The main science goals of the *JWST* include the first light from stars and galaxies during cosmic reionization, galaxy formation and evolution, star formation, planetary systems and the origin of life.

The on-board instruments include the near-infrared camera (NIRCam), the near-infrared spectrograph (NIRSpec), the near-infrared imager and slitless spectrograph (NIRISS), and the mid-infrared instrument (MIRI). The NIRCam instrument consists of two equivalent modules covering two adjacent fields of view ($2 \times 132'' \times 132''$) separated by $44''$. Its wavelength range is from 0.6 to 5 microns. Dichroics split the incoming light at $2.4\,\mu$m, enabling the short-wavelength ($0.6 - 2.3\,\mu$m) and the long-wavelength ($2.4 - 5.0\,\mu$m) detectors on each NIRCam module to simultaneously image the same field of view. At short wavelengths, the camera pixel resolution is $0.032''$, while it is $0.065''$ at long wavelengths. The point spread functions (PSF) have a full width at half maximum (FWHM) of $0.14''$ for the reddest broad band. The MIRI camera module provides wide-field ($74'' \times 113''$) broad-band imaging in the mid-infrared ($5 - 28\,\mu$m). The two bluest bands, at 5.6 and $7.7\,\mu$m respectively, are by far the most sensitive of the instrument. In these two bands, the PSF FWHM are $0.22''$ and $0.25''$ respectively, for a detector resolution of $0.11''$ per pixel. At wavelengths below $15\,\mu$m, the predicted background is dominated by zodiacal light, namely the sunlight scattered by interstellar dust along the ecliptic. At wavelengths longer than $15\,\mu$m, the thermal emission from the primary mirror and the sunshield dominates the background. Figure 2.1 illustrates the transmission curves of the NIRCam and MIRI broad and medium bands. In addition to these bands, NIRCam also include two extra-broad bands and seven narrow-band filters.

2.3. First observing programs

The Director's Discretionary Early Release Science (DD-ERS) programs consist of the first *JWST* observations to be performed, and are designed to demonstrate the capabilities of the telescope. The ERS observations will take place in the first 5 months of the *JWST* science operations. In the topic of galaxies and intergalactic medium, the Cosmic Evolution Early Release Science (CEERS; P.I.: S. L. Finkelstein) survey is the only approved ERS program including deep extragalactic imaging. With its parallel observations (NIRCam and MIRI) of the Extended Groth Strip (EGS) field, for a total area of $100\,\mathrm{arcmin}^2$, CEERS is expected to observe tens of $z > 9$ galaxies. This program will provide the first constraints on reionization at such high redshifts, hence the importance of providing realistic predictions of these future observations.

The Guaranteed Time Observations (GTO) are accorded to the teams of scientists who designed and constructed the telescope instruments. In this study, I focused on the cycle 1 GTO programs which are proposed before the launch date. The *JWST* Advanced Deep Extragalactic Survey (JADES) from the NIRSpec and NIRCam GTO teams, also referenced as the NIRCam-NIRSpec Galaxy Assembly Survey (P.I.: D. J. Eisenstein), will provide NIRCam imaging in the GOODS-South and GOODS-North fields (see Rieke et al. 2019b). JADES consists of a deep survey of $46\,\mathrm{arcmin}^2$ and a medium survey of $190\,\mathrm{arcmin}^2$, reaching depths of about 30

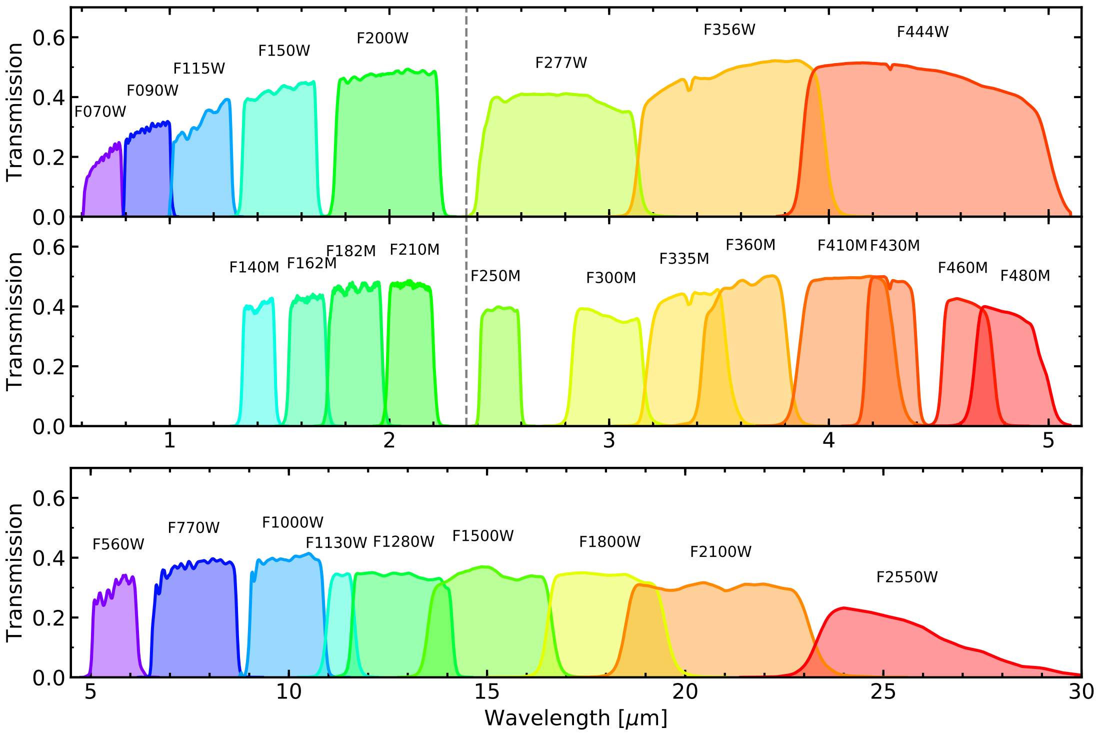

Figure 2.1. – Transmission curves of the NIRCam broad bands (*top*), NIRCam medium bands (*middle*) and MIRI broad bands (*bottom*). The vertical dashed line separates the short and long-wavelength NIRCam filters.

and 29 mag respectively (5σ, point-sources) in 7 broad-band and 2 medium-band filters. This configuration is well-suited for the study of high-redshift galaxies. Within the GOODS-South field, the *Hubble* Ultra-Deep field (HUDF) includes the deepest *HST* observations ever made. For the MIRI instrument, there are two deep extragalatic programs in this field (see Rieke et al. 2019a), including the "MIRI in the HUDF" program (P.I.: G. Rieke) and the "MIRI HUDF deep imaging survey" (P.I.: H.U. Norgaard-Nielsen). The first program consists of imaging in all the MIRI broad bands, with an emphasis on the 21 μm filter. In the second program, extremely deep observations at 5.6 μm will be performed, improving the estimated galaxy physical parameters (such as stellar mass) at $z > 4$ and the identification of the Balmer break at $z > 8$. Therefore, the HUDF will be of major scientific interest, with the extremely deep imaging with both NIRCam and MIRI, in addition to the existing *HST* data in the optical. These reasons motivated the simulation of the high-resolution images in this field to predict the future performance of the surveys.

2.4. Image simulation

Simulation is an important step to make realistic predictions for a future survey. It has the advantage to describe extended source (instead of point-source) detection limits, and source blending. The first effect leads to brighter detection limits because of the intrinsic surface brightness profile of the sources, the second affects both the detection and the photometry of nearby sources. In the case of the *JWST* surveys, the deep and high-resolution images will be strongly impacted by these two effects (Dawson et al. 2016). In this section, I present the tools and software used to generate simulated *JWST* and *HST* images, based on the actual knowledge of the instruments and the details of the future surveys. This includes the exposure time calculators, the simulated PSF generator and the image generator. While the paper presented in this chapter described all the scientific analyses, it did not include all the details about the image simulation.

Multiple *JWST* imaging simulators are still in development, including `pyNRC`[1], `Guitarra` (Willmer et al. 2020), the Space Telescope Imaging Product Simulator (`STIPS`[2]), and the Multi-Instrument Ramp Generator (`MIRAGE`; Chambers et al. 2019). Unfortunately, these simulators were not public or available at the beginning of this thesis.

2.4.1. WebbPSF

Simulated PSFs for the *JWST* instrument can be computed using `WebbPSF`[3]. This Python package generates modelled PSFs fits images based on the current understanding of the instruments. Multiple options are available in this software, including oversampling (only integers), position offset and jitter. Oversampling is the ratio between the camera pixel scale and the PSF image pixel scale. It may be useful to manipulate oversampled PSFs to properly simulate future astronomical images, in order to ensure a proper sampling of the central region of the PSF. To obtain any (non-integer) oversampling, I first generated images with a large oversampling, then interpolated the images to the desired oversampling. Figure 2.2 shows the modelled PSF profile of some NIRCam and MIRI broad bands. The hexagonal shape of the central part comes from the geometry of the primary mirror.

2.4.2. MIRISim

`MIRISim`[4] is a simulator in Python for both imaging and spectroscopy with the MIRI instrument. `MIRISim` generates raw and pre-processed images, to be reduced with the official *JWST* pipeline. The simulated products are the most

1. https://pynrc.readthedocs.io/en/latest/
2. https://stsci-stips.readthedocs.io/en/latest/
3. https://webbpsf.readthedocs.io/en/stable/
4. https://wiki.miricle.org//bin/view/Public/MIRISim_Public

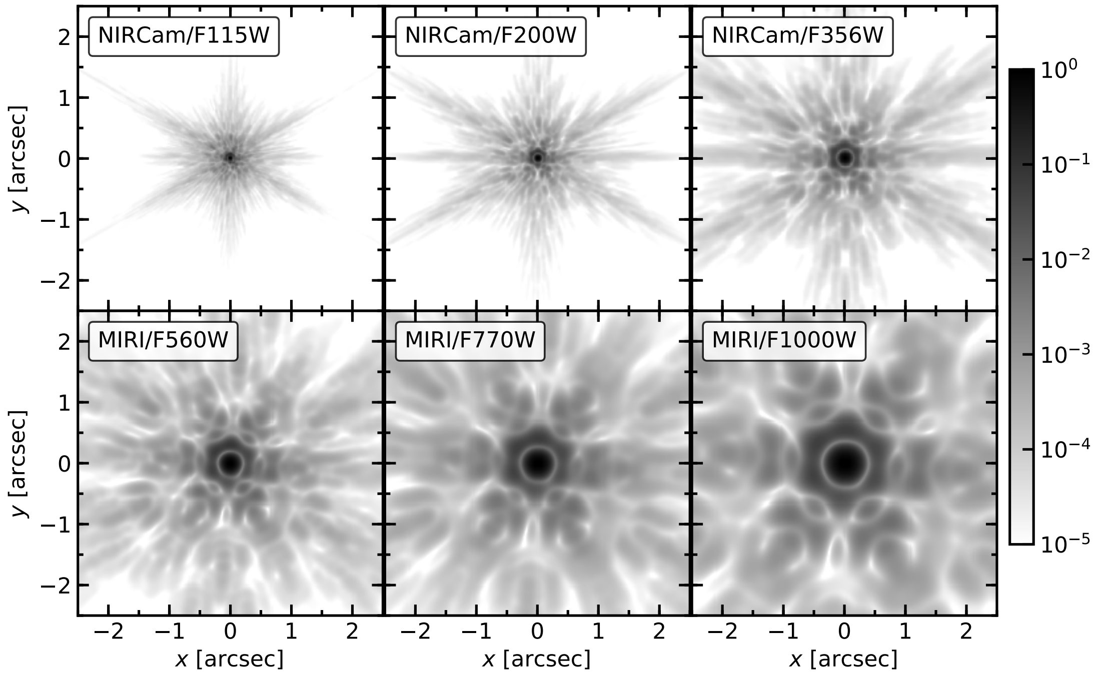

Figure 2.2. – Modelled PSF of three NIRCam broad bands (*top*) and three MIRI broad bands (*bottom*), generated with `WebbPSF`. The images are scaled to a maximum of one.

realistic to the future MIRI observations, according to the knowledge of the instrument. The images notably include correlated Poisson noise, read noise, dark current, cosmic rays, image distortions, dithering, and internally computed PSFs. In comparison with `WebbPSF`, the MIRI PSFs produced by `MIRISim` present an additional cruciform pattern with a relatively strong amplitude. Nonetheless, this effect may be overestimated by `MIRISim`, and is still under investigation. However, the `MIRISim` output sensitivities are known not to be as reliable as the official exposure time calculator (ETC, Pontoppidan et al. 2016). In addition, `MIRISim` remains computationally expensive to run, requiring 100 h to insert 1000 sources in one MIRI camera field (2.3 arcmin^2). For these reasons, I decided not to use `MIRISim` in this study.

2.4.3. `SkyMaker`

The simulated images were generated with the software `SkyMaker` (Bertin 2009). This package creates realistic astronomical images with a lot of flexibility. It only requires a configuration file, describing the instrument settings, and an input file, containing the list of sources to be injected. In addition, `SkyMaker` is highly optimized and multi-threaded, which is convenient to simulate large images. For these simulations, tens of 120 arcmin^2 images, including 300 000 sources, were

Table 2.1. – List of SkyMaker main configuration parameters (using an external PSF file).

Name	Default	Type	Description
IMAGE_NAME	sky.fits	string	Name of the output
IMAGE_SIZE	1024	integer	Size of the output [pix] (width or width,height)
GAIN	1.0	float	Gain [e^-/ADU]
WELL_CAPACITY	0	integer	Full well capacity [e^-] (0: infinite)
SATUR_LEVEL	65535	integer	Saturation level [ADU]
READOUT_NOISE	0	float	Read-out noise [e^-]
EXPOSURE_TIME	300.0	float	Total exposure time [s]
MAG_ZEROPOINT	26.0	float	Magnitude zeropoint [mag/(ADU/s)]
PIXEL_SIZE	0.200	float	Pixel size [arcsec]
PSF_TYPE	INTERNAL	keyword	Type of PSF (INTERNAL or FILE)
PSF_NAME	psf.fits	string	Name of the PSF fits image
AUREOLE_RADIUS	200	float	Range covered by aureole [pix] (0: no aureole)
PSF_OVERSAMP	5	float	PSF oversampling
TRACKERROR_TYPE	NONE	keyword	Tracking error (NONE, DRIFT or JITTER)
WAVELENGTH	0.8	float	Average wavelength analysed [μm]
BACK_MAG	20.0	float	Background surface brightness [mag/arcsec^2]
VERBOSE_TYPE	NORMAL	keyword	Verbose type (QUIET, NORMAL or FULL)
NTHREADS	0	integer	Number of simultaneous threads (0:automatic)

generated in a few minutes each. In this section, the main steps of the SkyMaker software are described. There is no official documentation, so the following gathers information from published papers (Erben et al. 2001), presentations, and my own experience of the code. Table 2.1 lists the configuration parameters which are used in the context of these simulations.

External PSF

The PSF can be either internally computed, or using an external PSF fits file. In this second case, the PSF oversampling must be given, namely the ratio between the image and the PSF pixel scales. The PSF pixel scale may preferably be generously sampled (at least 4 pixels per FWHM). Note that the oversampling should be larger than 0.25. In the case the external PSF file includes all the required effects, the aureole radius may be set to zero and the tracking error to NONE.

Noise model

The output image is in analog digital units (ADU). The background level is determined by the background surface brightness, namely the flux density per unit angular area. The noise is modelled by an uncorrelated Poisson noise, to which a Gaussian readout noise may be added. The amplitude of the Poisson noise is determined by the total exposure time t, and the source signal-to-noise S/N evolves as $\sqrt{t}$. In practice, this corresponds to the sky-dominated regime. To insert the Poisson noise into the image, the image in ADU units is converted to e^- units using the gain, the random Poisson noise is sampled, the well capacity sets the upper limit in e^- units, then the image is converted back to ADU units and the saturation level sets the upper limit.

Photometric zeropoint

The photometric zeropoint sets the conversion from ADU to flux units. In the case of `SkyMaker`, it is defined as the magnitude of an object producing 1 ADU/s on the detector. Note that this definition is distinct from the one used in `SExtractor`, where it is the magnitude of an object producing 1 ADU over the total exposure time t, so that:

$$\texttt{MAG\_ZEROPOINT}_{\texttt{SExtractor}} = \texttt{MAG\_ZEROPOINT}_{\texttt{SkyMaker}} + 2.5\log_{10}(t). \tag{2.1}$$

In order to estimate the zeropoint magnitudes of the future *JWST* images, one may use the exposure time calculator (ETC). One needs to create a configuration with no source, imposing a given (preferably high) background surface brightness, expressed in MJy/sr, and then measure the mean image value, expressed in e^-/s/pix. The ratio of these two quantities, multiplied by the gain, gives a reasonable estimate of the zeropoint.

Input catalog

The input catalog, containing the list of sources to be injected into the image, needs to have a specific format. In order to describe a source, the source type, coordinates, flux, and morphology are required. These parameters are listed in Table 2.2. Note that the center of the first pixel has the coordinates $(1, 1)$, so that the edges of the image are 0.5 and $n_{\rm pix} + 0.5$, where $n_{\rm pix}$ is the size of the image in one direction. In the case of point-sources like stars, only the coordinates and the flux are required. The source type for point-sources is 100. In the case of galaxies, the intrinsic surface brightness profile may be parametrized with the sum of two Sérsic profiles, for the bulge and the disk respectively. The Sérsic profile (Sérsic 1963) is defined as:

$$I(r) = I_e \exp\left[-b_n\left(\left(\frac{r}{r_e}\right)^{1/n} - 1\right)\right], \tag{2.2}$$

where n is the Sérsic index, r_e the effective radius and I_e the intensity at that radius. The parameter b_n is a function of n and the solution of $\Gamma(2n) = 2\gamma(2n, b_n)$, where Γ is the gamma function and γ is the lower incomplete gamma function. The solution of this equation can be approximated by (MacArthur et al. 2003):

$$b_n \approx \begin{cases} 2n - \dfrac{1}{3} + \dfrac{4}{405n} + \dfrac{46}{25515n^2} + \dfrac{131}{1148175n^3} + \dfrac{2194697}{30690717750n^4} & \text{if } n > 0.36, \\ 0.01945 - 0.8902n + 10.95n^2 - 19.67n^3 + 13.43n^4 & \text{otherwise.} \end{cases} \tag{2.3}$$

The two-dimensional integral of the Sérsic profile to $r = \infty$ gives the total flux f of the source, expressed as:

$$f = 2\pi r_e^2 I_e e^{b_n} n b_n^{-2n} \gamma(2n) q, \tag{2.4}$$

where q is the ratio between the minor axis b and the major axis a of the profile. The intrinsic surface brightness profile of galaxies can be remarkably parametrized with the sum of two Sérsic profiles. The bulge of the galaxy is commonly described with a Sérsic profile with an index of $n = 4$, corresponding to a de Vaucouleurs profile, and the disk with an index of $n = 1$, corresponding to an exponential profile. The source type for galaxies is 200, while the Sérsic index of the bulge may be explicitly modified using the source type 210. All the sources to be injected are listed in a single text file, each line describing a single source. The format to add a source to the list is the following:

— 100, x, y, m
— 200, x, y, m, B/T, $r_{\text{e,bulge}}$, q_{bulge}, ϕ_{bulge}, $r_{\text{e,disk}}$, q_{disk}, ϕ_{disk}
— 210, x, y, m, B/T, n_{bulge}, $r_{\text{e,bulge}}$, q_{bulge}, ϕ_{bulge}, $r_{\text{e,disk}}$, q_{disk}, ϕ_{disk}

Table 2.2. – List of `SkyMaker` catalog parameters.

Name	Unit	Description
type		Source type (100, 200 or 210)
x	pix	Coordinates
y	pix	
m	mag	Magnitude
B/T		Bulge-to-total flux fraction
n_{bulge}		Sérsic index of the bulge
$r_{\text{e,bulge}}$	arcsec	Semi-major half-light radius of the bulge
q_{bulge}		Axis ratio (b/a) of the bulge
ϕ_{bulge}	deg	Position angle of the bulge
$r_{\text{e,disk}}$	arcsec	Semi-major half-light radius of the disk
q_{disk}		Axis ratio (b/a) of the disk
ϕ_{disk}	deg	Position angle of the disk

2.5. Article

A&A 640, A67 (2020)
https://doi.org/10.1051/0004-6361/202037450

Astronomy & Astrophysics

Simulating JWST deep extragalactic imaging surveys and physical parameter recovery

O. B. Kauffmann[1], O. Le Fèvre[1], O. Ilbert[1], J. Chevallard[2], C. C. Williams[3], E. Curtis-Lake[4,5], L. Colina[6,7], P. G. Pérez-González[6], J. P. Pye[8], and K. I. Caputi[9]

[1] Aix Marseille Univ., CNRS, LAM, Laboratoire d'Astrophysique de Marseille, Marseille, France
e-mail: olivier.kauffmann@lam.fr
[2] Sorbonne Universités, UPMC-CNRS, UMR7095, Institut d'Astrophysique de Paris, 75014 Paris, France
[3] Steward Observatory, University of Arizona, 933 North Cherry Avenue, Tucson, AZ 85721, USA
[4] Cavendish Astrophysics, University of Cambridge, Cambridge CB3 0HE, UK
[5] Kavli Institute for Cosmology, University of Cambridge, Madingley Road, Cambridge CB3 0HA, UK
[6] Centro de Astrobiología, Departamento de Astrofísica, CSIC-INTA, Cra. de Ajalvir km.4, 28850 Torrejón de Ardoz, Madrid, Spain
[7] International Associate, Cosmic Dawn Center (DAWN) at the Niels Bohr Institute, University of Copenhagen and DTU-Space, Technical University of Denmark, Copenhagen, Denmark
[8] University of Leicester, School of Physics & Astronomy, Leicester LE1 7RH, UK
[9] Kapteyn Astronomical Institute, University of Groningen, PO Box 800, 9700 AV Groningen, The Netherlands

Received 6 January 2020 / Accepted 2 June 2020

ABSTRACT

We present a new prospective analysis of deep multi-band imaging with the *James Webb* Space Telescope (JWST). In this work, we investigate the recovery of high-redshift $5 < z < 12$ galaxies through extensive image simulations of accepted JWST programs, including the Early Release Science in the EGS field and the Guaranteed Time Observations in the HUDF. We introduced complete samples of ~300 000 galaxies with stellar masses of $\log(M_*/M_\odot) > 6$ and redshifts of $0 < z < 15$, as well as galactic stars, into realistic mock NIRCam, MIRI, and HST images to properly describe the impact of source blending. We extracted the photometry of the detected sources, as in real images, and estimated the physical properties of galaxies through spectral energy distribution fitting. We find that the photometric redshifts are primarily limited by the availability of blue-band and near-infrared medium-band imaging. The stellar masses and star formation rates are recovered within 0.25 and 0.3 dex, respectively, for galaxies with accurate photometric redshifts. Brown dwarfs contaminating the $z > 5$ galaxy samples can be reduced to <0.01 arcmin^{-2} with a limited impact on galaxy completeness. We investigate multiple high-redshift galaxy selection techniques and find that the best compromise between completeness and purity at $5 < z < 10$ using the full redshift posterior probability distributions. In the EGS field, the galaxy completeness remains higher than 50% at magnitudes $m_{\rm UV} < 27.5$ and at all redshifts, and the purity is maintained above 80 and 60% at $z \leq 7$ and 10, respectively. The faint-end slope of the galaxy UV luminosity function is recovered with a precision of 0.1–0.25, and the cosmic star formation rate density within 0.1 dex. We argue in favor of additional observing programs covering larger areas to better constrain the bright end.

Key words. galaxies: high-redshift – galaxies: photometry – galaxies: distances and redshifts – galaxies: fundamental parameters – galaxies: evolution

1. Introduction

The detection of distant sources has mainly been driven by multi-wavelength photometry, through deep imaging over selected areas of the sky. The *Hubble* Space Telescope (HST), with its Advanced Camera for Surveys (ACS) and Wide-Field Camera 3 (WFC3), enabled the discovery of many high-redshift galaxies with its deep optical and near-infrared (IR) imaging (e.g., Scoville et al. 2007; Koekemoer et al. 2007; Wilkins et al. 2011; Schenker et al. 2013; McLure et al. 2013; Bouwens et al. 2015), effectively covering the rest-frame ultraviolet (UV) region of these sources. Near-infrared observations are necessary to detect high-redshift galaxies because of the strong attenuation blueward of the Lyman limit by the intergalactic medium (IGM), and as the Universe becomes more neutral, the flux that is blueward of Lyman alpha also gets attenuated. The mid-infrared observations with the *Spitzer* Space Telescope have improved the characterization of galaxy physical properties that are required to constrain galaxy evolution from the epoch of reionization to the present day (e.g., Sanders et al. 2007; Caputi et al. 2015). In particular, *Spitzer* has provided most of the constraints on the rest-frame optical at high redshift (Oesch et al. 2014, 2018). The census of high-redshift sources is particularly important to estimate which sources contributed most of the ionizing photons necessary to support neutral hydrogen reionization. The latest accounts point to a high number of faint sources producing enough ionising photons (Bouwens et al. 2015; Robertson et al. 2015), which reconcile a late reionization supported by the latest cosmic microwave background (CMB) constraints on the Thomson scattering optical depth (Planck Collaboration VI 2020) and UV photons from galaxy counts (Madau & Dickinson 2014). Establishing a complete and unbiased census of galaxies and associated ionizing photons remains a priority in order to understand this important transition phase in the Universe, which is directly linked to the formation of the first galaxies.

Identifying high-redshift galaxies within, and following, the epoch of reionization ($5 < z < 12$) is challenging because of their low number density which decreases with redshift. The methods to select high-redshift candidates mostly rely on the identification of the dropout in continuum emission blueward of Lyman alpha (Steidel et al. 1996). Lyman break galaxies (LBG) can be identified through color-color selections, mainly using photometry in the rest-frame UV. Alternatively, photometric redshifts obtained from spectral energy distribution (SED) fitting make use of all the photometric information (e.g., McLure et al. 2013; Finkelstein et al. 2015), spanning the optical to near-infrared, but they do introduce model dependencies. With the large number of low-redshift sources, which are several orders of magnitude more numerous, the high-redshift galaxy samples are subject to contamination because of the similar colors of these sources in the observed frame. The main contaminants are low-redshift ($z \sim 1-2$) dust-obscured galaxies with very faint continuum in the visible bands (Tilvi et al. 2013). Brown dwarfs are other potential contaminants of the $z > 5$ galaxy samples because of their similar near-infrared colors. The number of detected sources increases with telescope sensitivity, which naturally leads to an increasing probability of finding multiple objects along the line-of-sight. Therefore, the impact of source blending becomes more important (Dawson et al. 2016). In the case of source confusion, the background estimation becomes more challenging and individual sources are harder to isolate. The background level by itself also affects source separation, so that extended sources with internal structures may be mistaken for multiple nearby objects. In addition, the galaxy morphology is more complex at high redshifts (Ribeiro et al. 2016), therefore requiring adapted source detection techniques.

The *James Webb* Space Telescope (JWST[1], Gardner et al. 2006), which is to be launched in 2021, will revolutionize near- and mid-infrared astronomy. It will provide the first subarcsecond high-sensitivity space imaging ever at wavelengths above 3 microns and up to 25 microns, overcoming the current limitations of ground-based and space-based observatories. The onboard instruments include two imaging cameras, the Near-Infrared Camera (NIRCam[2], Rieke et al. 2005), and the Mid-Infrared Instrument (MIRI[3], Rieke et al. 2015; Wright et al. 2015), which together cover the wavelength range from 0.6 to 28 microns. These capabilities are perfectly suited for the discovery and the study of high-redshift galaxies during the epoch of reionization at $z > 6$, in combination with the deep optical imaging from HST and other ancillary data.

Predictions are required for preparation of the deep JWST imaging programs. The observed number counts per field of view and their redshift distribution need to be quantified, as well as the source detectability and the completeness and purity of the selected samples, depending on the detection method. The most direct number count predictions require the integral of the luminosity function multiplied by the differential comoving volume over a given area and redshift interval. High-redshift luminosity functions may be estimated by either extrapolating some lower-redshift measurements or using semi-analytic modeling (Mason et al. 2015a; Furlanetto et al. 2017; Cowley et al. 2018; Williams et al. 2018; Yung et al. 2019).

These methods quantify the expected number of detectable sources in a given field, not the number of sources which may be extracted and correctly characterized. Alternatively, the recovery of the galaxy physical parameters may be simulated with mock galaxy photometry and SED-fitting procedures. Bisigello et al. (2016) tested the derivation of galaxy photometric redshifts with JWST broad-band imaging, considering multiple combinations of NIRCam, MIRI and ancillary optical bands. The galaxy physical parameter recovery was investigated using the same methodology (Bisigello et al. 2017, 2019). Analogously, Kemp et al. (2019) analyzed of the posterior constraints on the physical properties from SED-fitting with JWST and HST imaging.

The aim of this paper is to investigate how to best identify high-redshift galaxies in the redshift range $5 < z < 12$ from JWST deep-field imaging, to estimate their number counts, with associated completeness and purity, and how their physical parameters can be recovered, focusing on stellar mass (M_*) and star formation rate (SFR). We concentrate on the identification and characterization of high-redshift sources from photometry, which will be required to identify sources for spectroscopic follow-up with JWST (NIRSpec, Birkmann et al. 2016). The simulation of deep fields necessitates the construction of realistic mock samples of sources, including all galaxies at all redshifts, as well as stars from the Galaxy. Any contamination estimate relies on the ability to produce simulations with sources which have realistic distributions of physical properties as a function of redshift, including fluxes and shapes projected on the image plane, as currently documented. In determining magnitudes, we need to include emission lines with strength corresponding to what is actually observed. In this way the contamination of high-redshift galaxy samples by low-redshift interlopers and Galactic stars can be estimated. We neglect quasars and transient objects. Existing observations are not deep enough to use as a basis for predictions for JWST and therefore some extrapolations are needed. To take geometrical effects into account, we generate mock images from the current knowledge of the instruments, then extract and identify sources. This allows us to more realistically characterize the statistical properties of the galaxy population, and especially source blending, thanks to the complete source sample. Figure 1 summarizes our methodology to make our forecasts.

This paper is organized as follows. In Sect. 2 we present the mock source samples, including galaxies and stellar objects. Section 3 describes our methodology to simulate images, extract sources and measure photometry and physical parameters. The results of the physical parameter recovery are detailed in Sect. 4. Section 5 describes our source selection investigations, including the rejection of the stellar contaminants, high-redshift galaxy selection and luminosity function computation. We summarize and conclude in Sect. 6. Magnitudes are given the AB system (Oke 1974), and we adopt the standard ΛCDM cosmology with $\Omega_\mathrm{m} = 0.3$, $\Omega_\Lambda = 0.7$ and $H_0 = 70\,\mathrm{km\,s^{-1}\,Mpc^{-1}}$.

2. Mock source samples

2.1. Mock galaxy sample

We build our galaxy sample from the JADES extraGalactic Ultradeep Artificial Realizations v1.2 (JAGUAR[4], Williams et al. 2018) developed for the JWST Advanced Deep Extragalactic Survey (JADES). This phenomenological model of galaxy evolution generates mock galaxy catalogs with physical and morphological parameters, reproducing observed statistical functions. Publicly available realizations consist of complete samples of star-forming and quiescent galaxies with stellar mass

[1] http://www.stsci.edu/jwst
[2] https://jwst-docs.stsci.edu/near-infrared-camera
[3] https://jwst-docs.stsci.edu/mid-infrared-instrument
[4] https://neogal.iap.fr/JAGUAR_mock_catalogue/

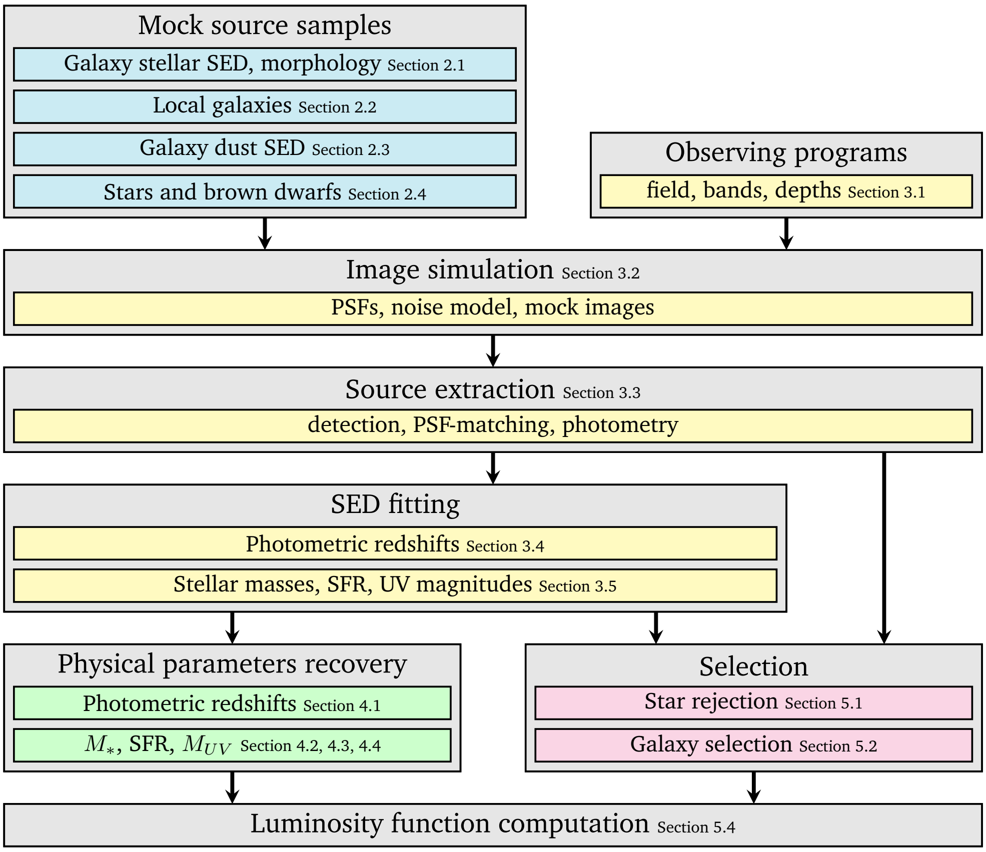

Fig. 1. Diagram summarizing the procedures to make our predictions. The gray boxes indicate the essential steps, and colored boxes show the detail of the subsections. The colors code for the main sections.

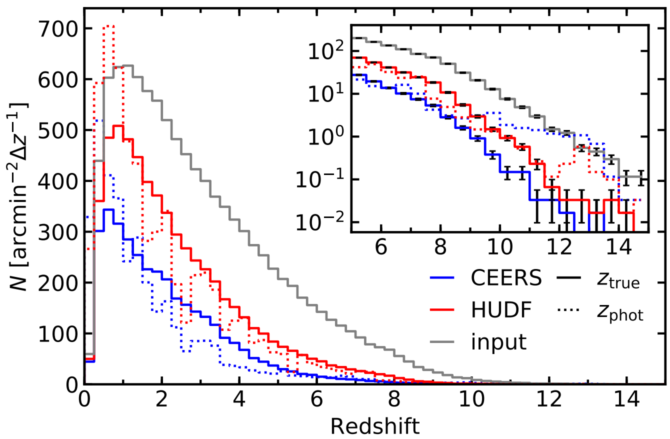

Fig. 2. Galaxy surface number density versus redshift. The gray line includes all the mock galaxies with stellar masses $\log(M_*/M_\odot) > 6$. The colored lines illustrate the redshift distribution of the detected sources in our CEERS and HUDF simulations. The solid and dashed lines represent input and photometric redshift distributions, respectively. The inset provides a zoom-in at high redshift, with Poisson error bars.

$6 < \log(M_*/M_\odot) < 11.5$ and redshift $0.2 < z < 15$ on areas of 11×11 arcmin^2, each containing $\sim 3 \times 10^5$ sources.

Stellar masses and redshifts are sampled from a continuous stellar mass function (SMF) model, constructed from the empirical SMF constraints of Tomczak et al. (2014) at $z < 4$ and the luminosity functions (LF) of Bouwens et al. (2015) and Oesch et al. (2018) at $z < 10$. We note that these observations support a rapid evolution of the UVLF at $z > 8$ inducing a strong decrease in galaxy number counts, which is still debated in the literature (e.g., McLeod et al. 2015, 2016). The SMF model separately describes star-forming and quiescent galaxies and is extrapolated beyond $z = 10$. Physical parameters (e.g., UV magnitude $M_{\rm UV}$, UV spectral slope β) are sampled from observed relationships and their scatter between $M_{\rm UV}$ and M_*, and $M_{\rm UV}$ and β. A spectral energy distribution (SED) is assigned to each set of physical parameters using BEAGLE (Chevallard & Charlot 2016). Williams et al. (2018) describe a galaxy star formation history (SFH) with a delayed exponential function and model stellar emission with the latest version of the Bruzual & Charlot (2003, hereafter BC03) population synthesis code. They consider the (line and continuum) emission from gas photoionized by young, massive stars using the models of Gutkin et al. (2016). Dust attenuation is described by the two-component model of Charlot & Fall (2000) and parametrized in terms of the $V-$band attenuation optical depth $\hat{\tau}_V$ and the fraction of attenuation arising from the diffuse ISM (set to $\mu = 0.4$), while IGM absorption follows the prescriptions of Inoue et al. (2014). No galaxies composed of metal-free population III stars are considered because of the lack of knowledge about these objects. No active galactic nuclei (AGN) models are considered either. Figure 2 shows the redshift distribution of the mock galaxy catalog.

Galaxy morphology is parametrized by one Sérsic function (Sérsic 1963) assumed to be wavelength-independent. Effective radii are sampled from a continuously evolving model with stellar mass and redshift, based on the observed size-mass relations in CANDELS and the 3D-HST survey by van der Wel et al. (2014). This model separately treats star-forming and quiescent galaxies, and extrapolates the observed trends down to $\log(M_*/M_\odot) = 6$. Axis ratio and Sérsic indices are sampled from the redshift-dependent distributions of van der Wel et al. (2012). The description of galaxy surface brightness profiles relies on observed UV magnitudes and apparent shape measurements, so that only the strong lensing shape distortions are neglected here. Magnification is naturally included, although we do not expect magnification bias to be important in JWST pencil-beam surveys containing few $M_{\mathrm{UV}} < -22$ galaxies (Mason et al. 2015b). The underlying assumptions on the morphology of galaxies, especially at $z > 2$, may have important consequences on whether a source can be recovered, with two main limitations. Size measurements which assume symmetry find that sizes decrease with redshift (Shibuya et al. 2015, although cf. Curtis-Lake et al. 2016), whereas one finds that sizes remain large and constant with redshift when more adapted isophotal limits are used (Ribeiro et al. 2016). This arises from galaxies becoming more complex, multi-component as redshift increases, therefore spreading the total flux over a large area with surface brightness becoming lower. In addition, a clumpy galaxy may be resolved at certain wavelengths but appear mono-component in others because of the change of intrinsic structure and/or the varying angular resolution. This could be an increasing problem with source identification and multi-wavelength photometry. While this work is based on symmetric profiles, we will investigate how multi-component galaxies can be detected in a future paper.

Galaxy coordinates are sampled from a uniform distribution over the surveyed area. We therefore neglect galaxy alignment from clustering or lensing. The position of galaxy pairs with large line-of-sight separations are independent, meaning that the blending of high-redshift galaxies with low-redshift sources should remain unchanged with and without clustering, at the first order. Multiple over-dense regions may happen to be on the same line of sight, however we neglect these cases. Moreover, we only simulate nonconfused, high-resolution imaging, so that we expect our predictions to be negligibly impacted by clustering.

Because of the rarity of the high-redshift sources, large areas of the sky need to be simulated to make predictions with sufficient statistical significance. We replicate three times the initial galaxy catalog covering $11 \times 11\,\mathrm{arcmin}^2$ to increase the simulated area and sample size. For each replication, stellar masses are sampled from a centered log-normal distribution with $\sigma = 0.1$ dex. This ensures that the difference in the resulting SMF remains below ~10% at $M_* < 10^{11}\,M_\odot$. Fluxes and SFRs are modified accordingly. Coordinates and galaxy position angles are randomized, and the other parameters kept unchanged.

2.2. Local galaxies

Low-redshift galaxies are one of the main sources of contamination for the high-redshift galaxy samples, notably because of the degeneracy between the Lyman and the Balmer breaks (e.g., Le Fèvre et al. 2015). Pencil-beam surveys contain very few local galaxies, however the apparent size of these objects are the largest on the sky, so that it is important to take them into account when simulating realistic blending.

The JAGUAR galaxy catalog does not include $0 < z < 0.2$ galaxies, because of the lack of low-redshift volume considered in building the stellar mass function in Tomczak et al. (2014). We sample redshifts and stellar masses at $M_* > 10^6\,M_\odot$ from the SMF continuous model of Wright et al. (2018) to fill this redshift interval. In that paper, the authors made use of the GAMA ($60\,\mathrm{deg}^2$), G10-COSMOS ($1\,\mathrm{deg}^2$) and 3D-HST ($0.274\,\mathrm{deg}^2$) data set gathered by Driver et al. (2018) to efficiently constrain both the bright and the faint ends of the SMF. For comparison, the area of the data used in Tomczak et al. (2014) is $316\,\mathrm{arcmin}^2$.

We sample about 460 (50) galaxies with $\log(M_*/M_\odot) > 6$ (8) over $11 \times 11\,\mathrm{arcmin}^2$. We assign the spectrum from the JAGUAR $0.2 < z < 0.4$ galaxy with the closest stellar mass to each sampled parameter set. The maximum stellar age in these galaxies is therefore underestimated. By construction, about half of these galaxies are quiescent. The morphological parameters are sampled from the same distributions as in JAGUAR.

2.3. Galaxy infrared spectra

Dust emission can make a significant contribution to the near- and mid-infrared galaxy spectrum. In addition, mid-infrared photometry may considerably help to identify low-redshift contaminants to high-redshift samples using photometric redshift estimation (e.g., Ilbert et al. 2009). Because the galaxy spectra in JAGUAR include stellar and nebular emission, we include the additional dust emission for a more accurate modeling of the galaxy mid-infrared spectra. We neglect dust emission for low-mass[5] quiescent galaxies because Williams et al. (2018) neglected dust attenuation for these objects.

We take the library of dust spectral energy distributions of Schreiber et al. (2018) constructed from the dust models of Galliano et al. (2011). These templates separately describe the dust grain continuum emission and the polycyclic aromatic hydrocarbon (PAH) emission. The contribution of an AGN torus to the dust emission is neglected. The dust temperature (T_{dust}) determines the shape of both components, the mid-to-total infrared color (IR8 $= L_{\mathrm{IR}}/L_{8\mu\mathrm{m}}$) sets their relative contributions and the infrared luminosity (L_{IR}) scales the sum.

We attribute T_{dust} and IR8 to all the mock galaxies following the empirical laws evolving with redshift from Schreiber et al. (2018), including the intrinsic scatter. These relations were calibrated from the stacked *Spitzer* and *Herschel* photometry (Schreiber et al. 2015). We estimate the infrared luminosities from the $V-$band attenuation optical depth $\hat{\tau}_V$, assuming that the absorbed flux is entirely re-emitted by the dust (energy balance). We neglect the birth clouds component of the Charlot & Fall (2000) attenuation curve, since the JAGUAR catalog only provides the summed emission from young and old stars. This may lead to underestimated dust emission, as well as the limitation to the diffuse ISM. Figure 3 indicates a better agreement between simulated and empirical counts in the MIRI/$F770W$ filter.

2.4. Mock star sample

In this section, we present our formalism to generate mock stars from the Milky Way in the field of view. The strategy to create the mock star catalog is the following: (1) estimate the number density per spectral type, (2) sample heliocentric distances and physical properties, then (3) assign the spectrum with the closest properties.

We make use of the Besançon Model of the Galaxy[6] (Robin et al. 2003, 2012, 2014) to generate mock stars of spectral type FGKM. This model of stellar population synthesis provides star samples with intrinsic parameters (mass, age, metallicity, effective temperature T_{eff}, surface gravity $\log g$). OBA stars are not sampled because of their rarity in pencil-beam surveys. We follow the galaxy model of Caballero et al. (2008) to determine the mean number of LTY stars per unit area. The galaxy density profile is modeled by an exponential thin-disk with the parameters from Chen et al. (2001), reliable

[5] With $\log(M_*/M_\odot) < 8.7 + 0.4z$.

[6] `http://model2016.obs-besancon.fr/`

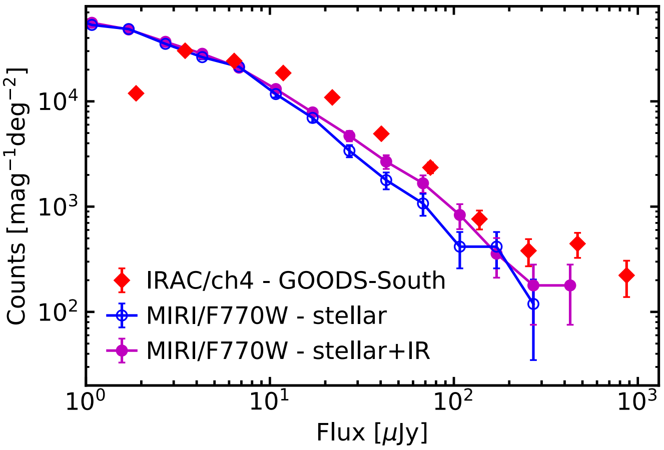

Fig. 3. Differential galaxy number counts in the MIRI/*F770W* filter with and without the dust emission, compared to the *Spitzer* IRAC/8 μm number counts measured in the GOODS-South field (Schreiber et al. 2017).

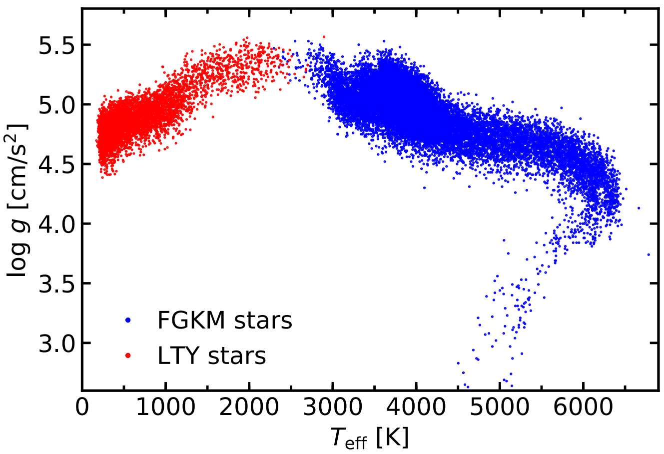

Fig. 4. Distribution of effective temperature and surface gravity for the mock FGKM stars from the Besançon model in blue, and our mock LTY stars in red.

at high galactic latitudes b. The surface density of objects at the central galactic coordinates (l, b) results from the integration of the density profile over heliocentric distance, scaled to the local number density. We take the predicted local number densities of Burgasser (2007) for L0 to T8 stars (see Caballero et al. 2008). Because of the small number of Y star observations, their number density is poorly constrained so we linearly extrapolate the local number densities of hotter stars to the cooler subtypes T9 and Y0-Y2. Star coordinates are sampled from a uniform distribution.

An effective temperature $T_{\rm eff}$ is assigned to each stellar subtype following the brown dwarf compilation[7] from Pecaut & Mamajek (2013). Surface gravity $\log g$ is computed from the stellar masses and radii, the latter being taken from the same compilation but imposing the lower bound of $0.1\,R_\odot$ (1 Jupiter radius). Stellar masses come from a linear model with $0.1\,M_\odot$ for type L0 and $0.02\,M_\odot$ for Y2. We include a bivariate Gaussian scatter to the duplet ($T_{\rm eff}$, $\log g$) with 10% relative dispersion. Figure 4 shows the sampled parameters for LTY stars. We sample the sedimentation efficiencies $f_{\rm sed}$ from Gaussian random distributions with mean $\mu = 2$ and scatter $\sigma = 1$ for L types, and

[7] http://www.pas.rochester.edu/~emamajek/

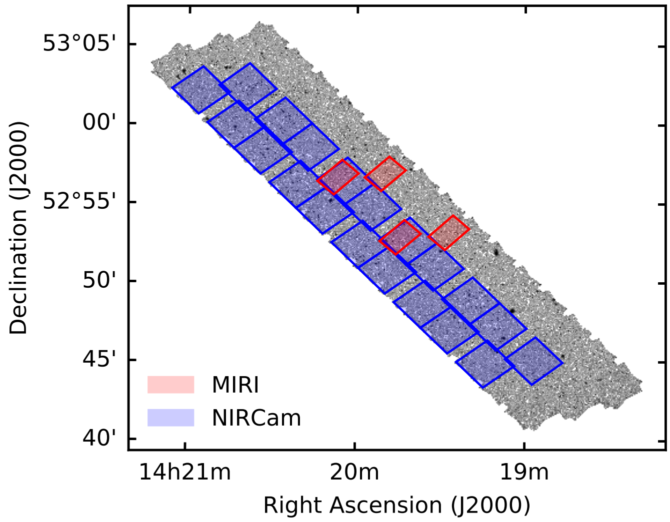

Fig. 5. CEERS layout in the EGS field. The 10 NIRcam imaging pointings are shown in blue and the 4 MIRI parallels in red. The ancillary HST/WFC3 H_{160}-band coverage is in gray. The pointings are all approximate until the final schedule. The parallel NIRSpec observations are not represented for clarity.

$\mu = 4.5$ and $\sigma = 0.5$ for T and Y types (Morley et al. 2012). This parameter describes the optical thickness of the metal clouds in the brown dwarf atmosphere.

We consider the modeled stellar spectra from Baraffe et al. (2015) at $1200 < T_{\rm eff} < 7000$ K (BT-Settl, CIFIST2011_2015), Morley et al. (2012) at $500 < T_{\rm eff} < 1200$ K and Morley et al. (2014) at $200 < T_{\rm eff} < 500$ K. These are physically-motivated high-resolution spectra from optical to mid-infrared, including absorption by water, methane, ammonia and metal clouds. We extrapolate the templates blueward of 6000 Å with a blackbody spectrum at the corresponding effective temperature if necessary. Cold brown dwarf spectra differ from blackbodies by several orders of magnitudes below 1 μm (Morley et al. 2014), hence we scale the blackbody spectrum to the bluest template point. We assign to each parameter set ($T_{\rm eff}$, $\log g$, $f_{\rm sed}$) the template with the closest parameters. We check that our modeling can reproduce the optical and near-IR magnitudes from the Besançon model output for F to M stars. Emitted spectra are finally scaled according to the stellar radii and heliocentric distances.

3. Methodology

3.1. Programs

In this paper, we consider two accepted JWST observing programs in the Extended Groth Strip (EGS) and the *Hubble* Ultra-Deep Field (HUDF). The existing HST imaging data in the optical and near-infrared are utilized in both fields. We exclusively simulate high-resolution space-based images and neglect ancillary ground-based data.

3.1.1. Cosmic Evolution Early Release Science survey

The Cosmic Evolution Early Release Science (CEERS[8]; P.I.: S. L. Finkelstein) survey is one of the JWST Early Release Science (ERS) programs. CEERS includes multiple imaging (NIRCam, MIRI) and spectroscopic observations over 100 arcmin^2 in the EGS HST legacy field. As shown in Fig. 5, the mosaic

[8] https://jwst.stsci.edu/observing-programs/approved-ers-programs

Table 1. Summary of the JWST imaging data in CEERS and the HUDF – limiting magnitudes.

Name	Area [(a)]	NIRCam									MIRI	
	[arcmin^2]	*F090W*	*F115W*	*F150W*	*F200W*	*F277W*	*F335M*	*F356W*	*F410M*	*F444W*	*F560W*	*F770W*
CEERS_1	96.8	–	28.7	28.9	29.1	29.2	–	29.2	–	28.7	–	–
CEERS_2	4.6	–	28.7	28.9	29.1	29.2	–	29.2	–	28.7	25.9	25.9
HUDF_1	4.7	29.9	30.3	30.3	30.3	30.6	29.9	30.5	29.9	30.1	–	–
HUDF_2	2.3	29.9	30.3	30.3	30.3	30.6	29.9	30.5	29.9	30.1	28.1	–

Notes. The magnitudes are 5σ point-source limits measured in 0.2″ and 0.6″ diameter apertures for NIRCam and MIRI, respectively. [(a)]The configurations without MIRI include the area of the configurations with MIRI.

Table 2. Summary of the HST imaging data – limiting magnitudes.

Field	Area [(a)]	ACS					WFC3			
	[arcmin^2]	*F435W*	*F606W*	*F775W*	*F814W*	*F850LP*	*F105W*	*F125W*	*F140W*	*F160W*
EGS	205	–	28.8	–	28.2	–	–	27.6	26.8 [(b)]	27.6
XDF	4.7	29.8	30.3	30.3	29.1	29.4	30.1	29.8	29.8	29.8

Notes. The magnitudes are 5σ limits measured in empty circular apertures of diameter 2× the PSF FWHM. [(a)]This corresponds to the WFC3 surveyed area. [(b)]The WFC3/*F140W* band in the EGS field is not used in this paper (see Sect. 3.1.1).

pattern consists of ten adjacent and nonoverlapping NIRCam imaging pointings (each NIRCam pointing includes two parallel and separated fields), covering the $1 < \lambda < 5\,\mu$m wavelength range, with four MIRI imaging parallels giving two NIRCam-MIRI overlaps. The estimated 5σ depths are ~29 mag for NIRCam and ~26 mag for MIRI (with 32 hours of science integration time). For simplicity, we treat the two distinct observing strategies listed in Table 1. These are the shallowest NIRCam-only and NIRCam-MIRI configurations of the survey, though all the pointings have similar filter choices and exposure times.

The EGS field is supported by the HST/CANDELS multiwavelength data (Stefanon et al. 2017). We consider the high-resolution HST imaging in the ACS/*F606W*, *F814W* and WFC3/*F125W*, *F160W* bands (Grogin et al. 2011; Koekemoer et al. 2011), as indicated in Table 2. These images reach the 5σ depths of 28.8, 28.2, 27.6 and 27.6 mag, respectively, measured in empty 0.24″, 0.24″, 0.38″ and 0.4″ diameter apertures. We do not use the WFC3/*F140W* imaging from 3D-HST (Brammer et al. 2012; Momcheva et al. 2016) because of its nonuniform layout. In the future, the Ultraviolet Imaging of the CANDELS Fields (UVCANDELS; P. I.: H. Teplitz) will provide deep WFC3/*F275W* and ACS/*F435W* imaging in the EGS field, covering most of the WFC3 footprint and reaching about 27 and 28 mag depths, respectively. These data are not simulated either.

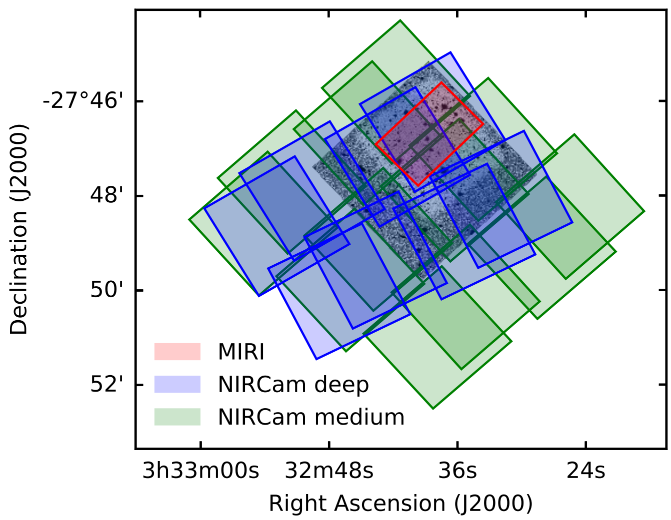

Fig. 6. NIRCam GTO and MIRI GTO layouts in the HUDF. The 4 NIRCam deep pointings are shown in blue, the 6 NIRCam medium pointings in green and the MIRI pointing in red. The ancillary WFC3/IR H_{160}-band coverage in the XDF field is in gray, and the deepest WFC3 region in light gray. The whole XDF field is covered with the deepest ACS data. The dither patterns and the parallel observations are not represented for clarity.

3.1.2. *Hubble* Ultra-Deep Field

Two programs of the Guaranteed Time Observations (GTO) teams are designed to observe the CANDELS GOODS-South field, both of them including deep imaging of the eXtreme Deep Field (XDF). The NIRCam-NIRSpec Galaxy Assembly Survey (P.I.: D. J. Eisenstein) in the GOODS-South and GOODS-North fields includes deep NIRCam preimaging of the HUDF for spectroscopic follow-ups, separated into "Deep" and "Medium" pointings as shown in Fig. 6. This program covers $0.8 < \lambda < 5\,\mu$m with broad-band imaging and two additional medium bands at 3.35 and 4.10 μm. In the GOODS-South field, the "Deep" ("Medium") survey covers 26 (40) arcmin^2 with 174 (42) hours of science time integration, and consists of four (six) NIRCam pointings. In both Deep and Medium pointings (separately), about one third of the area includes overlapping pointings. With NIRCam alone, Williams et al. (2018) predicted several thousands of detected galaxies at $z > 6$ and tens at $z > 10$ at <30 mag (5σ) within the total ~200 arcmin^2 survey in the GOODS-South and GOODS-North fields. The MIRI HUDF Deep Imaging Survey (P.I.: H. U. Norgaard-Nielsen) consists of MIRI imaging in the *F560W* filter across the 2.3 arcmin^2 of the MIRI field of view. This survey will reach depths of 28.3 mag (4σ) with 49 hours of science integration time for a

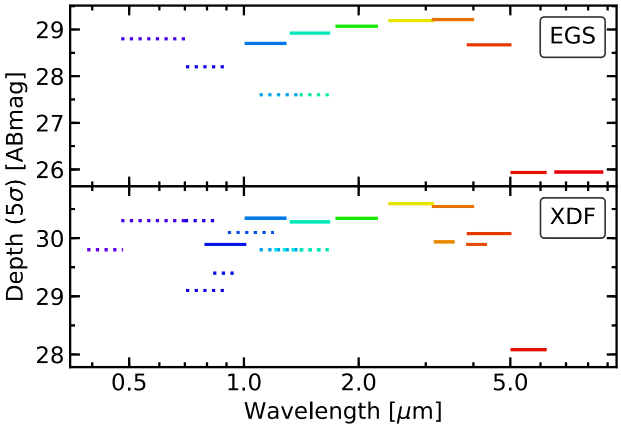

Fig. 7. Limiting magnitudes at 5σ in the simulated data sets in the EGS field (*top*) and the XDF (*bottom*). The list of bands and depths are listed in Tables 1 and 2. The solid lines represent the JWST bands and the dotted lines represent HST bands. The length of each segment is the FWHM of the filter transmission curve.

total of 60 hours. Its layout will be entirely covered by NIRCam imaging.

This field benefits from existing HST/ACS and WFC3/IR imaging, especially in the XDF with the deepest HST imaging ever achieved (Illingworth et al. 2013; Guo et al. 2013). These images cover the optical and near-IR domain $0.38 < \lambda < 1.68\,\mu$m with 9 filters, across 10.8 (4.7) arcmin^2 for the deepest optical (infrared) data. In most filters, the typical 5σ depth reaches 30 mag in the deepest region, measured in empty 0.35″ diameter apertures. We consider two configurations in the deepest WFC3/IR region as described in Table 1, combining the NIRCam Deep and Medium pointings without the respective overlaps, and either with or without MIRI. The bands and depths are listed in Tables 1 and 2, and represented in Fig. 7.

3.2. Mock image simulation

Mock images are generated with SkyMaker (Bertin 2009) from the convolution of point-like and extended sources (with any Sérsic index) with an external point spread function (PSF). Modeled PSF images are created with webbpsf[9] for JWST and TinyTim[10] (Krist et al. 2011) for HST, with an oversampling of five to avoid aliasing effects. The G2V star spectrum from Castelli & Kurucz (2004) is taken as source to generate polychromatic PSFs. In mock HST images, we include an additional jitter (Gaussian blurring) tuned to recover the measured PSF full width at half maximum (FWHM) in real data. The modeled PSF files are multiplied by a radial Fermic-Dirac kernel to limit edge effects around bright sources. Our noise model consists of a single (uncorrelated) Poisson component for photon noise. In real images we expect the noise to be sky-dominated especially for faint sources, we therefore neglect other noise components such as readout noise, inter-pixel capacitance and cosmic rays. Background levels and detection limits can be estimated with the Exposure Time Calculators (ETC) for HST[11] and JWST[12] (Pontoppidan et al. 2016). We tune the background surface brightnesses to reproduce the predicted or measured depths in each band.

[9] https://webbpsf.readthedocs.io/en/stable/
[10] http://www.stsci.edu/software/tinytim/
[11] http://etc.stsci.edu/
[12] https://jwst.etc.stsci.edu/

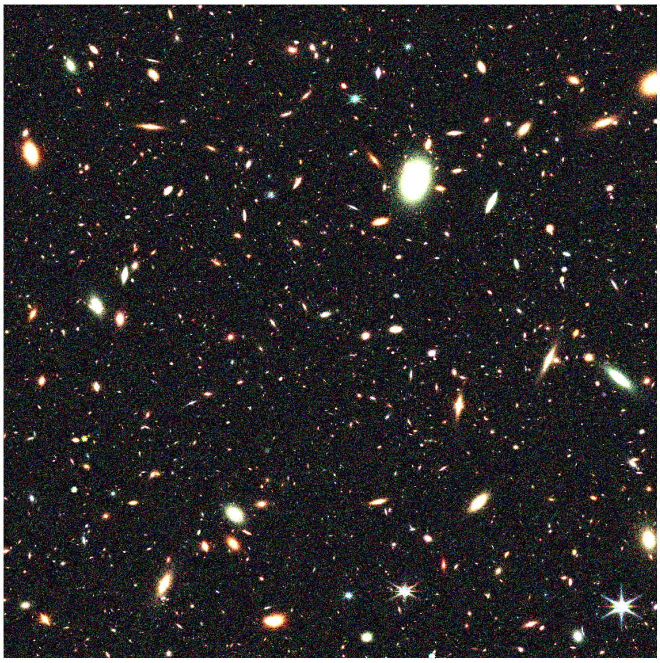

Fig. 8. Simulated composite image in the NIRCam/$F115W$, $F200W$ and $F356W$ bands to a depth of ~29 mag (5σ), following the CEERS observing strategy. The area is 4.5 arcmin^2 and the resolution 0.031″/pixel for all the images (see Sect. 3.2).

In each of the considered observing strategies, we generate mock images of 11×11 arcmin^2 including all the sources from the mock catalogs. The resulting predictions are then scaled down by numbers to match the area of the planned observations. We generate all images directly at the NIRCam short-wavelength pixel scale of 0.031″/pixel (the smallest among the instruments), avoiding astrometric and resampling issues. Saturation effects are neglected, since the effective saturation limit of stacked small exposure images, as well as the detector nonlinearity, may be difficult to model. Figure 8 shows an example of a simulated composite image in three NIRCam bands. Real images from future JWST surveys may depart from our mock images because of neglected instrumental effects.

3.3. Source extraction

Photometry is measured with SExtractor (Bertin & Arnouts 1996) in the dual-image mode. We successively use the NIRCam/$F115W$, $F150W$ and $F200W$ images as detection image, then combine the extracted catalogs with a 0.2″ matching radius. We use the "hot mode" SExtractor parameters from Galametz et al. (2013) optimized for faint sources, and we checked that we can effectively recover the sources detectable by eye. The redshift distribution of the detected galaxies in the CEERS and the HUDF configurations are represented in Fig. 2. We do not mask bright sources.

Aperture photometry generally provides the less noisy color measurements compared to Kron (Kron 1980) photometry MAG_AUTO (Hildebrandt et al. 2012), however this requires the images to be PSF-matched. We compute the PSF-matching kernels to the HST/$F160W$ band PSF with pypher[13] (Boucaud et al. 2016), from the PSF files used to create the mock images (neglecting PSF reconstruction). Each initial PSF file

[13] https://github.com/aboucaud/pypher

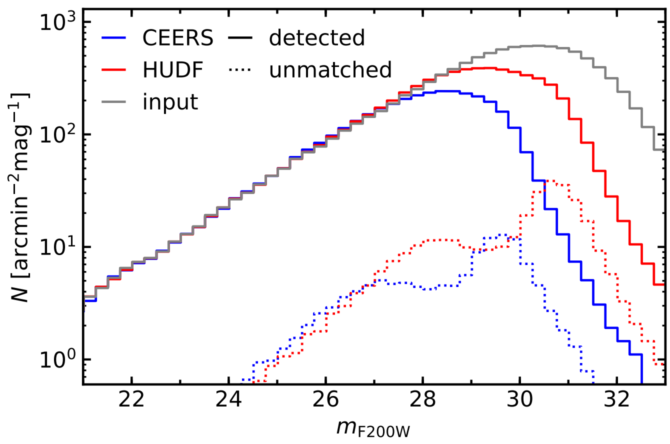

Fig. 9. Detected source number counts versus NIRCam/$F200W$ magnitude. The gray line indicates the input magnitudes of all the mock galaxies. The colored lines illustrate the measured magnitudes of detected sources in our CEERS and HUDF simulations. The solid lines include all the detected sources, the dashed lines represent unmatched sources only.

is resampled to the pixel scale of the target PSF, then the kernel is computed, resampled to the image pixel scale and convoluted with the image (Aniano et al. 2011). Fluxes are measured in 0.5″ diameter apertures (McLure et al. 2013; McLeod et al. 2015, 2016), ensuring at least 70% point-source flux is included in all bands. The PSF FWHM (respectively the 80% encircled energy radius for point source) are 0.145″ (0.28″) for the NIRCam 4.4 μm band and 0.25″ (0.49″) for the MIRI 7.7 μm band.

Following Laigle et al. (2016), we apply corrections to the aperture photometry. SExtractor is known to underestimate flux errors in the case of correlated noise (e.g., Leauthaud et al. 2007), arising from PSF-matching. We therefore apply a band-dependent correction to the measured flux errors, from the ratio of the median flux in empty apertures and the standard deviation of the source flux errors (Bielby et al. 2012). In addition, we scale both fluxes and flux errors with a source-dependent aperture to total correction, computed using MAG_AUTO measurements (Moutard et al. 2016). We exclude truncated photometry and reject objects with negative aperture flux in all bands. Finally, we match the detected object positions with the input source catalog, taking the nearest match within a 0.1″ search radius[14]. Figure 9 illustrates the detected number counts for both of the CEERS and HUDF configurations. The unmatched sources (indicated with dotted lines) present two components, the bright one including artifacts around stars and undeblended sources. We recall that the number of false detections is very sensitive to the noise model.

Galactic foreground extinction remains minimal in extragalactic fields at high galactic latitudes. In practice, it is often corrected by adjusting the image photometric zeropoints. We estimate the zeropoint corrections using the extinction curve of Fitzpatrick (1999) and the Milky Way dust map from Schlafly & Finkbeiner (2011). At the galactic latitude of the EGS field or the HUDF, the correction is at most 0.03 mag in the bluest considered band (ACS/$F435W$), therefore we decide to neglect galactic extinction in both the mock input spectra and the source extraction pipeline.

[14] Sources which are detected beyond this radius are either source pairs or false detections wrongly matched to undetected sources. The probability of the latter event is ~2%.

3.4. Photometric redshift estimation

To compute photometric redshifts, we perform SED-fitting with LePhare (Arnouts et al. 2002; Ilbert et al. 2006). Following Ilbert et al. (2009), we use the 31 templates including spiral and elliptical galaxies from Polletta et al. (2007) and a set of 12 templates of young blue star-forming galaxies using BC03 stellar population synthesis models. The BC03 templates are extended beyond 3 μm using the Polletta et al. (2007) templates, which include both PAH and hot dust emission from averaged *Spitzer*/IRAC measurements. This set of templates has been extensively tested by the COSMOS collaboration (e.g., Onodera et al. 2012; Laigle et al. 2016) and tested in hydrodynamical simulations (Laigle et al. 2019). We do not include the two templates of elliptical galaxies added in Ilbert et al. (2013) to avoid potential loss of information from degeneracies over the large redshift interval (Chevallard & Charlot 2016). Dust reddening is added as a free parameter ($E(B-V) \leq 0.5$) and the following attenuation laws are considered: Calzetti et al. (2000), Prevot et al. (1984), and two modified Calzetti laws including the bump at 2175 Å (Fitzpatrick & Massa 1986). Nebular emission lines are added following Ilbert et al. (2009). We impose that the absolute magnitudes satisfies $M_V > -24.5$ for CEERS and $M_B > -24$ in the HUDF, based on the LFs at $z < 2$ in Ilbert et al. (2005) and assuming this is still valid at $z > 2$. This SED-fitting prescription (e.g., SFH, attenuation) is distinct from the one used to generate the JAGUAR mock galaxies. This variability may reflect the potential disagreement between the fitted templates and reality, at least to a certain level.

The redshift probability distribution functions (PDFz) are measured in the redshift interval $0 < z < 15$. We perform SED-fitting using fluxes (not magnitudes) and do not use upper limits because this may remove essential information (Mortlock et al. 2012). We add a systematic error of 0.03 mag in quadrature to the extracted fluxes to include the uncertainties in the color-modeling (set of templates, attenuation curves). Photometric redshifts are defined as the median of the PDFz (Ilbert et al. 2013).

Star templates are also fitted to reproduce and quantify potential object misclassification. Similarly to Davidzon et al. (2017), we use the star templates from Bixler et al. (1991), Pickles (1998), Chabrier et al. (2000), the brown dwarfs templates from Baraffe et al. (2015) (see Sect. 2.4) and the BT-Settl grids with Caffau et al. (2010) solar abundances at lower temperatures. These templates partly differ from the set of templates used to generate the mock stars.

We do not attempt to fit AGN templates. SEDs which are AGN-dominated typically present a featureless power-law optical-to-infrared continuum, strong emission lines and Lyman alpha (Lyα) forest absorption especially at high redshifts. The observed emission of galaxies hosting AGNs strongly depends on the contribution of the two components. A large number of hybrid templates would be necessary to correctly characterize them, leading to risks of degeneracies in the SED-fitting procedure (Salvato et al. 2009). In addition, AGNs exhibit variable emission with timescales from minutes to decades. Source variability may be observed from multiple-exposure imaging and dithering in both CEERS and the HUDF, so that AGNs brighter than the detection limit with relatively short timescales should be identifiable.

3.5. Physical parameter estimation

We run LePhare a second time following Ilbert et al. (2015) to determine other physical parameters such as stellar mass (M_*), star formation rate[15] (SFR) and absolute UV magnitudes ($M_{\rm UV}$). Absolute magnitudes (uncorrected for attenuation) are computed using a top-hat filter of width 100 Å centered at 1500 Å rest-frame (Ilbert et al. 2005). Redshifts are fixed to the photometric redshifts from the first LePhare run. The grid of fitted galaxy templates consists of BC03 models assuming exponential SFHs with $0.1 < \tau < 30$ Gyr, and delayed SFHs ($\tau^{-2}te^{-t/\tau}$) peaking after 1 and 3 Gyr. Two metallicities are considered ($Z_\odot$, $0.5Z_\odot$). We allow $E(B-V) \leq 0.5$ and only include the Calzetti et al. (2000) starburst attenuation curve for simplicity and computational time (Ilbert et al. 2015 included two attenuation curves). Physical parameters are defined as the median of their marginalized probability distribution functions.

4. Physical parameter recovery

4.1. Photometric redshift recovery

The recovery of the photometric redshifts through SED-fitting can first be tested. The quality of the photometric redshifts is assessed with the following statistics (Ilbert et al. 2006): (1) the mean normalized residual $\langle\delta z\rangle$, with the normalized residuals $\delta z = (z_{\rm phot} - z_{\rm true})/(1 + z_{\rm true})$, (2) the normalized median absolute deviation (NMAD) $\sigma_{\rm NMAD} = 1.4826 \times {\rm med}(|\delta z - {\rm med}(\delta z)|)$, and (3) the fraction of catastrophic failures η, for which $|\delta z| > 0.15$.

Figure 10 represents the photometric and true redshifts for all the considered observing strategies, in multiple magnitude intervals. No selection is applied. We observe no systematic bias at $z_{\rm true} < 2$ in any configuration for the bright samples, for which the galaxy continuum redward of the Balmer break is sufficiently well sampled. However, the mean normalized residual becomes negative $\langle\delta z\rangle < -0.1$ at $z_{\rm true} > 2$, even in the brightest magnitude interval. This is probably due to the different attenuation curves in the mock galaxies and in LePhare. The effective, galaxy-wide attenuation curves of the JAGUAR mock galaxies (which employ the two-component attenuation law of Charlot & Fall 2000) are typically grayer (flatter) than the Calzetti et al. (2000) model in the infrared. The bump at 2175 Å in the attenuation curve utilized in LePhare and not JAGUAR may also be an issue.

In the CEERS_1 observing strategies, the number of catastrophic failures is significant even in the brightest magnitude bin. There are several explanations for that. At $z_{\rm true} < 4$, there is a significant number of sources whose redshift is underestimated. Attenuated blue galaxies may be confused with lower redshift unattenuated red galaxies. One of the main reasons for this is the degeneracy between the Lyman and the Balmer breaks, as confirmed from spectroscopic surveys (Le Fèvre et al. 2015). This confusion is enhanced by the lack of optical data in the EGS field, with no deep imaging blueward of HST/$F606W$, so that the Balmer break cannot be correctly identified at low redshift. This is the main reason for the outliers among bright sources. At $z_{\rm true} > 4$ the Lyα break becomes detectable in the HST bands. The number of catastrophic redshift underestimates is therefore reduced, especially for bright sources thanks to the NIRCam bands sampling both the Balmer and Lyα breaks. Strong emission lines may lead to overestimating the continuum, especially for observing strategies which only employ broad-band filters. This can have a significant impact on determining the position of the Balmer break. Quiescent galaxies appear to have a larger dispersion but a smaller outlier fraction than star-forming galaxies.

The two additional MIRI bands at 5.6 and 7.7 μm in the CEERS_2 observing strategy marginally improve the photometric redshift estimates. Both dispersion and outlier rate are larger in the brightest magnitude interval and smaller at fainter magnitudes. At high redshift $z > 4$, the MIRI filters cover the rest-frame near-IR or optical region, therefore sampling the stellar continuum or even the Balmer break. The photometric redshift dispersion is reduced by $\Delta\sigma_{\rm NMAD} = 0.01$ for $4 < z_{\rm true} < 7$ galaxies. Most of the faint NIRCam-detected sources, however, are not detected in MIRI at the depths which will be probed by the CEERS survey. For low-redshift $z < 4$ galaxies, the HST+NIRCam bands impose most of the constraints on photometric redshifts. We still observe fewer catastrophic failures because of Lyman-break misidentification when MIRI data are available, and a systematic bias lowered by 0.05 at $z_{\rm true} = 2$. This comes from a improved sampling of the stellar continuum with MIRI. However, the number of outliers with $z_{\rm true} < 4$ and $z_{\rm phot} > 4$ at $m_{F200W} < 26$ is increased. One of the reasons for more outliers among bright sources with MIRI may be the treatment of dust. The key feature appears to be the observed-frame mid-IR colors. Galaxies with good photometric redshifts mostly present decreasing mid-IR emission with increasing wavelength, whereas outliers often present increasing mid-IR emission. This feature can appear in our mock galaxies from (1) large dust continuum, remaining non negligible even at ~2−3 μm rest-frame because of high dust temperature, or (2) large PAH emission lines at 3.3, 6.2 and 7.7 μm. The infrared luminosities may be overestimated, notably because of the energy balance assumption. In contrast, we are not performing an energy balance in the fitting with LePhare, so that the attenuation and dust emission are disconnected. In addition, the Polletta et al. (2007) templates include dust emission from averaged *Spitzer*/IRAC measurements, so they may not include the mid-IR brightest galaxies. Consequently, LePhare tends to favor high-redshift solutions for low-redshift galaxies with bright and red mid-IR colors. Because of these uncertainties in the mid-IR modeling, one could increase the systematic error added in quadrature to the MIRI photometry. However, this would reduce the additional mid-IR information which is essential to their characterization of high-redshift sources. We therefore do not follow this option.

The main improvements in the HUDF configurations are the deeper HST and NIRCam photometry, leading to the considerable improvements in both the photometric redshift dispersion and outlier rates compared to CEERS. Spectral features such as the Lyman and Balmer breaks can be better captured with the twice more numerous HST bands in the red and near-IR filters. As a consequence, the number of low-redshift galaxies at $z < 3$ with $z_{\rm phot} > 4$ is significantly reduced. Moreover, the additional B_{435} band offers an improved sampling of the Balmer break at $z < 3$ and the Lyman break at $z > 4$. We find that the global outlier rates and photometric redshift dispersion are decreased by about 10% thanks to the addition of the blue band. Furthermore, the two NIRCam medium-bands marginally reduce the redshift outlier rates at $z > 6$ mostly. With the additional MIRI/$F560W$ band in HUDF_2, we do not observe any improvement in the global photometric redshift dispersion or outlier rate. In contrast, both of them are improved at high redshift and especially at $z > 10$, where MIRI provides the only information redward of the Balmer break.

Source blending may also lead to catastrophic photometric redshifts, because of contaminated photometry and incorrect colors. The photometric redshifts of blended high-redshift

[15] In LePhare, the measured SFR is instantaneous, whereas in JAGUAR it is averaged over the past 100 Myr. For exponential and delayed SFH with $\tau > 1$ Gyr, the difference between these two SFR definitions is no more than 5% (0.02 dex) at $z > 0.1$.

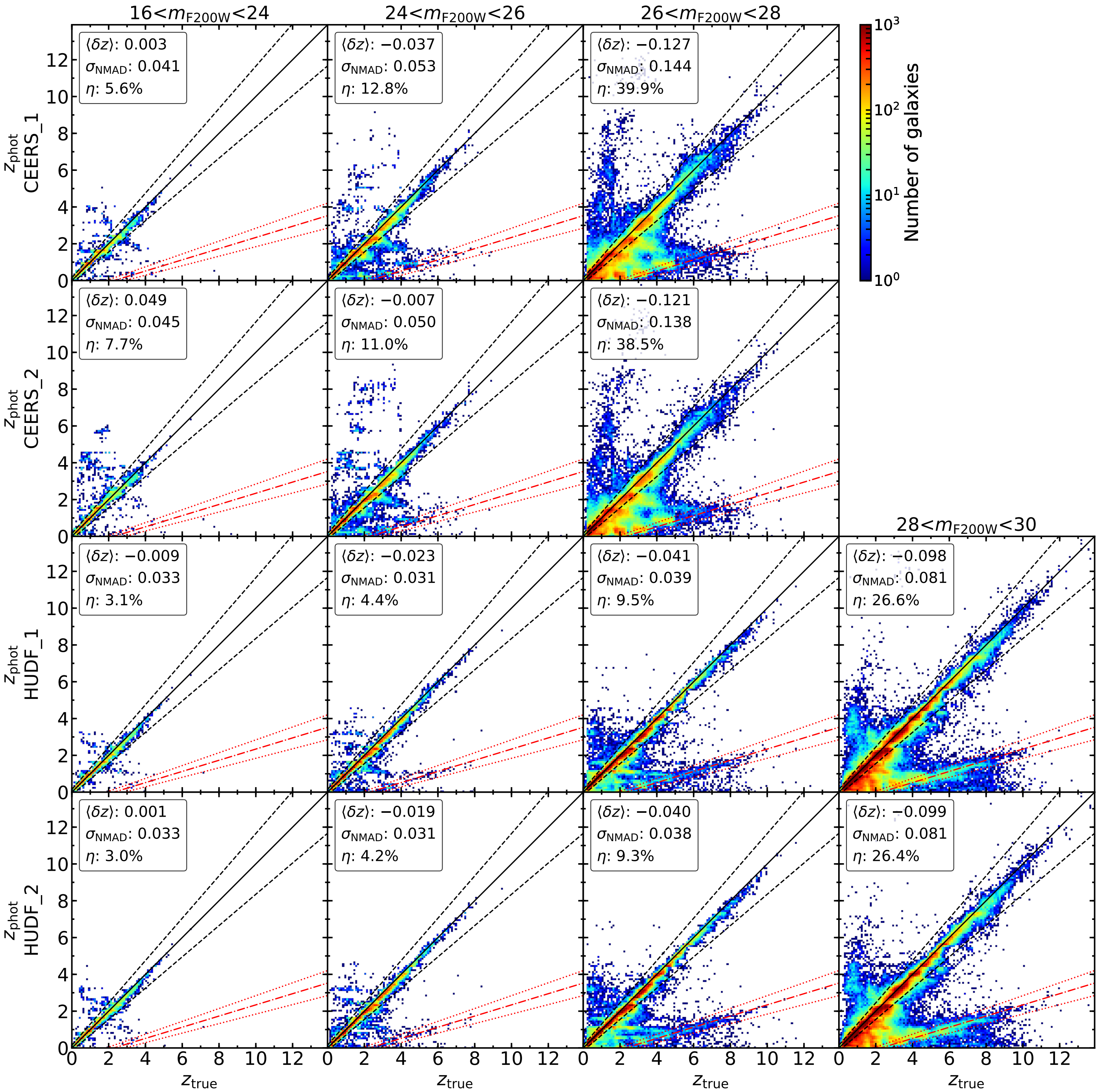

Fig. 10. Comparison between photometric and true redshifts, "true" redshifts being in this case the simulated redshifts as described in Sect. 2.1. The rows correspond to CEERS_1, CEERS_2, HUDF_1 and HUDF_2 observing strategies from top to bottom, and the columns represent observed NIRCam/$F200W$ magnitude intervals. Color indicates the number of sources. The mean normalized residual, the normalized median absolute deviation and the catastrophic error fraction η for all the detected sources are indicated. The solid black line shows the 1:1 relation and the dashed black lines the $\pm 0.15(1+z_{\rm true})$ threshold used to compute η. The degeneracy between the Balmer 4000 Å break and the Lyα 1216 Å break is identified by the dotted-dashed red line, with 15% errors in dotted red lines.

galaxies tend to be mostly underestimated, which is coherent with blended source pairs or groups which are most likely to contain at least one galaxy at $z \sim 1-2$. Figure 11 illustrates the fraction of detected sources with the SExtractor flags indicating blending (flag 2), contaminated photometry (flag 1), both (flag 3) or none (flag 0). The solid lines represent the photometric redshift outliers and dotted lines the whole detected sample. The number of flagged sources mostly decreases with increasing magnitudes, because faint sources typically need to be isolated to be detected, therefore unflagged. In contrast, faint sources with bright neighbors may remain undetected. Flagged objects represent a large portion of the detected sources, about 40% (65%) at $m_{F200W} < 26$ in CEERS (HUDF), which increases with the depth of the survey. We observe a significantly increased fraction of contaminated sources (flags 1+3) in the $z_{\rm phot}$ outliers, about twice as much as in the entire sample at $m_{F200W} < 26$

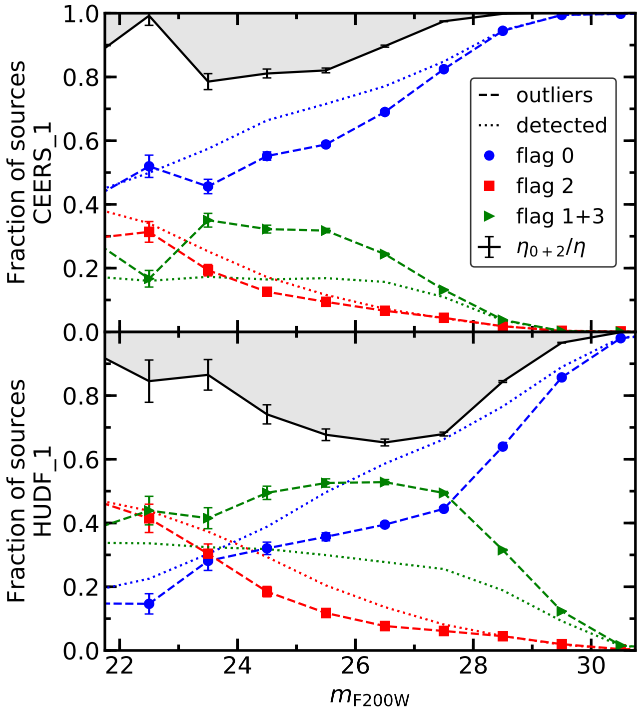

Fig. 11. Fraction of detected sources per SExtractor flags indicating blending (flag 2), contaminated photometry (flag 1), both (flag 3) or none (flag 0) versus observed NIRCam/$F200W$ magnitude. The rows correspond to the CEERS_1 (*top*) and HUDF_1 (*bottom*) observing strategies. The dashed lines indicate the flag fractions among photometric redshift outliers (summing to one), as defined in Sect. 4.1. The dotted lines represent the flag fractions in the whole detected sample (summing to one). The solid black line shows the ratio between the photometric redshift outlier rates η_{0+2} assuming all the sources have uncontaminated photometry (flags 0 or 2), and the standard outlier rates. The error bars are propagated Poisson errors.

in CEERS and at $m_{F200W} < 28$ in the HUDF. In the hypothetical case where all the detected sources had uncontaminated photometry (flags 0+2), the photometric redshift outlier rates η would be corrected by the indicated ratio η_{0+2}/η. This ratio reaches 80% at $24 < m_{F200W} < 26$ in CEERS, meaning that the outlier rate would decrease from 12% to 10% in this magnitude bin. Similarly in the HUDF, the outlier rate at $26 < m_{F200W} < 28$ would decrease from 9% to 6%. We observe no significant wavelength dependence of these values. These results indicate that source blending will definitely be an issue with deep JWST imaging.

4.2. Stellar mass recovery

The comparison between input stellar masses and those measured through SED-fitting is illustrated in Fig. 12 for the CEERS_1 and HUDF_1 observing strategies. The redshift intervals are centered at $z = 1, 2, 3, \ldots$ with a width of $\Delta z = 1$. The measured stellar masses agree well with the input ones.

In the CEERS_1 configuration, the stellar mass dispersion is below 0.25 dex at $\log(M_*/M_\odot) > 9$. Removing the photometric redshift outliers lowers the dispersion at $\log(M_*/M_\odot) > 9$ to 0.2 dex, and significantly reduces the number of catastrophic stellar mass estimates at $\log(M_*/M_\odot) < 8.5$. These low-mass objects are typically fainter and have noisier colors. The overall dispersion increases as the stellar mass decreases, from 0.25 dex to 0.5 dex for $\log(M_*/M_\odot)$ of 9 and 8, respectively, and for galaxies with good photometric redshifts, from 0.2 dex to up to 0.35 dex. Most of the outliers at $z < 4$ have stellar masses which are overestimated because of overestimated redshifts. The remaining cases are galaxies with nearby sources, boosting their aperture fluxes and affecting their colors. For blended galaxies with nevertheless correct colors and photometric redshifts, the total fluxes may not be correctly recovered through the deblending procedure despite the aperture-to-total flux correction. In the HUDF_1 strategy, both the number of outliers and the dispersion are smaller for low-mass galaxies, remaining below 0.45 dex up to $\log(M_*/M_\odot) = 7$ and even below 0.35 dex when discarding catastrophic photometric redshifts. Stellar masses are not significantly affected by redshift outliers above $\log(M_*/M_\odot) > 8$. The dispersion remains below 0.2 dex at $\log(M_*/M_\odot) > 9$ at all redshifts. These results mainly reflect the improvements in the photometric redshifts from deeper HST and NIRCam imaging and with the additional HST blue band. Moreover, the near-IR medium-band photometry enable the emission lines and the galaxy continuum to be better separated. The systematic overestimation and the dispersion at $z \geq 6$ are lowered by 0.05 dex only thanks to the medium bands, which are located close to the Balmer break in the rest-frame.

The median stellar mass lies between ±0.2 dex around the input value between $8 < \log(M_*/M_\odot) < 10$ at all redshifts and in both configurations, and is generally underestimated at $z \leq 3$ and overestimated at $z > 4$. These observations may again come from the steepness at $\lambda > 1\,\mu$m of the attenuation curves used in input and in the SED-fitting (see Sect. 4.1). More attenuation may hide more low-mass stars and therefore result in underestimated mass. At $\log(M_*/M_\odot) < 8$, the stellar mass estimates are systematically overestimated for galaxies with correct redshifts. This bias increases with redshift, and reaches at most 0.8 dex at $\log(M_*/M_\odot) = 7$. At $\log(M_*/M_\odot) > 10$ and $z < 6$, stellar masses are systematically underestimated by 0.15 − 0.2 dex. Massive galaxies are typically the most attenuated, and these galaxies effectively have large input attenuation $\hat{\tau}_V > 0.1$. The percentage of $\log(M_*/M_\odot) > 10$ galaxies with $\hat{\tau}_V > 1$ is 57%, and reaches 70% for the subset where mass is underestimated by at least 0.2 dex. Strong attenuation $E(B-V) > 0.5$ ($A_V > 2$) are not allowed in our LePhare configuration to avoid additional degeneracies between templates. The underestimated attenuation in SED-fitting may lead to underestimated stellar mass. In contrast, galaxies at $\log(M_*/M_\odot) \sim 9$ with $\hat{\tau}_V > 0.2$ have overestimated stellar masses, by 0.1, 0.2, 0.3 dex at $z = 4, 5, 6$ in both CEERS and the HUDF.

Quiescent galaxies have underestimated stellar masses in all the observing strategies, by 0.15 dex at $\log(M_*/M_\odot) > 9$ and by 0.5 dex below. These numbers are not reduced when removing photometric redshift outliers. High-mass quiescent galaxies typically have large metallicity, however observational constraints on the metallicity of low-mass galaxies are lacking. In JAGUAR, low-mass ($\log(M_*/M_\odot) < 8.7 + 0.4z$) quiescent galaxies are assigned random uniform metallicities between $-2.2 < \log(Z/Z_\odot) < 0.24$. The recovered stellar masses of $\log(M_*/M_\odot) < 9$ quiescent galaxies with $\log(Z/Z_\odot) < -0.5$ (> -0.5) are underestimated by up to 0.7 (0.4) dex. This dramatic underestimation of stellar mass for low-mass quiescent galaxies may come from the quiescent galaxy templates in LePhare which do not span the parameter space of the mock galaxies. In particular, only two metallicities ($\log(Z/Z_\odot) = 0, -0.3$) are allowed in the LePhare configuration to avoid degeneracies between templates. In addition, dust attenuation was neglected for low-mass quiescent galaxies in JAGUAR, which may also explain this systematic bias at low masses.

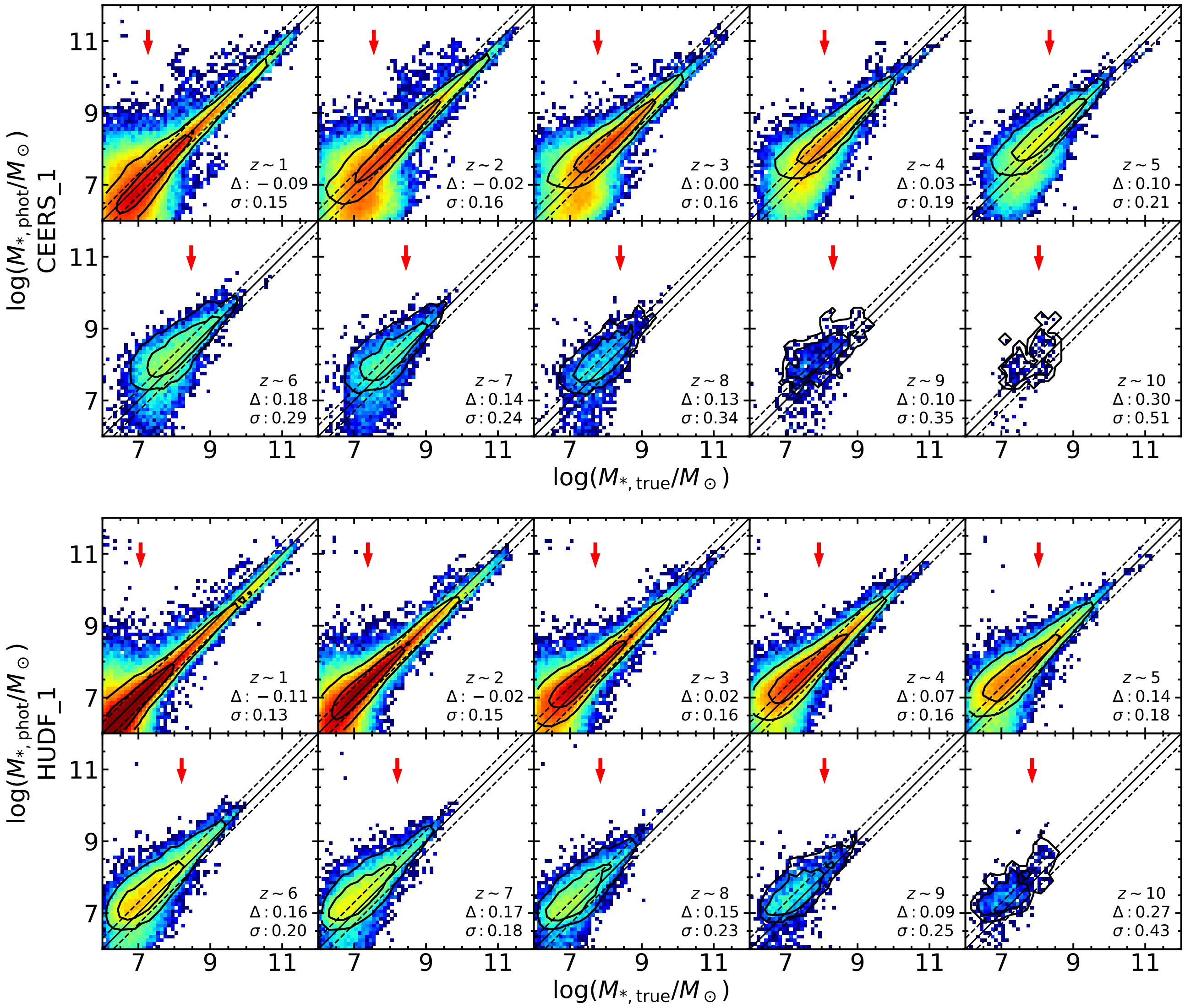

Fig. 12. Comparison between measured and input stellar masses, for the CEERS_1 and HUDF_1 observing strategies (*top and bottom* figures, respectively). Each panel represents an input redshift interval centered at $z_{\mathrm{true}} = 1, 2, 3, \ldots$ of width $\Delta z = 1$. Color indicates the number of sources in the whole sample, with the same color scale as in Fig. 10. The thick black contours represent the distribution of the sources with correct photometric redshift $|z_{\mathrm{phot}} - z_{\mathrm{true}}| < 0.15 z_{\mathrm{true}}$, including 68% and 95% of these sources, respectively. The median shift (Δ) and the NMAD (σ) for the sources with correct z_{phot} and $8 < \log(M_{*,\mathrm{true}}/M_\odot) < 10$ are indicated (in dex). The solid line shows the 1:1 relation and the dashed lines ±0.3 dex. The red arrows indicate the detected 90% stellar mass completeness.

The CEERS_2 strategy presents results equivalent to CEERS_1. This is not surprising because of the galaxy continuum already well sampled with NIRCam. At very high redshift $z > 10$ where NIRCam does not sample redward of the Balmer break, the photometric redshift estimates still rely on NIRCam, and the shallow MIRI imaging does not significantly improve the stellar mass estimates. With HUDF_2 however, the MIRI data are deep enough to slightly improve stellar masses at $z \geq 9$, with the scatter and systematic bias lowered by about 0.05 dex. This essentially comes from the improvement of photometric redshifts.

4.3. Star formation rate recovery

Figure 13 illustrates the galaxy star formation rate recovery in the CEERS_1 and HUDF_1 observing strategies. The results with the CEERS_2 and HUDF_2 configurations, respectively, are strictly similar.

The measured SFRs remain in correct agreement with the input values, however less precise than stellar mass estimates. We note that the SFR estimates may behave well because the assumed SFH in LePhare and in JAGUAR are similarly simple, meaning smooth exponential or delayed SFH. The low precision is primarily due to the degeneracy between SFR and dust attenuation, which affects the rest-frame UV, where the emission is dominated by hot, young stars. In an analogous work, Laigle et al. (2019) showed that with a similar LePhare configuration, attenuation is the main source of systematic uncertainties and dispersion in the SFR recovery. In addition, the missing nebular continuum emission in LePhare may also be an issue. For galaxies with good photometric redshifts, the SFR dispersion is 0.3 dex for the CEERS survey and 0.35 dex for HUDF, and remains stable over redshift and input SFR. In the HUDF, however, the recovered SFR distributions are skewed toward large SFRs at $z \geq 3$. This surely comes from the more difficult match between the input and the fitted galaxy templates,

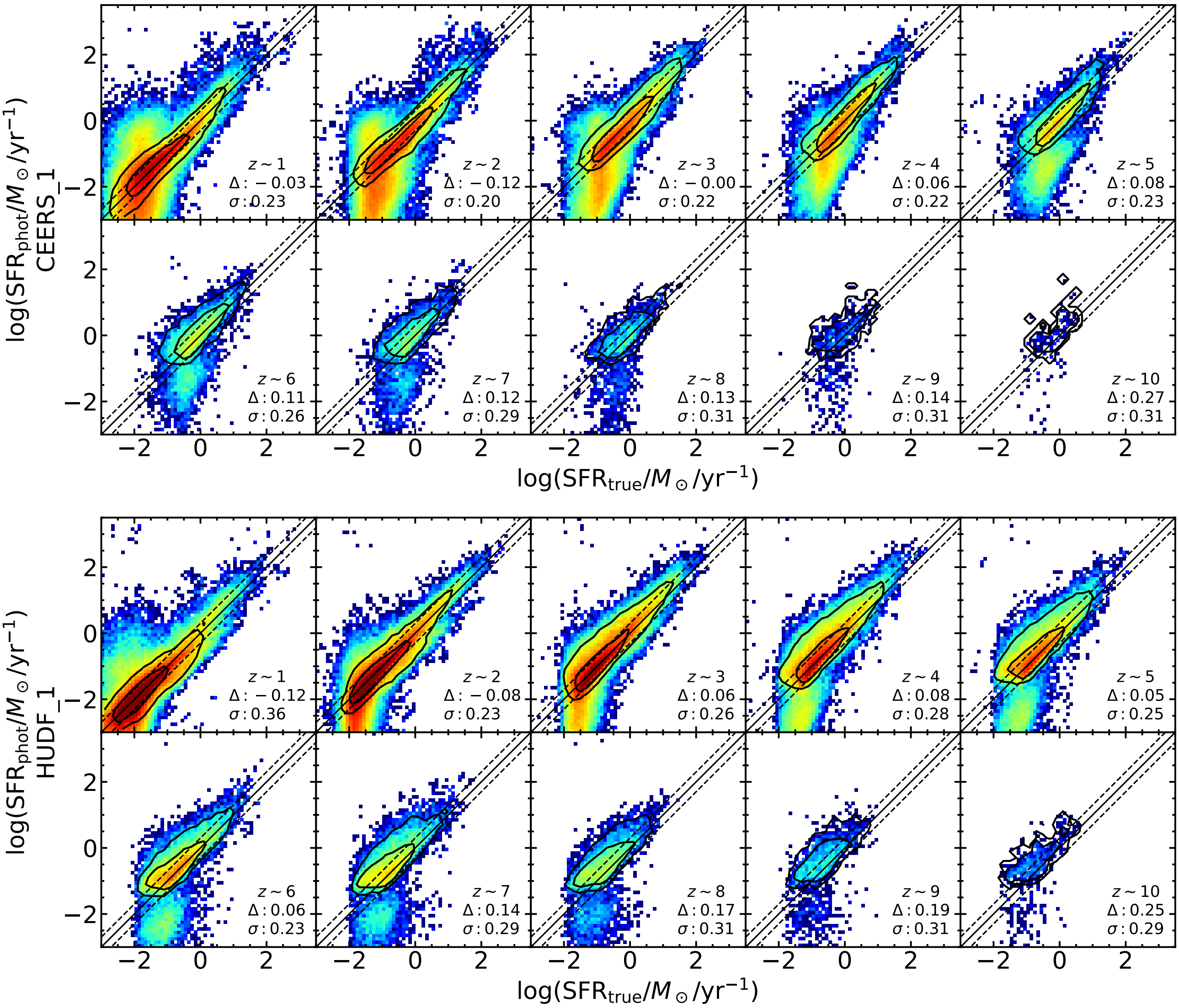

Fig. 13. Same as Fig. 12, but for star formation rate. The median shift (Δ) and the NMAD (σ) for the sources with correct $z_{\rm phot}$ and $-1 < \log({\rm SFR_{true}}/M_\odot/{\rm yr}^{-1}) < 1$ are indicated (in dex). The solid line shows the 1:1 relation and the dashed lines ±0.3 dex.

because of the increased depth in the HUDF and, at low redshift, the HST *B*-band, giving stronger constraints on the SFR tracers.

We observe that the median shift at ${\rm SFR_{true}} > 1\,M_\odot\,{\rm yr}^{-1}$ is bounded by ±0.2 dex at all redshifts in all the observing strategies. In particular, the most star-forming galaxies at $z < 6$ with ${\rm SFR_{true}} > 10\,M_\odot\,{\rm yr}^{-1}$ have systematically overestimated SFR estimates by 0.15 dex. This may come from the difference of attenuation curves assumed in JAGUAR and in LePhare. Additionally, most of the outliers at ${\rm SFR_{true}} > 1\,M_\odot\,{\rm yr}^{-1}$ have overestimated SFR estimates, similarly to the stellar mass outliers. Among galaxies with correct photometric redshifts, the systematic bias increases with decreasing ${\rm SFR_{true}}$ and as redshift increases, reaching 0.5 dex at $0.1\,M_\odot\,{\rm yr}^{-1}$ in CEERS and 0.4 dex in the HUDF. The large number of catastrophic failures at ${\rm SFR_{true}} < 1\,M_\odot\,{\rm yr}^{-1}$ at all redshifts comes from redshift misestimation. This feature appears in all the observing strategies, and its importance is only slightly reduced in the HUDF compared to CEERS. In our methodology to estimate galaxy physical parameters, imposing underestimated redshifts in the second SED-fitting run gives underestimated SFRs and vice versa. This would be a priori unknown in real surveys, so it shows the importance of simulations to make the necessary corrections.

4.4. Absolute UV magnitude recovery

Figure 14 illustrates the recovery of absolute UV magnitudes. There are features in common with the stellar mass and SFR measurements, such as outliers with mostly overestimated luminosities, and the dispersion from catastrophic photometric redshifts. In the CEERS configurations, the dispersion increases from 0.2 mag at $M_{\rm UV} = -20$ to 0.3 mag at $M_{\rm UV} = -18$ for $z \leq 3$ galaxies. At higher redshift, the distributions are typically 0.1 mag broader. The UV luminosities are overestimated by 0.15 mag at $z \sim 1$ and underestimated by at most 0.2 mag at $z \geq 2$ for sources with $M_{\rm UV} > -18$ and good photometric redshifts. In comparison, in the HUDF, the dispersion at $M_{\rm UV} < -18$ remains below 0.2 mag at all redshifts for sources with correct photometric redshifts, and below 0.25 mag (0.4) at $M_{\rm UV} < -17$ and $z \leq 3$ (≥ 3). The magnitudes are systematically overestimated by ~0.1 mag at $M_{\rm UV} > -18$. For low-redshift $z < 2$ galaxies, the improvements in the HUDF are driven by the additional B_{435}-band photometry and the smaller *K*-corrections required to compute the absolute UV magnitudes. In the JAGUAR galaxies, the birth cloud component of the dust attenuation may strongly affect the rest-frame UV emission. LePhare may underestimate

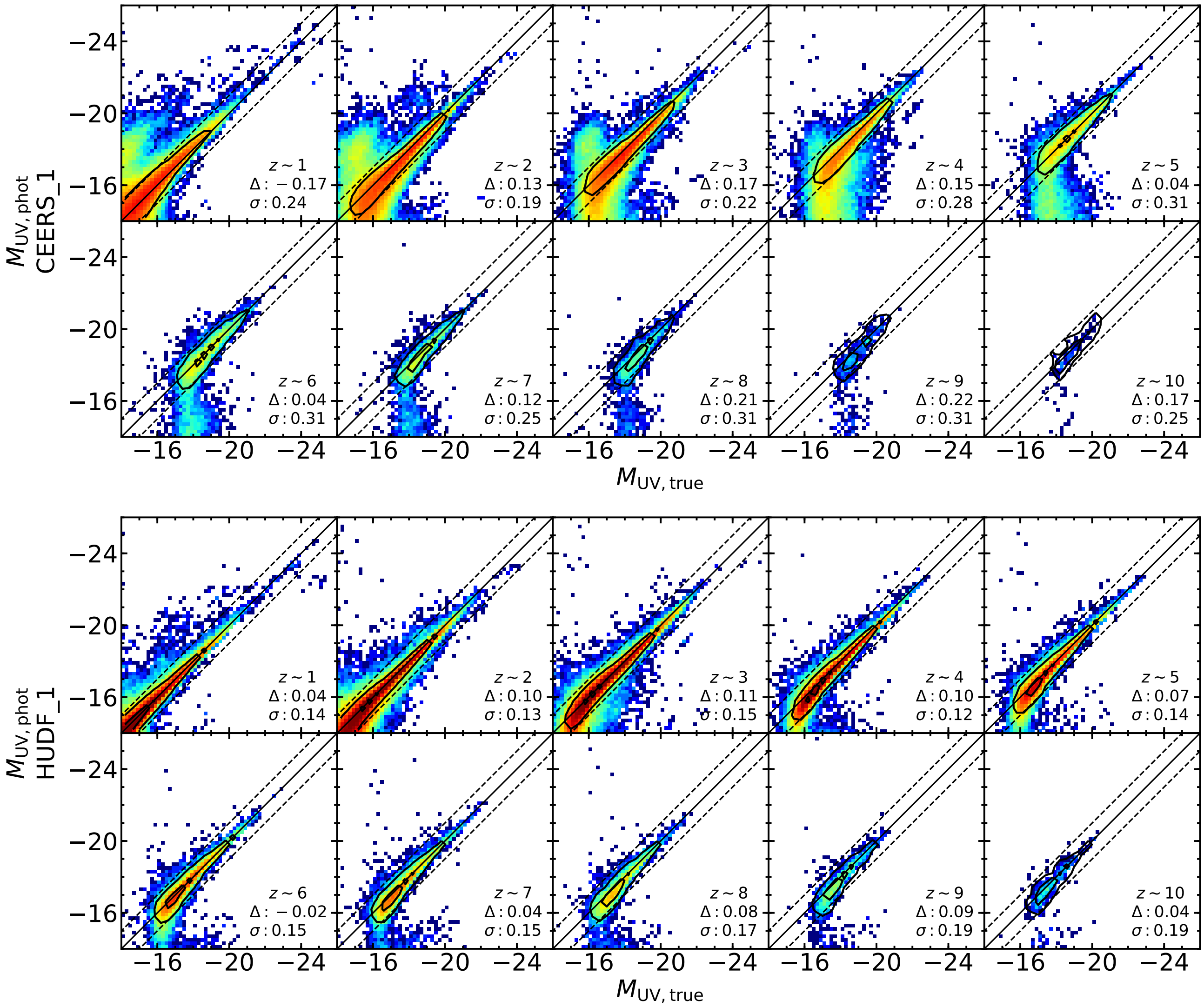

Fig. 14. Same as Fig. 12, but for absolute UV magnitude. The median shift (Δ) and the NMAD (σ) for the sources with correct $z_{\rm phot}$ and $-20 < M_{\rm UV} < -18$ are indicated (in mag). The solid line shows the 1:1 relation and the dashed lines ± 1 mag.

the attenuation especially at this wavelength, leading to underestimated UV luminosities. The NIRCam medium bands decrease the systematic bias and dispersion by about 0.03 mag at $z \geq 6$.

4.5. Comparison with previous works

Bisigello et al. (2016, 2017, 2019) investigated the recovery of the galaxy photometric redshifts and physical parameters with JWST broad-band imaging. The authors considered multiple galaxy samples, observed galaxies at $z < 7$ and simulated spectra constructed from BC03 and Zackrisson et al. (2011) population synthesis models at $z > 7$. All the combinations of a few discrete physical parameters were used to build the high-redshift galaxy samples. As a consequence, the distribution of these parameters among the real galaxy population at the given redshift was not respected. In addition, the source samples did not reproduce the redshift distribution of a flux-limited galaxy population, meaning that the contamination from foreground low-redshift galaxies into the high-redshift samples could not be estimated. The galaxy physical properties were then determined through SED-fitting with LePhare using the same galaxy templates as for the input spectra. Stellar and brown dwarf templates were not fitted, meaning that the nature of the sources was assumed to be known a priori. Bisigello et al. (2016) already showed that HST short-wavelength optical data could significantly reduce the photometric redshift dispersion and outlier rate. Bisigello et al. (2017) notably investigated the stellar mass recovery for $7 < z < 10$ galaxies with the eight NIRCam broad-bands and MIRI imaging. The recovered precision on stellar masses were similar to our results, as well as the systematic overestimation attributed to emission lines.

Kemp et al. (2019) analyzed the redshift and stellar mass recovery with JWST and HST imaging. The authors notably used the Empirical Galaxy Generator (EGG, Schreiber et al. 2017) to generate a complete magnitude-limited sample of $0 < z < 15$ and $5 < \log(M_*/M_\odot) < 12$ galaxies over 1.2 deg^2. This catalog included individual spectra with no emission lines, nonetheless the case of emission lines was treated with another sample of mock galaxies. The authors introduced and investigated two observing strategies including eight NIRCam bands with MIRI/$F770W$ parallels, and HST/V_{606} and i_{814} bands as ancillary data. These configurations are similar to the CEERS program, with similar choices of filters, exposure times and depths in the deepest regions. We come to the similar conclusions about MIRI, namely that its addition leads to an improvement in the photometric redshift recovery at $4 < z < 7$, though most of the constraints are coming from NIRCam and HST. The authors quantified the gain from additional deep HST/B_{435} imaging, which was revealed to be more important than whether MIRI imaging was available.

5. Source selection

In this section, we investigate the selection of high-redshift galaxies and the rejection of contaminants, then we give predictions about the number counts and the recovery of the galaxy luminosity function. The impact of the selection on the galaxy samples is assessed using galaxy completeness and purity. We define completeness as the fraction of input galaxies, in a given magnitude m and redshift z bin, which are selected and assigned to the correct redshift interval. Likewise, purity is the fraction of selected sources, in an observed magnitude $m^{\rm obs}$ and redshift z bin, which are high-redshift galaxies in this redshift interval. We define the redshift intervals $[z_i \pm \Delta z/2]$ with a width of $\Delta z = 1$ and centered at $z_i = 1, 2, 3, \ldots$ Let $N_{\rm input}$ be the number of input galaxies, $N_{\rm selected}$ the number of selected sources assigned to a redshift bin, and $N_{\rm correct}$ the number of selected galaxies which are assigned to the correct redshift interval. $N_{\rm selected}$ may include false detections. Completeness C and purity P can be written as:

$$C(m, z) = \frac{N_{\rm correct}(m, z)}{N_{\rm input}(m, z)}, \tag{1}$$

$$P(m^{\rm obs}, z) = \frac{N_{\rm correct}(m^{\rm obs}, z)}{N_{\rm selected}(m^{\rm obs}, z)}. \tag{2}$$

The number of detected objects depends on the observation and the source extraction, setting the maximum number of sources which can be recovered. There is then a trade-off between completeness, purity and sample size: no selection will give maximum completeness (maximum sample size) and likely minimum purity, whereas stringent selections will lower completeness (lowering sample size) and likely higher purity.

5.1. Star rejection

We first investigate the rejection of stellar objects contaminating the high-redshift galaxy samples. Commonly used criteria rely either on magnitude, colors, shape (or surface brightness) and the quality of the SED-fitting. We consider the following list of standard star rejection criteria, and we investigate the individual impact of each of them:

(i) $S < k$, with $k = 0.95, 0.9$

(ii) $(\mu_{\rm max} > 0.95 m_{F115W} - 1.9) \vee (\mu_{\rm max} > k)$ in CEERS, $(\mu_{\rm max} > 0.95 m_{F115W} - 2.2) \vee (\mu_{\rm max} > k)$ in the HUDF, with $k = 24, 25$

(iii) $(m_{F115W} - m_{F356W} > 0.7(m_{F606W} - m_{F115W}) - 1.55) \vee (m_{F115W} - m_{F356W} > 0.1(m_{F606W} - m_{F115W}) - 0.95)$ if $S/N_{F606W} > 2$, $(m_{F150W} - m_{F200W} > 0.25(m_{F200W} - m_{F444W}) - 0.75) \vee (m_{F150W} - m_{F200W} > 0)$ otherwise

(iv) $\chi^2_{\rm star} > k$, with $k = 0.5\nu, \nu$

(v) $\chi^2_{\rm gal} - \chi^2_{\rm star} < k$, with $k = \nu, 0$

with S defined as the source stellarity index, $\mu_{\rm max}$ is the maximum surface brightness, $\chi^2_{\rm star}$ and $\chi^2_{\rm gal}$ are the mean squared error from the SED-fitting of stellar and galaxy templates, respectively, ν is the number of degrees of freedom in the fitting (set to the number of bands minus three). The thresholds k define a soft (first value) and a stringent (second value) version for some selections. The symbol $\vee$ represents the logical OR.

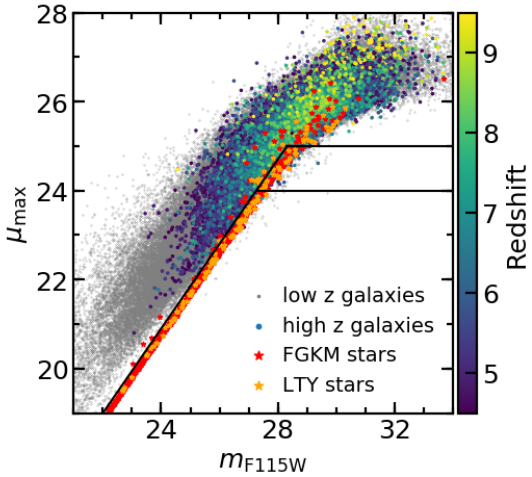

Fig. 15. Maximum surface brightness-magnitude selection criteria to remove stellar objects. Each marker represents the measured colors of a detected source in the CEERS_1 observing strategy. The colored points are high-redshift galaxies and the gray points indicate $z_{\rm true} < 4.5$ galaxies. The red and orange stars represent FGKM and LTY stars, respectively.

The first criterion (i) is based on the stellarity index S measured with SExtractor in the NIRCam/$F200W$ detection image. This is the posterior probability of a detected object to be a point-source (0 for extended source, 1 for point-source), according to its surface brightness profile. With high resolution imaging, brown dwarfs may be separated from resolved galaxies based on size (Tilvi et al. 2013). However, distant galaxies commonly appear point-like (e.g., bright star-forming blobs, faint galaxy hosting a bright AGN) and should not be discarded. The impact of this selection on galaxy completeness therefore depends on the morphology of the galaxies. This will need to be further investigated with simulations of more realistic galaxy light distributions. Similarly, stars tend to occupy a tight locus in the size (or surface brightness) – magnitude plane (Leauthaud et al. 2007). We construct the selection (ii) in the maximum surface brightness $\mu_{\rm max} - m_{F115W}$ plane as represented in Fig. 15. The parameter $\mu_{\rm max}$ is the surface brightness [mag arcsec^{-2}] of the brightest pixel belonging to the source, above the estimated background. The NIRCam/$F115W$ band is well adapted since stars mainly become fainter in redder bands and the emission of MLTY dwarfs drops in bluer bands. We then make use of the color-color selections (iii) following Davidzon et al. (2017). The adopted color diagrams are (HST/$F606W$–NIRCam/$F115W$) vs. (NIRCam/$F115W$–$F356W$) for objects detected at 2σ in the HST/$F606W$ band, and (NIRCam/$F150W$–$F200W$) vs. (NIRCam/$F200W$–$F444W$) for the other sources (Fig. 16). Finally, we consider selections based on the SED-fitting results, either (iv) the absolute quality of the stellar fit (Bowler et al. 2015), or (v) the relative quality of the stellar fit with respect to the galaxy fit (Ilbert et al. 2009).

Figure 17 illustrates the photometric redshift distribution of stellar objects in the CEERS_1 configuration, and the number of remaining stars after each rejection criterion is individually applied. In addition, the resulting differences of purity and completeness for the galaxy samples are indicated, for each redshift interval and integrated over magnitude. The purpose is to remove as many stellar contaminants as possible while maintaining a

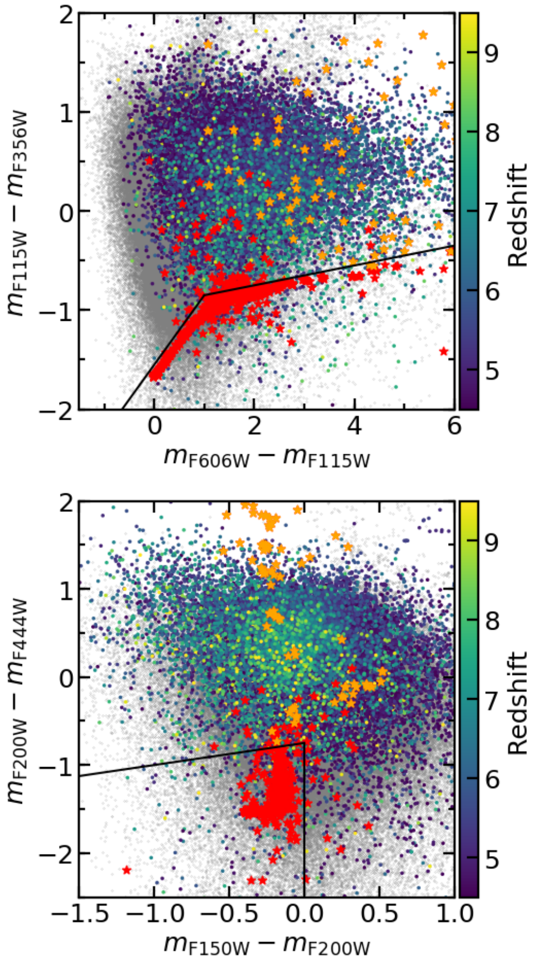

Fig. 16. Color-color selection criteria to remove stellar objects. Each marker represents the measured colors of a detected source in the CEERS_1 observing strategy. The colored points are high-redshift galaxies and the gray points indicate $z_{\rm true} < 4.5$ galaxies. The red and orange stars represent FGKM and LTY stars, respectively. Only sources detected at 2σ in the two reddest bands (in each panel) are indicated.

high galaxy completeness, and any gain in galaxy purity is an additional advantage in terms of statistics of the recovered galaxy population. As expected, the stellarity index cuts (i) manage to efficiently reject stars, about 65% (80%) for $S < 0.95$ (0.9), however lowering galaxy completeness of about 20% (60%) at all redshifts $z > 4$. In contrast, the surface brightness-magnitude selections (ii) remove a similar number of stars and maintain a high completeness and purity. Again, these impact on galaxy completeness depends on the assumed galaxy morphologies. The color-color cuts (iii) have a marginal effect on brown dwarfs with $z_{\rm phot} > 5$, whereas most of the stellar objects with $z_{\rm phot} < 2$ are effectively removed. Neither galaxy completeness nor purity are much affected. The optical and near-IR colors of cold brown dwarfs appear not to occupy the same stellar locus as hotter stars, and removing them in the color-color space would discard many galaxies at the same time. Finally, the criteria based on the absolute quality of the stellar fit (iv) only reject about 30% of the stars, though slightly modifying completeness and purity. In contrast, the selection with the difference of chi squares (v) removes 95% of the stars at all photometric redshifts, maintaining a solid completeness only lowered by 2% and even removing extra contaminants. We find similar results for the other observing strategies.

From these results, we can conclude that the combination of both the soft (ii) and the soft (v) criteria is the most efficient way of removing stars from the high-redshift galaxy candidates. This is used in the next sections. The remaining stellar contaminants in the $z > 4$ galaxy samples decrease from 0.26 ± 0.02 to 0.010 ± 0.004 arcmin^{-2} for CEERS_1 and from 0.18 ± 0.02 to 0.004 ± 0.003 arcmin^{-2} for HUDF_1. The differences between CEERS and the HUDF include the input density of stars at the respective sky coordinates, the depth and wavelength coverage of the observations. The addition of MIRI imaging improves the photometric redshifts of stars, with detected densities of 0.24 ± 0.02 arcmin^{-2} for CEERS_2 and 0.14 ± 0.02 arcmin^{-2} for HUDF_2. These lower values come from the mid-IR colors of stars which are less comparable to galaxy colors than in the near-IR. It should be mentioned that these selection criteria are specifically constructed to reject stars, nevertheless they are not the only criteria to have this effect. Color-color selections designed to select high-redshift galaxies based on their Lyman break may result in extra stellar rejection, whereas SED-fitting-based selections mainly rely on the types of criteria considered above. The final stellar rejection therefore depends on the entire set of selection criteria.

5.2. Galaxy selection at $z > 5$

In this section, we explore multiple procedures to select high-redshift galaxies and estimate the respective impact on galaxy completeness and purity. We use an alternative, more permissive definition of purity in this section only. A selected source, assigned to the redshift interval centered at z_i, is considered as a contaminant if $z_{\rm true} < z_i - 1$. Hence only low-redshift sources are considered as contaminants. This avoids classifying, for example, $z \sim 6.4$ galaxies which are scattering into our $z \sim 7$ selection as contaminants. We do not treat the specific case of faint Lyman alpha emitters (LAE), typically presenting a strong emission in only one or two bands. The redshift of these galaxies cannot be well constrained without narrow-band imaging or spectroscopy (Dunlop et al. 2013), which are not available here. In addition, we do not include criteria based on visual inspection. This technique may be used to discard sources based on shape or colors to consolidate purity, however with real images the resulting galaxy completeness becomes hard to estimate.

We consider three sets of selection criteria summarized in Table 3. These are based on Bouwens et al. (2015), Bowler et al. (2015) and Finkelstein et al. (2015), adapted to the present set of photometric bands and generalized to multiple redshift intervals. We do not include magnitude cuts. The criteria for the EGS field in Bouwens et al. (2015) rely on initial color-color preselections, then on photometric redshifts confirmation. Because of the lack of optical data, and medium or narrow band imaging, it is not possible to select galaxies with color criteria only. The Lyman break galaxies (LBG) color-color selections are represented in Fig. 18. The location of the Lyman alpha break relies on the V_{606} and i_{814} HST bands at $z < 8$. The galaxy colors redward of the break are quantified with NIRCam bands to take advantage of the increased depths compared to the WFC3 bands. Lower-redshift contaminants are expected to be excluded by imposing no detections ($S/N < 2$) blueward of the break. However, this fact is strictly valid at $z > 6$ where the IGM transmission is extremely low. The resulting high-redshift samples may be biased toward young UV bright sources and miss a significant fraction of the galaxies (Hughes et al. 1998; Le Fèvre et al. 2015; Finkelstein et al. 2015), including old or dusty galaxies. Contaminants for high-redshift samples constructed from color-color

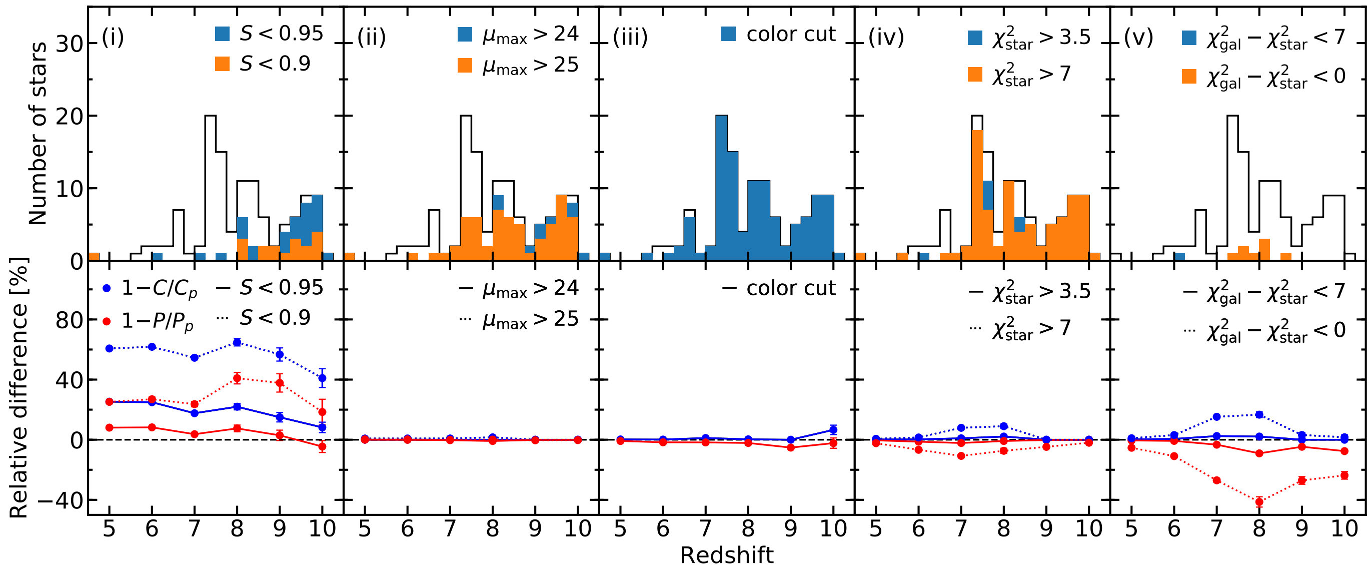

Fig. 17. *Top panels:* number of remaining stellar contaminants after applying the indicated selection criterion per photometric redshift interval, in the CEERS_1 observing strategy. Each column corresponds to one type of selection from Sect. 5.1. The black line indicates the photometric redshift distribution of the detected stars with $z_{\rm phot} > 5$. All the stars with lower photometric redshifts have $z_{\rm phot} < 2$. The colored bars represent the remaining stars after applying the indicated selection criterion. The soft selection (in blue) is always less restrictive than the stringent one (in orange), meaning that all second counts are also included in the first counts. *Bottom panels:* completeness C (in blue) and purity P (in red) of the high-redshift galaxy samples versus true redshift (integrated over magnitudes). The references C_p and P_p represent the completeness and purity assuming the selection is based on photometric redshifts only. The relative difference with respect to the reference is represented, so that positive values indicate lower completeness and purity. Different line styles represent the results for different selection criteria (as indicated in each panel).

Table 3. Sets of criteria to select high-redshift galaxies.

Set	Field		Criteria
Bouwens-like	EGS		$((m_{F606W} - m_{F814W} > 1.0) \wedge (m_{F115W} - m_{F150W} < 0.5) \wedge (m_{F606W} - m_{F814W} > 2.2(m_{F115W} - m_{F150W}) + 1.2)$
		$\vee$	$(m_{F814W} - m_{F115W} > 1.1) \wedge (m_{F115W} - m_{F150W} < 0.6) \wedge (m_{F814W} - m_{F115W} > 1.1(m_{F115W} - m_{F150W}) + 1.4)$
		$\vee$	$(m_{F115W} - m_{F150W} > 1.0) \wedge (m_{F150W} - m_{F200W} < 0.7) \wedge (m_{F115W} - m_{F150W} > 0.8(m_{F150W} - m_{F200W}) + 1.0))$
		$\wedge$	$z_{\rm phot}$ in z_i interval
	XDF		$((m_{F606W} - m_{F775W} > 0.8) \wedge (m_{F115W} - m_{F150W} < 0.8) \wedge (m_{F606W} - m_{F775W} > 1.5(m_{F115W} - m_{F150W}) + 1.0)$
		$\vee$	$(m_{F775W} - m_{F090W} > 0.6) \wedge (m_{F115W} - m_{F150W} < 0.8) \wedge (m_{F775W} - m_{F090W} > 0.8(m_{F115W} - m_{F150W}) + 0.8)$
		$\vee$	$(m_{F090W} - m_{F115W} > 0.7) \wedge (m_{F115W} - m_{F150W} < 1.0) \wedge (m_{F090W} - m_{F115W} > 0.7(m_{F115W} - m_{F150W}) + 0.9)$
		$\vee$	$(m_{F115W} - m_{F150W} > 0.8) \wedge (m_{F150W} - m_{F200W} < 1.0) \wedge (m_{F115W} - m_{F150W} > 0.8(m_{F150W} - m_{F200W}) + 0.9)$
		$\vee$	$(m_{F150W} - m_{F200W} > 0.8) \wedge (m_{F200W} - m_{F277W} < 1.0) \wedge (m_{F150W} - m_{F200W} > 0.8(m_{F200W} - m_{F277W}) + 0.9))$
		$\wedge$	$z_{\rm phot}$ in z_i interval
Bowler-like	all		$z_{\rm phot}$ in z_i interval
		$\wedge$	$((z_{\rm phot,sec} > z_i - \Delta z) \vee (\chi^2_{\rm sec} - \chi^2_{\rm gal} > 4))$
Finkelstein-like	all		PDFz integral under primary peak ≥ 0.7
		$\wedge$	PDFz integral in z_i interval ≥ 0.25
		$\wedge$	PDFz integral in z_i interval highest among intervals
		$\wedge$	PDFz integral in $[z_i - 1, \infty) \geq 0.5$
		$\wedge$	$(z_{\rm phot} > z_i - 2)$

Notes. The symbols $\wedge$ and $\vee$ represent the logical AND and OR, respectively.

criteria are usually low-redshift very red dusty galaxies or AGNs, and cool galactic stars. In the HUDF field, the deep HST optical imaging allows us to develop more redshift-specific color criteria. Nonetheless, we still rely on photometric redshift confirmation for these sources, especially at $z > 7$ where the NIRCam broad bands cannot precisely locate the Lyα break. The color criteria for the HUDF field are presented in Appendix B.

Alternatively, Bowler et al. (2015) criteria mainly use photometric redshifts and impose additional constraints on the location of the secondary photometric redshift $z_{\rm phot,sec}$. Similarly, Finkelstein et al. (2015) criteria make use of the whole posterior information to select objects based on the location and concentration of the PDFz in redshift intervals. In these two approaches, we do not include the criteria on the absolute quality of the

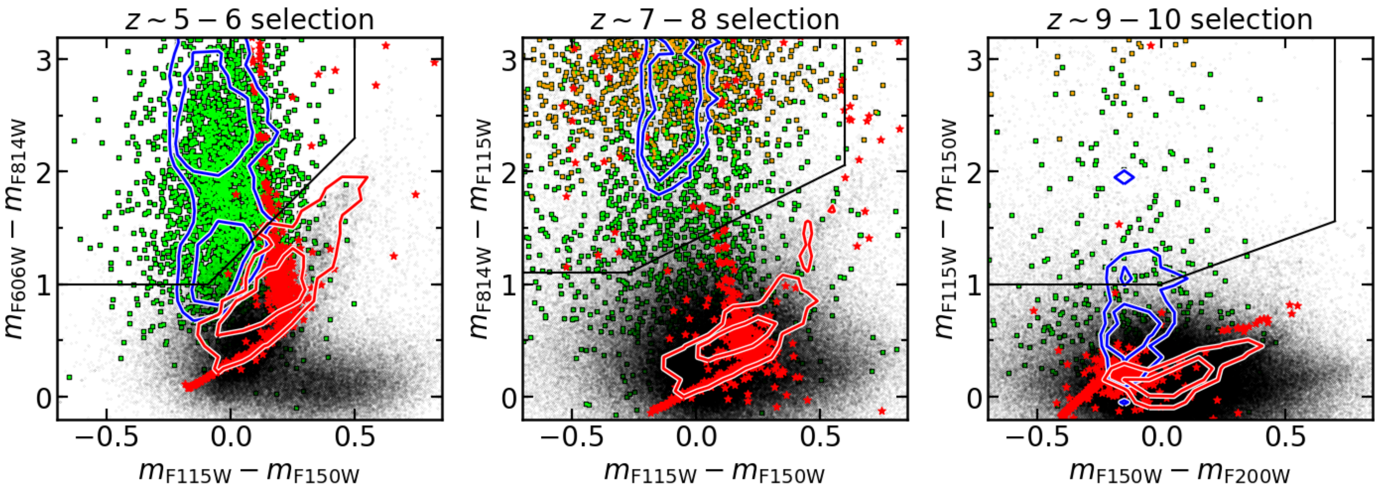

Fig. 18. Color-color selection criteria to preselect galaxies at $z \sim 5$–6, $z \sim 7$–8, $z \sim 9$–10 in the EGS field, with the Bouwens-like criteria in Table 3. The regions enclosed by the solid black line in the top-left corners show the color-color space region in which galaxies are preselected. The blue contours enclose 50% and 80% of the $z > 4.5$, $z > 6.5$, $z > 8.5$ galaxies input colors (without photometric scatter), and the red contours represent low-redshift quiescent galaxies. Each marker represents the measured colors for a detected source in the CEERS_1 observing strategy. Only sources detected at 5σ in the 3, 2, 2 reddest bands, respectively, are indicated. The green and orange squares are $z > 4.5$, $z > 6.5$, $z > 8.5$ galaxies, the orange squares indicating 1σ upper limits in the bluest band. The red stars are stellar objects, the black dots are low-redshift contaminants.

galaxy templates fit. Such criteria generally have a marginal impact on the final selection and, in our simulation, may just capture the differences between the input and the fitted templates.

Figure 19 illustrates the completeness and purity of the high-redshift galaxy samples in the CEERS_1 strategy, as a function of apparent observed-frame UV magnitudes $m_{\rm UV}$. The colored lines represent the three different selections. The results for photometric redshift only selected sources (dotted lines), and the completeness of the detected sources assuming that redshifts are perfectly recovered (dashed lines), are also shown for comparison. The results for the CEERS_2 strategy are very similar.

We find that about $5 \pm 2\%$ ($2 \pm 1\%$) of the bright galaxies at $z = 4 - 6$ (1–2) are not detected. This implies that bright nearby objects contaminate the photometry of these sources, for which the source detection or the deblending procedure failed. At fainter magnitudes, the drop of completeness is the consequence of both this effect becoming stronger for faint sources and the impact of noise. Figure 20 illustrates the probability of finding a brighter neighbor in the input source catalog centered within the 0.5″ diameter aperture. In the NIRCam/$F200W$ band, this probability is about 3% at 28 mag and converges to 13% at 33 mag. This gives a hint of the impact of blending alone on faint source photometry. Other scenarios are also possible, such as brighter neighbors outside of the aperture dominating the surface brightness of the faint source, therefore undetected or undeblended.

We find that the high-redshift galaxies selected through photometric redshifts only (before applying any other selection) already present significant incompleteness, even at $m_{\rm UV} < 27$. Many sources which are correctly identified as high-redshift galaxies present relatively broad PDFz, so the resulting photometric redshifts often reside in the previous or next redshift interval. This is emphasized by the redshift intervals whose widths are fixed and not increasing with redshift. The bright high-redshift galaxies with catastrophic photometric redshifts are typically identified as red low-redshift galaxies, however many of them present PDFz with multiple peaks and a correct secondary solution. These results reflect the lack of deep optical and/or near-IR medium-band imaging, in the rest-frame UV region of these sources, to better identify the Lyα break, and the lack of blue-band imaging to confirm the break. Detected sources with nearby bright extended objects may also present contaminated photometry and colors, even for relatively bright galaxies. At very high redshift $z \geq 9$, the rarity of the galaxies of interest compared to the significantly more numerous low-redshift contaminants (at $z \sim 2$) leads to relatively low purity, in addition to the degeneracy between the Lyman break and the Balmer break at low redshift.

We observe slight differences between the different selection sets with respect to galaxy completeness and purity. Firstly, the Bouwens-like criteria lead to an improvement in purity, especially at bright magnitudes, with a relatively limited loss of completeness. Photometric redshifts impose most of the constraints, therefore the results are robust against small changes in the color preselection. Nonetheless, this preselection effectively increases purity, especially at the bright ends. Secondly, the Bowler-like selection induces a smaller loss of galaxy completeness, and increases the purity at the faint end. The criterion on the second peak of the PDFz has a significant impact on both C and P, especially at the faint ends. Thirdly, the criteria from Finkelstein lead to the highest galaxy completeness at most magnitudes and redshifts. At the same time, the resulting purity is the highest at the faint ends and at all redshifts, especially at $z < 8$. The constraint on the weight of the primary PDFz peak increases the purity and slightly decreases the completeness at the faint end. All the additional criteria increase even more the faint-end purity, however lowering the completeness at bright magnitudes. With these criteria, we find that the galaxy completeness is higher than 50% for $m_{\rm UV} < 27.5$ sources at all redshifts, and purity remains above 80 and 60% at $z \leq 7$ and 10, respectively. From this comparison, we conclude that the PDFz criteria of Finkelstein result in the best trade-off between completeness and purity, and we keep these criteria in the next sections.

Figure B.2 illustrates the same analysis in the HUDF_1 configuration. The completeness after selecting galaxies is much

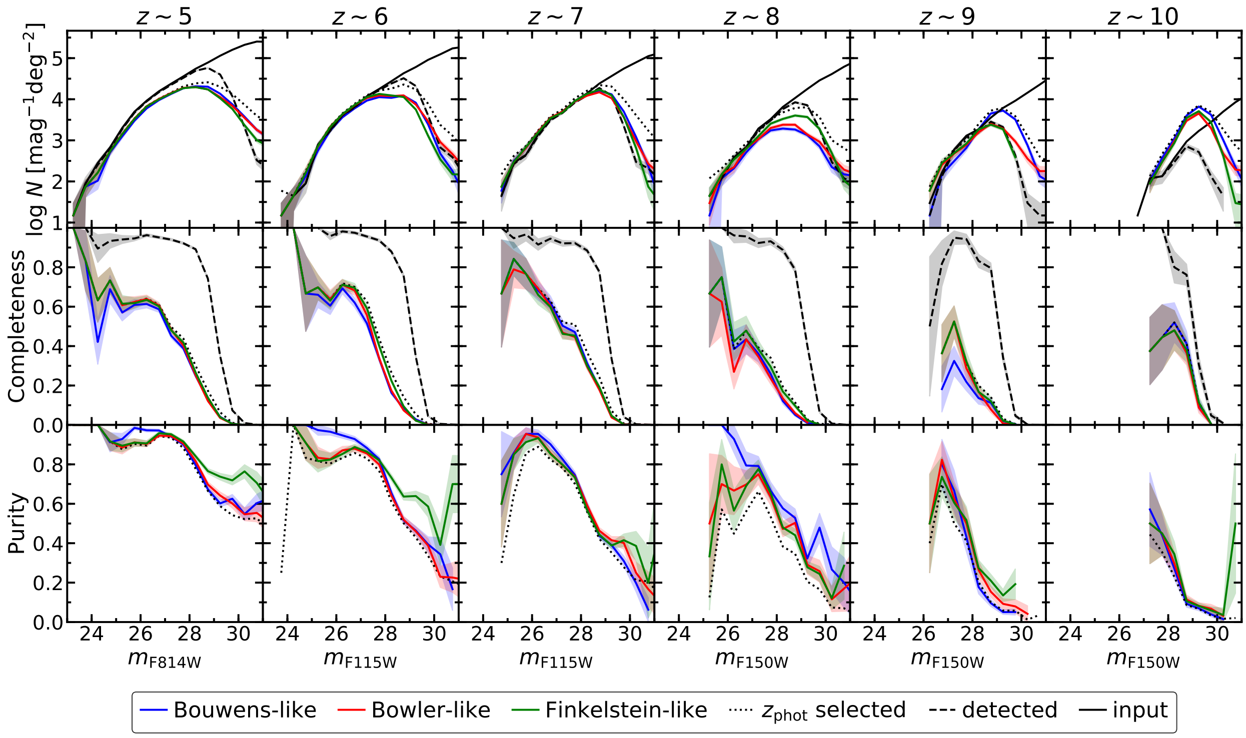

Fig. 19. High-redshift galaxy number counts (*top panels*), completeness (*middle panels*) and purity (*bottom panels*) versus apparent magnitude (in the band the nearest to rest-frame UV), in the CEERS_1 observing strategy. Each column corresponds to one redshift interval. Each colored line represents one set of selection criteria from Table 3. The solid black lines indicate the input number counts. The dashed black lines illustrate detected sources assuming the redshifts are perfectly recovered. The dotted black lines represent observed sources selected with photometric redshifts only. The shaded areas correspond to 1σ errors. The input and detected counts, and the measured completeness, are expressed in true magnitudes, while the selected counts and purity measurements are in observed magnitudes.

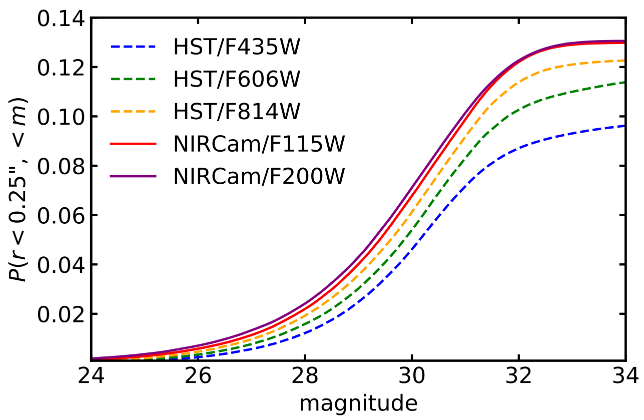

Fig. 20. Probability of finding at least one brighter neighbor in the input catalog centered within a 0.25″ radius. The line styles and colors represent different bands.

closer to the completeness assuming perfectly recovered redshifts. This is mainly due to the deeper NIRCam imaging and the additional HST B band. We observe similar features between the three selection sets as for the CEERS configuration. With the Finkelstein selection, the galaxy completeness remains higher than 50% at $m_{\rm UV} < 29$ at all redshifts, and the purity above 80% at $m_{\rm UV} < 30$.

Furthermore, completeness and purity may a priori depend on other physical parameters such as galaxy size. Completeness is about twice larger for galaxies with input effective radius $r_{\rm e} < 0.2$ kpc at $m_{\rm UV} > 29$ in CEERS and $m_{\rm UV} > 31$ in the HUDF. These sources are right at the detection limits, where completeness is only a few percent. We observe no significant evidence of purity varying with galaxy size. This variability should be taken into account when computing the luminosity function. Nonetheless, previous studies (e.g., Grazian et al. 2012; Finkelstein et al. 2015) found that the luminosity functions derived with or without including the size-luminosity relation remain similar. Despite this statement may depend on the assumed galaxy morphology, especially at high redshift, we decide to neglect the galaxy size variability of the completeness in the next sections.

5.3. Number counts predictions

We quantify the number of detected and selected sources in the high-redshift galaxy samples. Figures 19 and B.2 show the predicted number counts per magnitude and redshift, for the CEERS_1 and HUDF_1 observing strategies. The results are equivalent for the CEERS_2 and HUDF_2 configurations, respectively. The selected counts designate the selected objects following the indicated selection and assigned to the corresponding redshift interval. These are computed using observed magnitudes. In contrast, the detected and the input counts are computed using true magnitudes and redshifts. The drop at $m_{\rm UV} > 31$ at all redshifts comes from the stellar mass lower limit in the input galaxy catalog. The apparent disagreement between the input and the selected counts at $z\sim10$ comes from photometric scatter.

For the CEERS_1 observing strategy, we expect about 916, 435, 232, 56, 19, 7 true high-redshift galaxies at $m_{\rm UV} < 29$ which are correctly assigned to the selected samples at $z\sim5, 6, 7, 8, 9, 10$, respectively. In comparison, the input number counts are 3039, 1522, 774, 318, 101, 21. These numbers agree with the predictions from the CEERS program description ($20-80$ sources at $z = 9-13$), though closer to the lower bound. One explanation may be source blending and the resulting increase in the photometric redshift outlier rates. Faint sources may even not be detected because of bright nearby objects, especially bright extended galaxies and stars, lowering the detected number counts. In addition, the high-redshift number counts importantly depend on the assumed evolution of the UVLF at $z > 8$, so that the rapid evolution assumed here gives lower number counts than with a slower evolution. For the HUDF_1 configuration, we expect 205, 135, 65, 20, 6, 2 selected sources at $m_{\rm UV} < 31$ and $z \sim 5, 6, 7, 8, 9, 10$, respectively, compared to the 628, 367, 222, 112, 40, 12 input counts. These numbers indicate that the GTO programs in the HUDF are more suitable than CEERS to study very faint galaxies at $z \geq 8$, in which case deeper imaging is required. On the other hand, the larger survey area in the EGS field enables more galaxies at $z \sim 5-6$ to be detected, including rare intrinsically bright sources.

5.4. Computing the galaxy luminosity function

In this section, we discuss the computation of the galaxy UV luminosity function from the selected galaxy number counts and the measured completeness and purity. The luminosity function is the comoving volume number density as a function of the intrinsic luminosity. The observed number density may suffer from incompleteness and impurities, therefore the observed LF needs to be corrected to recover the intrinsic LF using magnitude-dependent scaling factors.

The input galaxy UVLF in JAGUAR is constructed from the convolution of the stellar mass function and the $M_{\rm UV}(M_*)$ relation. Because of the stellar mass lower limit $\log(M_*/M_\odot) > 6$, the LF decreases at the faint end with a maximum situated between $-16 < M_{\rm UV} < -15$ at $4 < z < 10$. The position of this turn-over is still debated in the literature (e.g., Livermore et al. 2017; Bouwens et al. 2017), therefore we restrict ourselves to $M_{\rm UV} < -16$ where the faint end remains almost linear. We fit this input UVLF at $M_{\rm UV} > -22$ with a double-power-law model (DPL), parametrized as (Bowler et al. 2015):

$$\phi(M) = \frac{\phi^*}{10^{0.4(\alpha+1)(M-M^*)} + 10^{0.4(\beta+1)(M-M^*)}}, \tag{3}$$

where ϕ^* and M^* are the characteristic density and magnitude, α and β denote the faint and bright-end slopes. The difference between the input UVLF and the fitted model at $z \leq 10$ is at most 10% between $-22 < M_{\rm UV} < -17$.

We make forecasts for the recovery of the UVLF with the following approach. We take the selected galaxy $M_{\rm UV}$ number counts from our simulations, multiply them by the ratio of the survey area to the simulated area, and sample Poisson random vectors taking these values as the mean. The sampled counts are then corrected for incompleteness and impurities through the scaling correction factors, estimated from the number of input sources (function of true magnitudes) divided by the number of selected objects (function of observed magnitudes) from our simulations. This scaling therefore includes photometric scatter and $M_{\rm UV}$ recovery. We recall that absolute magnitudes are not corrected for dust attenuation. We use the classic estimator of the LF (Felten 1976), consisting of the absolute UV magnitude number counts divided by the comoving volume in the whole redshift interval. The LF uncertainties are the quadratic sum of the Poisson errors, cosmic variance errors (Trenti & Stiavelli 2008) and scaling correction uncertainties. By construction, the corrected LF values equal the input LF ones, however the uncertainties are broadened depending on the selected sample sizes. We fit each scaled Poisson random vector at $M_{\rm UV} < -16$ with a DPL model, using flat priors and a Markov chain Monte Carlo (MCMC) method to sample the posterior probability distribution. We finally marginalize over the Poisson samplings to determine the median parameters and errors. Both the statistical and the systematic errors on the parameters are included, though in reality one would have one Poisson sampling and only determine the statistical errors.

The recovered LFs are presented in Fig. 21 and Table A.1 for the CEERS_1 configuration covering about 100 arcmin^2. We do not present the results for the HUDF strategy, because the 4.7 arcmin^2 survey area cannot impose much statistical constraint on the LF, despite the increased depths. The differences between the selected and the corrected counts are significant, especially beyond $M_{\rm UV} > -18$ where the galaxy samples become highly incomplete. At $M_{\rm UV} < -18$, the scaling corrections are still $\sim$1–2 at all redshifts. Poisson uncertainties dominate the LF error budget at the bright end where the number counts are low, while cosmic variance errors reach up to 70% of the total variance at fainter magnitudes. In practice, large-scale structure effects will impact all magnitude the bins in a coherent way, but depend somewhat on the bias (e.g., Robertson et al. 2014). Scaling corrections contribute to about 10% of the total variance at almost all magnitudes and redshifts. As with real images, the corrections remain strongly dependent on the modeling assumptions, including galaxy morphology, star formation histories and dust attenuation. These results reflect that accurate simulations are required to correctly recover the galaxy counts, which can be severely affected by incompleteness and contamination. The number counts brightward of M^* decrease with increasing redshift, leading to a lack of constraints on the bright end. For this reason, we fix the DPL parameters β and M^*, at $z \geq 9$, to the input values when performing the fit. The obtained parameters are presented in Table 4. The faint-end slopes are effectively constrained with an absolute error of $\sim$0.1 at $z \leq 7$ and $\sim$0.25 at $z \geq 8$.

Within the CEERS area of 100 arcmin^2, the input galaxy UVLF predicts about 71, 36, 19, 12, 3.3 and 1.3 input galaxies with $M_{\rm UV} < M^*$ at $z \sim 5, 6, 7, 8, 9, 10$, respectively. These numbers indicate that the bright end of the UVLF cannot be constrained at $z \geq 7$, even assuming that all these galaxies are identified. Nonetheless, the NIRCam GTO program in the GOODS fields covering 200 arcmin^2, particularly the "Medium" survey, will bring additional constraints on the bright end of the UVLF up to $z \leq 8$. In spite of the depths of these programs, the main limitation remains the small JWST field of view. As an alternative, the Euclid[16] deep fields will include optical and near-IR imaging extended over tens of square degrees (Laureijs et al. 2011). These surveys, with the optical (e.g., Subaru Hyper Suprime-Cam) and mid-infrared (e.g., *Spitzer* Legacy Survey) counterparts, will reach the required depth to identify high-redshift galaxies, despite a lower resolution than JWST. The Euclid Deep Fields will probe the bright end of the luminosity function up to $z \sim 7$ or more, which will provide constraints complementary to the deep JWST surveys.

In addition, we predict the recovery of the cosmic SFR density $\rho_{\rm SFR}$. We integrate the UVLF to $M_{\rm UV} = -16$. The UV luminosity densities are converted into SFR densities using $\kappa_{\rm UV} = 1.15 \times 10^{-28}\, M_\odot\,{\rm yr}^{-1}({\rm erg/s/Hz})^{-1}$, where a 0.1–100 $M_\odot$ Salpeter initial mass function and a constant SFR are assumed

[16] http://www.euclid-ec.org

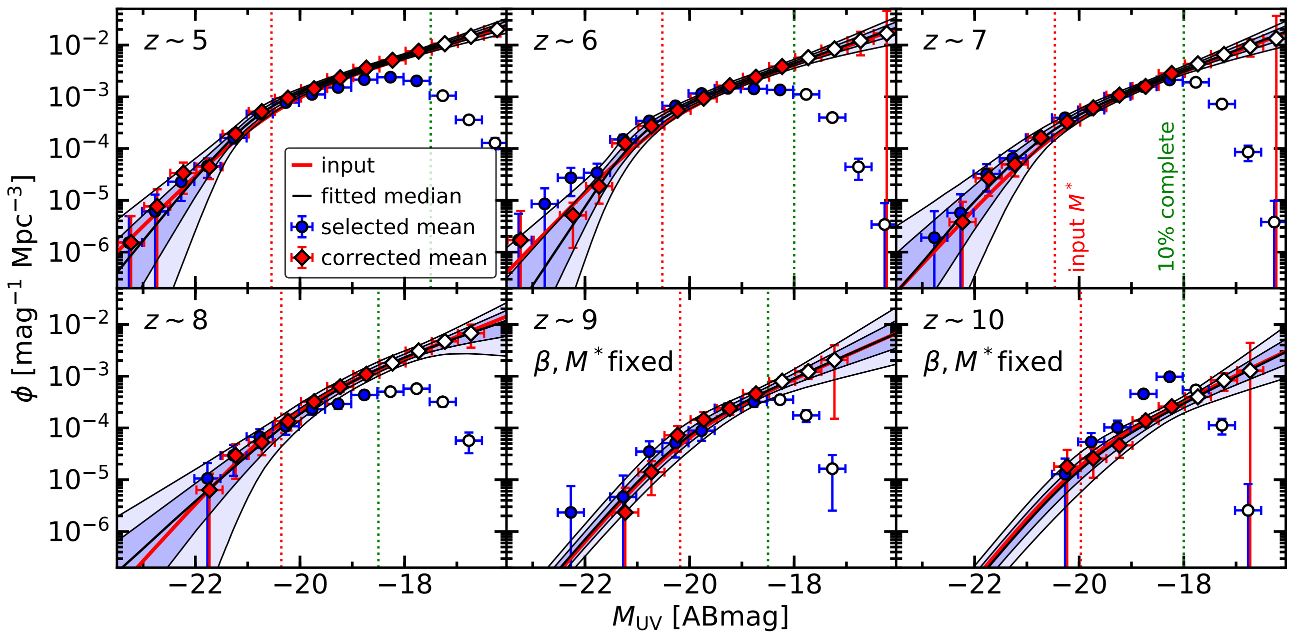

Fig. 21. Galaxy UV luminosity functions for multiple redshift intervals, for the CEERS_1 observing strategy. The blue dots indicate the estimated mean of the selected counts, and the red diamonds represent the selected counts corrected for incompleteness and impurity. The open symbols are the points where the completeness is below 10%. The error bars are Poisson errors for the former and the quadratic sum of Poisson and scaling errors for the latter. Multiple Poisson random vectors are sampled from the blue dots, scaled to correct for incompleteness and impurity and fitted with a double power-law function, with the indicated fixed parameters. The black lines show the model with the median fitted parameters, after marginalizing over all the sampled counts. The colored areas indicate 1σ and 2σ credibility errors. The red lines represent the input luminosity functions (fitted with a DPL model). The dotted red lines show M^* from the input LF, and the dotted green lines indicate the 10% completeness limit.

Table 4. Parametric fitting of the recovered UVLF.

z	ϕ^* [10^{-3} Mpc^{-3}]	M^* [mag]	α	β	$\log\rho_{\rm SFR}$ [$M_\odot$ yr^{-1} Mpc^{-3}]
			Input		
5	0.92	−20.54	−1.78	−3.50	−1.64
6	0.55	−20.52	−1.87	−3.63	−1.80
7	0.35	−20.46	−1.96	−3.73	−1.96
8	0.24	−20.36	−2.03	−3.79	−2.11
9	0.09	−20.18	−2.13	−3.95	−2.53
10	0.04	−19.97	−2.22	−4.07	−2.96
			Recovered		
5	$0.80^{+0.54}_{-0.27}$	$-20.84^{+0.39}_{-0.27}$	$-1.77^{+0.10}_{-0.08}$	$-4.10^{+0.71}_{-1.21}$	$-1.57^{+0.03}_{-0.03}$
6	$0.42^{+0.44}_{-0.17}$	$-20.85^{+0.48}_{-0.35}$	$-1.89^{+0.15}_{-0.11}$	$-4.79^{+1.00}_{-1.56}$	$-1.75^{+0.03}_{-0.03}$
7	$0.32^{+0.39}_{-0.17}$	$-20.67^{+0.55}_{-0.53}$	$-1.94^{+0.15}_{-0.11}$	$-3.93^{+0.73}_{-1.18}$	$-1.89^{+0.05}_{-0.04}$
8	$0.96^{+2.45}_{-0.76}$	$-19.39^{+1.04}_{-1.05}$	$-1.84^{+0.49}_{-0.28}$	$-3.27^{+0.43}_{-1.13}$	$-2.13^{+0.07}_{-0.07}$
9	$0.10^{+0.04}_{-0.03}$	−20.18	$-2.09^{+0.24}_{-0.22}$	−3.95	$-2.51^{+0.10}_{-0.10}$
10	$0.03^{+0.02}_{-0.01}$	−19.97	$-2.25^{+0.25}_{-0.27}$	−4.07	$-3.00^{+0.10}_{-0.09}$

(Madau & Dickinson 2014). The results, uncorrected for dust attenuation, are reported in Table 4. The SFR densities are correctly recovered and the expected errors remain below 0.1 dex, as long as the faint-end slope is well constrained. However, the errors are underestimated because of the fixed LF parameters at $z \geq 9$, and the scaling corrections recovering the input number counts. In addition, we do not apply any magnitude cuts, which would significantly lower the number of faint selected sources. In the ideal case where all the detected sources have perfectly recovered redshifts and absolute magnitudes, the errors on α and $\rho_{\rm SFR}$ are lowered by about 20% at $z < 8$. The cases at $z > 8$ are more sensitive to the determination of α from small number counts at the very faint end. Using all the input sources over the survey area at $\log(M_*/M_\odot) > 6$, we estimate that about 50% of the total errors arise from the limited area. This argues again in favor of surveys including larger cosmological volumes.

6. Summary and conclusion

In this paper, we forecast the performance of accepted JWST deep imaging surveys regarding the detection and analysis of high-redshift galaxies. In particular, we estimate the galaxy physical parameters, optimize the candidate selection with respect to galaxy completeness, purity and the total number of sources, then compute the UV luminosity function and the cosmic star formation rate density. We treat two JWST imaging programs, including CEERS in the EGS field, and HUDF GTO, and simulate the ancillary HST data for these fields. We construct complete mock samples of galaxies, local stars and brown dwarfs, representative of the current understanding of these populations using the latest observed luminosity and mass functions extrapolated to low masses, and high redshifts. The photometry of these sources is simulated through astronomical image generation, following the current knowledge of the JWST instruments. We extract the sources with SExtractor and estimate the source physical properties using SED-fitting.

Our main results can be summarized as follows:

– We find that the photometric redshifts estimated in the CEERS configuration are mainly limited by the lack of blue-band data. The additional MIRI bands marginally improve the photometric redshifts at faint magnitudes and at high redshift, where MIRI covers the rest-frame optical. Source blending contributes to up to 20% of the photometric redshift outliers in CEERS, and 40% in the HUDF.

– Stellar masses are recovered within 0.2 dex at $z \leq 5$ and 0.25 dex at $z > 5$, and are systematically overestimated by 0.1 dex at high redshift. Star formation rates are scattered over 0.3 dex and the most star-forming galaxies have a systematic bias of 0.1 to 0.2 dex. Numerous catastrophic SFR estimates arise from photometric redshift outliers.
– Galactic brown dwarfs contaminating the $z \geq 5$ galaxy samples can be effectively discarded, reaching a residual density of < 0.01 arcmin^{-2}. The impact on galaxy completeness remains minimal, although dependent on the assumed galaxy morphology.
– We find that the $5 < z < 10$ galaxy selection based on the redshift posterior probability distribution from SED-fitting gives the best compromise between completeness and purity. In the CEERS configuration, galaxy completeness remains above 50% at $m_{\rm UV} < 27.5$ and purity is higher than 80 and 60% at $z \leq 7$ and 10, respectively. In the HUDF strategy, the galaxy samples are more than 50% complete at $m_{\rm UV} < 29$ and 80% pure at $m_{\rm UV} < 30$ at all redshifts.
– We provide scaling correction factors for the selected galaxy number counts to recover the intrinsic number counts in the CEERS configuration. The values typically range from 1 to 2 at $M_{\rm UV} < -18$, but increase a lot at fainter magnitudes. This scaling is sensitive to the source modeling used as input, the source extraction and template fitting procedure, as well as the choice of ancillary data. Thus, the provided factors are strictly valid when using the same procedure presented here. However, our results show how crucial these types of calculations are to correctly recovering the luminosity function.
– The faint-end slope of the galaxy UV luminosity function in CEERS can be recovered with an error of ± 0.1 at $z = 5$ and ± 0.25 at $z = 10$, despite the significant dependence on the correction factors. We estimate that at least 300 arcmin^2 would be necessary to constrain the bright end up to $z = 8$.

We remind the reader that our forecasts are based on future JWST and existing HST imaging data, meaning that we neglect ancillary spectroscopy and ground-based imaging which may improve the results. In addition, the UVCANDELS program will enlarge the wavelength coverage in the EGS field, which may modestly improve the estimated photometric redshifts and the purity of the high-redshift galaxy samples.

In the future, we plan to include more realistic galaxy morphologies and use our simulations to fully exploit data from JWST imaging surveys. In addition, we plan to extend our simulations to the Euclid Deep Fields.

Acknowledgements. OI acknowledges the funding of the French Agence Nationale de la Recherche for the project "SAGACE". CCW acknowledges support from the National Science Foundation Astronomy and Astrophysics Fellowship grant AST-1701546. ECL acknowledges support from the ERC Advanced Grant 695671 "QUENCH". LC acknowledges support from the Spanish Ministry for Science and Innovation under grants ESP2017-83197 and MDM-2017-0737 "Unidad de Excelencia María de Maeztu – Centro de Astrobiología (CSIC-INTA)". JPP acknowledges the UK Science and Technology Facilities Council and the UK Space Agency for their support of the UK's JWST MIRI development activities. KIC acknowledges funding from the European Research Council through the award of the Consolidator Grant ID 681627-BUILDUP.

References

Aniano, G., Draine, B. T., Gordon, K. D., & Sandstrom, K. 2011, PASP, 123, 1218
Arnouts, S., Moscardini, L., Vanzella, E., et al. 2002, MNRAS, 329, 355
Baraffe, I., Homeier, D., Allard, F., & Chabrier, G. 2015, A&A, 577, A42
Bertin, E. 2009, Mem. Soc. Astron. It., 80, 422
Bertin, E., & Arnouts, S. 1996, A&AS, 117, 393
Bielby, R., Hudelot, P., McCracken, H. J., et al. 2012, A&A, 545, A23
Birkmann, S. M., Ferruit, P., Rawle, T., et al. 2016, Proc., SPIE, 9904
Bisigello, L., Caputi, K. I., Colina, L., et al. 2016, ApJS, 227, 19
Bisigello, L., Caputi, K. I., Colina, L., et al. 2017, ApJS, 231, 3
Bisigello, L., Caputi, K. I., Colina, L., et al. 2019, ApJS, 243, 27
Bixler, J. V., Bowyer, S., & Laget, M. 1991, A&A, 250, 370
Boucaud, A., Bocchio, M., Abergel, A., et al. 2016, A&A, 596, A63
Bouwens, R. J., Illingworth, G. D., Oesch, P. A., et al. 2015, ApJ, 803, 34
Bouwens, R. J., Oesch, P. A., Illingworth, G. D., Ellis, R. S., & Stefanon, M. 2017, ApJ, 843, 129
Bowler, R.A.A., Dunlop, J.S., McLure, R.J., et al. 2015, MNRAS, 452, 1817
Brammer, G. B., van Dokkum, P. G., Franx, M., et al. 2012, ApJS, 200, 13
Bruzual, G., & Charlot, S. 2003, MNRAS, 344, 1000
Burgasser, A. J. 2007, ApJ, 659, 655
Caballero, J. A., Burgasser, A. J., & Klement, R. 2008, A&A, 488, 181
Caffau, E., Ludwig, H.-G., Bonifacio, P., et al. 2010, A&A, 514, A92
Calzetti, D., Armus, L., Bohlin, R. C., et al. 2000, ApJ, 533, 682
Caputi, K. I., Ilbert, O., Laigle, C., et al. 2015, ApJ, 810, 73
Castelli, F., & Kurucz, R. L. 2004, A&A, 419, 725
Chabrier, G., Baraffe, I., Allard, F., & Hauschildt, P. 2000, ApJ, 542, 464
Charlot, S., & Fall, S. M. 2000, ApJ, 539, 718
Chen, B., Stoughton, C., Smith, J. A., et al. 2001, ApJ, 553, 184
Chevallard, J., & Charlot, S. 2016, MNRAS, 462, 1415
Cowley, W., Baugh, C., Cole, S., Frenk, C., & Lacey, C. 2018, MNRAS, 474, 2352
Curtis-Lake, E., McLure, R. J., Dunlop, J. S., et al. 2016, MNRAS, 457, 440
Davidzon, I., Ilbert, O., Laigle, C., et al. 2017, A&A, 605, A70
Dawson, W. A., Schneider, M. D., Tyson, J. A., & Jee, M. J. 2016, ApJ, 816, 11
Driver, S. P., Andrews, S. K., da Cunha, E., et al. 2018, MNRAS, 475, 2891
Dunlop, J. S. 2013, The First Galaxies (Astrophysics and Space Science Library), eds. T. Wiklind, B. Mobasher, & V. Bromm, 223
Felten, J. E. 1976, ApJ, 207, 700
Finkelstein, S. L., Ryan, R. E., Jr, Papovich, C., et al. 2015, ApJ, 810, 71
Fitzpatrick, E. L. 1999, PASP, 111, 63
Fitzpatrick, E. L., & Massa, D. 1986, ApJ, 307, 286
Furlanetto, S., Mirocha, J., Mebane, R., & Sun, G. 2017, MNRAS, 472, 1576
Galametz, A., Grazian, A., Fontana, A., et al. 2013, ApJS, 206, 10
Galliano, F., Hony, S., Bernard, J.-P., et al. 2011, A&A, 536, A88
Gardner, J. P., Mather, J. C., Clampin, M., et al. 2006, Proc., SPIE, 6265
Grazian, A., Castellano, M., Fontana, A., et al. 2012, A&A, 547, A51
Grogin, N. A., Kocevski, D. D., Faber, S. M., et al. 2011, ApJS, 197, 35
Guo, Y., Ferguson, H. C., Giavalisco, M., et al. 2013, ApJS, 207, 24
Gutkin, J., Charlot, S., & Bruzual, G. 2016, MNRAS, 462, 1757
Hildebrandt, H., Erben, T., Kuijken, K., et al. 2012, MNRAS, 421, 2355
Hughes, D. H., Serjeant, S., Dunlop, J., et al. 1998, Nature, 394, 241
Ilbert, O., Tresse, L., Zucca, E., et al. 2005, A&A, 439, 863
Ilbert, O., Arnouts, S., McCracken, H. J., et al. 2006, A&A, 457, 841
Ilbert, O., Capak, P., Salvato, M., et al. 2009, ApJ, 690, 1236
Ilbert, O., McCracken, H. J., Le Fèvre, O., et al. 2013, A&A, 556, A55
Ilbert, O., Arnouts, S., Floc'h, E. L., et al. 2015, A&A, 579, A2
Illingworth, G. D., Magee, D., Oesch, P. A., et al. 2013, ApJS, 209, 6
Inoue, A. K., Shimizu, I., Iwata, I., & Tanaka, M. 2014, MNRAS, 442, 1805
Kemp, T. W., Dunlop, J. S., McLure, R. J., et al. 2019, MNRAS, 486, 3087
Koekemoer, A. M., Aussel, H., Calzetti, D., et al. 2007, ApJS, 172, 196
Koekemoer, A. M., Faber, S. M., Ferguson, H. C., et al. 2011, ApJS, 197, 36
Krist, J. E., Hook, R. N., & Stoehr, F. 2011, Proc., SPIE, 8127
Kron, R. G. 1980, ApJS, 43, 305
Laigle, C., Davidzon, I., Ilbert, O., et al. 2019, MNRAS, 486, 5104
Laigle, C., McCracken, H. J., Ilbert, O., et al. 2016, ApJS, 224, 24
Laureijs, R., Amiaux, J., Arduini, S., et al. 2011, ArXiv e-prints [arXiv:1110.3193]
Le Fèvre, O., Tasca, L. A. M., Cassata, P., et al. 2015, A&A, 576, A79
Leauthaud, A., Massey, R., Kneib, J.-P., et al. 2007, ApJS, 172, 219
Livermore, R. C., Finkelstein, S. L., & Lotz, J. M. 2017, ApJ, 835, 113
Madau, P., & Dickinson, M. 2014, ARA&A, 52, 415
Mason, C. A., Trenti, M., & Treu, T. 2015a, ApJ, 813, 21
Mason, C. A., Treu, T., Schmidt, K. B., et al. 2015b, ApJ, 805, 79
McLeod, D. J., McLure, R. J., Dunlop, J. S., et al. 2015, MNRAS, 450, 3032
McLeod, D. J., McLure, R. J., & Dunlop, J. S. 2016, MNRAS, 459, 3812
McLure, R. J., Dunlop, J. S., Bowler, R. A. A., et al. 2013, MNRAS, 432, 2696
Momcheva, I. G., Brammer, G. B., van Dokkum, P. G., et al. 2016, ApJS, 225, 27
Morley, C. V., Fortney, J. J., Marley, M. S., et al. 2012, ApJ, 756, 172
Morley, C. V., Marley, M. S., Fortney, J. J., et al. 2014, ApJ, 787, 78
Mortlock, D. J., Patel, M., Warren, S. J., et al. 2012, MNRAS, 419, 390
Moutard, T., Arnouts, S., Ilbert, O., et al. 2016, A&A, 590, A102
Oesch, P. A., Bouwens, R. J., Illingworth, G. D., et al. 2014, ApJ, 786, 108

Oesch, P. A., Bouwens, R. J., Illingworth, G. D., Labbé, I., & Stefanon, M. 2018, ApJ, 855, 105
Oke, J. B. 1974, ApJS, 27, 21
Onodera, M., Renzini, A., Carollo, M., et al. 2012, ApJ, 755, 26
Pecaut, M. J., & Mamajek, E. E. 2013, ApJS, 208, 9
Pickles, A. J. 1998, PASP, 110, 863
Planck Collaboration VI. 2020, A&A, in press, https://doi.org/10.1051/0004-6361/201833910
Polletta, M., Tajer, M., Maraschi, L., et al. 2007, ApJ, 663, 81
Pontoppidan, K. M., Pickering, T. E., Laidler, V. G., et al. 2016, Proc., SPIE, 9910
Prevot, M. L., Lequeux, J., Maurice, E., Prevot, L., & Rocca-Volmerange, B. 1984, A&A, 132, 389
Ribeiro, B., Le Fèvre, O., Tasca, L. A. M., et al. 2016, A&A, 593, A22
Rieke, M. J., Kelly, D., & Horner, S. 2005, Proc., SPIE, 5904
Rieke, G. H., Wright, G. S., Böker, T., et al. 2015, PASP, 127, 584
Robertson, B. E., Ellis, R. S., Dunlop, J. S., et al. 2014, ApJ, 796, L27
Robertson, B. E., Ellis, R. S., Furlanetto, S. R., & Dunlop, J. S. 2015, ApJ, 802, L19
Robin, A. C., Reylé, C., Derriére, S., & Picaud, S. 2003, A&A, 409, 523
Robin, A. C., Marshall, D. J., Schultheis, M., & Reylé, C. 2012, A&A, 538, A106
Robin, A.C., Reylé, C., Fliri, J., et al. 2014, A&A, 569, A13
Salvato, M., Hasinger, G., Ilbert, O., et al. 2009, ApJ, 690, 1250
Sanders, D. B., Salvato, M., Aussel, H., et al. 2007, ApJS, 172, 86
Schenker, M. A., Robertson, B. E., Ellis, R. S., et al. 2013, ApJ, 768, 196
Schlafly, E. F., & Finkbeiner, D. P. 2011, ApJ, 737, 103
Schreiber, C., Pannella, M., Elbaz, D., et al. 2015, A&A, 575, A74
Schreiber, C., Elbaz, D., Pannella, M., et al. 2017, A&A, 602, A96
Schreiber, C., Elbaz, D., Pannella, M., et al. 2018, A&A, 609, A30
Scoville, N., Aussel, H., Brusa, M., et al. 2007, ApJS, 172, 1
Shibuya, T., Ouchi, M., & Harikane, Y. 2015, ApJS, 219, 15
Sérsic, J. L. 1963, BAAA, 6, 41
Stefanon, M., Yan, H., Mobasher, B., et al. 2017, ApJS, 229, 32
Steidel, C. C., Giavalisco, M., Pettini, M., Dickinson, M., & Adelberger, K. L. 1996, ApJ, 462, L17
Tilvi, V., Papovich, C., Tran, K.-V. H., et al. 2013, ApJ, 768, 56
Tomczak, A. R., Quadri, R. F., Tran, K.-V. H., et al. 2014, ApJ, 783, 85
Trenti, M., & Stiavelli, M. 2008, ApJ, 676, 767
van der Wel, A., Bell, E. F., Häussler, B., et al. 2012, ApJS, 203, 24
van der Wel, A., Franx, M., van Dokkum, P. G., et al. 2014, ApJ, 788, 28
Wilkins, S. M., Bunker, A. J., Stanway, E., Lorenzoni, S., & Caruana, J. 2011, MNRAS, 417, 717
Williams, C. C., Curtis-Lake, E., Hainline, K. N., et al. 2018, ApJS, 236, 33
Wright, G. S., Wright, D., Goodson, G. B., et al. 2015, PASP, 127, 595
Wright, A. H., Driver, S. P., & Robotham, A. S. G. 2018, MNRAS, 480, 3491
Yung, L. Y. A., Somerville, R. S., Finkelstein, S. L., Popping, G., & Davé, R. 2019, MNRAS, 483, 2983
Zackrisson, E., Rydberg, C.-E., Schaerer, D., Östlin, G., & Tuli, M. 2011, ApJ, 740, 13

Appendix A: Additional table

Table A.1. Galaxy absolute magnitude number counts for luminosity function computation in CEERS_1 observing strategy.

M_{UV}	$\mathbb{E}[N]$	C	P	S
		$z \sim 5$		
−22.75	0.8 ± 0.2	0.8 ± 0.2	1 ± 0	1.2 ± 0.3
−22.25	3.0 ± 0.3	0.7 ± 0.1	0.93 ± 0.06	1.5 ± 0.2
−21.75	6.0 ± 0.5	0.83 ± 0.07	0.83 ± 0.07	1.0 ± 0.1
−21.25	21.0 ± 0.9	0.76 ± 0.04	0.83 ± 0.04	1.19 ± 0.08
−20.75	61 ± 2	0.67 ± 0.03	0.75 ± 0.02	1.11 ± 0.05
−20.25	101 ± 2	0.64 ± 0.02	0.84 ± 0.02	1.22 ± 0.04
−19.75	146 ± 2	0.62 ± 0.02	0.85 ± 0.01	1.29 ± 0.03
−19.25	198 ± 3	0.52 ± 0.01	0.79 ± 0.01	1.54 ± 0.04
−18.75	281 ± 3	0.44 ± 0.01	0.73 ± 0.01	1.68 ± 0.04
−18.25	313 ± 4	0.283 ± 0.008	0.62 ± 0.01	2.13 ± 0.05
−17.75	266 ± 3	0.149 ± 0.005	0.48 ± 0.01	3.8 ± 0.1
−17.25	137 ± 2	0.044 ± 0.002	0.39 ± 0.02	10.2 ± 0.4
−16.75	47 ± 1	<0.01	0.42 ± 0.03	41 ± 3
−16.25	16.8 ± 0.8	<0.01	0.35 ± 0.05	155 ± 17
		$z \sim 6$		
−22.25	3.2 ± 0.4	1 ± 0	0.2 ± 0.1	0.2 ± 0.1
−21.75	4.0 ± 0.4	0.6 ± 0.1	0.6 ± 0.1	0.6 ± 0.1
−21.25	17.6 ± 0.8	0.70 ± 0.05	0.67 ± 0.05	0.84 ± 0.07
−20.75	40 ± 1	0.66 ± 0.04	0.63 ± 0.03	0.80 ± 0.05
−20.25	78 ± 2	0.68 ± 0.03	0.68 ± 0.02	0.82 ± 0.03
−19.75	136 ± 2	0.69 ± 0.02	0.62 ± 0.02	0.81 ± 0.03
−19.25	171 ± 3	0.53 ± 0.02	0.54 ± 0.02	1.12 ± 0.04
−18.75	166 ± 3	0.32 ± 0.01	0.47 ± 0.02	1.69 ± 0.06
−18.25	159 ± 3	0.169 ± 0.008	0.40 ± 0.02	2.8 ± 0.1
−17.75	130 ± 2	0.062 ± 0.004	0.33 ± 0.02	5.2 ± 0.2
−17.25	47 ± 1	<0.01	0.30 ± 0.03	21 ± 1
−16.75	5.2 ± 0.5	<0.01	0.35 ± 0.09	275 ± 54
−16.25	0.4 ± 0.1	<0.01	0.5 ± 0.4	4913 ± 3474
		$z \sim 7$		
−22.25	0.6 ± 0.2	1 ± 0	0.3 ± 0.3	0.7 ± 0.5
−21.75	3.4 ± 0.4	0.86 ± 0.09	0.88 ± 0.08	0.82 ± 0.05
−21.25	6.8 ± 0.5	0.85 ± 0.07	0.56 ± 0.09	0.8 ± 0.1
−20.75	16.8 ± 0.8	0.65 ± 0.05	0.65 ± 0.05	1.02 ± 0.09
−20.25	42 ± 1	0.60 ± 0.04	0.58 ± 0.03	0.82 ± 0.05
−19.75	58 ± 2	0.50 ± 0.03	0.51 ± 0.03	1.10 ± 0.06
−19.25	108 ± 2	0.44 ± 0.02	0.45 ± 0.02	1.05 ± 0.05
−18.75	164 ± 3	0.34 ± 0.02	0.32 ± 0.02	1.01 ± 0.04
−18.25	223 ± 3	0.22 ± 0.01	0.22 ± 0.01	1.33 ± 0.05
−17.75	201 ± 3	0.063 ± 0.005	0.19 ± 0.01	2.27 ± 0.08
−17.25	76 ± 2	<0.01	0.21 ± 0.02	9.0 ± 0.5
−16.75	9.2 ± 0.6	<0.01	0.15 ± 0.05	108 ± 16
−16.25	0.4 ± 0.1	<0.01	<0.01	3512 ± 2483
		$z \sim 8$		
−21.75	1.0 ± 0.2	0.7 ± 0.3	0.6 ± 0.2	0.6 ± 0.2
−21.25	2.8 ± 0.3	0.6 ± 0.1	0.6 ± 0.1	1.0 ± 0.2
−20.75	6.4 ± 0.5	0.5 ± 0.1	0.44 ± 0.09	0.8 ± 0.1
−20.25	10.4 ± 0.6	0.45 ± 0.06	0.58 ± 0.07	1.2 ± 0.2
−19.75	21.8 ± 0.9	0.39 ± 0.04	0.53 ± 0.05	1.4 ± 0.1
−19.25	28 ± 1	0.23 ± 0.02	0.44 ± 0.04	2.1 ± 0.2
−18.75	41 ± 1	0.16 ± 0.02	0.26 ± 0.03	2.5 ± 0.2
−18.25	48 ± 1	0.060 ± 0.008	0.21 ± 0.03	3.6 ± 0.2
−17.75	54 ± 1	0.014 ± 0.003	0.14 ± 0.02	5.4 ± 0.3
−17.25	30 ± 1	<0.01	0.09 ± 0.02	15 ± 1
−16.75	5.4 ± 0.5	<0.01	0.07 ± 0.05	118 ± 23
−16.25	<0.01	<0.01	<0.01	<0.01
		$z \sim 9$		
−21.25	0.4 ± 0.1	<0.01	<0.01	0.5 ± 0.6
−20.75	3.0 ± 0.3	0.5 ± 0.2	0.5 ± 0.1	0.4 ± 0.1
−20.25	4.4 ± 0.4	0.52 ± 0.09	0.6 ± 0.1	1.4 ± 0.3
−19.75	7.6 ± 0.6	0.35 ± 0.06	0.37 ± 0.08	1.6 ± 0.3
−19.25	20.8 ± 0.9	0.27 ± 0.04	0.31 ± 0.05	1.0 ± 0.1
−18.75	27 ± 1	0.12 ± 0.02	0.16 ± 0.03	1.4 ± 0.1
−18.25	30 ± 1	0.05 ± 0.01	0.12 ± 0.03	2.3 ± 0.2
−17.75	15.0 ± 0.8	<0.01	0.11 ± 0.04	7.0 ± 0.9
−17.25	1.4 ± 0.2	<0.01	<0.01	126 ± 48
−16.75	<0.01	<0.01	<0.01	<0.01
−16.25	<0.01	<0.01	<0.01	<0.01
		$z \sim 10$		
−20.25	1.0 ± 0.2	0.3 ± 0.2	0.4 ± 0.2	1.4 ± 0.7
−19.75	4.2 ± 0.4	0.4 ± 0.2	0.3 ± 0.1	0.5 ± 0.1
−19.25	8.2 ± 0.6	0.6 ± 0.1	0.22 ± 0.06	0.4 ± 0.1
−18.75	36 ± 1	0.43 ± 0.07	0.08 ± 0.02	0.30 ± 0.04
−18.25	76 ± 2	0.16 ± 0.04	0.04 ± 0.01	0.26 ± 0.03
−17.75	42 ± 1	<0.01	0.03 ± 0.01	0.74 ± 0.08
−17.25	8.8 ± 0.6	<0.01	0.05 ± 0.03	7 ± 1
−16.75	0.20 ± 0.09	<0.01	<0.01	501 ± 501
−16.25	<0.01	<0.01	<0.01	<0.01

Notes. Per columns, the expectation value of the selected number counts, completeness, purity and scaling correction factor.

Table A.1. continued.

Appendix B: Galaxy selection at z > 5 in the HUDF

To select our high–redshift galaxies in the HUDF in the Bouwens-like set of criteria, we first preselect sources at $z \sim 5$ to 12 using the selection criteria in Table 3. These color criteria are represented in Fig. B.1. The high-redshift candidates are then confirmed with photometric redshifts. Figure B.2 indicates the high-redshift galaxy completeness and purity for the Bouwens-, Bowler- and Finkelstein-like criteria.

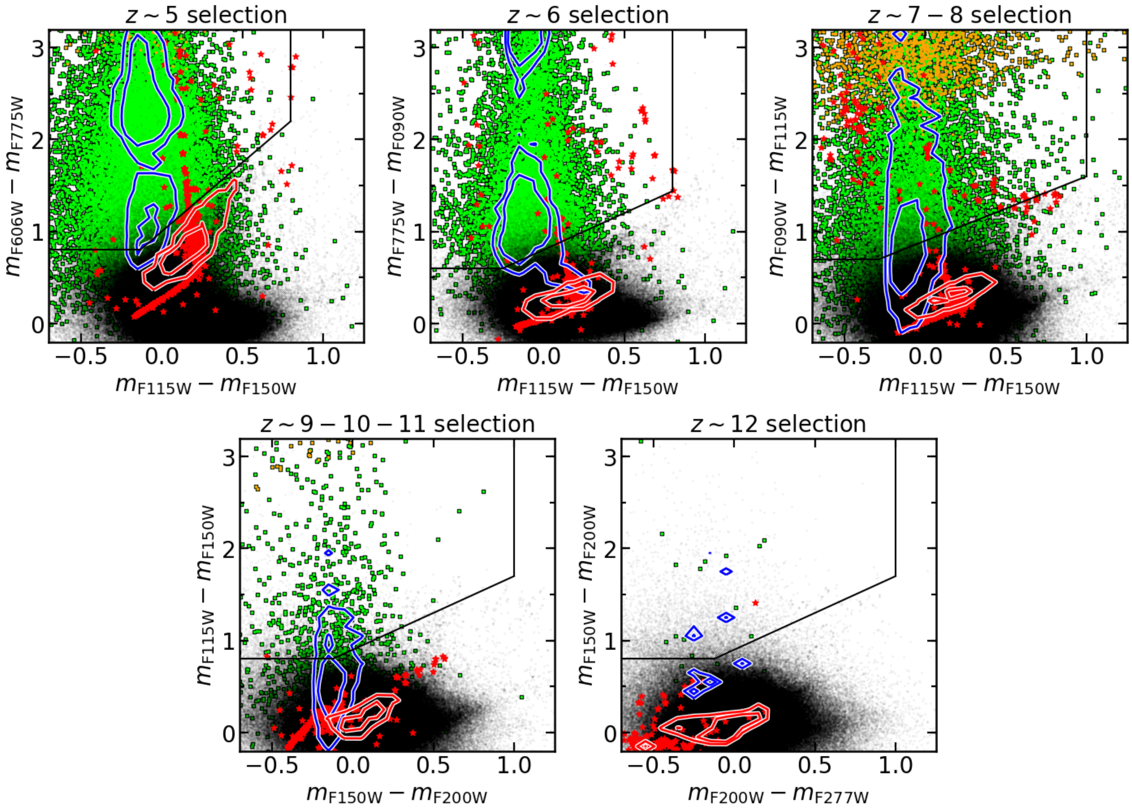

Fig. B.1. Same as Fig. 18, but in the HUDF, for the HUDF_1 observing strategy.

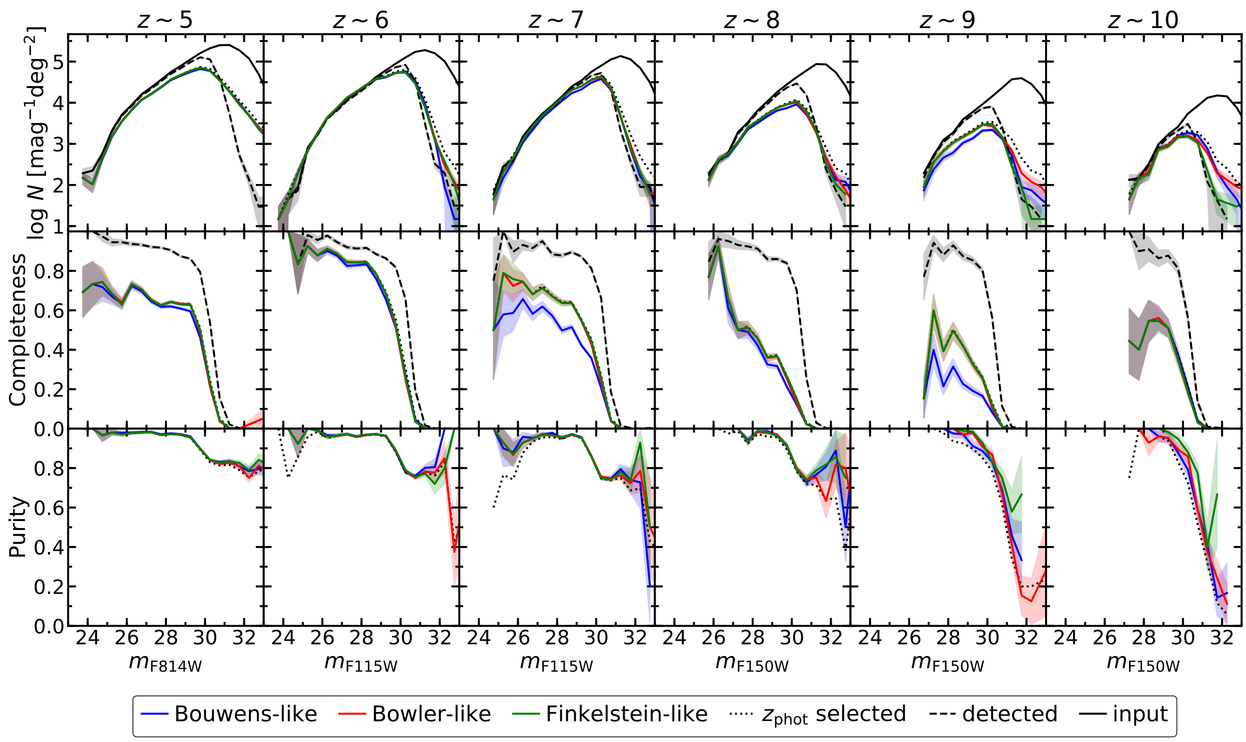

Fig. B.2. Same as Fig. 19, but for the HUDF_1 observing strategy.

3. Processing the imaging data in the COSMOS field

3.1. Introduction

The cosmic evolution survey (COSMOS; Scoville et al. 2007) is an astronomical survey over 2 $\deg^2$ of the sky. It benefits from a large variety of photometric and spectroscopic data, covering wavelengths from the X-ray to the radio. The optical and infrared photometric catalog named COSMOS2015 (Laigle et al. 2016) gathered all the high-resolution imaging data in the COSMOS field, and has been widely used by the community for a diversity of science cases. Over the past few years, the on-going surveys with the Subaru and VISTA telescopes have provided deeper imaging data; in the optical with Hyper Suprime-Cam (HSC) and in the near-infrared with UltraVISTA. Additionally, the final mid-infrared IRAC images from the *Spitzer* space telescope have been processed. Using this new set of imaging data, the COSMOS collaboration, including myself, provided to the community an updated multi-wavelength photometric catalog, named COSMOS2020. This catalog was constructed using improved data processing, which I present in this chapter. This work is of major importance notably for the *Euclid* mission, as COSMOS will be one of the *Euclid* calibration fields.

3.2. Preparation for the *Euclid* mission

The COSMOS field will contribute to the next-generation deep and wide-field imaging surveys, like the *Euclid* mission. The *Euclid* space telescope (Laureijs et al. 2011) is an optical and near-infrared telescope, which will be launched in 2022. With its primary mirror of 1.2 m diameter, the collective area is about 1 m^2. The on-board instruments include the visible imager (VIS; Cropper et al. 2016) and the near infrared spectrometer and photometer (NISP; Maciaszek et al. 2016), with a field of view of 0.53 $\deg^2$ and a pixel scale of $0.1''$ and $0.3''$, respectively. The photometric bands are the very broad band (R+I+Z) for the VIS and the Y, J and H broad bands for the NISP. This mission includes two planned surveys, the wide survey covering 15 000 $\deg^2$ (more than one third of the sky) to a depth of 24 mag (5σ), and the deep survey covering 40 $\deg^2$ with 2 mag deeper imaging. The Euclid deep fields are located in the North Ecliptic Pole (NEP) for the Euclid Deep Field North (EDFN), in the South Ecliptic Pole (SEP) for the Euclid Deep Field

South (EDFS), and in the Chandra Deep Field South (CDFS) for the Euclid Deep Field Fornax (EDFF). In order to constrain gravity, dark energy and dark matter, the primary science is based on galaxy clustering and weak lensing measurements.

In complement to the *Euclid* data, the Cosmic Dawn Survey aims to obtain uniform multi-wavelength imaging data over 50 $\deg^2$, in the Euclid Deep and Calibration fields. It mainly consists of the final mid-infrared images from the *Spitzer* space telescope, and optical data from the on-going Hawaii-Two-0 (H20) survey. The Euclid Calibration fields include COSMOS, the Subaru-XMM Deep Field (SXDF), the VIMOS VLT Deep Survey (VVDS) fields, the Great Observatories Origins Deep Survey North (GOODS-N) field, and the Extended Groth Strip (EGS), in addition to NEP and EDFF. The *Spitzer* observations in the IRAC/channel 1 and 2 are described in (Moneti et al. in prep.), and reach the depth of 26.4 mag (1σ) in channel 1 over a total of 20 $\deg^2$ (see Sect. 3.3.1 and Appendix B). The H20 survey will include Hyper Suprime-Cam *grizy* deep imaging from the Subaru telescope (reaching 27 mag depths), and spectroscopy from the Deep Imaging Multi-Object Spectrograph (DEIMOS) at Keck telescope, over the 20 $\deg^2$ of the two primary Euclid Calibration fields (EDFN and EDFF).

In this era of precision cosmology, scientific analyses are limited by systematic rather than statistical errors, which need to be tackled down. One essential step for this purpose is an accurate calibration. Hence, the COSMOS field will be one of the primary calibration fields for the *Euclid* mission, thanks to its deep imaging data in many optical and infrared bands. Multiple simulations of the observations to be performed with *Euclid* are based on the COSMOS data (Jouvel et al. 2009). The photometry from the *Euclid* images will benefit from the experience with the COSMOS data, as multiple extraction techniques can be optimized and compared (see Sect. 3.4). Similarly, all the methods developed here will be applied in parallel to the Cosmic Dawn data. Multiple photometric redshift algorithms were also compared during the *Euclid* data challenges [1], using the deep COSMOS data as reference. Photometric redshifts from *Euclid* photometry, in addition to complementary ground-based optical data, will need be tested and validated using large spectroscopic redshift samples. The wealth of spectroscopic redshifts already available and the coming follow-ups in the COSMOS field (Masters et al. 2019) will fulfill this purpose. Alternatively, machine learning methods for photometric redshifts, such as the nearest neighbors $P(z)$ (NNPZ), utilizes photometric redshifts computed in fields with many bands to calibrate photometric redshifts in shallower fields with fewer bands (Cunha et al. 2009). Once again, this can be performed with COSMOS data (Desprez et al. in prep.). The shape measurements for the VIS instrument will also be calibrated with the high-resolution imaging in COSMOS.

1. http://www.isdc.unige.ch/euclid/overview-of-the-data-challenges.html?showall=1

3.3. Imaging data in the COSMOS field

The COSMOS field combines imaging data from both ground and space-based observatories, with distinct advantages regarding the wavelength coverage and the field of view. COSMOS is the first wide field benefiting from deep high-resolution imaging with the *Hubble* space telescope (*HST*), with i-band observations with the Advanced Camera for Surveys (ACS) reaching 27.2 mag of depth (10σ, point-source) over 1.7 deg^2 (Koekemoer et al. 2007). Despite the high sensitivity of the near-infrared detectors on-board *HST*, the Wide Field Camera 3 (WFC3) with it field of view of 4.65 arcmin^2 would require too much time to observe the entire COSMOS field. In contrast, the ground-based near-infrared surveys such as UltraVISTA can provide this wide field imaging. Observing from the ground at these wavelengths is however challenging, because of the bright and time-variable sky background and the inefficiency of CCD detectors in the infrared.

3.3.1. Infrared data

The UltraVISTA survey (McCracken et al. 2012) provides deep near-infrared imaging over 1.5 deg^2 of the COSMOS field, with four "ultra-deep" stripes covering 0.62 deg^2, and four "deep" stripes. These images were taken with the wide-field near-infrared camera (VIRCAM) on the 4 m-diameter VISTA telescope in Chile. In the (latest) fourth data release (DR4), the depths of the Y, J, H, K_s broad-band images, at 1.0, 1.2, 1.6 and 2.2 microns respectively, reach $25-26$ mag (3σ). The $NB118$ narrow-band imaging covers the ultra-deep stripes only and reaches 24 mag (3σ).

The COSMOS field also benefits from the mid-infrared *Spitzer* imaging data from the Cosmic Dawn Survey. Since the *Spitzer* mission is ending in 2020, all the existing data from the Infrared Array Camera (IRAC) were stacked to provide the final processed *Spitzer* images in multiple fields. The IRAC broad bands include channels 1, 2, 3 and 4 at 3.6, 4.5, 5.8, and 8 microns, respectively. In COSMOS, the IRAC data notably combines the *Spitzer* Large Area Survey with Hyper Suprime-Cam (SPLASH; Steinhardt et al. 2014), covering 3.8 deg^2, and the *Spitzer* Matching Survey of the UltraVISTA ultra-deep Stripes survey (SMUVS; Ashby et al. 2018), providing deeper imaging over the UltraVISTA deep stripes. The data processing is described the Moneti et al. in prep. in Appendix B.

3.3.2. Optical data

The CFHT Large Area U-band Deep Survey (CLAUDS) provides u-band imaging data at 0.38 microns (Sawicki et al. 2019), obtained with the camera MegaCam at the Canada France Hawai telescope (CFHT). In addition to this new data, the reprocessed data in the old filter noted u^* (Laigle et al. 2016) is also included. These two images reach 27 mag depths over most of the UltraVISTA footprint.

The deepest optical data in the COSMOS field is provided by Hyper Suprime-Cam (HSC) on the Subaru telescope in Hawaii. In particular, the HSC Subaru Strategic Program (HSC-SSP; Aihara et al. 2018) includes deep imaging in the g, r, i, z, y broad bands over $2.2\,\mathrm{deg}^2$, at 0.48, 0.62, 0.77, 0.89 and 0.98 microns respectively. In the second data release (Aihara et al. 2019), the depths reach 27 to 28 mag at 3σ with an homogeneous coverage over the entire COSMOS field.

The old Subaru/Suprime-Cam data in the COSMOS field include optical imaging in 7 broad bands, 12 medium bands and 2 narrow bands (Taniguchi et al. 2007; Taniguchi et al. 2015). In comparison with the HSC data, the depths of the broad-band images are about 1 mag shallower. Nonetheless, the Suprime-Cam medium and narrow bands, with depths of about 26 mag (3σ), provide complementary spectral information. These images are particularly useful for the characterization of the low-redshift sources, from the improved sampling of the Balmer break and emission lines (Laigle et al. 2016).

3.4. Data reduction and analysis

The strategy for the processing of the imaging data in the COSMOS field is the following. Source detection is performed with a combined image constructed from the images in the i, z bands from HSC and the Y, J, H, K_s bands from UltraVISTA. Combining multiple images brings to light extremely faint sources, which may be barely visible in single images. This near-infrared detection is primarily focused on high-redshift sources, which are undetected in blue optical bands. As a consequence, blue low-redshift sources may not be detected, hence would be missing from the final catalog.

Photometry is extracted following two distinct approaches, leading to two separate photometric catalogs, called the CLASSIC catalog and `the Farmer` catalog. The first "classic" approach uses equivalent methods to the COSMOS2015 photometric catalog. Both the detection and photometry of the high-resolution images are performed with `SExtractor` (Bertin et al. 1996) in dual-image mode (where one image is used for detection and an other for measurements). The photometry is extracted in fixed $2''$ and $3''$ diameter apertures. To ensure that the apertures include the same features at all wavelengths, the science images are PSF-homogenized. Multiple corrections are applied to the measured magnitudes, including the magnitude error scaling and the aperture-to-total magnitude corrections. The IRAC photometry is performed with the software `IRACLEAN` (Hsieh et al. 2012), using the high-resolution image as prior to fit the surface brightness profiles of the sources in the confused low-resolution images. In this case, the algorithm iteratively subtract point-like profiles from the images.

In the second approach, the photometry in all the bands is extracted with `the Tractor` (Lang et al. 2016), another model-fitting software. The morphology of the sources is determined through a decision tree, separating point and extended sources. In contrast with the Classic catalog, this method directly provides total magnitudes, performs an improved deblending in the high-resolution images, and extracts all the images in a consistent way. Nonetheless, the photometry from `the Tractor` needs to be rigorously validated, hence the importance of Classic photometry for comparison.

Finally, the photometric redshifts and physical parameters of the sources, including stellar mass, star-formation rates and absolute magnitudes, are estimated through SED-fitting with both the `LePhare` and `EAZY` (Brammer et al. 2008) codes. The configuration used in `LePhare` is the same as Laigle et al. 2016 for COSMOS2015. The strategy adopted in `EAZY` is essentially equivalent, with the primary differences being the set of population synthesis templates and the fitting procedure. With the two photometric catalogs and two photometric redshift codes, the results from the four combinations can be compared.

The resulting COSMOS2020 catalog is a collective effort within the COSMOS collaboration. In this context, my contribution mainly includes the processing and extraction of the high-resolution images for the Classic catalog, in addition to flagging, masking, depth computation, star-galaxy separation, and catalog validation. Hence, I reported these points in the article describing the COSMOS2020 catalog. The following subsections present some of these steps in more details.

3.4.1. Astrometry

All the images are calibrated using the Gaia astrometric reference, with a center at $(\mathrm{R.A.}, \mathrm{Dec.}) = (150.1163213, 2.2009731)$ deg and a pixel scale of $0.15''$. The old data from COSMOS2015, including the MegaCam u^* band and the Suprime-Cam broad, medium and narrow bands, was reprocessed to correct the astrometry. This was performed through the following steps. The coordinates of the bright stars in the image, detected with `SExtractor`, are compared to a reference list of stars, extracted from the UltraVISTA K_s-band image already calibrated with Gaia. This is performed with the software `Scamp` (Bertin 2006), which estimates the coordinate shift between the current and previous astrometric reference. In particular, the old Suprime-Cam images presented significant shifts of about one pixel ($0.15''$), locally in large spatial regions of the images. The images were then recalibrated to the target astrometry using the software `SWarp` (Bertin et al. 2002).

3.4.2. Flagging

There are multiple effects requiring flagging for each of the scientific images, including missing data, saturated and bad pixels. Saturation in charge-coupled devices (CCD) originates from the finite well capacity of individual pixels. If the well capacity is almost reached, the detector response becomes non-linear with respect to the input photon flux. The resulting pixel value is therefore underestimated. If the well is full, electrons overflow into neighbor pixels, leading to bleeding effects.

In addition, over-saturation may lead to bad pixels (nan values). All these effects may arise in the center of bright sources such as stars. Saturated pixels need to be discarded. Pixels with no data also need to be identified, as the images from different surveys have different footprints. In particular, we identified an error in `SExtractor` using the dual-image mode. Sources detected in the combined detection image, but laying in a region of the measurement image with no data, may have non-zero (meaningless) photometry. Therefore, I modified the flag images to have a specific flag for the missing data, and imposed the flux of the flagged sources. This step was necessary for the MegaCam U bands and the Suprime-Cam broad and medium bands.

3.4.3. Depth measurement

The depth of an image is a measure of the performance of a survey, and of the brightness of the faintest detectable objects. Hence, I measured the depth in all of the COSMOS images to assess the quality of the data. In this case, the depths are measured in empty apertures of a given diameter, following three steps. Firstly, the sources in each image are detected, as well as the segmentation map indicating the patch of pixels belonging to each source. Secondly, random coordinates are sampled over the entire field, and the coordinates with any pixel belonging to a source within the aperture radius are rejected. This ensures that all the apertures are empty. Thirdly, the flux is measured within these empty apertures. The 1σ depths are finally computed by taking the 3σ-clipped standard deviation of these fluxes.

Figure 3.1 shows the 3σ depth maps measured in $2''$ diameter apertures, for a few COSMOS bands. In this case, the depths are computed locally inside square cells. The spatial variations of the total exposure time are illustrated by the local depth fluctuations. For the UltraVISTA bands, the deep and ultra-deep stripes are clearly identified. All the HSC images present a uniform exposure over the COSMOS field. The majority of the UltraVISTA footprint includes deep IRAC imaging, with the deepest parts over the ultra-deep stripes.

In addition to the COSMOS field, I estimated the depth of the IRAC/channel 1 images in the Cosmic Dawn Survey (Sect. 3.2). This includes the deep *Spitzer* images in the Euclid Deep Fields, namely EDFN, EDFS and EDFF, and in the Euclid Calibration Fields, including COSMOS, the Extended Groth Strip (EGS), the Hubble deep field North (HDFN), and the XMM-Newton deep field (XMM). For each field, I computed the cumulative coverage area below a given depth limit, and plotted the depth as a function of area in Fig. 3.2. The total depth, summed over the fields, is also represented. This is part of the validation and quality control of the data, and is included in Moneti et al. (in prep).

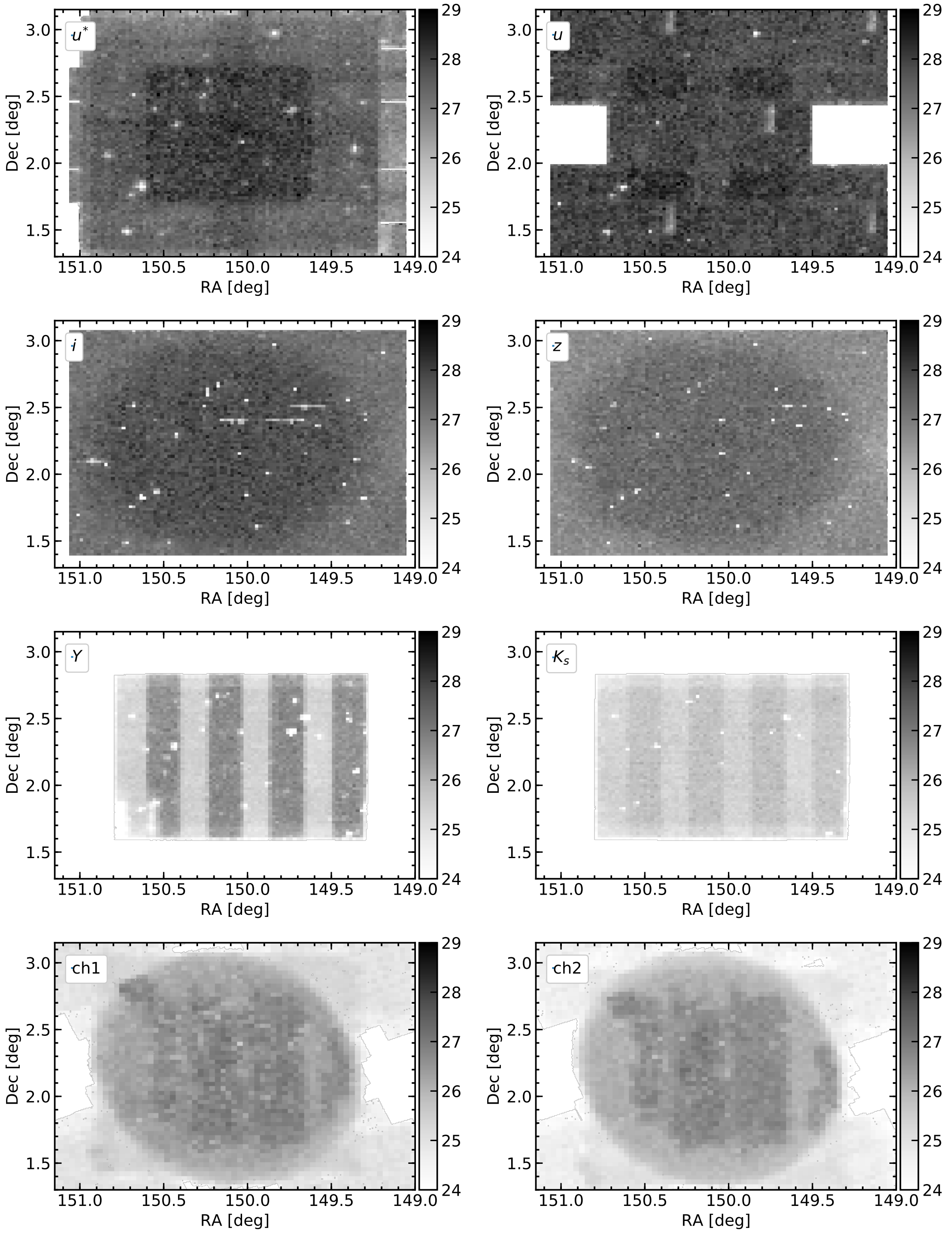

Figure 3.1. – Depth map of the imaging data in the COSMOS field. The depths at 3σ are measured in empty $2''$ diameter apertures. From top to bottom, the two MegaCam U bands, two HSC optical bands, two UltraVISTA near-infrared bands, and the IRAC channel 1 and 2.

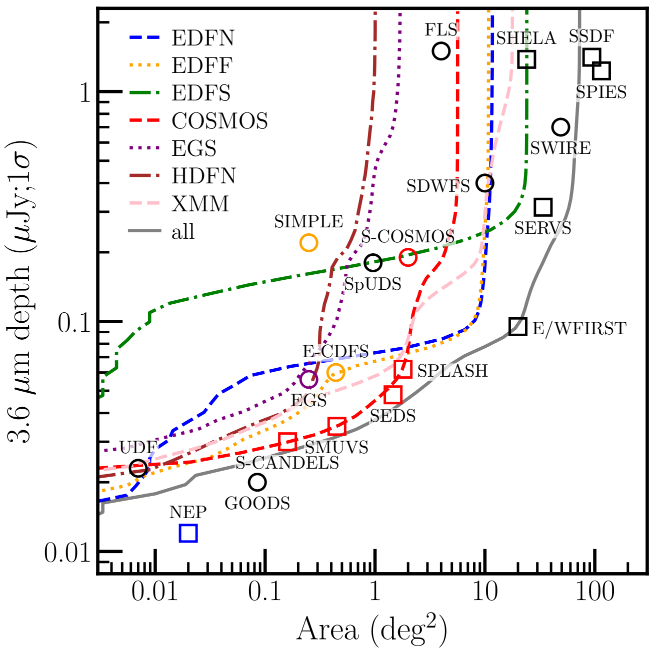

Figure 3.2. – Sensitivity of the *Spitzer*/IRAC channel 1 data as a function of cumulative area coverage, in the Cosmic Dawn Survey. The colored lines illustrates 1σ depths measured in empty $2.5''$ diameter apertures in each field, and the grey solid line is the depth over the total area summed over the fields. The data points indicate point-source sensitivities at 1σ compiled in Ashby et al. 2018. The circles and squares represent surveys executed during cryogenic and warm missions, respectively.

3.4.4. PSF homogenization

The point spread function (PSF) describes the response of an instrument to a point-like source. It depends on the wavelength, the instrument, the position within the image, and in the case of ground-based imaging, on the atmosphere. In the case of aperture photometry, it is required to sample the same structures of the sources in order to obtain reliable color measurements. This can be performed through the homogenization of the PSFs from band to band, and also within the images. Nonetheless, the spatial dependence of the PSF and the impact on aperture photometry is limited in the majority of the COSMOS bands (see Laigle et al. 2016). For COSMOS2020, I performed the PSF homogenization of all the high-resolution images updating the method of Laigle et al. 2016, and in particular correcting for the spatial PSF dependence of the reprocessed Suprime-Cam images.

The first step was to measure the mean PSF in each image. All the bright sources were detected using `SExtractor`, setting a high detection threshold. I selected the stars using the half-light radius versus magnitude space, as illustrated

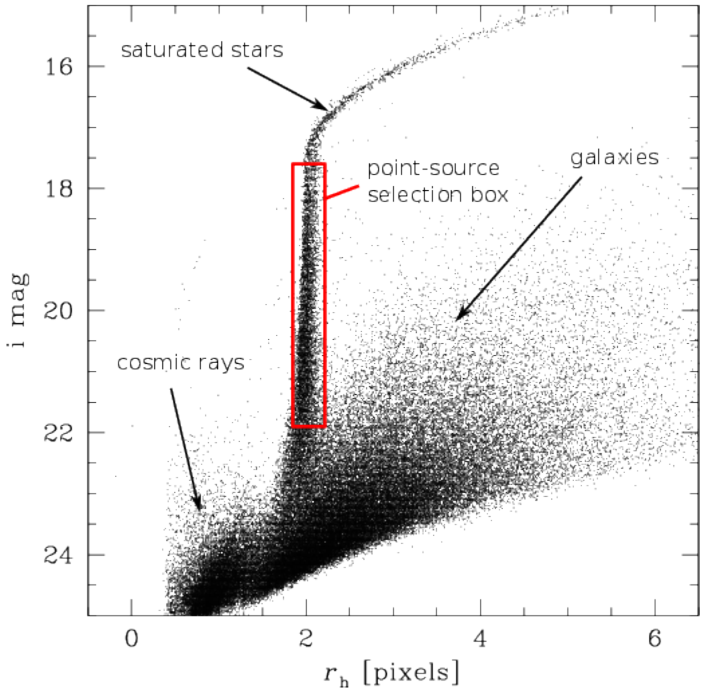

Figure 3.3. – Kron-aperture magnitude as a function of half-light radius for sources detected in the i-band with the Megaprime instrument in the CFHTLS. Source: `PSFEx` User Manual

in Fig. 3.3. Point-sources lay on a specific line while extended sources have larger radii and are more scattered. The brightest stars may be saturated and need to be excluded, as well as the blended stars which can be identified using the flag images. In addition, the coordinates of the selected stars were matched with the clean ACS star catalog (Leauthaud et al. 2007). The *HST*/ACS data in the COSMOS field have an improved resolution compared to ground-based images, in which case point-like sources are easier to properly identify. Additional selection criteria were applied based on morphology to remove elliptical sources, as the center of the point-source surface brightness profile is expected to be circular. The PSF images in all the bands were computed with `PSFEx` (Bertin 2013), using the lists of selected stars. In addition to the PSF estimates, `PSFEx` can provide convolution kernels to modify the PSF of the image to a target PSF, chosen to be a Moffat profile (Moffat 1969) with a given width and slope. The science images were then convolved with these kernels to obtain images with reasonably similar PSFs. Finally, I compared the convolved PSF profiles with the target profile for validation.

In the case of the old Suprime-Cam imaging, in particular the medium and narrow bands, the PSFs are highly spatially dependent. More problematically, the PSF fluctuations present sharp transitions because of the stacking of observations with very different seeings. The Suprime-Cam medium-band data provide key

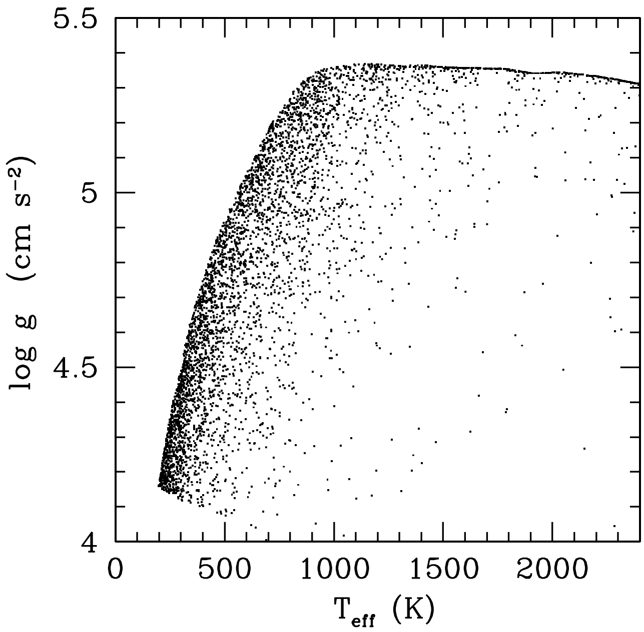

Figure 3.4. – Distribution of the effective temperature and surface gravity of the simulated local field population of brown dwarfs from Saumon et al. 2008.

information about the SED of galaxies, in particular at low redshifts, and improve the accuracy of the photometric redshift estimates. For these reasons, we proposed to reprocess this data to correct for the spatial variability of the PSFs. We used the individual exposures and rescaled the images to the target astrometry. Then, I homogenized the PSFs in every single exposure file, applying the same method as for the other bands (see previous paragraph). The only difference was the necessity to automatically identify the stars in the magnitude versus size diagrams, because of the large number of images to process. The radius thresholds, previously set by hand based on visual inspection, were defined based on the typical radius of the stellar sequence, computed using a sigma-clipped median. At last, the PSF-homogenized exposure images were stacked.

3.4.5. Star-galaxy separation

The separation between stars and galaxies may be performed through observed photometry, colors and morphology. One of the methods to identify stars uses the significance from the SED-fitting (see Chapter 2). For COSMOS2020, I built an updated library of stellar templates for `LePhare`, using the brown dwarf templates used in Kauffmann et al. 2020 and derived from theoretical models. The templates with irrelevant sets of physical parameters were rejected, based on the constraints from Saumon et al. 2008. Figure 3.4 represents the distribution of effective temperature T_{eff} and surface gravity $\log g$ of simulated brown dwarf populations. The rejected templates mostly have either cold temperatures ($T_{\text{eff}} < 1000\,\text{K}$) with large surface gravity ($\log g > 5$), or low surface gravity ($\log g < 4$).

3.5. Article

The article below presents the COSMOS2020 catalog. All the imaging data are presented, including the data reduction pipelines and quality assessments. The two photometric catalogs are described, and the resulting photometry rigorously compared. Using both catalogs, the physical parameters (redshift, stellar mass, absolute magnitudes and colors) are estimated using `LePhare` and `EAZY`. In writing this article, I was responsible for the sections related to the aperture photometry in the CLASSIC catalog, and participated to the data description, detection method, SED-fitting procedure, and star-galaxy separation.

Draft version December 23, 2020
Typeset using LATEX **twocolumn** style in AASTeX62

COSMOS2020: A panchromatic view of the Universe to z∼10 from two complementary catalogs

J. R. Weaver,[1,2] O. B. Kauffmann,[3] O. Ilbert,[3] H. J. McCracken,[4] A. Moneti,[4] S. Toft,[1,2] G. Brammer,[1,2] M. Shuntov,[4] I. Davidzon,[1,2] B. C. Hsieh,[5] C. Laigle,[4] A. Anastasiou,[1,2] C. K. Jespersen,[1,2] J. Vinther,[1,2] P. Capak,[1] C. M. Casey,[6] B. Milvang-Jensen,[1,2] B. Mobasher,[7] D. B. Sanders,[8] S. Arnouts,[3] H. Aussel,[9] J. S. Dunlop,[10] A. Faisst,[11] M. Franx,[12] L. J. Furtak,[4] J. P. U. Fynbo,[1,2] T. Greve,[1,13] S. Gwyn,[14] J. S. Kartaltepe,[15] D. Kashino,[16,17] V. Kokorev,[1,2] O. Le Fèvre,[3] S. Lilly,[16] D. Masters,[18,11,*] G. Magdis,[1,13,2,19] V. Mehta,[20] Y. Peng,[21] D. A. Riechers,[22] M. Salvato,[23] M. Sawicki,[24,†] C. Scarlata,[20] N. Scoville,[25] R. Shirley,[26,27] A. Sneppen,[1,2] V. Smolčić,[28] C. Steinhardt,[1,2] D. Stern,[18] M. Tanaka,[29,30] Y. Taniguchi,[31] H. I. Teplitz,[11] M. Vaccari,[32] W.-H. Wang,[33] L. Zalesky,[8] and G. Zamorani[34]

[1]Cosmic Dawn Center (DAWN)
[2]Niels Bohr Institute, University of Copenhagen, Jagtvej 128, 2200 Copenhagen, Denmark
[3]Aix Marseille Univ, CNRS, LAM, Laboratoire d'Astrophysique de Marseille, Marseille, France
[4]Institut d'Astrophysique de Paris, UMR 7095, CNRS, and Sorbonne Université, 98 bis boulevard Arago, 75014 Paris, France
[5]nstitute of Astrophysics & Astronomy, Academia Sinica, Taipei 10617, Taiwan
[6]The University of Texas at Austin 2515 Speedway Blvd Stop C1400 Austin, TX 78712 USA
[7]Department of Physics and Astronomy, University of California, Riverside, 900 University Avenue, Riverside, CA 92521, USA
[8]Institute for Astronomy, University of Hawaii, 2680 Woodlawn Drive, Honolulu, HI 96822, USA
[9]AIM UMR 7158, CEA, CNRS, Université Paris-Saclay, Université Paris Diderot, Sorbonne Paris Cité, F-91191 Gif-sur-Yvette, France
[10]Institute for Astronomy, University of Edinburgh, Royal Observatory, Edinburgh, EH9 3HJ, UK
[11]Infrared Processing and Analysis Center, California Institute of Technology, 1200 E. California Blvd, Pasadena, CA, 91125, USA
[12]Leiden Observatory, Leiden University, P.O.Box 9513, NL-2300 AA Leiden, The Netherlands
[13] DTU-Space, Technical University of Denmark, Elektrovej 327, DK2800 Kgs. Lyngby, Denmark
[14]Herzberg Astronomy and Astrophysics, National Research Council of Canada, 5071 West Saanich Rd., Victoria, BC V9E 2E7, Canada
[15]School of Physics and Astronomy, Institute of Technology, 84 Lomb Memorial Drive, Rochester, NY 14623, USA
[16]Department of Physics, ETH Zürich, Wolfgang-Pauli-Strasse 27, 8093 Zurich, Switzerland
[17]Institute for Advanced Research, Nagoya University, Furocho, Chikusa, Nagoya, Aichi, 464-8602, Japan
[18]Jet Propulsion Laboratory, California Institute of Technology 4800 Oak Grove Drive Pasadena, CA 91109, USA
[19]Institute for Astronomy, Astrophysics, Space Applications and Remote Sensing, National Observatory of Athens, GR-15236 Athens, Greece
[20]Minnesota Institute for Astrophysics, University of Minnesota, 116 Church St SE, Minneapolis, MN 55455, USA
[21]Kavli Institute for Astronomy and Astrophysics, Peking University, 5 Yiheyuan Road, Beijing 100871, China
[22]Department of Astronomy, Cornell University, Space Sciences Building, Ithaca, NY 14853, USA
[23]Max-Planck-Institut für extraterrestrische Physik, Giessenbachstrasse, D-85748 Garching, Germany
[24]Department of Astronomy & Physics and the Institute for Computational Astrophysics, Saint Mary's University, 923 Robie Street, Halifax, Nova Scotia, B3H 3C3, Canada
[25]California Institute of Technology, 1200 E. California Boulevard, Pasadena, CA, 91125, USA
[26]Astronomy Centre, Department of Physics & Astronomy, University of Southampton, Southampton, SO17 1BJ, UK
[27]Institute of Astronomy, University of Cambridge, Madingley Road, Cambridge CB3 0HA, UK
[28]Department of Physics, Faculty of Science, University of Zagreb, Bijenička cesta 32, 10000 Zagreb, Croatia
[29]National Astronomical Observatory of Japan, 2-21-1 Osawa, Mitaka, Tokyo 181-8588, Japan
[30]Department of Astronomical Science, The Graduate University for Advanced Studies, SOKENDAI, Mitaka, Tokyo, 181-8588, Japan
[31]The Open University of Japan, 2-11, Wakaba, Mihama-ku, Chiba 261-8586, Japan
[32]Inter-university Institute for Data Intensive Astronomy, Department of Physics and Astronomy, University of the Western Cape, Robert Sobukwe Road, 7535 Bellville, Cape Town, South Africa
[33]Institute of Astrophysics & Astronomy, Academia Sinica, Taipei 10617, Taiwan
[34]Istituto Nazionale di Astrofisica - Osservatorio di Astrofisica e Scienza dello Spazio, via Gobetti 93/3, I-40129, Bologna, Italy

(Received December 23, 2020; Revised December 23, 2020; Accepted December 23, 2020)

Corresponding author: John R. Weaver
john.weaver@nbi.ku.dk

Submitted to ApJS

ABSTRACT

The Cosmic Evolution Survey (COSMOS) has become a cornerstone in extragalactic astronomy. Since the last public catalog in 2015, a wealth of new imaging and spectroscopic data has been collected in the COSMOS field. This paper describes the collection, processing, and analysis of the new imaging data to produce a new reference photometric redshift catalog. Source detection and multi-waveband photometry is performed for 1.7 million sources across the $2\,\mathrm{deg}^2$ of the COSMOS field, $\sim$890 000 of which are measured with all available broadband data, using both traditional aperture photometric methods and a new profile-fitting photometric extraction tool `The Farmer` which this team has developed. The two resulting photometric catalogs are compared. Photometric redshifts are computed for all sources in each catalog utilizing two independently developed photometric redshift codes. Finally, a comparison is made between the performance of the photometric methodologies and of the redshift codes to demonstrate an exceptional degree of self-consistency in the resulting photometric redshifts. The $i < 21$ sources have sub-percent photometric redshift accuracy and even the faintest sources at $25 < i < 27$ reach a precision of 5 %. Finally, these results are discussed in the context of previous, current, and future surveys in the COSMOS field. Both photometric catalogs and their photometric redshift solutions and physical parameters will be made available through the usual astronomical archive systems (CDS, ESO Phase 3, IRSA).

Keywords: catalogs — galaxies: evolution — galaxies: high-redshift — galaxies: photometry – methods: observational — techniques: photometric

1. INTRODUCTION

Photometric surveys are an essential component of modern astrophysics. The first surveys of the sky with photographic plates (Bigourdan 1888) permitted a quantitative understanding of our Universe; longer exposures on increasingly larger telescopes led to the first accurate understanding of the true size and scale of our Universe (Hubble 1934). Recent breakthroughs have been enabled by wide-field cameras capable of covering several square degrees at a time becoming available (such as MegaCam, Boulade et al. 2003), coupled with wide-field spectroscopic instruments capable of collecting large numbers of spectroscopic redshifts like the Visible Multi-Object Spectrograph (VIMOS; Le Fèvre et al. 2003) and the Multi-Object Spectrograph For Infrared Exploration (MOSFIRE; McLean et al. 2012).

The launch of the Hubble Space Telescope (HST) led to the first Hubble Deep Field catalog (HDF; Williams et al. 1996) which, although limited to an area of $3\,\mathrm{arcmin}^2$ in four optical bands to 28 AB depth, revealed the morphological complexity of the distant Universe. This first step gave way to an explosion of data from similar surveys (see Madau & Dickinson 2014, and references therein). The installation of the Advanced Camera for Surveys (ACS) on HST led to a dramatic increase in the field-of-view and sensitivity of optical observations from space. This advancement laid the groundwork for the Great Observatories Origins Deep Survey (GOODS; Giavalisco et al. 2004) which captured multi-band ACS observations over two 16×10 arcmin fields to depths in excess of 29 AB – GOODS-North and GOODS-South. These observations provided crucial information about the nature of high-redshift galaxies, their rest-frame properties, and helped guide the development of methods to select different classes of objects. Although deep ground-based near-infrared imaging achieved notable successes (e.g., FIRESurvey; Labbé et al. 2003), the installation of the near-infrared camera WFC3 on HST in 2012 expanded our ability to probe the distant Universe allowing, for the first time, spatially-resolved measurements of rest-frame optical light at early cosmic times, to depths unreachable from ground-based facilities because of the high infrared sky background. The eventual combination of ACS and WFC3 was then used to capture the deepest image ever taken of the Universe – the Hubble Ultra Deep Field (HUDF; Beckwith et al. 2006) – in seven bands over an area of $10\,\mathrm{arcmin}^2$. Together with ground-based spectroscopy, it was then possible to confirm some of the most distant galaxies which likely contributed to the reionization of the Universe (e.g., Robertson et al. 2013; Ishigaki et al. 2018). However, the transformative power of these forerunner observations was limited by their small area which complicated the detection of and statistical inferences about

[*] NASA Postdoctoral Program (NPP) Fellow
[†] Canada Research Chair

rare high-redshift populations due to cosmic variance. The Cosmic Assembly Near-infrared Deep Extragalactic Legacy Survey (CANDELS; Dahlen et al. 2013; Grogin et al. 2011; Koekemoer et al. 2011) placed observations over five different fields to combat cosmic variance, complemented by unprecedented depth and seven HS bands, and enabled precise measurements of the physical parameters of galaxies over cosmic time. Despite these significant advantages and the groundbreaking science they allowed, their individual areas still proved too small to effectively combat cosmic variance to the extent required to probe large numbers of galaxies at high-redshift.

The Cosmic Evolution Survey (COSMOS; Scoville et al. 2007) began in 2006 with a $1.8\,\mathrm{deg}^2$ mosaic with HS/ACS, reaching a depth of 27.2 AB in the F814W band (Scoville et al. 2007). This was the largest single allocation of HST orbits at the time and remains the largest contiguous area ever mapped with HST. Since then the field has been covered with deep observations by virtually all major extragalactic astronomical facilities.

As one of the five CANDELS fields, 3 % of the COSMOS area has been covered by HST/WFC3 F475W, F606W, F125W and F160W bands. Ground-based broad- and narrow-band observations with Subaru Suprime-Cam were some of the first to be performed over the entire area in 2006, providing one of the largest imaging data sets available at that time (Capak et al. 2007). Mid-infrared observations of the entire COSMOS field were also taken using the Spitzer Space Telescope (Sanders et al. 2007).

The key to exploiting these multi-wavelength data sets has been 'photometric redshift' estimation (hereafter photo-z), in which template spectral energy distributions are fit to photometry to estimate distances and physical parameters of galaxies (see Salvato et al. 2019, for a review). This has enabled the construction of large statistical samples of galaxies with well-characterised photometric redshifts calibrated to subsets of galaxies with accurate spectroscopic redshifts. COSMOS has been a benchmark testing ground for photo-z measurement techniques, due to its unrivaled multi-wavelength imaging data and thousands of measured spectroscopic redshifts.

Over the years, several COSMOS photometric catalogs have been publicly released (Capak et al. 2007; Ilbert et al. 2009; Ilbert et al. 2013; Muzzin et al. 2013; Laigle et al. 2016). Each of these releases followed new availability of progressively deeper data, such as the intermediate-band Subaru/Suprime-Cam data (Taniguchi et al. 2015) and the VISTA near-infrared coverage (McCracken et al. 2012; Milvang-Jensen et al. 2013). The most recent release, COSMOS2015 (Laigle et al. 2016), contains half a million galaxies detected in the combined $zYJHK_s$ images from the Subaru and VISTA telescopes. Four ultra-deep stripes in VISTA and Spitzer, although non-uniform, cover a total area of $0.62\,\mathrm{deg}^2$ (e.g., Ashby et al. 2018). Photometric redshifts computed with a template-fitting method reach a sub-percent precision at $i < 22.5$. This methodology was applied also to the Subaru-XMM Deep Field (Mehta et al. 2018), the only other deep degree-scale field to feature similarly deep near- and mid-infrared coverage.

For more than a decade the COSMOS field has occupied an outstanding position in the modern landscape of deep surveys, and has been relied upon to address fundamental scientific questions about our Universe. The $2\,\mathrm{deg}^2$ of COSMOS has been used to trace large-scale structure (Scoville et al. 2013; Laigle et al. 2018), discover groups and clusters (e.g., Capak et al. 2011; Casey et al. 2015; Hung et al. 2016; Cucciati et al. 2018), and link galaxies to their dark matter halos (e.g., Leauthaud et al. 2007; McCracken et al. 2015; Legrand et al. 2019). The COSMOS photo-z distribution is used as reference to establish the true redshift distribution in redshift slices in the Dark Energy Survey (DES; Troxel et al. 2018), a crucial component when estimating cosmological parameters with weak lensing (e.g., Mandelbaum 2018). COSMOS demonstrated feasibility of combining space-based shape measurements with ground-based photometric redshifts to map the spatial distribution of dark matter (Massey et al. 2007), a method which will be used by the *Euclid* mission (Laureijs et al. 2011). Already COSMOS is being used to prepare essential spectroscopic observations for the mission (Masters et al. 2019) and to study biases in shape analyses. The COSMOS photometric data are used to predict the quality of *Euclid* photo-z (Duprez et al., in prep.), as well as the number of [O II] and Hα emitters expected for future dark energy surveys (Saito et al. 2020). Hence, the photometric catalogs created in COSMOS play a crucial role in cosmic shear surveys (Albrecht et al. 2006).

The combination of its depth in the visible and near-infrared, and the wide area covered, makes COSMOS ideal for identifying the largest statistical samples of the rarest, brightest, and most massive galaxies, such as ultra massive quiescent galaxies to $z \sim 4$ (e.g., Stockmann et al. 2020; Schreiber et al. 2018; Valentino et al. 2020), as well as extremely luminous $z \sim 5-6$ starbursts (e.g., Riechers et al. 2010, 2014, 2020; Pavesi et al. 2018; Casey et al. 2019), quasars (e.g., Prescott et al. 2006; Heintz et al. 2016), and UV-bright star-forming galaxies at $6 < z < 10$ (e.g., Caputi et al. 2015; Stefanon et al. 2019; Bowler et al. 2020). With rich multi-wavelength coverage at all accessible wavelengths from the X-ray (Civano et al. 2016) to the radio (Smolčić et al. 2017), an accurate picture of the galaxy stellar mass assembly was established with this data set, including numerous estimates of the galaxy stellar mass function (e.g., Ilbert et al. 2013; Muzzin et al. 2013; Davidzon et al. 2017), star formation rate density (e.g., Gruppioni et al. 2013; Novak et al. 2017), mass and star formation rate relation (Karim et al. 2011; Rodighiero et al. 2011; Ilbert et al. 2015; Lee et al. 2015; Leslie et al. 2020), and star formation quenching (e.g., Peng et al. 2010). A large number of follow-up programs have been conducted, including extensive spectroscopic coverage (e.g., Lilly et al. 2007; Le Fèvre et al. 2015; van der Wel et al. 2016; Hasinger et al. 2018), integral field spectroscopy (e.g., Förster Schreiber et al. 2009), and ALMA observations (Scoville et al. 2017; Le Fèvre et al. 2019).

This paper presents 'COSMOS2020', the latest release of the COSMOS catalog. The principal additions comprise new ultra-deep optical data from the Hyper Suprime-Cam (HSC) Subaru Strategic Program (SSP) PDR2 (SSP; Aihara et al. 2019), new Visible Infrared Survey Telescope for Astronomy (VISTA) data from DR4 reaching at least one magnitude deeper in the K_s-band over the full area, and the inclusion of all Spitzer IRAC data ever taken in COSMOS. Legacy data sets (such as the Suprime-Cam imaging) have also been reprocessed. All imaging data is now aligned with Gaia: DR1 (Gaia Collaboration et al. 2016) for the optical and near-infrared data and DR2 (Gaia Collaboration et al. 2018) for the U-bands and IRAC data (see Moneti et al., in prep). This is reflected in band-to-band astrometric precision much improved compared to Laigle et al. (2016). Taken together, these additions result in a doubling of the number of detected sources and an overall increase in photometric homogeneity of the full data set.

This release features an alternative profile-fitting method to extract photometry, in addition to the traditional aperture-based technique. Previous COSMOS catalogs were created with `SExtractor` (Bertin & Arnouts 1996), wherein each image is first homogenized to a common 'target' point-spread function (PSF). Fluxes are then extracted within circular apertures (Capak et al. 2007; Ilbert et al. 2009; Laigle et al. 2016). While this approach is widely applied in the literature (e.g., Hildebrandt et al. 2012), other approaches avoid this homogenization process in order to preserve the structure of images. The most common alternative is prior-based techniques (e.g., De Santis et al. 2007; Laidler et al. 2007; Merlin et al. 2016) which use the highest resolution image as a prior, convolve it with the corresponding PSF of the lower resolution images and utilize the normalization of the PSF convolved prior image to estimate the flux in the lower resolution images. Such an approach was instrumental to extract Spitzer/IRAC photometry in the CANDELS catalogs. Recently, `The Tractor` (Lang et al. 2016) has been developed to perform profile-fitting photometry. Instead of a prior cut from a high resolution image (e.g., HST), `The Tractor` derives entirely parametric models from one or more images containing some degree of morphological information. This has two immediate advantages in that `The Tractor` does not require an high resolution image from HST and can hence be readily and consistently applied to ground-based data sets, nor does it require that all the images are aligned on the same or integer-multiple pixel grid. Because the models are purely parametric, `The Tractor` can provide shape measurements for resolved sources in addition to fluxes. `The Tractor` has already been applied to several deep imaging surveys (Nyland et al. 2017; Dey et al. 2019).

For COSMOS2020, two independent catalogs are created using different techniques. One is created using the same standard method as Laigle et al. (2016) where aperture photometry is performed on PSF-homogenized images, with the exception of IRAC where PSF-fitting with the `IRACLEAN` software (Hsieh et al. 2012) is used. This is the CLASSIC catalog. The other catalog is created with `The Farmer` (Weaver et al., in prep.), a software package which generates a full multi-wavelength catalog utilizing `The Tractor` to perform the modelling. In this sense, `The Farmer` provides broadly reproducible source detection and photometry which `The Tractor`, requiring a custom driving script, cannot do by itself. A detailed comparison of both photometric catalogs and the quality of the photo-z derived from each of them follows. By utilizing these two methods in tandem it is possible too evaluate the reliability of COSMOS2020. This work presents a detailed analysis of the advantages of each method and provide quantitative arguments which could guide photometric extraction choices for future photometric surveys. The most compelling advantage, however, lies not in discriminating between the catalogs but rather in using them constructively to evaluate the significance, accuracy, and precision of scientific results, a feature which has not yet been possible from a single COSMOS catalog release.

The paper is organized as follows. In Section 2, the imaging data set and the data reduction are presented. Section 3 describes the source extraction and photometry. The photometry from the two photometric catalogs are compared in Section 4. Section 5 presents the photometric redshift measurements. In Section 6, the physical parameters of the sources in the catalog are presented. Section 7 presents our summary and conclusions.

A standard ΛCDM cosmology with $H_0 = 70\,\mathrm{km\,s^{-1}\,Mpc^{-1}}$, $\Omega_\mathrm{m} = 0.3$ and $\Omega_\Lambda = 0.7$ is adopted throughout this work. All magnitudes are expressed in the AB system (Oke 1974).

2. OBSERVATIONS AND DATA REDUCTION

2.1. *Overview of included data*

The principal improvements in COSMOS2020 compared to previous catalogues are much deeper HSC optical images and deeper near-infrared images from UltraVISTA. In addition, this release contains the definitive reprocessing of all Spitzer data ever taken on COSMOS. 'Legacy' or pre-existing data sets present in COSMOS2015 were reprocessed to take advantaged of improved astrometry from Gaia (the only exceptions being external ancillary data such as GALEX). All the images are sampled to a 0$''$.15 pixel scale.

Figure 1 illustrates the footprint of the observations in the COSMOS field. Complete details of included data are listed in Table 1. Figure 2 shows the filter transmission curves. Figure 3 indicates the depths of the photometric data and provides a comparison with the COSMOS2015 depths. The depth computations are explained in Section 3.1.3 and follow largely the methods in Laigle et al. (2016). As in previous releases, in each band the image and the corresponding weight-map is resampled on the same tangent point using `SWarp` (Bertin et al. 2002). These images will be made publicly available through the COSMOS website at the NASA/IPAC Infrared Science Archive (IRSA) [1].

2.2. *U-band data*

Many previous programs have observed the COSMOS field in U-band using the Canada-France-Hawaii telescope (CFHT) and the MegaCam instrument, the most efficient wide-field U-band instrument. For COSMOS2020, all archival MegaCam COSMOS U data are recombined in addition to new data taken as part of the CFHT Large Area U-band Deep Survey (CLAUDS), which use a new bluer u filter (Sawicki et al. 2019). The old filter, noted u^*, corresponds to the u-band used in Laigle et al. (2016). The depths[2] of the u and the u^* images are reported in Table 1. The main motivations in reprocessing these data is to make deeper U-band images for the field, make use of the new improved Gaia

[1] https://irsa.ipac.caltech.edu/Missions/cosmos.html

[2] The reported u^*-band depth is deeper than COSMOS2015 because this work averages over the UltraVISTA layout, compared to the entire field in Laigle et al. (2016).

Table 1. Summary of UV-optical-IR data used in the catalogs

Instrument /Telescope (Survey)	Band	Central[a] λ [Å]	Width[b] [Å]	Depth[c] ($2''/3''$) ±0.1	Error Fact.[d] ($2''/3''$) ±0.1
GALEX	FUV	1526	224	...	...
	NUV	2307	791	25.5[e]	...
MegaCam	u	3709	518	27.8/27.2	1.7/2.0
/CFHT	u^*	3858	598	27.7/27.1	1.4/1.6
ACS/*HST*	F814W	7890	1373	26.5[f]	...
HSC	g	4847	1383	28.1/27.5	1.4/1.8
/Subaru	r	6219	1547	27.8/27.2	1.4/1.7
HSC-SSP	i	7699	1471	27.6/27.0	1.5/1.9
PDR2	z	8894	766	27.2/26.6	1.4/1.7
	y	9761	786	26.5/25.9	1.4/1.7
Suprime-Cam	B	4488	892	27.8/27.1	1.5/1.8
/Subaru	g^+	4804	1265	26.1/25.6	5.5/5.8
	V	5487	954	26.8/26.2	2.1/2.3
	r^+	6305	1376	27.1/26.5	1.6/1.9
	i^+	7693	1497	26.7/26.1	1.5/1.8
	z^+	8978	847	25.7/25.1	1.5/1.7
	z^{++}	9063	1335	26.3/25.7	2.3/2.6
	$IB427$	4266	207	26.1/25.6	2.0/2.2
	$IB464$	4635	218	25.6/25.1	3.1/3.3
	$IA484$	4851	229	26.5/25.9	1.5/1.7
	$IB505$	5064	231	26.1/25.6	1.6/1.8
	$IA527$	5261	243	26.4/25.8	1.7/2.0
	$IB574$	5766	273	25.8/25.3	2.4/2.5
	$IA624$	6232	300	26.4/25.7	1.4/1.7
	$IA679$	6780	336	25.6/25.1	2.5/2.7
	$IB709$	7073	316	25.9/25.4	2.2/2.3
	$IA738$	7361	324	26.1/25.5	1.5/1.7
	$IA767$	7694	365	25.6/25.1	2.1/2.2
	$IB827$	8243	343	25.6/25.1	2.4/2.6
	$NB711$	7121	72	25.5/24.9	1.2/1.4
	$NB816$	8150	120	25.6/25.1	2.3/2.5
VIRCAM	Y^{UD}	10216	923	26.6/26.1	2.8/3.1
/VISTA	Y^{Deep}			25.3/24.8	2.7/2.8
UltraVISTA	J^{UD}	12525	1718	26.4/25.9	2.7/2.9
DR4	J^{Deep}			25.2/24.7	2.5/2.7
	H^{UD}	16466	2905	26.1/25.5	2.6/2.9
	H^{Deep}			24.9/24.4	2.4/2.6
	K_s^{UD}	21557	3074	25.7/25.2	2.4/2.6
	K_s^{Deep}			25.3/24.8	2.4/2.6
	$NB118$	11909	112	24.8/24.3	2.8/2.9
IRAC	ch1	35686	7443	26.4/25.7	...
/*Spitzer*	ch2	45067	10119	26.3/25.6	...
	ch3	57788	14082	23.2/22.6	...
	ch4	79958	28796	23.1/22.5	...

[a] Median of the transmission curve.
[b] Full width of the transmission curve at half maximum.
[c] Depth at 3σ computed on PSF-homogenized images (except for IRAC images) in empty apertures with the given diameter.
[d] Multiplicative correction factor for photometric flux uncertainties in the Classic catalog, computed over the UltraVISTA layout (see Section 3.1.3).
[e] Depth at 3σ given in Zamojski et al. (2007).
[f] Depth given in Leauthaud et al. (2007).

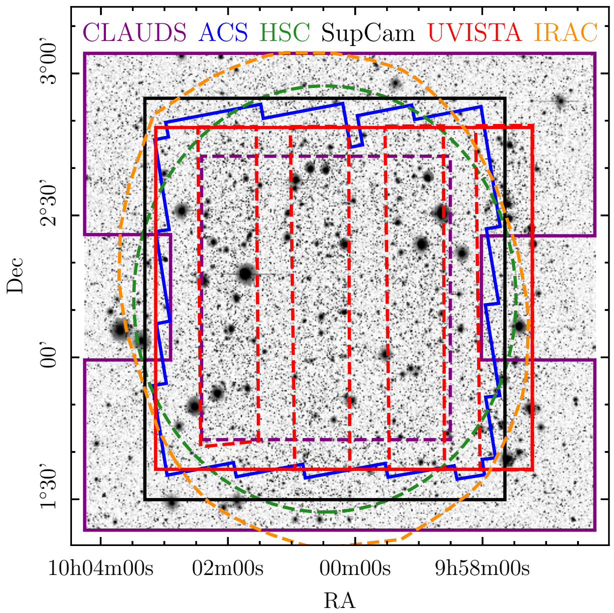

Figure 1. Schematic of the COSMOS field. The background image corresponds to the $izYJHK_s$ detection image. The solid lines represent survey limits, and the dashed lines indicate the deepest regions of the images. In the case of UltraVISTA, the dashed lines illustrate the 'ultra-deep' stripes. In the case of CLAUDS, the solid line shows the limit of the u-band image and the dashed line shows the deepest region of the u^*-band image.

astrometric reference, and resample each individual image onto the same COSMOS tangent point.

Starting with the complete data set in both filters, these data were pre-processed by the *Elixir* pipeline (Magnier & Cuillandre 2004) at the CFHT before being ingested into the Canadian Astronomy Data Center, where the astrometric and photometric calibrations are recomputed using the image stacking pipeline *MegaPipe* (Gwyn 2008). Images with sky fluxes above $\log10(\mathrm{ADU/sec}) > -0.1$ were rejected. The images were visually inspected and images with obvious flaws (bad tracking, bad seeing) were rejected. Several images were rejected during the calibration stage. A re-inspection of these images revealed that they had seeing worse than $1.4''$; they were also rejected. In total, there were 649 u^* images and 500 u images. The median seeing of this final sample is $0\farcs9$. The two final stacked images were resampled onto the COSMOS tangent point and pixel scale and combined using a weighted 2.8 sigma clipping. The astrometric calibration used the Gaia DR2 reference catalog (Gaia Collaboration et al. 2018). The final images have an absolute astrometric uncertainty of 20 mas. The u-band calibration has been improved over earlier versions by carefully mapping the zeropoint variation across the mosaic for each observing run. While the Sloan Digital Sky Survey (SDSS) is used as the photometric reference, it is not used as in-field standards, to avoid propagating any local errors in the SDSS u-band calibration into our work. Instead, zeropoints are computed per night using all available images. Images taken on photometric nights were used to calibrate data taken in non-photometric conditions (see Section 3 of Sawicki et al. 2019 for more details). In summary, both u and u^* images have equivalent depths; however the newer u images do not cover the entire COSMOS field but have two gaps at the left and right middle edges of the field (Figure 1).

2.3. *Optical data*

Wide-field optical data have played a key role in measuring COSMOS photometric redshifts. The commissioning of Subaru's 1.8 deg^2 Hyper Suprime-Cam (HSC; Miyazaki et al. 2018) instrument has enabled more efficient and much deeper broad-band photometric measurements over the entire COSMOS area. HSC/y data were already included in Laigle et al. (2016). For COSMOS2020, this work uses the second public data release (PDR2) of the HSC Subaru Strategic Program (HSC-SSP) comprising the g, r, i, z, y bands (Aihara et al. 2019).

The public stacks in COSMOS suffer from scattered light from the presence of bright stars in the field and the small dithers used. These are not removed at the image combination stage. Therefore all the individual, calibrated pre-warp CCD images (*calexp* data) from the SSP public server are processed. These images were recombined with `SWarp` using `COMBINE_TYPE` set to `CLIPPED` with a 2.8σ threshold (see Gruen et al. 2014 for details). This removes a large fraction of the scattered light and satellite trails. As for the other data, images are centered on the COSMOS tangent point with a $0\farcs15$ pixel scale. The Gaia DR1 astrometric solution computed by the HSC-SSP team which agrees well with the solutions used here in other bands.

Finally, the Subaru Suprime-Cam data used in COSMOS2015 are retained for this work (Taniguchi et al. 2007, 2015), including 7 broad bands (B, g^+, V, r^+, i^+, z^+, z^{++}), 12 medium bands ($IB427$, $IB464$, $IA484$, $IB505$, $IA527$, $IB574$, $IA624$, $IA679$, $IB709$, $IA738$, $IA767$, $IB827$), and two narrow bands ($NB711$, $NB816$). However, because the COSMOS2015 stacks had been computed with the old COSMOS astrometric reference, it was necessary to return to the individual images and recompute a new astrometric solution using Gaia DR1 with `Scamp` (Bertin 2006). The opportunity was taken

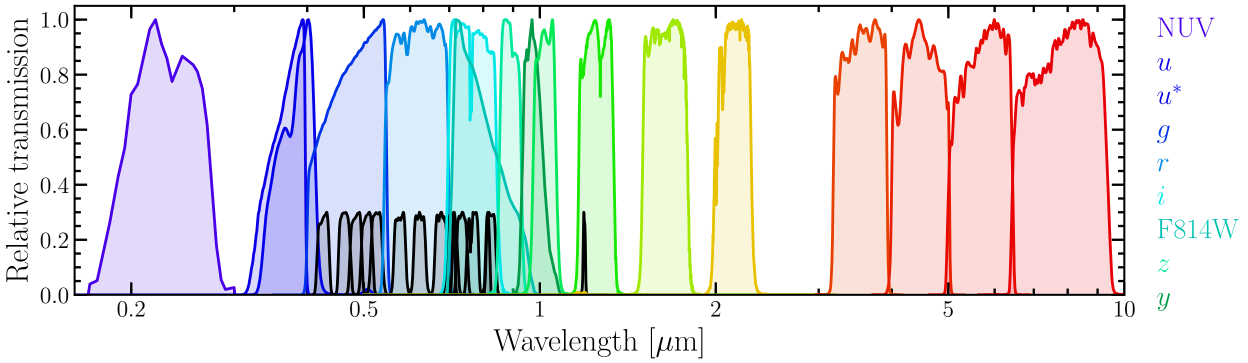

Figure 2. Relative transmission curves for the photometric bands used. The effect of atmosphere, telescope, camera optics, filter, and detector are included. The black curves represent medium and narrow bands. The profiles are normalized to one for the broad bands, and to 0.3 for the medium and narrow bands.

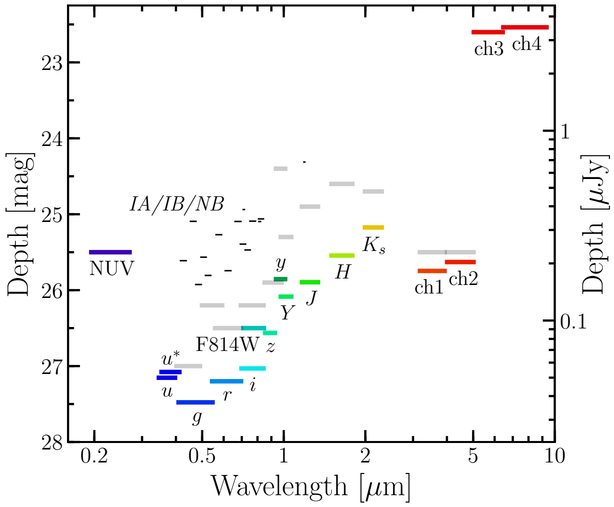

Figure 3. Depths at 3σ measured in empty $3''$ diameter apertures in PSF-homogenized images, except for NUV and IRAC images. The NUV depth is from Zamojski et al. (2007) and the F814W depth from Leauthaud et al. (2007). For the Y, J, H, K_s bands, the depths in the ultra-deep regions are indicated. The length of each segment is the FWHM of the filter transmission curve. The thin black segments show the depths of the medium and narrow bands. The grey segments indicate the depths of the images used in Laigle et al. (2016) for comparison.

to perform a tile-level PSF homogenization on the individual images. (see Section 3.1.2).

2.4. *Near-infrared data*

The $YJHK_s$ broad-band and $NB118$ narrow-band data from the fourth data release[3] (DR4) of the UltraVISTA survey (McCracken et al. 2012) are used. This release includes the images taken from December 2009 to June 2016 with the VIRCAM instrument on the VISTA telescope. Compared to DR2, the images are up to 0.8 mag deeper in the ultra-deep stripes (for the J and H bands), and 1 mag in the deep stripes (for the K_s band). The additional $NB118$ narrow-band image only covers the ultra-deep region. Characterisation of the $NB118$ filter is in Milvang-Jensen et al. (2013). Only the publicly available stacks are used.

2.5. *Mid-infrared data*

The infrared data comprise Spitzer/IRAC channel 1,2,3,4 images from the Cosmic Dawn Survey (Moneti et al., in prep.). This consists of all IRAC data taken in the COSMOS field up to the end of the mission in January 2020. This includes the Spitzer Extended Deep Survey (SEDS; Ashby et al. 2013), the Spitzer Large Area Survey with Hyper Suprime-Cam (SPLASH; Steinhardt et al. 2014), the Spitzer-Cosmic Assembly Deep Near-infrared Extragalactic Legacy Survey (S-CANDELS; Ashby et al. 2015), and the Spitzer Matching Survey of the UltraVISTA ultra-deep Stripes survey (SMUVS; Ashby et al. 2018). The resulting images have a $0\farcs6$ pixel scale, and are resampled to the $0\farcs15$ pixel scale of the optical and near-infrared images. The astrometric calibration used the Gaia DR2 reference. This work adopts the processed mosaics with stellar sources removed. Full details of this processing is given in Moneti et al. (in prep.).

2.6. *X-ray, ultraviolet, radio, and sub-mm data*

The COSMOS2020 catalog is matched with ancillary photometric catalogs using positional cross-matching within a radius of $0\farcs6$, where unambiguous matches can be made. The X-ray photometry from the *Chandra* COSMOS Legacy survey (Civano et al. 2016; Marchesi et al. 2016) are used. Also included are the near-UV ($0.23\,\mu$m) and far-UV ($0.15\,\mu$m) observations from the COSMOS GALEX catalog (Zamojski et al. 2007).

[3] http://ultravista.org/release4/dr4_release.pdf

The *HST*/ACS F814W high-resolution photometry from Leauthaud et al. (2007) covering 1.64 $\deg^2$ of the COSMOS field[4] are included, as well as morphological parameters. Only clean (unblended) sources from that catalog are kept.

Included also is the far-infrared to millimeter photometry from the COSMOS Super-deblended catalog (Jin et al. 2018), including *Spitzer*/MIPS (24 μm), *Herschel*/PACS (100, 160 μm) and SPIRE (250, 350, 500 μm), JCMT/SCUBA2 (850 μm), ASTE/AzTEC (1.1 mm), IRAM/MAMBO (1.2 mm) and VLA (1.4, 3 GHz). This catalog used the COSMOS2015 coordinates as a prior. Sources with unclean deblending are not inccluded based on the 'goodArea' flag.

2.7. *Masking*

Photometric extraction of sources can be significantly affected by the spurious flux of nearby bright stars, galaxies, and various other artefacts in the images. Thus, it is of interest to mark these sources. For this purpose, the COSMOS2020 catalog provides flags for objects in the vicinity of bright stars, and for objects affected by various artefacts.

The bright-star mask from the HSC-SSP PDR2 (Coupon et al. 2018) are used to flag these sources. In particular, masks are taken from the Incremental Data Release 1 revised bright-star masks that uses Gaia DR2 as a reference star catalog, where stars brighter than $G = 18$ mag are masked. About 18 % of sources in the catalog are masked as being in the vicinity of bright stars. Furthermore, artifacts in the Suprime-Cam images are masked using the same masks as in COSMOS2015.

Finally, masks for the UltraVISTA deep and ultra-deep regions are provided as shown in Figure 1.

2.8. *Astrometry*

The astrometry in the previous COSMOS catalogs was based on radio interferometric data. However, with the advent of Gaia, a new, highly precise astrometric reference is available. For all data described here, astrometric solutions were computed using Gaia data. In the case where data presented in previous papers is included, the astrometric solutions were recomputed and data resampled. The UltraVISTA, HSC, and the reprocessed Suprime-Cam images were calibrated using the Gaia DR1 astrometric reference (Gaia Collaboration et al. 2016). Figure 4 shows the difference in position between sources in the classic catalog with HSC i-band total magnitudes between 14 and 19 magnitudes and sources in Gaia DR2. The agreement with the reference catalog is excellent, with a standard deviation in both axes of $\sim$ 10 mas and an offset of $\sim$ 1 mas, much better than any previous COSMOS catalog. Furthermore, there are no systematic trends of these offsets in either right ascension or declination over the entire field, unlike previous catalogues. (It is also worth noting that this improved astrometric precision consequently enables photometric measurements in smaller apertures for faint, unresolved sources.)

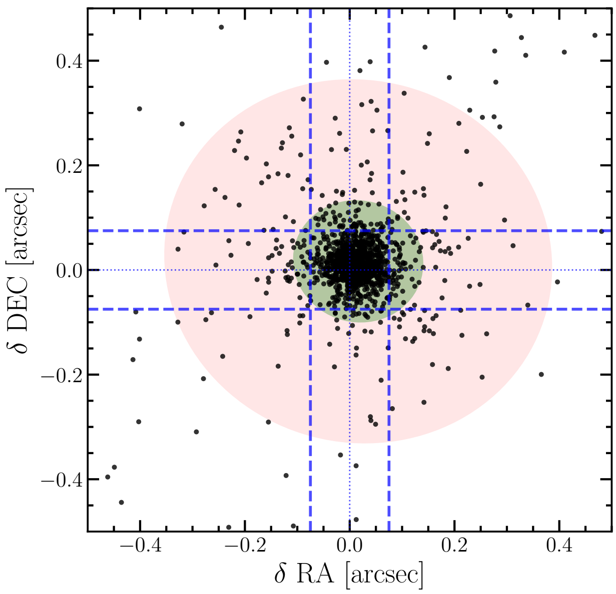

Figure 4. Coordinate offset between sources in the Gaia DR1 catalog and sources extracted in the combined detection image. The spacing between the dashed lines corresponds to the linear dimension of a pixel in the resampled images. Light and dark shaded regions are ellipses containing 68 % and 99 % of all sources respectively. For clarity, only one in ten sources are plotted.

2.9. *Spectroscopic data*

The spectroscopic data are collected from several spectroscopic surveys, conducted with different target selection criteria and instruments. Within this paper, the spec-z are used to evaluate the accuracy of the photo-z. Therefore, this work only includes spec-z with the highest confidence level. If the observation of one object is duplicated, only the spec-z associated to the highest confidence level is kept.

Two large programs were conducted at ESO-VLT with the VIMOS instrument (Le Fèvre et al. 2003) to cover the COSMOS field. The zCOSMOS survey (Lilly et al. 2007) gathers 600 h of observation and is split into a bright and a faint component. The zCOSMOS-bright

[4] The ACS observations in the F475W and F606W bands cover about 5 % of the field, so these are not included in the catalog.

surveys targeted 20 000 galaxies selected at $i^* \leq 22.5$, being by construction highly representative of bright sources. The zCOSMOS-faint survey (Kashino et al., in prep) targeted star-forming galaxies selected with $B_J < 25$ and falling within the redshift range $1.5 \lesssim z \lesssim 3$. The VIMOS Ultra Deep Survey (VUDS; Le Fèvre et al. 2015) includes a randomly selected sample of galaxies at $i < 25$, as well as a pre-selected component at $2 < z < 6$. For all these surveys, only the most secure redshifts are included, namely the sources with flag 3 and 4 corresponding to a confidence level above 95 %. Included are 8280, 739 and 944 galaxies from the zCOSMOS-bright, zCOSMOS-faint and VUDS surveys, respectively.

Data from the Complete Calibration of the Color-Redshift Relation Survey (C3R2; Masters et al. 2019) are also added. The galaxies were selected to fill the color space using the self organising map (Kohonen 1982) algorithm. Depending on the expected redshift range, various instruments from the Keck telescopes were used, specifically LRIS, DEIMOS, and MOSFIRE. While this sample of 2056 galaxies is representative in colors, it is not designed to be representative in magnitudes.

A large sample of 4353 galaxies taken at Keck with DEIMOS, with various selections over a large range of wavelengths from the X-ray to the far-infrared and radio (Hasinger et al. 2018) are included. Such diversity of selection is crucial to estimate the quality of the photo-z for specific populations known to provide less robust results (e.g., Casey et al. 2012).

The FMOS near-infrared spectrograph at Subaru enables tests of the photo-z in the redshift range $1.5 < z < 3$ sometimes referred to as the "redshift desert" (Le Fèvre et al. 2013). The sample from Kashino et al. (2019) contains 832 bright star-forming galaxies at $z \sim 1.6$ with stellar masses $\log_{10}(M_{\rm sim}/M_\odot) > 9.5$ following the star-forming main sequence.

Also added are 447 sources observed with MUSE at ESO/VLT (Rosani et al. 2020). The sample includes faint star-forming galaxies at $z < 1.5$ and Lyman alpha emitters at $z > 3$, and can be used to test the photo-z in a magnitude regime as faint as $i > 26$.

Finally, other smaller size samples are added including Darvish et al. (in prep.) and Chu et al. (in prep.) with MOSFIRE, passive galaxies at $z > 1.5$ (Onodera et al. 2012), star-forming galaxies at $0.8 < z < 1.6$ from Comparat et al. (2015). The full compilation of spec-z in the COSMOS field, including the contributing survey programs, is described in Salvato et al. (in prep.).

3. SOURCE DETECTION AND PHOTOMETRY

3.1. *The* Classic *catalog*

3.1.1. *Source Detection*

The "chi-squared" $izYJHK_s$ detection image (Szalay et al. 1999) is created with `SWarp` from the non-homogenized images, combined with the `CHI_MEAN` option. The inclusion of the HSC/i, z-band data increases the catalog completeness for the relatively bluer objects. In particular, the HSC/i-band image is very deep and has excellent seeing of around $0.''6$. Laigle et al. (2016) did not include i-band data in their detection image. The inclusion of the deep i-band in this detection strategy is the main reason for the higher number of sources detected in the COSMOS2020 catalog compared to COSMOS2015, likely driven by small, blue galaxies at low and intermediate redshift. The increased depth of the near-infrared bands also contributes to the greater number of detected sources.

For the Classic catalog, the detection is performed using `SExtractor` (Bertin & Arnouts 1996) with parameters listed in Table 3. The main difference with respect to COSMOS2015 is `DETECT_MINAREA` set to 5 pix instead of 10 pix, which is made possible thanks to the lower number of spurious sources in the detection image compared to COSMOS2015, owing to the addition of the i-band and deeper imaging in general. The number of detected sources reaches 1 720 700 over the whole field, with 790 579 sources in the HSC-unmasked UltraVISTA region.

3.1.2. *Point spread function homogenization*

The procedure to homogenize the PSF in the optical/near-infrared images is similar to the one presented in Laigle et al. (2016). In the first step, `SExtractor` is used to extract a catalog of bright sources. Stars are identified by cross-matching coordinates with point sources in the *HST*/ACS catalog in COSMOS (Koekemoer et al. 2007; Leauthaud et al. 2007). Saturated stars are removed according to the flag maps, and their position in the half-light radius versus apparent magnitude diagram. The PSF is modelled using `PSFEx` (Bertin 2013) with the polar shapelet basis functions (Massey & Refregier 2005). The convolution kernels are computed using `PSFEx`, setting the target PSF as a Moffat profile (Moffat 1969) with parameters $(\theta, \beta) = (0.''8, 2.5)$, where θ is the FWHM and β is the atmospheric scattering coefficient (identical to Laigle et al. 2016). In contrast with Laigle et al. (2016), `PSF_SAMPLING` is set to `1` to fix the kernel pixel scale. The entire images are then convolved with these kernels.

The spatial variability of the PSF across the field for the CLAUDS, HSC and UltraVISTA bands is ignored. However, for the Suprime-Cam medium bands, the resulting impact of the PSF variability on aperture photometry can be as high as 0.1 mag (as discussed in Laigle et al. 2016). Therefore, in this work the psf is homogenized in each Suprime-Cam band per individual exposure. The single exposure files (SEFs) at the original pixel scale of $0\farcs2$ are resampled to the target tangent point with the pixel scale of $0\farcs15$. This removes astrometric distortions before performing the homogenization. The bright object extraction, PSF modelling and kernel computation are done in the same way as for the other images. Stars are identified in the half-light radius versus apparent magnitude diagram, automatically adjusting the radius threshold using sigma clipping. The PSF-homogenized SEFs are finally coadded to build the final stacks. Frames with high sky noise ($> 3.5\times$ the median noise) are rejected, representing 1, 5, 28, 16, and 4 images in the B, g^+, z^+, z^{++}, and $NB816$ bands, respectively, out of a total of 2219 images. In the case of high noise, only a few objects are detected, giving a higher probability of astrometric issues.

Figure 5 illustrates the precision of the PSF homogenization procedure. The integral of the best-fitting PSF within apertures of radius r is plotted as a function of the radius for all band, before and after the homogenization. All these functions are normalized by the integral of the target Moffat profile within the same apertures. The ratios of the integrals differ from 1 by less than 5 % at all apertures for most of the bands. The worst agreement occurs for the Suprime-Cam/g^+ band which has a particularly broad initial PSF. However, the difference with the target PSF is below 10 % in all apertures also for this band.

Figure 6 presents the spatial variation of the PSF across the field for the Suprime-Cam/$IB464$ band, before and after PSF-homogenization per exposure. This band has the greatest PSF spatial variability before homogenization among the considered bands. The homogenized image effectively presents significantly less variations.

3.1.3. *Aperture photometry*

Optical and near-infrared fluxes measured in 2″ and 3″ diameter apertures are extracted using `SExtractor` from PSF-homogenized images. Fixed-apertures ensure that the same structures are sampled in different bands for each source, which is necessary for reliable measurement of colors and photometric redshifts.

The photometric errors computed with `SExtractor` are underestimated in the case of correlated noise in the image (e.g., Leauthaud et al. 2007). The aperture flux errors and magnitude errors are therefore re-scaled with band-dependent correction factors applied to all sources (Bielby et al. 2012); see Mehta et al. (2018) for a detailed

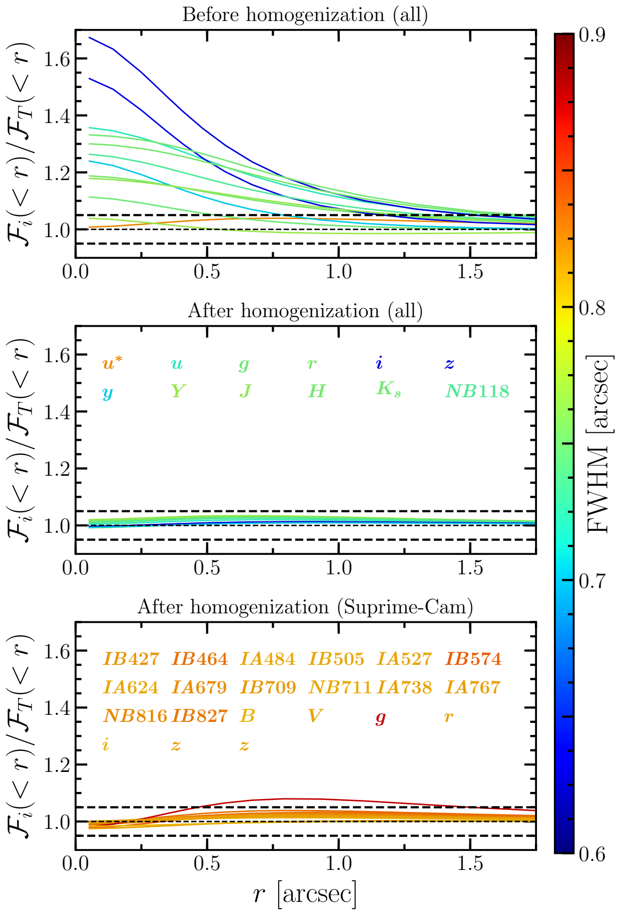

Figure 5. Best-fitting Moffat profile PSF integrated in circular apertures, $\mathcal{F}_i$, normalized to the target PSF $\mathcal{F}_T$, as a function of the aperture radius for all bands. *Top:* Before PSF-homogenization, for all bands except Suprime-Cam. *Middle:* After PSF-homogenization, for all bands except Suprime-Cam. *Bottom:* After PSF-homogenization, for Suprime-Cam bands. The horizontal dashed lines indicate ±5 % relative offset. The color map reflects the PSF FWHM before homogenization for all bands and after homogenization for the Suprime-Cam bands.

description. In the PSF-homogenized images, the flux is measured in empty apertures (using the segmentation map estimated in each image) randomly placed over the field. The depths are computed from the standard deviation (3σ clipped) of the fluxes in empty apertures inside the UltraVISTA layout. The correction factors are then the ratio between the standard deviations of the fluxes measured in empty apertures and the median flux errors in the source catalog, as in Laigle et al. (2016). This is performed separately for 2″ and 3″ diameter apertures, and in the case of UltraVISTA photometry, the deep and ultra-deep regions are treated separately. The 3σ depth estimates and the correction factors are listed in

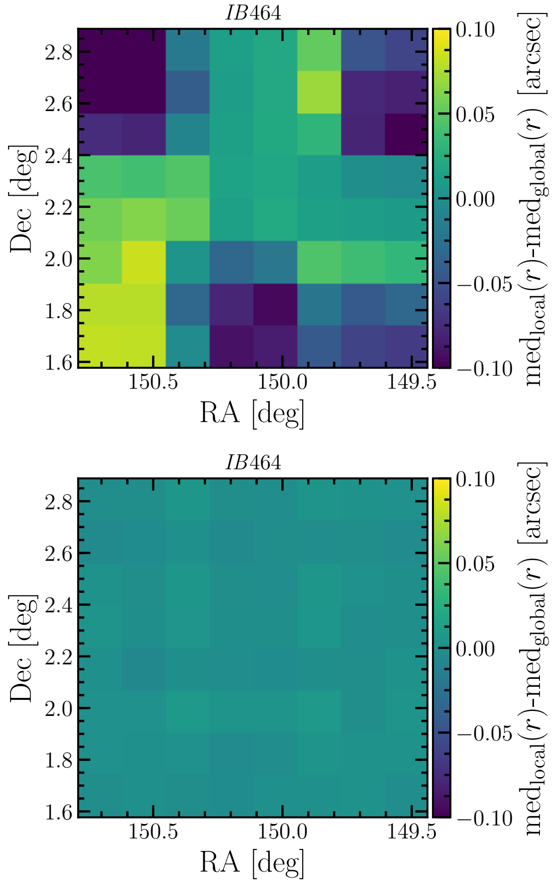

Figure 6. Distribution of the difference between the local and the global median half-light radius for the selected stars in the *IB*464 band, as a function of position, before (*top*) and after (*bottom*) PSF-homogenization.

Table 1 and illustrated in Figure 3. The flux and the magnitude errors are already corrected in the Classic catalog, as it was done for the COSMOS2015 catalog. The 3σ depth of the IRAC bands are computed using the same approach, after tuning the `SExtractor` configuration to the IRAC images.

Aperture photometry may underestimate the total flux of the sources. Optical and near-infrared aperture fluxes (and flux uncertainties) are converted to total fluxes using a source-dependent correction equivalent to the one adopted by Laigle et al. (2016). The correction is computed as the ratio between the pseudo-total flux f_{AUTO}, defined using band-dependent Kron apertures (Kron 1980), and the aperture flux f_{APER}, averaged over the HSC/g, r, i, z, y and UltraVISTA/Y, J, H, K_s broad bands. Each ratio is weighted by the inverted quadratic sum of the pseudo-total and the aperture signal-to-noise:

$$o = \frac{1}{\sum_i w_i} \sum_i \left(\frac{f_{\mathrm{AUTO}}}{f_{\mathrm{APER}}} \right)_i w_i, \tag{1}$$

where the weights are defined as

$$w_i = \frac{1}{\left(\frac{\sigma_{\mathrm{AUTO}}}{f_{\mathrm{AUTO}}} \right)_i^2 + \left(\frac{\sigma_{\mathrm{APER}}}{f_{\mathrm{APER}}} \right)_i^2}, \tag{2}$$

with σ_{AUTO} the f_{AUTO} uncertainties, and σ_{APER} the f_{APER} uncertainties (corrected for correlated noise). The sum only includes the filters in which both f_{AUTO} and f_{APER} are positive and unsaturated. As a result, the optical and near-infrared colors remain unaffected. This step is required because of the total fluxes measured with the GALEX and IRAC data, to obtain meaningful colors using these bands. These offsets are available (in magnitude units) in the Classic catalog for both $2''$ and $3''$ diameter apertures.

3.1.4. *IRAC photometry*

Flux extraction is performed on the *Spitzer*/IRAC images using the `IRACLEAN` software (Hsieh et al. 2012). The infrared images of IRAC have a larger PSF (with FWHM between 1.″6 and 2.″0) compared to the optical data and are significantly affected by confusion noise, which prevents reliable aperture photometry extraction. To tackle this issue, `IRACLEAN` uses a high-resolution image (and its segmentation map) as a prior to identify the centroid and the boundaries of the source, and iteratively subtract a fraction of its flux ('cleaning') until it reaches some convergence criteria specified by the user. `IRACLEAN` works in the approximation that an IRAC source can be modelled as a scaled Dirac delta function convolved with the PSF.

For each source identified in the segmentation map, the software uses a box of fixed size as a filter in the low-resolution image to find the centroid and estimate the flux within a given (square) aperture. The PSF is convolved with a Dirac delta function with an amplitude equal to a fraction of that aperture flux, and then subtracted from the image. Filtering and centroid positioning are executed within the object's boundaries as defined by the prior high-resolution segmentation map. This procedure is repeated on the residual image produced by the previous iteration until the flux of the treated source becomes smaller than a specified threshold. In this case, a minimum signal-to-noise ratio of 2.5 is set so that an object will be considered completed once its aperture flux, compared to the background, becomes smaller than that value. This also implies that not all the sources detected in the prior image will be extracted by `IRACLEAN`. Moreover, since sky background is recomputed at each iteration, the signal of a faint source – initially disregarded – may emerge from the background after several passes on the nearby objects.

Besides the threshold below which to stop cleaning, the filtering box size, the square aperture to measure IRAC flux, and the fraction of flux to subtract at each iteration are also user-controlled parameters. In this configuration a box of size 7×7 pixel is adopted to filter and to find the centroid, and a square aperture of size 9×9 pixel to estimate the aperture flux; the fraction of flux subtracted for each cleaning step is 20 %. The final flux of each object is the sum of the fluxes subtracted at each step. Since the centroid position is allowed to change at every iteration the source is eventually modelled by a combination of Dirac delta functions that are not necessarily centred at the same point. The flux error is computed using the residual map by measuring the fluctuations in a local area around the object. The workings of `IRACLEAN` are described in Hsieh et al. (2012).

This implementation adopts the high-resolution $izYJHK_s$ detection image and its segmentation map produced by `SExtractor`. In order to parallelize the processing of the images, a mosaic of 14×14 tiles is made with a $0\farcm3$ overlap in each direction. The PSF is modelled on a grid with spacing of $29''$ across the full IRAC image in order to take into account its spatial variation using the software `PRFmap` (A. Faisst, private communication). When modeling the PSF at each grid point, the code takes into account that the final IRAC mosaic is made of multiple overlapping frames that can have different orientations with a PSF that is not rotationally symmetric. `PRFmap` models the PSF in each of the frames that overlap at a grid point and stacks them to produce the PSF model of the mosaic at that location. `IRACLEAN` thus provides photometry in channel 1 and 2 for more than a million sources over the whole field.

3.2. *`The Farmer` catalog*

3.2.1. *Source Detection*

The source detection step is entirely equivalent to the procedure adopted for the Classic catalog. `The Farmer` utilizes the `SEP` code (Barbary 2016) to provide pythonic source detection, extraction, and segmentation, as well as background estimation with near identical performance as classical `SExtractor`. This analysis is limited the present catalog to the UltraVISTA area (outside the HSC bright star masks) as to not introduce inhomogenities in the source modelling with respect to the constraining bands available which differ due to inhomogenous coverage. The detection parameters are configured identically between `SExtractor` and `SEP` where possible. Crucially, given that model-based photometry from `The Farmer` cannot be readily applied to saturated bright stars and sources contaminated by stellar halos, the HSC PDR2 bright star masks are adopted a priori to ensure the reliability of the derived photometry (see Section 2.7). While there are 893 793 sources in the entire `The Farmer` catalog, only 794 011 sources lie within UltraVISTA footprint but outside the conservative HSC bright star halo masks. This is nearly identical to the number of sources detected in the Classic catalog (it differs by less than 0.01 %).

Once sources are detected, `The Farmer` attempts to identify crowded regions with multiple nearby sources which although deblended at detection, may suffer from blended pixels that can adversely affect the photometry. Hence, to avoid double-counting flux and to achieve the most robust modelling possible, these sources are modelled simultaneously. Such crowded regions are identified by dilating the source segment map, which assigns pixels to sources, in order to form groups of sources defined by contiguous dilated pixels. Sources which are not in crowded areas are expected to be a group of one source, whereas sources in crowded regions end up members of larger groups to be modelled together.

3.2.2. *PSF creation*

In contrast with the PSF-homogenization strategy employed in the Classic catalog, it is the model themselves which are convolved with the PSF in each band in `The Tractor`. In this work a spatially constant PSF for u, u^*, as well as all HSC and UltraVISTA bands as obtained with `PSFEx` is adopted. Point-source candidates are selected as described in Section 3.1.2. `The Farmer` benefits from particularly large PSF renderings which include information in the wings of the PSFs.

For IRAC, `The Farmer` employs `PRFMap` to provide a spatially-varying PSF to each group of sources based on their nearest PRF sampling point. This is not only advantageous to the photometry, but is also consistent with the `IRACLEAN` procedure described in section 3.1.4. The PSFs are then re-sampled to match the $0\farcs15$ pixel scale of the mosaics.

Another consideration, introduced for the Classic catalog in section 3.1.2, is the highly variable PSF of the Suprime-Cam medium bands. Although `The Farmer`, and model-based photometry in general, are not compatible with the PSF-homogenization, it is possible to overcome highly variable PSFs in model-based photometry by providing a particular PSF to a group of sources in the same way as `PRFMap`. However, `PRFMap` produces a theoretical PSF sampled over a fixed grid. Lacking sufficient theoretical PSFs for the Subaru medium bands, a spatial grid is constructed using the PSF FWHM measured from a sample of point-like sources nearest to each grid point. The FWHM distribution is then discretized to form a set of PSFs at a gauge small enough to provide accurate PSFs for each grid point while maintaining the spatial sampling required to describe the variations across the field. Hence, for each medium band a 20×20 grid consisting of 10 PSFs is built with a typical resolution less than a tenth of a pixel. Then for a particular group of sources `The Farmer` provides the nearest PSF sample to be used in the forced photometry modeling.

3.2.3. *Model Determination*

`The Farmer` employs five discrete models to describe resolved and unresolved, stellar and extragalactic sources:

1. **PointSource** models are taken directly from the PSF used. They are parameterized by flux and centroid position and are appropriate for unresolved sources.
2. **SimpleGalaxy** models use a round, exponential light profile with a fixed $0.45''$effective radius such that they describe marginally resolved sources and mediate the choice between PointSource and a resolved galaxy model. They are parameterized also by flux and centroid position.
3. **ExpGalaxy** models use an exponential light profile. They are parameterized by flux, centroid position, effective radius, axis ratio, and position angle.
4. **DevGalaxy** models use a de Vaucouleurs light profile. They are parameterized by flux, centroid position, effective radius, axis ratio, and position angle.
5. **CompositeGalaxy** models use a combination of ExpGalaxy and DevGalaxy models. They are concentric, and hence share one centroid. There is a total flux parameter as well as a fraction of total flux parameter to distribute the flux between the two components. Components have their own effective radii, axis ratios, and position angles.

These five models form `The Farmer`'s decision tree, whose goal is to both determine the most suitable model for a given source, and provide an optimized set of parameters to describe the shape and position of the source. For the present catalog, each model is determined and optimized with simultaneous constraints from each band used to create the combined $izYJHK_s$ detection image, as to ensure that the selection function is not adversely affected from a particular choice of modelling band.

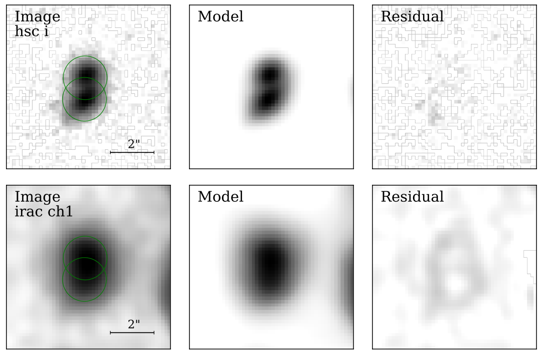

Figure 7. Demonstration of the model-fitting method from `The Tractor`. A pair of detected but blended sources is shown in the HSC i-band (*top*) and is modelled using `The Farmer` with $YJHK_s$ images to provide a parameterized solution which is suitably optimized, and from which the total flux is measured. The same pair of sources but shown in the less resolved IRAC Channel 1 (*bottom*), where the model is taken from the optical-NIR solution and re-optimized for flux alone using the Channel 1 image and PSF. The extremely blended nature of this pair is underscored by the overlapping $2''$apertures, consistent with the methodology of the Classic catalog. Pixel values are logarithmically scaled between the RMS level and 95 % of the peak flux per pixel.

As described in detail in Weaver et al. (in prep.) and summarized here, `The Farmer` processes each group of sources using its decision tree to correctly select the most appropriate model for each source in the group, and does so simultaneously to avoid hysteresis owing to the choice of model for neighboring sources. The decision tree starts with unresolved or marginally resolved models (1,2) and moves towards more complex, resolved ones (3,4,5). Each level of the decision tree assumes the same initial conditions, excepting that some sources may already be assigned a model type in the latter stages. Once a model type has been assigned to each source, the final ensemble of models is re-optimized to ensure that the derived model parameters reflect the actual model ensemble as to avoid borrowing a potentially inappropriate solution from earlier in the tree.

3.2.4. *Forced Photometry*

With the model catalog complete for all detected sources, `The Farmer` can measure total model fluxes for every band of interest. `The Farmer` does this in a "forced photometry" mode, similar to the "dual-image" mode in `SExtractor`. In brief, the model catalog of a given group is initialized with the optimized parameters from the preceding stage. For each band, model centroids are allowed to vary with a strict Gaussian prior of 0.3 pix to prevent catastrophic failures. By doing so, The Farmer can overcome subtle offsets in astrometric frames between different images, and this can be done on an object-by-object basis to even overcome spatially varying offsets which may arise due to bulk flows in the astrometry. The optimization of these models produces total fluxes and flux uncertainties for each band of interest, keeping the shape parameters fixed. The flux measurement is obtained directly from the scaling factor required to match the models, which are normalized to unity, to the source in question. However, the flux uncertainties are derived by computing a quadrature sum over the weight map which is itself weighted by the unit profile of the model, in a similar manner as traditional aperture methods but where variance of the central pixel is emphasized. Importantly, unlike the CLASSIC catalog (see Section 3.1.3), the flux uncertainties reported in The Farmer catalog are not corrected with empty apertures. The aperture-derived procedure used in CLASSIC is inappropriate for model-based photometry, and although it may be expected that model-based methods would produce more precise measurements, they may still underestimate the true extent of correlated noise in the images and hence underestimate the uncertainty. This will be further discussed in Weaver et al. (in prep), and briefly evaluated later in Section 5.3 in terms of photometric redshift precision.

3.2.5. *Advantages*

An important distinction between the two catalogs is that The Farmer provides total fluxes natively, without the need to correct for aperture sizes or perform PSF-homogenization. Since this advantage can be leveraged over different resolution regimes, The Farmer obtains photometric measurements which are self-consistent. Additional metrics are also readily available from The Farmer. This includes the goodness-of-fit reduced χ^2_N estimate computed for the best-fit model of each source on a per-band basis, obtained by dividing the χ^2 value by the number of degrees of freedom, i.e. the pixels belonging to the segment for each source minus the number of fitted parameters. Measurements of source shape are provided for resolved sources, and as such they yield estimates of effective radii, axis-ratios, and position angles. These measurements are directly fitted in The Farmer, unlike in SExtractor where they are estimated from moments of the flux distribution. Uncertainties on shape parameters are deliverable as well, in the sense that they are a fitted parameter which is the result of a likelihood maximization and not a directly calculated quantity. Likewise, centroids for both the modelling and forced photometry stages are also fitted parameters, and are delivered with associated uncertainties.

4. COMPARISON

With the photometry from the two independent methods in hand, this section presents a comparison of the photometric catalogs as measured by differences in magnitudes, colors, and photometric uncertainties. In addition, a comparison is made with literature results of galaxy number counts. The primary motivation for these tests is to validate the two catalogs, in particular the performance of the relatively newer photometry from The Tractor generated with The Farmer. The performance of The Tractor code has been demonstrated previously (see Lang et al. 2016), hence this work focuses on additional validation of the performance particular to The Farmer configuration used here. Additional validation of The Farmer where its performance is benchmarked against simulated galaxy images is provided in Weaver et al (in prep.).

A matched sample is constructed consisting of objects common to both catalogs. This consists of 857 741 sources from The Farmer catalog which have companions within the CLASSIC catalog within 0.″6, which corresponds to to 99.2 % of The Farmer sources. Most are matched well below 0.″6. Those which are unmatched are typically marginally detected sources, or blends which are de-blended by only one of the detection procedures.

4.1. *Magnitudes*

A comparison of broadband magnitudes derived independently with the two methods is shown by Figure 8. One medium band is included for reference. Here the re-scaled 2″ total aperture magnitudes are used to compare with the model magnitudes from The Farmer. The comparison is limited only to sources brighter than the 3σ depth as reported in Table 1 and indicated by the vertical dashed lines. For bands not included in the detection CHI_MEAN, these depths are upper bounds. The quadradure combined $\pm3\sigma$ and $\pm1\sigma$ uncertainty envelopes on ΔMag computed from the photometric uncertainties are shown for reference by the grey dotted curves.

In general, there is excellent agreement between the photometric measurements obtained by the two methods. As shown in Figure 8, the median systematic difference in magnitude in each band is typically below 0.1 mag, and in some cases is noticeably smaller. After accounting for these systematic differences, the observed median in all cases lies within the expected 3σ uncertainty thresholds, which correspond to the expected uncertainty from the difference in magnitude, and in most cases is found to be $\lesssim 0.25$ mag for the faintest sources. There is also noticeably low scatter between the measurements, as illustrated by the tight 68% range

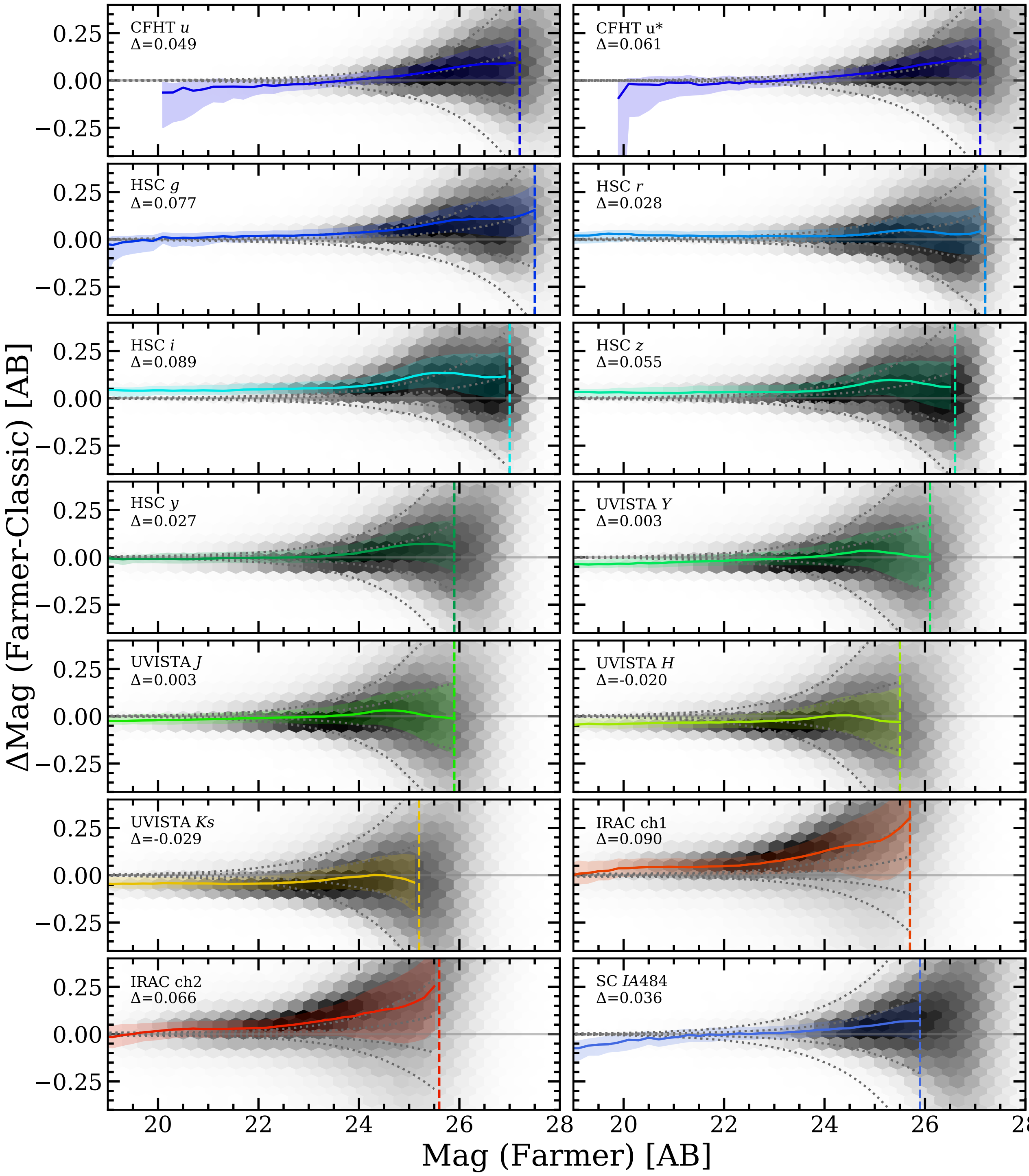

Figure 8. Summary of the differences in broad-band magnitudes measured by `The Farmer` and Classic catalogs, ΔMag. Magnitudes for Classic are the re-scaled 2″total magnitudes. For UltraVISTA, sources in both the ultra-deep and deep regions are shown. Agreement for individual sources is shown by the underlying density histogram which is described by the overlaid median binned by 0.2 AB with an envelope containing 68 % of points per bin (solid line and shaded area). 1σ and 3σ photometric uncertainty estimates on ΔMag are indicated by the grey dotted curves. The 3σ depths measured with 3″ diameter apertures as reported in Table 1 are shown by vertical dashed lines. The median Δ magnitude computed for the unbinned data, for sources brighter than the depth limit, is reported in each panel, as well as the corresponding filter.

envelopes about the medians. In most cases the 68% range envelope on the median spans the same range as the expected $\pm 1\sigma$ uncertainty envelope, the coincidence of which provides the first evidence validating the photometric uncertainties, discussed in full later in this section. Hence it is established by multiple quantitative means that the two photometric measurements are broadly consistent.

A closer inspection, however, reveals a minor second-order curvature observed at the threshold where sources become unresolved in our ground-based NIR detection images, around ~ 24.5 mag. At these magnitudes, photometry from `The Farmer` tends to be slightly fainter than reported by `SExtractor` (or `IRACLEAN` for channel 1 and channel 2). However, these differences are generally very small and by median estimate are within the 3σ uncertainties for all bands. The fact that these features occur around the resolution thresholds of each band may indicate that sources are inadequately modelled as `The Farmer` must choose between a resolved or unresolved model. If a resolved source is fitted with an unresolved model then the flux may be underestimated. Differences (in bands other than IRAC) may also arise from imperfections in rescaling the $2''$ apertures to total fluxes, compared to the native total fluxes obtained with `The Tractor`. This is particularly relevant given the high density of sources which can led to inaccurate estimates of object size, for instance, resulting in an inaccurate total fluxes. Regarding the IRAC photometry, which was obtained in both instances by profile-fitting techniques, discrepancies for faint sources cannot arise from aperture corrections. However, whereas `IRACLEAN` performs iterative subtraction of the PSF until convergence and sums all of the flux which has been subtracted, `The Farmer` solves for the flux as a model parameter without iterative subtraction. Yet, there is no evidence that any residual flux remaining from `The Farmer` fitting is significant enough to explain the observed discrepancy. Another potential difference which might explain the trend with brightness is that `IRACLEAN` performs iterative local background subtraction whereas `The Farmer` performs a static background subtraction before performing photometry. However, it remains unclear as to exactly which methodology is most accurate. Definitively elucidating the cause of this observed discrepancy can only be obtained though simulation and is hence included in detail in Weaver et al. (in prep).

4.2. *Colors*

A comparison of six colors which contribute significantly to constraining an SED is shown in Figure 9. In similar fashion to the previous comparison, the distributions are described with a running median and 68 % range up to the nominal 3σ depth which is averaged for the two bands of interest. The expected $\pm 3\sigma$ and $\pm 1\sigma$ uncertainty thresholds on Δcolor computed from the color uncertainties are shown by the grey dotted curves.

There is excellent agreement in colors, in some cases well-beyond the level of agreement achieved between individual bands. The median difference in color Δ for each band is below 0.05 mag. In the first three panels there is no evidence of significant disagreement beyond the 1σ level up to the depth limit. Indeed, there is a lack of systematic difference in color and the observed scatter is well below the expected 1σ uncertainty in the difference in color. The remaining panels show some level of systematic disagreement which is significant for bright sources. However, colors for faint sources are statistically consistent as they lie within the $\pm 1\sigma$ thresholds on the color uncertainty. This may be helped by the fact that aperture-to-total rescaling is not necessary here to compute colors for the CLASSIC catalog, eliminating any relevant uncertainties present when comparing magnitudes only. In general, there is no evidence for a significant systematic difference in colors obtained by the two methods. Second-order curvatures are only visible at the faintest magnitudes, and are not significant even at the 1σ level after correcting for median shifts. The most significant deviation in color shown here is K_s-ch1, which features a relatively large systematic offset for bright sources and a strong second-order curvature for faint sources whereby `The Farmer` obtains systematically bluer colors. Given that K_s magnitudes are well-matched between the two catalogs, this discrepancy in color must originate from the disagreement in faint IRAC channel 1 fluxes demonstrated in Figure 8. However, after correcting for the systematic median offset, the median curvature of the K_s- ch1 lies between the 3σ color uncertainty thresholds.

4.3. *Photometric uncertainties*

One critically important aspect to compare is photometric uncertainties. The uncertainties from `SExtractor` are measured by quadrature summation of the $1/\sigma^2$ inverse-variance per-pixel (i.e. weight) map corresponding to the aperture on the source in the image. In contrast, `The Tractor` reports minimum variance estimates on the photometric uncertainty, although still using the same weight map. For point-like sources, this is simply a quadrature addition of weight map pixels weighted by the unit-normalized model profile. The valuation thereby prioritizes the per-pixel uncertainty directly under the peak of the model profile, and

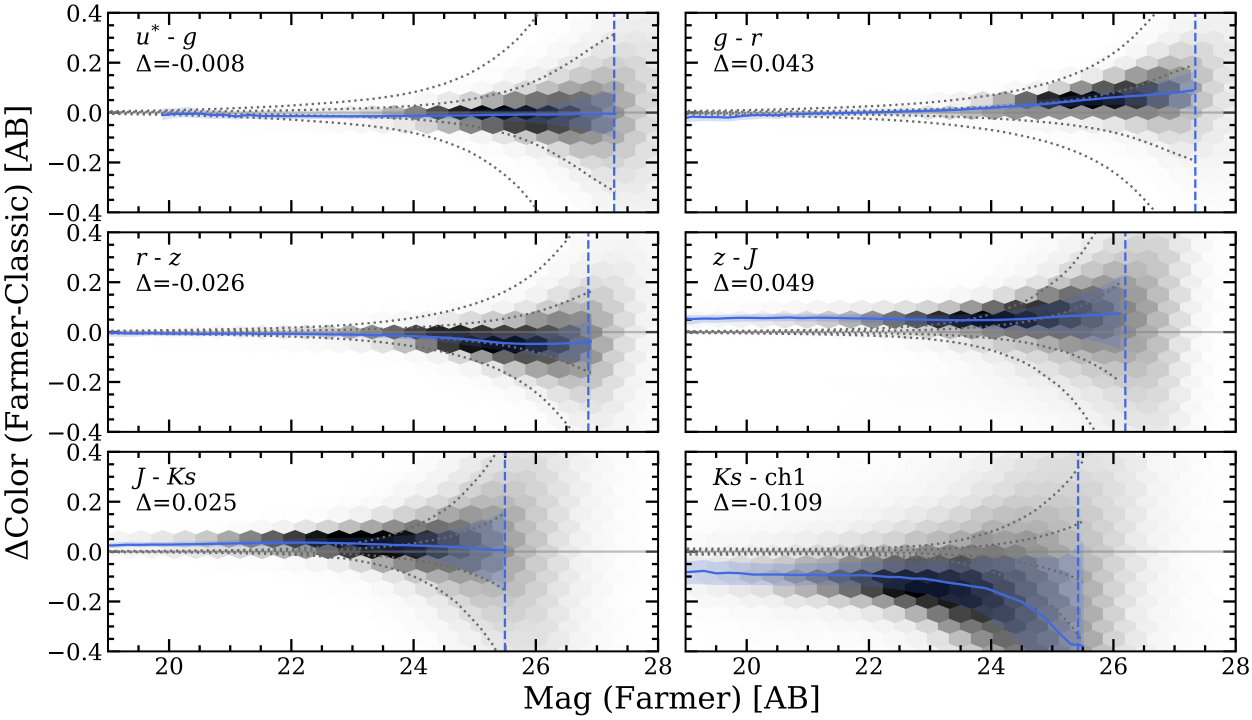

Figure 9. Comparison of broad-band colors between the `The Farmer` and Classic catalogs, Δcolor. `The Farmer` magnitudes of the first color term in each panel are shown on the x-axis. Colors for individual sources are shown by the underlying density histogram which is described by the overlaid median binned by 0.2 AB with a 68 % confidence interval. 1σ and 3σ photometric uncertainty estimates on the colors are indicated by the grey dotted curves and the mean 3σ depth computed from both bands of interest and measured with 3″ diameter apertures as reported in Table 1 are shown by vertical dashed lines, brighter than the median Δ are reported.

weights less the per-pixel uncertainty near the edges of the model.

As shown in Figure 10, colored binned medians with an envelope enclosing 68 % of sources per bin indicate the distribution of magnitude uncertainties as a function of magnitude per band as measured by `The Farmer` for the primary broad-bands, as well as a medium band for reference. For the UltraVISTA bands, this distribution has one locus for the deep and another for the ultra-deep areas, most noticeably for the Y, J and H bands which feature the greatest difference in depth, as recorded in Table 1. For comparison, binned medians on the uncorrected magnitude uncertainties from the Classic catalog using empty apertures are indicated by the grey dashed curves. The corrected magnitude uncertainties from the Classic catalog, used in fitting SED templates, are indicated by the grey dotted curves. The samples used in this particular comparison are not matched, but rather limited to only sources within the UltraVISTA area and clear of stellar halos indicated by the HSC bright star masks.

Photometric uncertainties are observed to be smoothly and monotonically increasing with source faintness. For `The Farmer`, there is no evidence for discontinuities related to the transition between the resolved and unresolved regimes. There is, however, a difference between the magnitude uncertainties whereby those acquired with `SExtractor` and corrected are in every case larger than those from `The Farmer` for all bands except IRAC, where `IRACLEAN` was used. Yet in the case of the initial, uncorrected `SExtractor` uncertainties, this difference is much smaller. Moreover the two sets of uncertainties are in better agreement in the bluer u, u^*, and HSC bands where the spatial resolution is generally better than in the UltraVISTA bands. The opposite is true when comparing IRAC photometry, whereby `The Farmer` reports larger uncertainties than IRACLEAN. However, a noticeable level of consistency is achieved by `The Farmer` in that uncertainties from IRAC are similar to those from UltraVISTA, which should be expected given the similarity in the depths reported in Table 1. This consistency is not present in the Classic catalog,

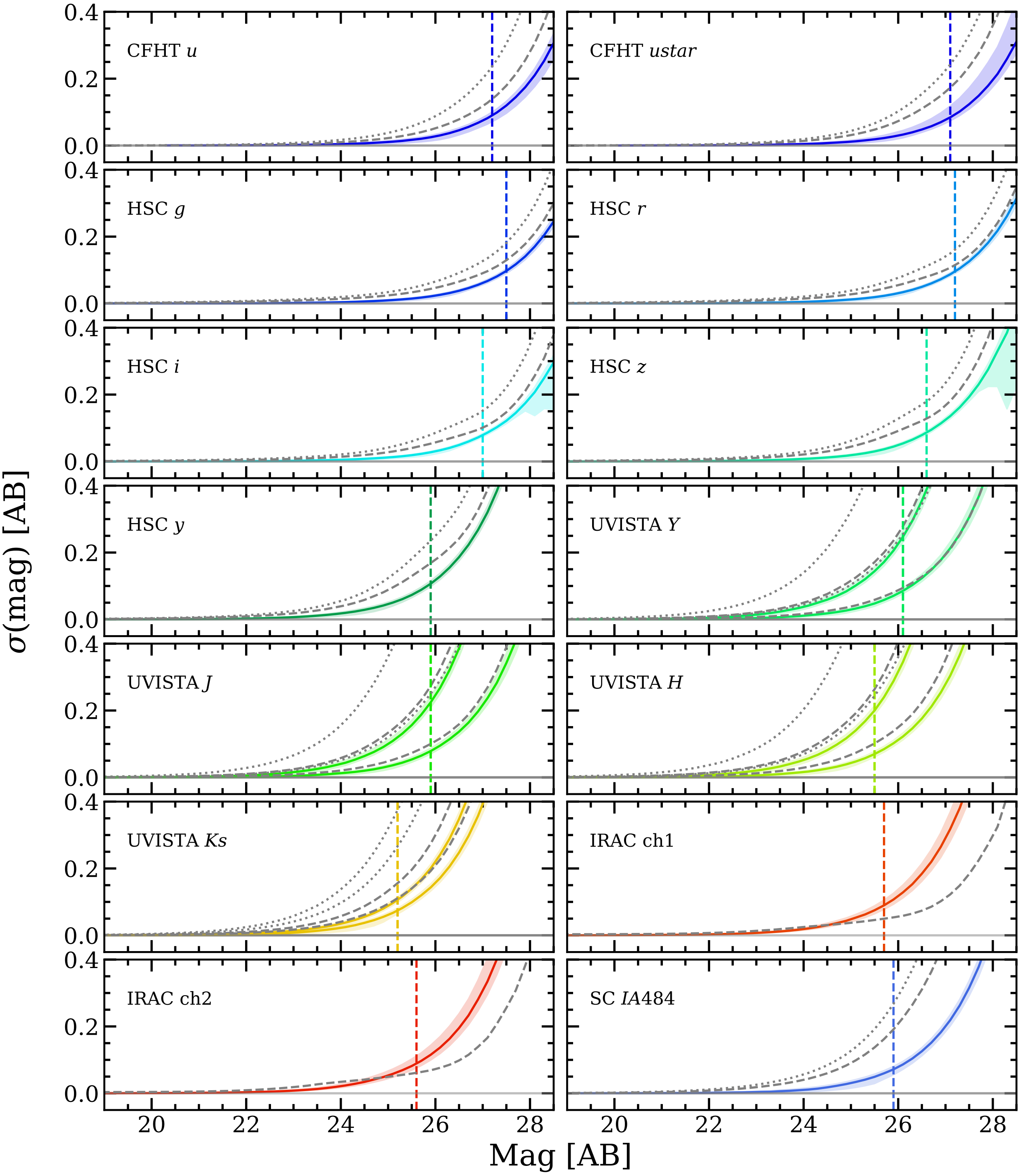

Figure 10. Growth of photometric uncertainties as a function of magnitude. The colored curves indicate the distributions for individual sources in `The Farmer` catalog, described by the running median and a tight envelope containing 68 % of sources. The grey curves represent the median growth of uncertainty for the total magnitudes in the CLASSIC catalog derived from $2''$ aperture photometry, shown by the dashed and dotted curves for the uncorrected and corrected uncertainties, respectively. The 3σ depths measured with $3''$ diameter apertures as reported in Table 1 are shown by vertical dashed lines. The two curves shown for each band in $YJHK_s$ are due to different depths of the deep and ultra-deep regions.

due to the difference between the methods of extraction from UltraVISTA and IRAC images.

Given that the photometric uncertainties measured with `The Farmer` are intrinsically linked to the underlying weight map, it is possible to quantify the internal consistency of these uncertainties using the reduced χ^2_N statistic, described in Section 3.2.5. In general, χ^2_N values are roughly unity for all bands. While this provides one measure of internal consistency, both the uncertainties reported by `The Farmer` and the χ^2 statistics fail to take into account pixel co-variance, which may be quite large, particularly in the lower resolution UltraVISTA mosaics which have been upsampled from their native $0\farcs34$ per pixel to $0\farcs15$ per pixel. It is then reasonable to conclude on this basis that although the uncertainties provided by `The Farmer` may be underestimated, they are indeed internally consistent with measurements which likewise ignore correlated noise, such as χ^2, and are in general suitable for use in SED-fitting. Additional correction of the photometric uncertainties from both `The Farmer` and Classic catalogs appropriate for SED-fitting is discussed further in Section 5.

4.4. *Galaxy number counts*

Galaxy number counts from this work are now compared with measurements in the literature. Figure 11 shows the galaxy number counts measured for bands on either end of the `CHI_MEAN` detection, namely K_s (left panel) and i (right panel). The star-galaxy separation from `LePhare` used to produce galaxy-only samples is described later in Section 5.1 and is carried out identically for both catalogs.

The area used for counts for `The Farmer` is smaller than in Classic, as photometry is not returned in the case of model failure with `The Tractor`, most often in the presence of unexpected bright stars or large resolved galaxies which cannot be adequately modelled with one of the assumed smooth galaxy profiles. Hence the effective survey area is diminished by subtracting the area occupied by sources for which a model is not available. The directly comparable galaxy counts from COSMOS2015 are included for the deep and ultra-deep regions, as the detection and photometry are equivalent to the Classic approach. The $izYJHK_s$-detected K_s-band galaxy number counts from both catalogs are separately computed over the $0.812/0.757\,\mathrm{deg}^2$ of the HSC-masked ultra-deep region of UltraVISTA, and over the $0.592/0.536\,\mathrm{deg}^2$ of the deep region for the Classic and `The Farmer` catalogs, respectively. There is good agreement with previous studies both within COSMOS (McCracken et al. 2012; Laigle et al. 2016) and from other surveys (Aihara et al. 2011; Bielby et al. 2012; Fontana et al. 2014) over the regime where comparison is possible. The counts from the two COSMOS2020 catalogs are extremely similar, with slightly deeper counts computed with `The Farmer`, which may be explained by the degree to which sources are de-blended using the models, which contributes to detecting fainter sources by discounting flux from nearby sources. Notably, the COSMOS2020 completeness limit is ~ 1 mag deeper relative to COSMOS2015.

Similarly presented are the $izYJHK_s$-detected i-band galaxy number counts computed over the entire $1.403/1.234\,\mathrm{deg}^2$ of the HSC-masked UltraVISTA region for the Classic and `The Farmer` catalogs, respectively. Literature results from the i-selected counts of Leauthaud et al. (2007) and Ilbert et al. (2009) are included for reference; they are higher than the COSMOS2020 counts at the faint end. This could be due to spurious detections. Alternatively, these counts originate from an i-band image of greater depth than the shallowest band included in our `CHI_MEAN` detection image. In principle, by detecting with a `CHI_MEAN` $izYJHK_s$ for a NIR-selected sample, one may exclude sources which, although i-band detected, do not have significant detections in redder bands and so may obtain a `CHI_MEAN` value less than the detection threshold of 1.5. This potentiality was ruled out by computing the Classic number counts using the i-band image as detection image, which resulted in consistent i-band counts to those derived with the `CHI_MEAN`. Hence, the apparent lack of faint galaxies from this work is likely driven by spurious detections in the number counts from the literature.

Additionally included are the i-band galaxy number counts from the HSC-SSP DR1 (Aihara et al. 2018), whose detection is performed in each of the g, r, i, z, y band separately and the lists of sources are then merged. The addition of these bluer bands (which are not present in our detection image) increases their completeness close to the detection limit relative to COSMOS2020.

The shift to lower counts at bright magnitudes for the Leauthaud et al. (2007) counts can be explained by bright galaxies typically having a fainter ACS/F814W flux than in the HSC/i band, by about 0.05 mag, because of the different filter transmission curves.

5. PHOTOMETRIC REDSHIFTS

Photometric redshifts are computed using both Classic and `The Farmer` catalogues. First, Galactic extinction at each object position are corrected for using the Schlafly & Finkbeiner (2011) dust map[5]. In the next

[5] Schlafly & Finkbeiner (2011) re-scaled the entire Schlegel et al. (1998) dust map by a factor of 0.86.

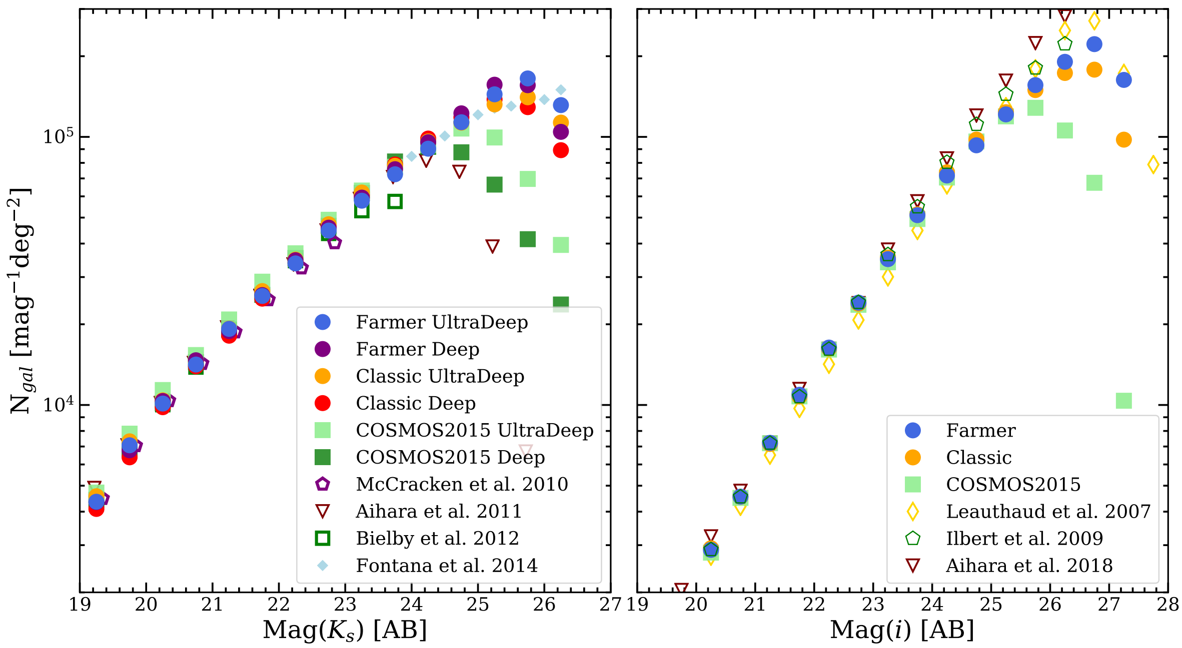

Figure 11. i- and K_s-band galaxy number counts of the $izYJHK_s$-detected galaxies in the UltraVISTA ultra-deep and deep regions, compared to a selection of literature measurements. The bins follow increments of 0.5 mag, with the exception of Fontana et al. (2014) using 0.25 mag.

sections, photometric redshifts are computed using both `LePhare` (Arnouts et al. 2002; Ilbert et al. 2006) and `EAZY` (Brammer et al. 2008), followed by a comparison between the two methods.

5.1. *LePhare*

The first set of photo-z is computed following the same method as in Laigle et al. (2016), using the template-fitting code `LePhare`[6] (Arnouts et al. 2002; Ilbert et al. 2006) and applying the same configuration as Ilbert et al. (2013).

The original set of templates (Ilbert et al. 2009) includes elliptical and spiral templates from Polletta et al. (2007) interpolated into 19 templates to increase the resolution, and 12 blue star-forming galaxy models from Bruzual & Charlot (2003, hereafter BC03). Two additional BC03 templates with exponentially declining star-formation rate (SFR) were added to improve the photo-z of quiescent galaxies (Onodera et al. 2012). Extinction is a free parameter with reddening $E(B-V) \leq 0.5$, and the considered attenuation curves are those of Calzetti et al. (2000), Prevot et al. (1984), and two modifications of the Calzetti law including the bump at 2175 Å (Fitzpatrick & Massa 1986) with two different amplitudes. Emission lines are added using the relation between the UV luminosity and [OII] emission line flux, as well as fixed ratios between dust-corrected emission lines following Ilbert et al. (2009). It is imposed that he absolute magnitude in the rest-frame Suprime-Cam/B band is $M_B \geq -24$ mag which acts as a unique prior.

Both galaxy and stellar templates are fitted with `LePhare`. Stellar templates include the stellar library from Pickles (1998), the white dwarf templates of Bohlin et al. (1995), and the brown dwarf templates from Chabrier et al. (2000), Baraffe et al. (2015, BT-Settl/CIFIST2011_2015) and Morley et al. (2012, 2014). All the brown dwarf templates extend to at least 10 μm in the infrared. The blue limit of these templates is between 0.3 and 0.6 μm, and the flux density at bluer wavelengths is set to zero. Indeed, cool brown dwarfs belong to the very faint population of sources, and are expected not to be detected in the optical. Stellar templates with an effective temperature $T_{\rm eff} < 4000$ K are rejected in the case that the physical parameters do not satisfy the constraints from Saumon & Marley (2008).

The predicted fluxes for the templates are computed using a redshift grid with a step of 0.01 and a maximum redshift of 10. 0.02 mag is added in quadrature to the photometric errors of the data in the optical, 0.05 mag for J, H, K_s, Ch 1, and the three narrow

[6] https://www.cfht.hawaii.edu/~arnouts/LEPHARE/lephare.html

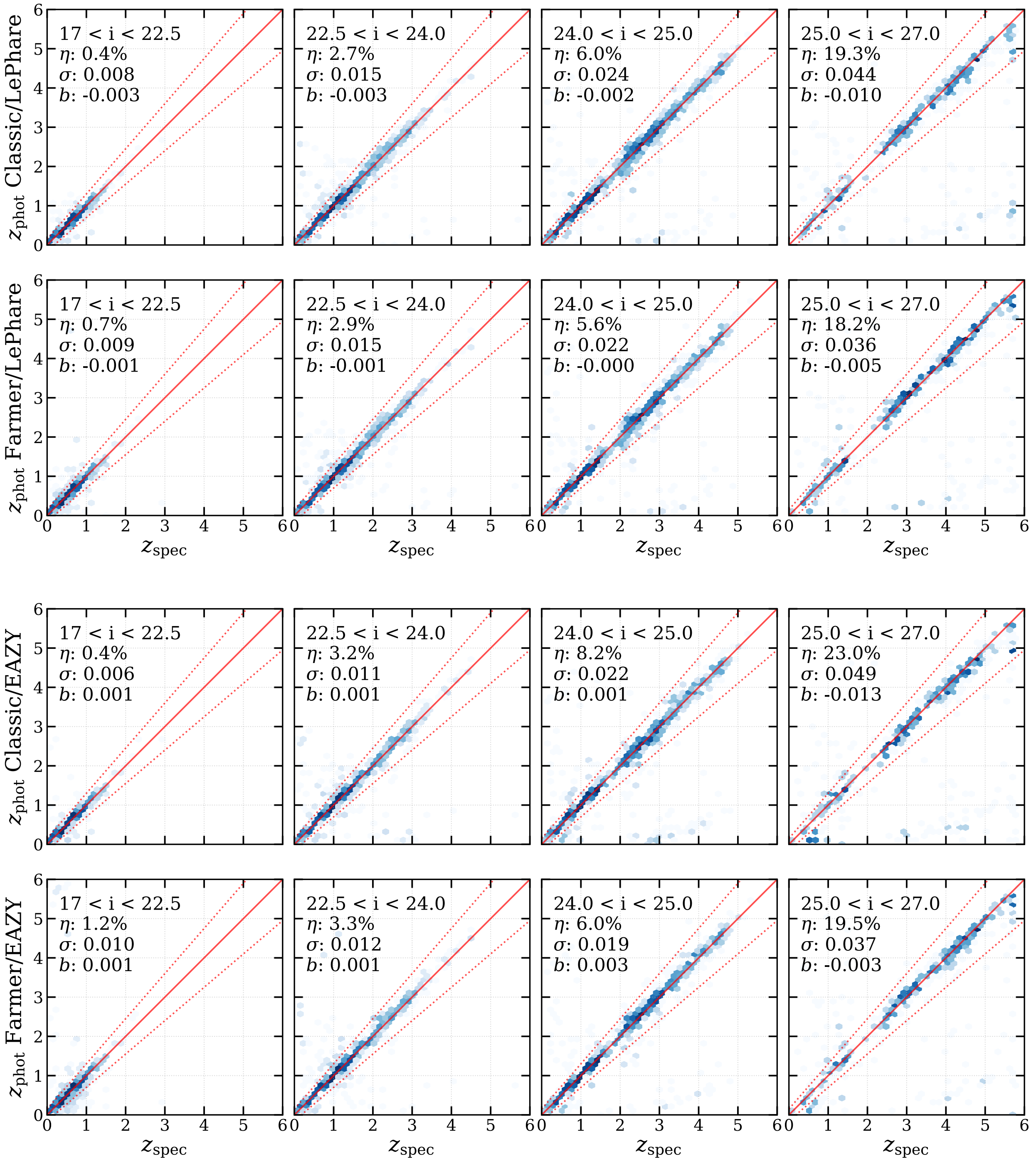

Figure 12. Photometric redshifts computed with `LePhare` and `EAZY`, split by apparent magnitude bin (from $i < 22.5$ on the left to $25 < i < 27$ on the right). *Top:* photo-z versus spec-z for the CLASSIC and `The Farmer` photometric catalogs computed with `LePhare`. *Bottom:* photo-z versus spec-z for the CLASSIC and `The Farmer` photometric catalogs computed with `EAZY`. The red solid line corresponds to the one-to-one relation, and the dashed lines correspond to the photo-z at $\pm 0.15(1 + z_{\rm s})$. The fraction of sources outside the dashed lines (noted η), the precision measured with the normalized absolute deviation (noted σ), and the overall bias (noted b) are indicated in each panel. The nature of the off-diagonal points are discussed in the text.

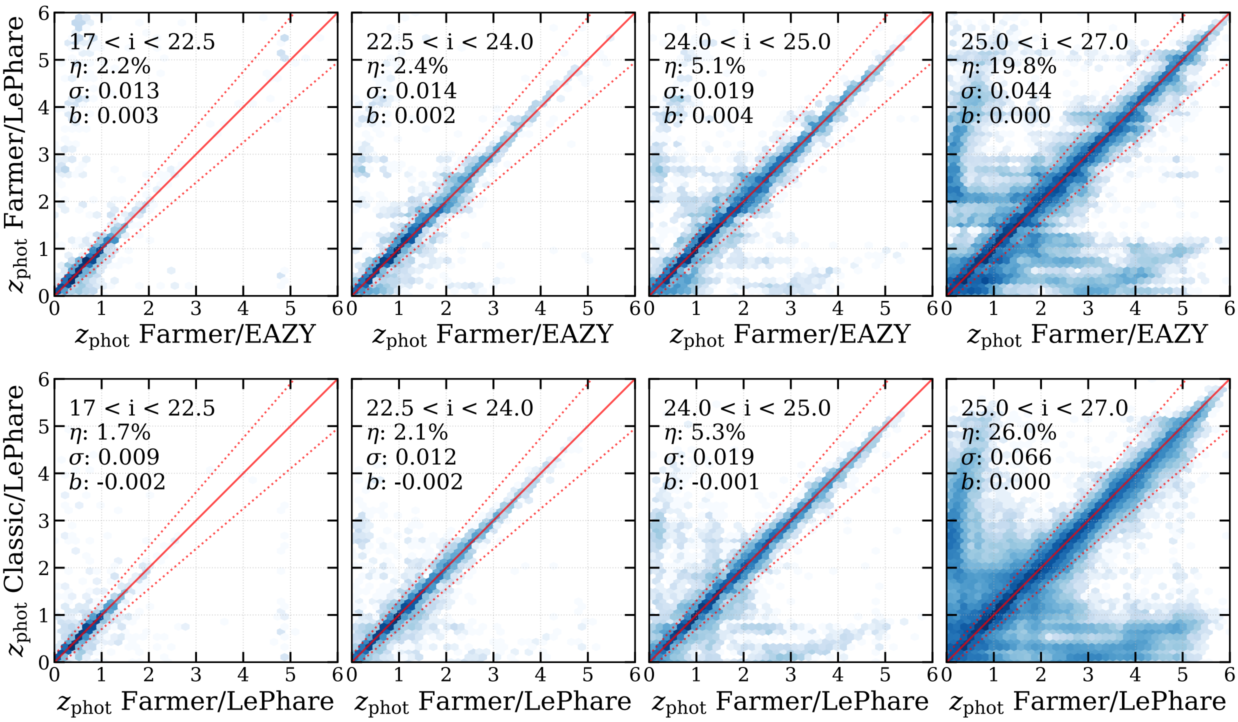

Figure 13. Photometric redshifts computed with `LePhare` and `EAZY` for the CLASSIC and `The Farmer` photometric catalogs, split by apparent magnitude bin (from $i < 22.5$ on the left to $25 < i < 27$ on the right). *Top:* Comparison between the photometric redshifts computed with `LePhare` and `EAZY` for the full `The Farmer` photometric catalog. *Bottom:* Comparison between the photo-z derived from the CLASSIC and `The Farmer` full catalogs computed with `LePhare` (excluding masked regions). The nature of the two groups of off-diagonal points are discussed in the text.

bands, and 0.1 mag for Ch 2. Such an approach is common in numerous surveys (e.g. Arnouts et al. 2007), i.e., to include uncertainties in the color-modelling (higher in the narrow bands due to the emission lines and in near-infrared). Fluxes and not magnitudes are used to perform the fit, with the advantage of not introducing upper-limits. Given the uncertainties in the calibration of the Suprime-Cam/g^+, and the availability of deeper HSC images at the same wavelength, this band is not included in the fit. Similarly, the shallow z^+ photometry is not used, since the Suprime-Cam/z^{++} and HSC/z images are deeper and already cover this wavelength range. IRAC 3 and 4 channels are not included given the difficulty to model the polycyclic aromatic hydrocarbons (PAH) lines in the mid-infrared[7] and their shallower depth (Sanders et al. 2007).

The absolute calibration is optimized in each band following the same procedure as Ilbert et al. (2006). After having set the redshift to the spec-z value for the sample with spectroscopic redshifts, the photometric offset in each band are derived by minimizing the difference between the predicted and observed fluxes. This procedure is applied iteratively until the convergence of the offsets. The offset values are given in Table 2.

A key output of the photo-z code is the likelihood of the observed photometry given the redshift, $\mathcal{L}(\mathrm{data}|z)$, after having marginalized over the template set. The photo-z point-like estimate, noted z_{phot}, is defined as the median of the likelihood distribution. 68 % uncertainties around z_{phot}, with $z_{\mathrm{phot}}^{\mathrm{min}}$ ($z_{\mathrm{phot}}^{\mathrm{max}}$) are defined corresponding to 34 % of the likelihood surface below (above) the median. In order to obtain photo-z uncertainties close to the expected values, as shown in Section 5.3, flux uncertainties are multiplied by a factor of 2.

Finally, stars and galaxies are classified by combining morphological and SED criteria. The stellar sequence is isolated by comparing half-light radii and magnitude for bright sources in the *HST*/ACS and Subaru/HSC images. All the point-like sources falling on this sequence are classified as stars at $i < 23$ and $i < 21.5$ for ACS and HSC images, respectively. Point-like quasar

[7] The 6.2μm and 7.7μm PAH lines contribute to IRAC channel 4 at $z < 0.3$, and the 3.3μm to both channel 3 and 4 but with a lower contribution.

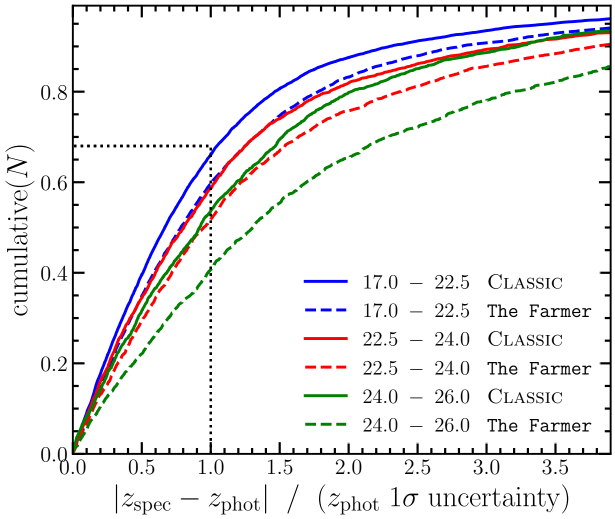

Figure 14. Cumulative distribution of the ratio between $|z_{\rm phot} - z_{\rm spec}|$ and the photo-z 1σ uncertainty, for both photometric catalogs and using `LePhare`. The photo-z 1σ uncertainty is taken as the maximum between ($z_{\rm phot} - z_{\rm phot}^{\rm min}$) and ($z_{\rm phot}^{\rm max} - z_{\rm phot}$). The solid and dashed lines correspond to the uncertainties from the Classic and `The Farmer` catalogs, respectively. For an unbiased estimate of the photo-z 1σ uncertainties, the cumulative number should reach 0.68 when the ratio equals 1 (black dotted line). The distributions are shown per bin of i-band magnitude.

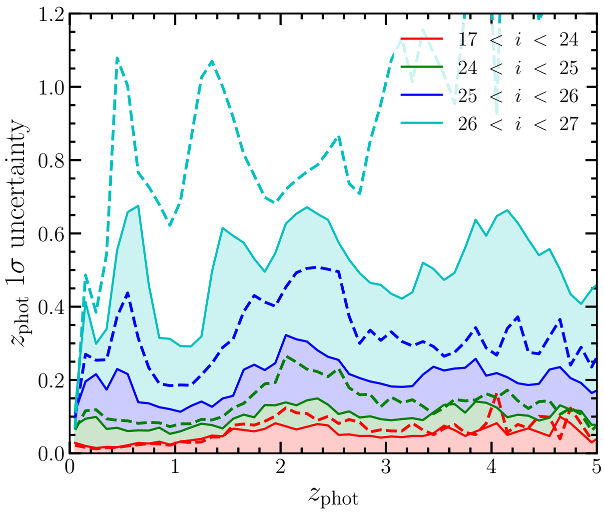

Figure 15. Median of the photo-z 1σ uncertainties (defined as in Section 5.3) shown as a function of redshift. The shaded areas corresponds to the COSMOS2020 Classic catalog computed with `LePhare` and dashed lines correspond to the COSMOS2015 catalog. The distributions are shown per bin of i-band magnitude.

sources are also removed by this criterion. Any source with $\chi^2_s < \chi^2_g$ is classified as a star, with χ^2_s and χ^2_g

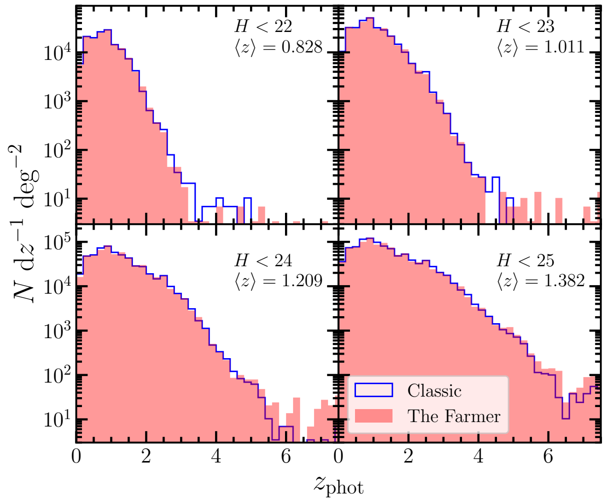

Figure 16. Redshift distribution for the Classic (blue) and `The Farmer` (pink) full catalogs computed with `LePhare`. Each panel corresponds to a different magnitude limit in H-band from `The Farmer`.

being the best χ^2 obtained using the stellar and galaxy templates, respectively. This criterion is applied only for sources detected at 3σ in K-band or the 3.6μm IRAC channel, since the lack of near-infrared data could increase the risk of stellar contamination in the galaxy sample (Daddi et al. 2004; Coupon et al. 2009).

5.2. *EAZY*

Photometric redshifts are computed along with physical parameters using an updated version of the `EAZY` code[8] (Brammer et al. 2008) rewritten in Python. `EAZY` shares much of the strategy outlined for `LePhare` in the previous section, with the primary difference being the source of the population synthesis templates and how they are fit to the observed photometry. This computation uses a set of 17 templates derived from the Flexible Stellar Population Synthesis models (Conroy et al. 2009; Conroy & Gunn 2010) with a variety of dust attenuation and ages from log-normal star formation histories that are chosen to broadly span the rest-frame UVJ color-space populated by galaxies over $0 < z < 3$. For each galaxy in the catalog, `EAZY` fits a non-negative linear combination of these templates integrated through the redshifted filter bandpasses to the observed flux densities and associated uncertainties. In this way, `EAZY` fits combinations of dust attenuation and star-formation histories to efficiently span the continuous color space populated by the majority of galaxies across the survey. For the `EAZY` photo-z estimates, the Subaru Suprime-Cam

[8] https://www.github.com/gbrammer/eazy-py

broad-band photometric measurements are not used, as these are generally significantly shallower than other nearby filters. Furthermore, the GALEX FUV + NUV and IRAC channel 3 and 4 photometry are ignored, as these bands are relatively shallow and have broad PSFs that are difficult to rectify with the other deeper filters.

As with `LePhare`, `EAZY` iteratively derives multiplicative corrections to both the individual photometric bands and the templates. With the comprehensive spectroscopic redshift catalog available here, photo-z of the fits are fixed to the spectroscopic value, though the iterations can also be performed deriving photo-z at each step, if there is a concern that objects with spectroscopic redshifts are a strongly biased subset of the target population for which photo-z are to be derived (i.e., the full catalog). At each step of the iteration, the median fractional residual is computed both for all bands individually and for all measurements in all bands sorted as a function of rest-frame wavelength. With many filters that overlap in the observed frame and galaxies across a broad range of redshifts, the catalog can largely break the degeneracy between systematic offsets in individual filters (e.g., from poor photometric calibration) and systematic effects resulting from the properties of the template set (e.g., continuum shape and emission line strengths). The correction routine is stopped after five iterations, where the updates are generally less than 1 %. The multiplicative corrections to the photometric bands, expressed in magnitude, are listed in Table 2.

For the final photometric redshift estimates, `EAZY` uses the "template error function" and apparent magnitude prior as described by Brammer et al. (2008).

5.3. *Photometric Redshift Validation*

One particular aspect of this work different from Laigle et al. (2016) is the availability of two photometric catalogs created with different methods to extract the photometry (see Section 3). By applying the same photo-z code to the CLASSIC and `The Farmer` catalogs, it is possible to assess if one method to extract the photometry produces better results than the other. This is done by quantifying the precision of the photo-z using the normalized median absolute deviation (NMAD, Hoaglin et al. 1983), defined as

$$\sigma_{\rm NMAD} = 1.48 \times \text{median}\left(\frac{|\Delta z - \text{median}(\Delta z)|}{1 + z_{\rm spec}}\right), \quad (3)$$

following Brammer et al. (2008) as it is less sensitive to outliers compared to the normal definition Ilbert et al. (e.g. 2006). The fraction of outliers is noted η and defined, following Hildebrandt et al. (2012), as galaxies whose photometric and spectroscopic redshifts deviate by $|\Delta z| > 0.15\,(1 + z_{\rm spec})$. Lastly, the bias is noted b and is defined as the median difference between photo-z and spec-z.

The comparisons between photo-z and spec-z are shown for both CLASSIC and `The Farmer` catalogs in combination with `LePhare` and `EAZY` in Figure 12 and summarized in Figure 17. As a general trend for both catalogs, the photo-z precision (given by σ_{NMAD}) is on the order of $0.01(1 + z)$ at $i < 22.5$, and the precision is degraded at fainter magnitude, but is still better than $0.025(1 + z)$ at $i < 25$. For both catalogs, there is a population of galaxies with $z_{\rm spec} > 2$ and $z_{\rm phot} < 1$.

Table 2. Values of the magnitude offsets used to optimize the absolute calibration in each band, derived with `LePhare` and `EAZY` for both photometric catalogs. When no value is indicated, the band was not used in the fit. The relative calibrations are normalized in K_s. Observed photometry may be corrected by adding the appropriate values.

Band	LePhare The Farmer	LePhare CLASSIC	EAZY The Farmer	EAZY CLASSIC
NUV	−0.352	−0.029	...	...
u	−0.077	−0.006	−0.196	...
u^*	−0.023	0.053	−0.054	−0.021
g	0.073	0.128	0.006	0.055
r	0.101	0.127	0.090	0.124
i	0.038	0.094	0.043	0.121
z	0.036	0.084	0.071	0.121
y	0.086	0.100	0.118	0.145
B	...	−0.075	...	...
V	...	0.123	...	...
r^+	...	0.035	...	...
i^+	...	0.051	...	...
z^{++}	...	0.095	...	...
*IB*427	−0.104	−0.013	−0.199	−0.133
*IB*464	−0.044	−0.008	−0.129	−0.098
*IA*484	−0.021	0.022	−0.084	−0.046
*IB*505	−0.018	0.025	−0.073	−0.037
*IA*527	−0.045	0.033	−0.087	−0.038
*IB*574	−0.084	−0.032	−0.124	−0.062
*IA*624	0.005	0.031	0.004	0.038
*IA*679	0.166	0.208	0.154	0.214
*IB*709	−0.023	−0.009	−0.022	0.024
*IA*738	−0.034	0.003	−0.030	0.022
*IA*767	−0.032	−0.015	−0.013	0.01
*IB*827	−0.069	−0.001	−0.057	0.022
*NB*711	−0.010	0.023	...	...
*NB*816	−0.064	−0.021	...	...
Y	0.054	0.049	0.078	0.085
J	0.017	0.025	0.047	0.057
H	−0.045	−0.044	−0.034	−0.036
K_s	0.000	0.000	0.000	0.000
*NB*118	...	−0.017	...	...
ch1	−0.212	−0.087	−0.102	0.021
ch2	−0.219	−0.111	−0.044	0.025

This population is explained by the misidentification between the Lyman and Balmer breaks in the observed SED. This degeneracy appears clearly when comparing the photo-z derived for the full catalogs in Figure 13, especially in the faint regime when the degraded signal-to-noise is not sufficient to well constrain the position of the break. The same figure also shows a simple demonstration of the remarkable similarity between the catalogs with the same photo-z code (`LePhare`) and the photo-z codes with the same catalog (`The Farmer`). The photo-z quality is similar between both catalogs, with a slight trend of having better results at $i < 22.5$ for the Classic catalog, while `The Farmer` catalog provides better results at fainter magnitudes.

The photo-z uncertainties are also an important aspect of the photo-z quality. If well estimated, the fraction of spec-z which belong to the interval $\left[z_{\rm phot}^{\rm min}, z_{\rm phot}^{\rm max}\right]$ should be at 0.68. Figure 14 shows the cumulative distribution of the ratio between $|z_{\rm phot} - z_{\rm spec}|$ and the 1σ uncertainty derived for the `LePhare` photo-z solutions. The 1σ uncertainty is defined as the maximum between $(z_{\rm phot} - z_{\rm phot}^{\rm min})$ and $z_{\rm phot}^{\rm max} - z_{\rm phot}$. The cumulative distribution does not reach 0.68 at $i > 22.5$, which indicates that the photo-z 1σ uncertainties are underestimated. However, the uncertainties remain slightly underestimated despite the factor 2 applied to the flux uncertainties when running `LePhare` or `EAZY`. This effect was already seen in Laigle et al. (2016). No attempt has been made to artificially increase the size of the photo-z uncertainties since this effect could be caused by a selection bias in our spectroscopic sample of faint galaxies. The effect is more pronounced in the `The Farmer` catalog since photometric uncertainties are not re-scaled at the level of the photometric catalog, as it is done for the Classic catalog (see Section 4.3). Part of the differences between `The Farmer` and Classic is explained by the larger photometric uncertainties associated to Classic (see Sec.4.3). These larger uncertainties explains the more realistic photo-z errors in Classic, and may also help to explain the lower precision for faint sources as the photo-z are more uncertain.

Figure 15 illustrates the evolution with redshift of the 1σ photo-z uncertainties in several i-band magnitude bins, as derived from the `LePhare` photo-z. There is an increase of the 1σ uncertainty between $z < 1$ and $1.5 < z < 2.5$. This increase is explained by the Balmer break being shifted out of the medium band coverage, as well as blue galaxies at high redshift with low signal-to-noise in the near-infrared bands. Since the photo-z based on the Classic catalog are estimated using similar techniques as Laigle et al. (2016), the photo-$z$uncertainties computed with both catalogs can be compared. For this comparison, the photo-z uncertainties in both catalogues are re-scaled in order to make them consistent with 68 % of the spec-z falling into the 1σ error[9]. The result is this comparison is that the photo-z are improved at $1.4 < z < 3$ at all magnitudes owing to the gain in UltraVISTA depth, and at faint magnitudes ($i > 25$) over the full redshift range thanks to the new HSC data. While COSMOS2015 photo-z were unreliable at $i > 26$, the new catalog can be used also at fainter magnitude, depending on the scientific application. It is possible to approximately match the photo-z uncertainties of COSMOS2020 to those of COSMOS2015 by shifting COSMOS2020 by 0.7 magnitude.

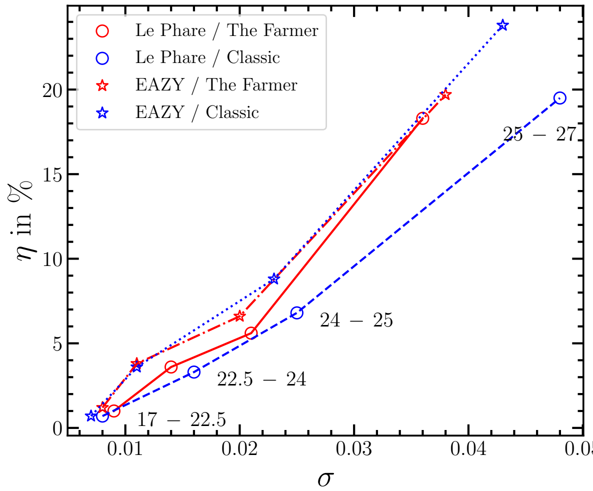

Figure 17. Comparison between the precision (σ_{NMAD}) and the outlier fraction for the two catalogues (the Classic in blue and `The Farmer` in red), and for the two photo-z codes (`LePhare` with circles and `EAZY` with stars). The statistics are computed per i-band apparent magnitude bin, as indicated on the side of the points.

Figure 16 shows the photo-z distribution of sources common to both catalogs in four selections of H-band magnitude. As expected, the mean redshift increases toward faint magnitude from $z \sim 0.82$ at $H < 22$ to $z \sim 1.37$ at $H < 25$. There is an excellent agreement between the mean redshifts of both catalogs, within $\sim 0.01 - 0.02$. The mainly near-infrared selection in $izYJHK_s$ allows for the detection of a significant sample of galaxies above $z > 6$ ($100 - 300$ at $H < 25$ depending on the catalog). `The Farmer` catalog includes an higher density of $z > 6$

[9] the COSMOS2020 photo-z uncertainties are re-scaled by a factor $1 + 0.1\,(i - 21)$ for the galaxies fainter than $i > 21$. Applying the same method and using the new spec-z sample, the COSMOS2015 photo-z uncertainties are re-scaled by a factor 1.3.

sources (by a factor almost two in the faintest bin). This is discussed in detail in Kauffmann et al. (in prep.).

6. PHYSICAL PROPERTIES OF COSMOS GALAXIES

Now a first characterization of the sources classified as galaxies in Section 5.1 can be described. Physical properties such as absolute magnitudes and stellar mass are computed through `LePhare` with the same configuration used for COSMOS2015: a template library generated by BC03 models is fit to the observed photometry after fixing the redshift of each target to the photo-z estimated in the previous `LePhare` run (for more details, see Laigle et al. 2016).

The present analysis is limited to a classification of COSMOS2020 galaxies between star forming and quiescent, and a subsequent determination of their stellar mass completeness as a function of redshift; further investigation is deferred to future studies. Moreover, the following illustrates only the results generated with `The Farmer` and `LePhare` to provide the most direct comparison to Laigle et al. (2016) template fitting while demonstrating the effectiveness of the new `The Farmer` photometry. There are no significant differences when repeating the analysis with either Classic photometric baseline or `EAZY`.

6.1. *Galaxy classification*

Previous studies have devised a variety of techniques to identify quiescent galaxies by means of broad-band photometry. To this purpose, Williams et al. (2009) provides a prescription utilizing $U-V$ and $V-J$ rest-frame colors which has been broadly adopted in the literature (e.g., Muzzin et al. 2013; Tomczak et al. 2014). Ilbert et al. (2013) and Arnouts et al. (2013) proposed to improve the selection by replacing $U-V$ with NUV $-\, r$, since the latter can better separate galaxies with different star formation histories (see also Leja et al. 2019).

This analysis adopts the rest-frame NUV $-\, r$ vs. $r-J$ diagram described in Ilbert et al. (2013), where quiescent galaxies are defined to be those with $M_{\rm NUV} - M_r > 3\,(M_r - M_J) + 1$ and $M_{\rm NUV} - M_r > 3.1$. Measurements are provided by `LePhare` by convolving the best-fit template with the appropriate passband in the observed frame. Figure 18 shows the restframe $NUVrJ$ color-color diagram in six redshift bins from $z = 0.1$ to 6. The assembly of the quiescent population at late cosmic times is evident, along with the corresponding decrease in the star-forming population. Quiescent galaxies are rare at $z > 2$ (e.g., Ilbert et al. 2013; Muzzin et al. 2013; Tomczak et al. 2014; Davidzon et al. 2017) but the large cosmic volume probed by COSMOS allows us to identify a significant number of candidates. However, a portion of them are expected to be star-forming galaxies that contaminate the high-z quiescent locus due to large uncertainties in their rest-frame colors (especially at $z > 2.6$ where M_J corresponds to observed wavelengths redder than channel 2).

6.2. *Stellar Mass Completeness*

The stellar mass completeness of our galaxy sample is empirically computed following the method described in Pozzetti et al. (2010), discriminating between star-forming and quiescent populations. This method is commonly used in the literature (e.g., Ilbert et al. 2013; Moustakas et al. 2013). It converts the detection limit of a given survey, given by the apparent magnitude $m_{\rm lim}$, into a redshift-dependent threshold in stellar mass $M_{\rm lim}$ computed using the mass-to-light ratio of galaxies brighter than $m_{\rm lim}$. Their stellar masses, estimated via template fitting, are re-scaled by a factor $10^{-0.4(m_i - m_{\rm lim})}$, where m_i is the magnitude of the i-th galaxy. One can determine $M_{\rm lim}$ in a given redshift bin from the distribution of such re-scaled masses: e.g., their 95$^{\rm th}$ percentile can define the smallest mass at which most of the objects would still be observable.

The case of COSMOS2020 is more complicated because it is now possible to quantify $m_{\rm lim}$ not in a single band but for the `CHI_MEAN` $izYJHK_s$ detection image itself. Adopting the sensitivity limit in the K_s band (Table 1) is a conservative choice that disregards the numerous NIR-faint objects detected thanks to the deep HSC photometry. This bias has already been discussed for COSMOS2015 (see Davidzon et al. 2017) and it is now more relevant after the addition of the i-band in the `CHI_MEAN` image which was not considered in 2015. Therefore the analysis proceeds as in Davidzon et al. (2017) by computing $m_{\rm lim}$ in IRAC channel 1, using CANDELS (Nayyeri et al. 2017) as a reference parent catalog[10]. Source completeness in channel 1 is related not only to the properties of the IRAC mosaic itself, but also to the depth of the $izYJHK_s$ image, which is used as a prior for source extraction (Section 3.1.4 and 3.2.1). Moreover, channel 1 probes the bulk of stellar mass at $z > 2.5$, where the Balmer break is shifted beyond the optical-NIR bands.

A common sample is constructed by cross-matching IRAC channel 1 sources of COSMOS2020 to the deeper CANDELS catalog in the ~ 200 arcmin^2 where the two overlap. At $m_{\rm lim} = 26$ mag, about 75 % of the CAN-

[10] In the COSMOS field, CANDELS detection image *HST*/F160W has a 5σ limit at 27.56 mag within 0.″34 diameter apertures, corresponding to twice the PSF FWHM.

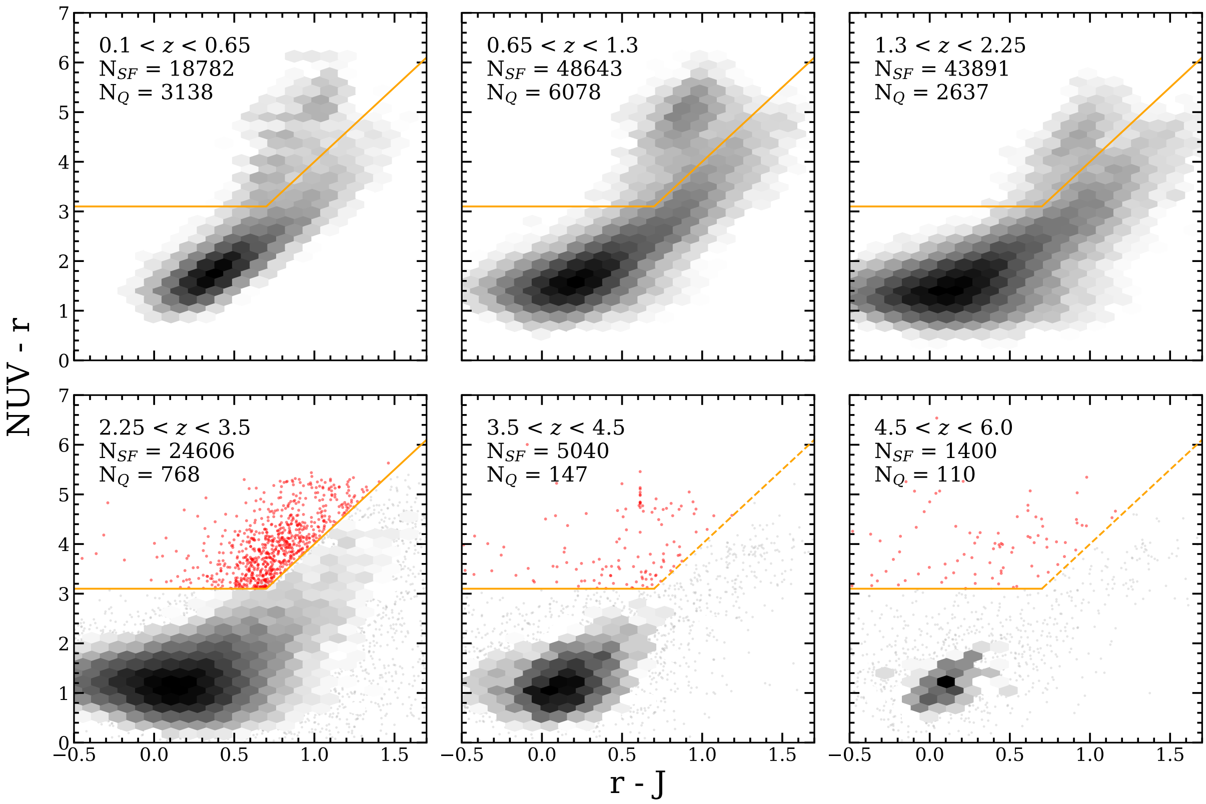

Figure 18. Identification of quiescent galaxies in bins of redshift by selection in rest frame NUV $-r$ and $r-J$ colours using the `LePhare` results computed with `The Farmer` for sources which lie above their respective mass completeness limit. Selection is made using the prescription of Ilbert et al. (2013) shown in yellow. Owing to sparsity, quiescent galaxies at $z > 2.25$ are shown by individual red points. $r-J$ colors are highly uncertain at $z > 2.6$ where the rest-frame M_J is unconstrained by observations, and hence have an uncertain classification marked by the yellow dashed line.

DELS sources are also recovered by `The Farmer`[11]; the completeness at that magnitude was $< 50\,\%$ in COSMOS2015. With $m_{\rm lim}$ in hand, galaxy masses are re-scaled to compute $M_{\rm lim}$ in bins of redshift (see Figure 19), to which a polynomial function in $1+z$ if fitted. The result is $M_{\rm lim}(z) = -1.46\times10^7(1+z)+7.60\times10^7(1+z)^2$ for $z < 6.0$, which is more complete by $\sim$0.5 dex compared to Davidzon et al. (2017). Since the boundary used here is the 95th percentile of the re-scaled mass distribution and the choice of $m_{\rm lim}$ already implied that about 25% of the objects are missing, it is expected that $M_{\rm lim}$ corresponds to a 70% completeness threshold.

The procedure is repeated separately for the star-forming and the quiescent sample, both shown in Figure 19. Quiescent galaxies start to be incomplete at stellar masses 0.4 dex higher than the total sample since they have larger mass-to-light ratios. $M_{\rm lim}$ at $z < 2.5$ is additionally computed starting from the K_s limit (Table 1) and following precisely the procedure of Laigle et al. (2016). However, due to the nearly uniform coverage of the new data set, there is not a significant difference between the completeness limits of the ultra-deep and deep regions. The K_s-based completeness is fit by the function $M_{\rm lim}(z) = -3.55\times10^8(1+z) + 2.70\times10^8(1+z)^2$ for $z < 2.5$ and is more complete by 0.5 dex compared to the same threshold found in COSMOS2015 (Laigle et al. 2016).

7. CONCLUSIONS

This paper describes the creation and validation of COSMOS2020, a new set of two multi-wavelength catalogs of the distant Universe, each of which includes photometric redshifts and other physical parameters computed from two independent codes. COSMOS2020 builds on more than a decade of panchromatic observations on the COSMOS field. Compared to previous

[11] The fraction of recovered CANDELS sources is the same with the Classic catalog.

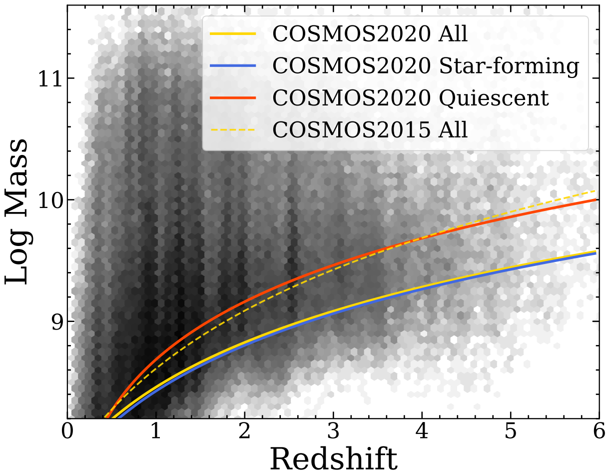

Figure 19. Mass completeness for the total sample (yellow), as well as the star-forming (blue) and quiescent (red) populations using quantities derived from `The Farmer` and `LePhare` considering magnitude limits of IRAC channel 1. Limits are calculated based on the method introduced in Pozzetti et al. (2010) in a manner consistent with COSMOS2015 (Davidzon et al. 2017, yellow dashed). For visual clarity, the total sample limit has been raised by 0.02 dex so that both it and the star-forming limit are visible.

releases, COSMOS2020 features significantly deeper optical, infrared, and near-infrared data all tied to a highly precise astrometric reference frame, Gaia DR2.

Starting from a very deep multi-band detection image and using two different photometric extraction codes, one based on aperture photometry and one based on a profile-fitting technique, two photometric catalogs have been extracted. These photometric catalogs were then used to estimate photometric redshifts and stellar masses using two different codes, `LePhare` and `EAZY`. This enables us, for the first time, to make a robust estimate of the systematic errors introduced by photometric extraction and photometric redshift estimation over a large redshift baseline with an unprecedented number of objects over $2\,\mathrm{deg}^2$. Our results show that all methods are in remarkable agreement. Comparing to COSMOS2015, COSMOS2020 gains almost one order of magnitude in photometric redshift precision compared to Laigle et al. (2016). In the brightest bin, $i < 22.5$, the catalogs reach sub-percent redshift precision and outlier fraction. Even in the faintest $25 < i < 27$ bins, photometric redshift precision is still $\sim 4\,\%$ with an outlier fraction of $\sim 20\,\%$. A detailed comparison shows that at bright magnitudes the classic aperture catalog is marginally superior whereas at faint magnitudes the trend is reversed with the profile fitting technique providing a better result. This close agreement provides a unique validation of our measurement and photometric redshift techniques. Superseding our previous catalogues, COSMOS2020 represents an unparalleled deep and wide picture of the distant Universe. It will be of invaluable assistance in preparing for the next generation of large telescopes and surveys.

One can already start to imagine what COSMOS2025 might contain. After fifteen years of observations, the UltraVISTA survey will have been completed, providing an unparalleled near-infrared view of COSMOS. These data, combined with the *Spitzer* data presented here, will lay the foundation for a next-generation catalog combining deep high-resolution optical and infrared imaging data from *Euclid* with ultra-deep optical data from *Rubin*. Such a catalog will be an important step towards producing a mass-complete survey comprising every single galaxy in a representative volume from the present day to the epoch of reionization.

This paper is dedicated to Olivier Le Fèvre. Spectroscopic redshifts from his VIMOS instrument (often collected in surveys that he designed and led) played an invaluable role in preparing this catalog.

The authors would like to thank Nathaniel Strickley, Kate Gould, Dustin Lang, and Emmanuel Bertin for helpful discussions. We gratefully acknowledge the contributions of the entire COSMOS collaboration consisting of more than 100 scientists. The HST COSMOS program was supported through NASA grant HST-GO-09822. More information on the COSMOS survey is available at http://www.astro.caltech.edu/cosmos.

The authors wish to recognize and acknowledge the very significant cultural role and reverence that the summit of Mauna Kea has always had within the indigenous Hawaiian community. We are most fortunate to have the opportunity to conduct observations from this mountain. This work is based on data products from observations made with ESO Telescopes at the La Silla Paranal Observatory under ESO program ID 179.A-2005 and on data products produced by CALET and the Cambridge Astronomy Survey Unit on behalf of the UltraVISTA consortium. This work is based in part on observations made with the NASA/ESA Hubble Space Telescope, obtained from the Data Archive at the Space Telescope Science Institute, which is operated by the Association of Universities for Research in Astronomy, Inc., under NASA contract NAS 5-26555. Some of the data presented herein were obtained at the W.M. Keck Observatory, which is operated as a scientific partnership among the California Institute of Technology, the University of California and the National Aeronautics and Space Administration. The Observatory was made possible by the generous financial support of the W.M. Keck Foundation. This research is also partly supported by the Centre National d'Etudes Spatiales (CNES).

The Cosmic Dawn Center (DAWN) is funded by the Danish National Research Foundation under grant No. 140. ST, GB and JW acknowledge support from the European Research Council (ERC) Consolidator Grant funding scheme (project ConTExt, grant No. 648179). OI acknowledges the funding of the French Agence Nationale de la Recherche for the project "SAGACE". HJMcC acknowledges support from the PNCG. ID has received funding from the European Union's Horizon 2020 research and innovation programme under the Marie Skłodowska-Curie grant agreement No. 896225. This work used the CANDIDE computer system at the IAP supported by grants from the PNCG and the DIM-ACAV and maintained by S. Rouberol. BMJ is supported in part by Independent Research Fund Denmark grant DFF - 7014-00017. CMC thanks the National Science Foundation for support through grants AST-1714528, AST-1814034 and AST-2009577, and additionally the University of Texas at Austin College of Natural Sciences, and the Research Corporation for Science Advancement from a 2019 Cottrell Scholar Award sponsored by IF/THEN, an initiative of Lydia Hill Philanthropies. The work of DS was carried out at the Jet Propulsion Laboratory, California Institute of Technology, under a contract with NASA. GEM acknowledges the Villum Fonden research grant 13160 "Gas to stars, stars to dust: tracing star formation across cosmic time". DR acknowledges support from the National Science Foundation under grant numbers AST-1614213 and AST-1910107. D.R. also acknowledges support from the Alexander von Humboldt Foundation through a Humboldt Research Fellowship for Experienced Researchers. MS acknowledges the support of the Natural Sciences and Engineering Research Council of Canada (NSERC)

This research made use of several software packages including numpy (van der Walt et al. 2011), matplotlib (Hunter 2007), and Astropy, a community-developed core Python package for Astronomy (Astropy Collaboration et al. 2013).

Each author contributed to the paper as follows: AM, HJMcC, PC, SG processed the imaging data; JW, OK, ID, MSh, BCH produced the photometric catalogs; JW, OI, GB produced the photometric redshifts and physical parameters catalogs; HJMcC, ST supervised this study. All these authors contributed to the validation and testing of the catalogues. The second group of authors (CL to DS) covers those who have either made a significant contribution to assemble the data products or to the scientific analysis. The remaining authors (SA to GZ) contributed in a some way to the data products, conceptualization, validation, and/or analysis of this work.

REFERENCES

Aihara, H., Allende Prieto, C., An, D., et al. 2011, ApJS, 193, 29

Aihara, H., Arimoto, N., Armstrong, R., et al. 2018, PASJ, 70, S4

Aihara, H., AlSayyad, Y., Ando, M., et al. 2019, Publications of the Astronomical Society of Japan, 71, 114. http://adsabs.harvard.edu/abs/2019PASJ...71..114A

Albrecht, A., Bernstein, G., Cahn, R., et al. 2006, arXiv e-prints, astro

Arnouts, S., Moscardini, L., Vanzella, E., et al. 2002, MNRAS, 329, 355. http://adsabs.harvard.edu/abs/2002MNRAS.329..355A

Arnouts, S., Walcher, C. J., Le Fèvre, O., et al. 2007, A&A, 476, 137

Arnouts, S., Le Floc'h, E., Chevallard, J., et al. 2013, A&A, 558, A67

Ashby, M. L. N., Willner, S. P., Fazio, G. G., et al. 2013, The Astrophysical Journal, 769, 80. http://adsabs.harvard.edu/abs/2013ApJ...769...80A

—. 2015, The Astrophysical Journal Supplement Series, 218, 33. http://adsabs.harvard.edu/abs/2015ApJS..218...33A

Ashby, M. L. N., Caputi, K. I., Cowley, W., et al. 2018, The Astrophysical Journal Supplement Series, 237, 39. http://adsabs.harvard.edu/abs/2018ApJS..237...39A

Astropy Collaboration, Robitaille, T. P., Tollerud, E. J., et al. 2013, A&A, 558, A33

Baraffe, I., Homeier, D., Allard, F., & Chabrier, G. 2015, A&A, 577, A42

Barbary, K. 2016, The Journal of Open Source Software, 1, 58. http://joss.theoj.org/papers/10.21105/joss.00058

Beckwith, S. V. W., Stiavelli, M., Koekemoer, A. M., et al. 2006, AJ, 132, 1729

Bertin, E. 2006, in Astronomical Society of the Pacific Conference Series, Vol. 351, Astronomical Data Analysis Software and Systems XV, ed. C. Gabriel, C. Arviset, D. Ponz, & S. Enrique, 112

Bertin, E. 2013, Astrophysics Source Code Library, ascl:1301.001. http://adsabs.harvard.edu/abs/2013ascl.soft01001B

Bertin, E., & Arnouts, S. 1996, A&AS, 117, 393. http://adsabs.harvard.edu/abs/1996A%26AS..117..393B
Bertin, E., Mellier, Y., Radovich, M., et al. 2002, in Astronomical Society of the Pacific Conference Series, Vol. 281, Astronomical Data Analysis Software and Systems XI, ed. D. A. Bohlender, D. Durand, & T. H. Handley, 228
Bielby, R., Hudelot, P., McCracken, H. J., et al. 2012, A&A, 545, A23. http://adsabs.harvard.edu/abs/2012A%26A...545A..23B
Bigourdan, G. 1888, Bulletin Astronomique, Serie I, 5, 303
Bohlin, R. C., Colina, L., & Finley, D. S. 1995, AJ, 110, 1316
Boulade, O., Charlot, X., Abbon, P., et al. 2003, in Society of Photo-Optical Instrumentation Engineers (SPIE) Conference Series, Vol. 4841, Proc. SPIE, ed. M. Iye & A. F. M. Moorwood, 72–81
Bowler, R. A. A., Jarvis, M. J., Dunlop, J. S., et al. 2020, MNRAS, 493, 2059
Brammer, G. B., van Dokkum, P. G., & Coppi, P. 2008, ApJ, 686, 1503
Bruzual, G., & Charlot, S. 2003, Monthly Notices of the Royal Astronomical Society, 344, 1000. http://adsabs.harvard.edu/abs/2003MNRAS.344.1000B
Calzetti, D., Armus, L., Bohlin, R. C., et al. 2000, The Astrophysical Journal, 533, 682. http://adsabs.harvard.edu/abs/2000ApJ...533..682C
Capak, P., Aussel, H., Ajiki, M., et al. 2007, The Astrophysical Journal Supplement Series, 172, 99. http://adsabs.harvard.edu/abs/2007ApJS..172...99C
Capak, P. L., Riechers, D., Scoville, N. Z., et al. 2011, Nature, 470, 233
Caputi, K. I., Ilbert, O., Laigle, C., et al. 2015, ApJ, 810, 73
Casey, C. M., Berta, S., Béthermin, M., et al. 2012, ApJ, 761, 140
Casey, C. M., Cooray, A., Capak, P., et al. 2015, ApJL, 808, L33
Casey, C. M., Zavala, J. A., Aravena, M., et al. 2019, ApJ, 887, 55
Chabrier, G., Baraffe, I., Allard, F., & Hauschildt, P. 2000, ApJ, 542, 464
Civano, F., Marchesi, S., Comastri, A., et al. 2016, ApJ, 819, 62
Civano, F., Marchesi, S., Comastri, A., et al. 2016, The Astrophysical Journal, 819, 62. http://adsabs.harvard.edu/abs/2016ApJ...819...62C
Comparat, J., Richard, J., Kneib, J.-P., et al. 2015, A&A, 575, A40
Conroy, C., & Gunn, J. E. 2010, ApJ, 712, 833
Conroy, C., Gunn, J. E., & White, M. 2009, ApJ, 699, 486
Coupon, J., Czakon, N., Bosch, J., et al. 2018, PASJ, 70, S7
Coupon, J., Ilbert, O., Kilbinger, M., et al. 2009, A&A, 500, 981
Cucciati, O., Lemaux, B. C., Zamorani, G., et al. 2018, A&A, 619, A49
Daddi, E., Cimatti, A., Renzini, A., et al. 2004, ApJ, 617, 746
Dahlen, T., Mobasher, B., Faber, S. M., et al. 2013, ApJ, 775, 93
Davidzon, I., Ilbert, O., Laigle, C., et al. 2017, A&A, 605, A70
De Santis, C., Grazian, A., Fontana, A., & Santini, P. 2007, NewA, 12, 271
Dey, A., Schlegel, D. J., Lang, D., et al. 2019, AJ, 157, 168
Fitzpatrick, E. L., & Massa, D. 1986, The Astrophysical Journal, 307, 286. http://adsabs.harvard.edu/abs/1986ApJ...307..286F
Fontana, A., Dunlop, J. S., Paris, D., et al. 2014, A&A, 570, A11
Förster Schreiber, N. M., Genzel, R., Bouché, N., et al. 2009, ApJ, 706, 1364
Gaia Collaboration, Brown, A. G. A., Vallenari, A., et al. 2016, Astronomy & Astrophysics, 595, A2. http://www.aanda.org/10.1051/0004-6361/201629512
—. 2018, Astronomy & Astrophysics, 616, A1. https://www.aanda.org/10.1051/0004-6361/201833051
Giavalisco, M., Ferguson, H. C., Koekemoer, A. M., et al. 2004, ApJL, 600, L93
Grogin, N. A., Kocevski, D. D., Faber, S. M., et al. 2011, ApJS, 197, 35
Gruen, D., Seitz, S., & Bernstein, G. M. 2014, PASP, 126, 158
Gruppioni, C., Pozzi, F., Rodighiero, G., et al. 2013, MNRAS, 432, 23
Gwyn, S. D. J. 2008, PASP, 120, 212
Hasinger, G., Capak, P., Salvato, M., et al. 2018, ApJ, 858, 77
Heintz, K. E., Fynbo, J. P. U., Møller, P., et al. 2016, A&A, 595, A13
Hildebrandt, H., Erben, T., Kuijken, K., et al. 2012, MNRAS, 421, 2355
Hoaglin, D. C., Mosteller, F., & Tukey, J. W. 1983, Understanding robust and exploratory data analysis, Wiley Series in Probability and Mathematical Statistics, (John Wiley,)
Hsieh, B.-C., Wang, W.-H., Hsieh, C.-C., et al. 2012, The Astrophysical Journal Supplement Series, 203, 23. https://doi.org/10.1088%2F0067-0049%2F203%2F2%2F23
Hubble, E. 1934, ApJ, 79, 8

Hung, C.-L., Casey, C. M., Chiang, Y.-K., et al. 2016, ApJ, 826, 130
Hunter, J. D. 2007, Computing in Science Engineering, 9, 90
Ilbert, O., Arnouts, S., McCracken, H. J., et al. 2006, A&A, 457, 841. http://adsabs.harvard.edu/abs/2006A%26A...457..841I
Ilbert, O., Capak, P., Salvato, M., et al. 2009, ApJ, 690, 1236
Ilbert, O., McCracken, H. J., Le Fèvre, O., et al. 2013, Astronomy and Astrophysics, 556, A55. http://adsabs.harvard.edu/abs/2013A%26A...556A..55I
Ilbert, O., Arnouts, S., Le Floc'h, E., et al. 2015, A&A, 579, A2
Ishigaki, M., Kawamata, R., Ouchi, M., et al. 2018, ApJ, 854, 73
Jin, S., Daddi, E., Liu, D., et al. 2018, The Astrophysical Journal, 864, 56. http://adsabs.harvard.edu/abs/2018ApJ...864...56J
Karim, A., Schinnerer, E., Martínez-Sansigre, A., et al. 2011, ApJ, 730, 61
Kashino, D., Silverman, J. D., Sanders, D., et al. 2019, ApJS, 241, 10
Koekemoer, A. M., Aussel, H., Calzetti, D., et al. 2007, ApJS, 172, 196. https://ui.adsabs.harvard.edu/abs/2007ApJS..172..196K/abstract
Koekemoer, A. M., Faber, S. M., Ferguson, H. C., et al. 2011, ApJS, 197, 36
Kohonen, T. 1982, Biol. Cybern., 43, 59
Kron, R. G. 1980, ApJS, 43, 305. http://adsabs.harvard.edu/abs/1980ApJS...43..305K
Labbé, I., Franx, M., Rudnick, G., et al. 2003, AJ, 125, 1107
Laidler, V. G., Papovich, C., Grogin, N. A., et al. 2007, PASP, 119, 1325
Laigle, C., McCracken, H. J., Ilbert, O., et al. 2016, ApJS, 224, 24. http://adsabs.harvard.edu/abs/2016ApJS..224...24L
Laigle, C., Pichon, C., Arnouts, S., et al. 2018, MNRAS, 474, 5437
Lang, D., Hogg, D. W., & Mykytyn, D. 2016, Astrophysics Source Code Library, ascl:1604.008. http://adsabs.harvard.edu/abs/2016ascl.soft04008L
Laureijs, R., Amiaux, J., Arduini, S., et al. 2011, arXiv e-prints, arXiv:1110.3193
Le Fèvre, O., Saisse, M., Mancini, D., et al. 2003, in Society of Photo-Optical Instrumentation Engineers (SPIE) Conference Series, Vol. 4841, Proc. SPIE, ed. M. Iye & A. F. M. Moorwood, 1670–1681
Le Fèvre, O., Cassata, P., Cucciati, O., et al. 2013, A&A, 559, A14
Le Fèvre, O., Tasca, L. A. M., Cassata, P., et al. 2015, A&A, 576, A79
Le Fèvre, O., Béthermin, M., Faisst, A., et al. 2019, arXiv e-prints, arXiv:1910.09517
Leauthaud, A., Massey, R., Kneib, J.-P., et al. 2007, ApJS, 172, 219. https://iopscience.iop.org/article/10.1086/516598/meta
Lee, N., Sanders, D. B., Casey, C. M., et al. 2015, ApJ, 801, 80
Legrand, L., McCracken, H. J., Davidzon, I., et al. 2019, MNRAS, 486, 5468
Leja, J., Tacchella, S., & Conroy, C. 2019, ApJL, 880, L9
Leslie, S., Schinnerer, E., Liu, D., et al. 2020, arXiv e-prints, arXiv:2006.13937
Lilly, S. J., Le Fèvre, O., Renzini, A., et al. 2007, ApJS, 172, 70
Madau, P., & Dickinson, M. 2014, ARA&A, 52, 415
Magnier, E. A., & Cuillandre, J. C. 2004, PASP, 116, 449
Mandelbaum, R. 2018, ARA&A, 56, 393
Marchesi, S., Civano, F., Elvis, M., et al. 2016, The Astrophysical Journal, 817, 34. http://adsabs.harvard.edu/abs/2016ApJ...817...34M
Massey, R., & Refregier, A. 2005, Monthly Notices of the Royal Astronomical Society, 363, 197. http://adsabs.harvard.edu/abs/2005MNRAS.363..197M
Massey, R., Rhodes, J., Ellis, R., et al. 2007, Nature, 445, 286
Masters, D. C., Stern, D. K., Cohen, J. G., et al. 2019, ApJ, 877, 81
McCracken, H. J., Milvang-Jensen, B., Dunlop, J., et al. 2012, Astronomy and Astrophysics, 544, A156. http://adsabs.harvard.edu/abs/2012A%26A...544A.156M
McCracken, H. J., Wolk, M., Colombi, S., et al. 2015, MNRAS, 449, 901
McLean, I. S., Steidel, C. C., Epps, H. W., et al. 2012, in Society of Photo-Optical Instrumentation Engineers (SPIE) Conference Series, Vol. 8446, Ground-based and Airborne Instrumentation for Astronomy IV, ed. I. S. McLean, S. K. Ramsay, & H. Takami, 84460J
Mehta, V., Scarlata, C., Capak, P., et al. 2018, ApJS, 235, 36
Merlin, E., Bourne, N., Castellano, M., et al. 2016, A&A, 595, A97
Milvang-Jensen, B., Freudling, W., Zabl, J., et al. 2013, A&A, 560, A94
Miyazaki, S., Komiyama, Y., Kawanomoto, S., et al. 2018, PASJ, 70, S1
Moffat, A. F. J. 1969, Astronomy and Astrophysics, 3, 455. http://adsabs.harvard.edu/abs/1969A%26A.....3..455M

Morley, C. V., Fortney, J. J., Marley, M. S., et al. 2012, ApJ, 756, 172
Morley, C. V., Marley, M. S., Fortney, J. J., et al. 2014, ApJ, 787, 78
Moustakas, J., Coil, A. L., Aird, J., et al. 2013, ApJ, 767, 50
Muzzin, A., Marchesini, D., Stefanon, M., et al. 2013, The Astrophysical Journal Supplement Series, 206, 8. http://adsabs.harvard.edu/abs/2013ApJS..206....8M
Muzzin, A., Marchesini, D., Stefanon, M., et al. 2013, ApJ, 777, 18
Nayyeri, H., Hemmati, S., Mobasher, B., et al. 2017, ApJS, 228, 7
Novak, M., Smolčić, V., Delhaize, J., et al. 2017, A&A, 602, A5
Nyland, K., Lacy, M., Sajina, A., et al. 2017, ApJS, 230, 9
Oke, J. B. 1974, ApJS, 27, 21. http://adsabs.harvard.edu/abs/1974ApJS...27...21O
Onodera, M., Renzini, A., Carollo, M., et al. 2012, ApJ, 755, 26
Pavesi, R., Riechers, D. A., Sharon, C. E., et al. 2018, ApJ, 861, 43
Peng, Y.-j., Lilly, S. J., Kovač, K., et al. 2010, ApJ, 721, 193
Pickles, A. J. 1998, PASP, 110, 863
Polletta, M., Tajer, M., Maraschi, L., et al. 2007, The Astrophysical Journal, 663, 81. http://adsabs.harvard.edu/abs/2007ApJ...663...81P
Pozzetti, L., Bolzonella, M., Zucca, E., et al. 2010, A&A, 523, A13
Prescott, M. K. M., Impey, C. D., Cool, R. J., & Scoville, N. Z. 2006, ApJ, 644, 100
Prevot, M. L., Lequeux, J., Maurice, E., Prevot, L., & Rocca-Volmerange, B. 1984, Astronomy and Astrophysics, 132, 389. http://adsabs.harvard.edu/abs/1984A%26A...132..389P
Riechers, D. A., Capak, P. L., Carilli, C. L., et al. 2010, ApJL, 720, L131
Riechers, D. A., Carilli, C. L., Capak, P. L., et al. 2014, ApJ, 796, 84
Riechers, D. A., Hodge, J. A., Pavesi, R., et al. 2020, ApJ, 895, 81
Robertson, B. E., Furlanetto, S. R., Schneider, E., et al. 2013, ApJ, 768, 71
Rodighiero, G., Daddi, E., Baronchelli, I., et al. 2011, ApJL, 739, L40
Rosani, G., Caminha, G. B., Caputi, K. I., & Deshmukh, S. 2020, A&A, 633, A159
Saito, S., de la Torre, S., Ilbert, O., et al. 2020, MNRAS, 494, 199
Salvato, M., Ilbert, O., & Hoyle, B. 2019, Nature Astronomy, 3, 212
Sanders, D. B., Salvato, M., Aussel, H., et al. 2007, ApJS, 172, 86
Saumon, D., & Marley, M. S. 2008, ApJ, 689, 1327
Sawicki, M., Arnouts, S., Huang, J., et al. 2019, Monthly Notices of the Royal Astronomical Society, 489, 5202. http://adsabs.harvard.edu/abs/2019MNRAS.489.5202S
Schlafly, E. F., & Finkbeiner, D. P. 2011, The Astrophysical Journal, 737, 103. http://adsabs.harvard.edu/abs/2011ApJ...737..103S
Schlegel, D. J., Finkbeiner, D. P., & Davis, M. 1998, The Astrophysical Journal, 500, 525. http://adsabs.harvard.edu/abs/1998ApJ...500..525S
Schreiber, C., Glazebrook, K., Nanayakkara, T., et al. 2018, A&A, 618, A85
Scoville, N., Aussel, H., Brusa, M., et al. 2007, ApJS, 172, 1. https://ui.adsabs.harvard.edu/abs/2007ApJS..172...1S/abstract
Scoville, N., Abraham, R. G., Aussel, H., et al. 2007, ApJS, 172, 38
Scoville, N., Arnouts, S., Aussel, H., et al. 2013, ApJS, 206, 3
Scoville, N., Lee, N., Vanden Bout, P., et al. 2017, ApJ, 837, 150
Smolčić, V., Novak, M., Bondi, M., et al. 2017, A&A, 602, A1
Stefanon, M., Labbé, I., Bouwens, R. J., et al. 2019, ApJ, 883, 99
Steinhardt, C. L., Speagle, J. S., Capak, P., et al. 2014, The Astrophysical Journal Letters, 791, L25. http://adsabs.harvard.edu/abs/2014ApJ...791L..25S
Stockmann, M., Toft, S., Gallazzi, A., et al. 2020, ApJ, 888, 4
Szalay, A. S., Connolly, A. J., & Szokoly, G. P. 1999, AJ, 117, 68
Taniguchi, Y., Scoville, N., Murayama, T., et al. 2007, The Astrophysical Journal Supplement Series, 172, 9. http://adsabs.harvard.edu/abs/2007ApJS..172....9T
Taniguchi, Y., Kajisawa, M., Kobayashi, M. A. R., et al. 2015, Publications of the Astronomical Society of Japan, 67, 104. http://adsabs.harvard.edu/abs/2015PASJ...67..104T
Tomczak, A. R., Quadri, R. F., Tran, K.-V. H., et al. 2014, ApJ, 783, 85
Troxel, M. A., MacCrann, N., Zuntz, J., et al. 2018, PhRvD, 98, 043528
Valentino, F., Tanaka, M., Davidzon, I., et al. 2020, ApJ, 889, 93
van der Walt, S., Colbert, S. C., & Varoquaux, G. 2011, Computing in Science Engineering, 13, 22

van der Wel, A., Noeske, K., Bezanson, R., et al. 2016, ApJS, 223, 29

Williams, R. E., Blacker, B., Dickinson, M., et al. 1996, AJ, 112, 1335

Williams, R. J., Quadri, R. F., Franx, M., van Dokkum, P., & Labbé, I. 2009, ApJ, 691, 1879

Zamojski, M. A., Schiminovich, D., Rich, R. M., et al. 2007, The Astrophysical Journal Supplement Series, 172, 468. http://adsabs.harvard.edu/abs/2007ApJS..172..468Z

APPENDIX

A. CATALOG DESCRIPTION

Table 3. SExtractor parameters used for the aperture detection and photometry.

Name	Value
ANALYSIS_THRESH	1.5
BACKPHOTO_THICK	30
BACKPHOTO_TYPE	LOCAL
BACK_FILTERSIZE	3
BACK_SIZE	128
BACK_TYPE	AUTO
CLEAN	Y
CLEAN_PARAM	1.0
DEBLEND_MINCONT	0.00001
DEBLEND_NTHRESH	32
DETECT_MAXAREA	100000
DETECT_MINAREA	5
DETECT_THRESH	1.5
DETECT_TYPE	CCD
FILTER	Y
FILTER_NAME	gauss_4.0_7x7.conv
GAIN	band-dependent
MAG_ZEROPOINT	band-dependent
MASK_TYPE	CORRECT
PHOT_APERTURES	13.33,20.00,47.33
PHOT_AUTOAPERS	13.3,13.3
PHOT_AUTOPARAMS	2.5,3.5
PHOT_FLUXFRAC	0.2,0.5,0.8
re-scale_WEIGHTS	N
SATUR_LEVEL	30000
THRESH_TYPE	ABSOLUTE
WEIGHT_GAIN	N
WEIGHT_TYPE	MAP_WEIGHT,MAP_WEIGHT

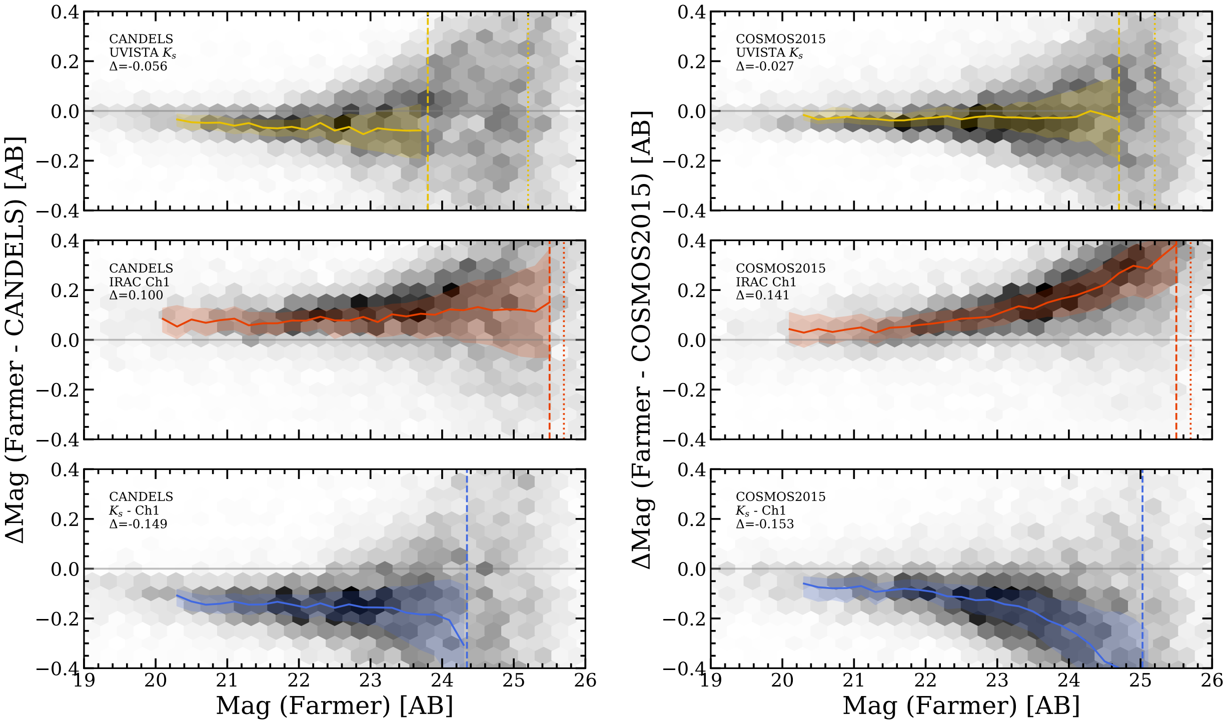

Figure 20. Comparison of broad-band K_s and IRAC channel 1 magnitudes and color between the `The Farmer` catalog of this work with those of CANDELS (Nayyeri et al. 2017) and COSMOS2015 (Laigle et al. 2016). Individual sources are shown by the underlying density histogram which is described by the overlaid median binned by 0.2 AB with an envelope containing 68 % of sources per bin. For the magnitudes, depths are shown for the comparison sample (dashed) and for COSMOS2020 (dotted), corresponding to 3σ depths measured with $3''$ diameter apertures. For colors, averaged 3σ depth computed from both bands of interest measured with $3''$ diameter apertures. The median Δ offset in magnitude are reported. for sources below the dashed magnitude limit.

B. PHOTOMETRIC COMPARISON FOR REFERENCE

The comparisons shown in Section 4 are here augmented by comparing this work to two well-know COSMOS-field catalogs in the literature for which this work is readily comparable: CANDELS (Nayyeri et al. 2017, using UltraVISTA DR1 and IRAC/SPLASH) and COSMOS2015 (Laigle et al. 2016, using UltraVISTA DR2 and IRAC/SPLASH). As shown in Figure 20, broad-band K_s and IRAC channel 1 magnitudes and their colors are compared up to the depth limit of the shallower literature data set indicated by the vertical dashed line. For fairness, the sample includes only the ∼18,000 sources which are common to all three catalogs with $0.6''$.

A brief analysis reveals three main points. Firstly, the COSMOS2020 depths exceed both those in CANDELS and COSMOS2015, as indicated by the vertical dashed and dotted lines, which manifests in the high scatter beyond the brightest magnitude limit. This restricts a meaningful comparison to sources below this limit. Secondly, the comparison with COSMOS2015 looks identical to the comparison of those bands between `The Farmer` and Classic, both in terms of offset and any trends with magnitude. This suggests that the Classic photometry is highly consistent with COSMOS2015, as verified directly during the catalog preparation process. Finally, the comparison of the `The Farmer` photometry with CANDELS is broadly similar. Although the K_s offset is larger than in comparisons with COSMOS2015 and Classic, the trend with magnitude in channel 1 is more constant than with either COSMSO2015 or Classic. The differences in K_s and channel 1 are similarly reflected in the colors, being more constant when comparing with CANDELS but not COSMOS2015. The similarity in the comparison with COSMOS2015 and Classic is expected, since both employed the same methodologies, by design. Similarly, the model-fitting employed in the IRAC photometry in CANDELS is more similar to that used by `The Farmer` and hence their agreement is unsurprising.

4. Identifying galaxies at high redshift

4.1. Introduction

The deep multi-wavelength imaging over the $2\,\mathrm{deg}^2$ of the COSMOS field provides an opportunity to search of high-redshift galaxies during the epoch of reionization. Since the rest-frame UV photons are redshifted to wavelengths $\lambda > 1\,\mu$m at $z > 6$, the detection of these rare, intrinsically bright galaxies mostly relies on the deep near-infrared images. Using previous data releases of the on-going UltraVISTA survey, galaxy samples were identified at $z > 6$ (Bowler et al. 2014; Bowler et al. 2015) and even $z > 8$ (Stefanon et al. 2017; Stefanon et al. 2019), giving strong constraints on the bright end of the galaxy UV luminosity function. Bowler et al. 2020 already used the latest UltraVISTA release (DR4), but did not have access to the deep optical images from HSC-SSP DR2 nor the final *Spitzer* images in the mid-infrared. With the COSMOS2020 photometric catalog, we have the possibility to provide updated results for the study of star-forming galaxies within the epoch of reionization. The deep near-infrared imaging from UltraVISTA still provides the core of the detection power, complemented with IRAC images from the Cosmic Dawn Survey to detect the galaxy rest-frame optical emission, and the optical HSC data to reject low-redshift contaminants. Furthermore, the combined analysis of both the Classic and `the Farmer` catalogs brings new insights in the selection of high-redshift galaxies, adding robustness to the sample of candidates.

In this chapter, I present the search for galaxies at $z > 7.5$ in the COSMOS field using the COSMOS2020 photometric catalog. The applied selection criteria and the resulting galaxy sample are described. These candidates are compared to the results from Stefanon et al. 2019 and Bowler et al. 2020 in the COSMOS field. Finally, I estimate the galaxy UV luminosity function at $8 \leq z \leq 10$. In the study, the standard ΛCDM cosmology is assumed, with $\Omega_m = 0.3$, $\Omega_\Lambda = 0.7$ and $H_0 = 70\,\mathrm{km\,s^{-1}\,Mpc^{-1}}$. Magnitudes are given in the AB system (Oke 1974).

4.2. Galaxy selection

We search for bright galaxy candidates at $z > 7.5$ in the COSMOS field using both COSMOS2020 catalogs. The selection is primarily based on photometric redshifts estimated from SED-fitting with `LePhare`, and on the posterior redshift probability distributions (PDFz). I computed photometric redshifts over the redshift range $0 < z < 10$ using 35 bands (see chapter 3). It is required that both the redshift of the minimum χ^2 template and the median redshift are at $z > 7.5$. The median redshift is estimated from the PDFz, which is obtained after marginalization over all the galaxy templates (see Sect. 1.6.2). The minimum χ^2 redshift describes the galaxy template with the minimum χ^2 among all templates at all redshifts, which is not necessarily at the peak of the PDFz. In the case of multimodal or broad PDFz, the location of the median may be uncertain, so the minimum χ^2 redshift may be used. By combining both of these estimators, we ensure that both the peak of the PDFz, and the majority of the PDFz weight, are located at high redshift.

The selected candidates are required to be brighter than $H = 25.6$ mag, and to be detected at 5σ in at least one band, at 3σ in at least two bands, and at 1σ in at least three bands, among the H, K_s, ch1 and ch2 bands. This ensures that at least two colors are reliable to estimate photometric redshifts. As a consequence, sources only detected in IRAC images are not included. Furthermore, the $z > 7.5$ galaxies are not expected to be detectable blueward of Lyman alpha at $(1 + z)\lambda = 1\,\mu$m, because of the absorption by the neutral IGM. We do not apply explicit magnitude cuts to the optical photometry, and instead rely on the results from SED-fitting. Sources with a strong detection in any of the optical bands are rejected through visual inspection. We exclusively search for candidates over the UltraVISTA area, and the sources located in the masked regions near bright stars in the HSC images are rejected. This corresponds to an area of $1.404\,\mathrm{deg}^2$. Using the Classic aperture photometry, only the bands with unsaturated photometry are used, based on the constructed flag images. We apply these selection criteria separately on both the Classic and `the Farmer` catalogs, and then check the results from the other catalog. Spurious sources and artifacts are rejected through the visual inspection of the science images.

With `the Farmer` catalog, the photometry is occasionally underestimated for sources in a number of heavily crowded regions or near bright stars, especially in the optical bands. In such regions, the photometry of all the grouped sources is simultaneously estimated. This may lead to high χ^2 in the surface brightnesss template-fitting, thus to unreliable photometry. The underestimated optical fluxes artificially form a break which may be interpreted as a Lyman break at high redshift. We emphasize that these sources are clearly visible in the optical images, and significantly detected in the Classic catalog. Therefore, these problematic candidates can be easily rejected through visual inspection. This concerns about 25 % of the pre-selected candidates from `the Farmer` catalog. It is not clear why the optical images are more affected than in the near-infrared, although the images are deeper in the optical, so this might be related to background subtraction. The photometry with `the Farmer` is currently under investigation to attempt to solve this issue.

The high-redshift galaxy samples at $z > 7$ are expected to be contaminated by cool brown dwarfs from the Milky Way (Sect. 1.6.3). The COSMOS field covers a relatively large area of the sky, so the potential number of brown dwarf contaminants is significant. Since the galaxies of interest are too faint to extract robust morphological parameters, brown dwarfs need to be separated based on observed colors. Brown dwarf templates were already fitted to the source photometry in the COSMOS2020 catalog (Sect. 3.4.5). Hence, we classify as brown dwarfs the sources for which the difference of significance is $\chi^2_{\rm gal} - \chi^2_{\rm star} > 0$, where $\chi^2_{\rm gal}$ and $\chi^2_{\rm star}$ are the reduced χ^2 for the best-fitted galaxy and stellar templates, respectively. The same criteria is applied in both the Classic and `the Farmer` catalogs. In the selected galaxy sample, four candidates are classified as brown dwarfs according to the Classic catalog, and two distinct candidates with `the Farmer`.

Since the high-redshift galaxies are directly selected from the COSMOS2020 catalog, the detection is performed using the combined $izYJHK_s$ image, which may not be optimized for $z > 8$ star-forming galaxies. These galaxies are not expected to be visible in the i and z bands, so that the signal may be diluted in the combined detection image. Nonetheless, the high-redshift candidates are primarily selected from colors, which necessitate significant detections in multiple broad bands. As discussed in Sect. 4.3.3, the high-redshift candidates identified in previous studies and undetected in the combined detection image are barely visible by eye in the H and K_s bands, resulting in limited precision on the photometric redshift estimates. Hence, the selected galaxy sample is not expected to be severely incomplete because of the combined $izYJHK_s$ detection, as long as the candidates present significant detections in multiple infrared bands.

4.3. Galaxy sample

The selected high-redshift galaxy sample consists of 36 candidates, including 21 new candidates which are not already presented in the literature. Table 4.1 and Table 4.2 present the coordinates, photometry, photometric redshifts and physical parameters of the selected candidates. The identifiers are from the Classic catalog, and are always indicated starting with the letters ID in the following discussion. The photometry is corrected for the Milky Way extinction and systematic zeropoint offsets. These zeropoint offsets are estimated from the SED-fitting of galaxies with spectroscopic redshifts (Sect. 3). We note that the photometry and physical parameters are from `the Farmer` catalog, except for the candidate ID1356755 for which the Classic results are used. For this candidate, the median photometric redshift is $z_{\rm phot} = 8.7$ using the Classic photometry and `LePhare`, whereas most of the PDFz weight computed with `the Farmer` catalog is at low redshift. The independent results from `EAZY` with `the Farmer` photometry attribute the higher photometric redshift of $z_{\rm phot} = 9.8$. For this reason, we still include this candidate into the galaxy sample using the Classic results.

All of the selected candidates have $24.5 < H < 25.6$ mag, except one particularly bright candidate ID454766 at $H = 24$ mag. With the tabulated photometric redshifts, the galaxy sample includes 15 candidates in the range $7.5 < z < 8.5$, 16 candidates at $8.5 < z < 9.5$ and 3 candidates at $z > 9.5$. There are two candidates (ID485056, ID1274544) with photometric redshifts $z = 7.4$ with `the Farmer` and at $z > 7.5$ with CLASSIC, so we still include them in the $z = 8$ galaxy sample.

One major result from this selection is the identification of galaxy candidates which are blended with nearby sources in the high-resolution images. These candidates are isolated thanks to the template-fitting photometry from `the Farmer`, and would be rejected using the CLASSIC selection only. For this reason, the next sections separately describe unblended and blended candidates. The high-redshift candidates previously identified in the COSMOS field by Stefanon et al. 2019 and Bowler et al. 2020 are discussed separately.

Figure 4.1 indicates the coordinates of the new and previously identified candidates over the COSMOS field. Most of the candidates are located in the UltraVISTA ultra-deep stripes. Few new candidates are located in the southern extremity of the easternmost ultra-deep stripe (at high right ascension), including imaging in UltraVISTA DR4 for the first time. This corner was masked up to DR3 (included), because of the unstable quantum efficiency of the detector. The processed region in DR4 therefore has a higher noise, particularly in the Y-band. Similarly, many new candidates are within the westernmost ultra-deep stripe (at low right ascension). This region is fully covered with optical HSC imaging, in particular with the deep SSP survey, which was not the case with the old Suprime-Cam data. However, the HSC imaging is about 0.5 mag shallower on the outer part of the field, so that the contamination by low-redshift galaxies is slightly more probable. This concerns 9 new candidates. In addition, 5 candidates are outside of the IRAC SPLASH layout, with limited mid-infrared constraints.

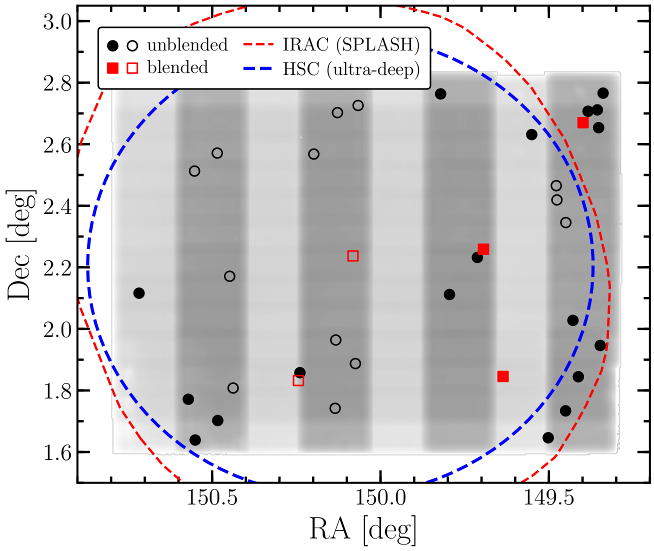

Figure 4.1. – Coordinates of the $z > 7.5$ candidates in the COSMOS field. The black and red markers are unblended and blended candidates, respectively. The empty markers are recovered, previously identified candidates from Stefanon et al. 2019 and Bowler et al. 2020. The background image is the UltraVISTA H-band weight map. The red dotted indicates the *Spitzer*/IRAC coverage of the SPLASH survey, and the blue dotted line represents the deep central region of the HSC images.

Table 4.1. – Coordinates and observed photometry of the selected $z > 7.5$ candidates. The first columns indicate the ID and coordinates from the CLASSIC catalog. The other columns give the photometry from `the Farmer` catalog, corrected for Milky Way extinction and systematic zeropoint offsets.

ID	R.A. [J2000]	Dec. [J2000]	J [mag]	H [mag]	K_s [mag]	ch1 [mag]	ch2 [mag]
234500	10:02:12.08	01:38:20.22	25.76 ± 0.12	25.60 ± 0.09	25.27 ± 0.10	24.67 ± 0.03	24.22 ± 0.02
241443	09:58:00.45	01:38:46.82	25.31 ± 0.07	24.87 ± 0.07	24.41 ± 0.06	23.97 ± 0.03	23.83 ± 0.02
295952	10:01:56.01	01:42:08.37	26.96 ± 0.20	25.17 ± 0.05	25.03 ± 0.07	26.80 ± 0.20	> 24.9
327551	09:57:48.08	01:44:01.39	25.47 ± 0.05	24.80 ± 0.04	25.03 ± 0.06	25.88 ± 0.15	26.07 ± 0.14
336101	10:00:32.32	01:44:31.22	25.68 ± 0.06	25.28 ± 0.05	25.59 ± 0.10	24.74 ± 0.02	24.44 ± 0.02
365776	10:02:16.98	01:46:16.88	> 25.0	25.28 ± 0.06	25.70 ± 0.13	25.68 ± 0.08	> 24.7
403992	10:01:45.04	01:48:28.42	25.96 ± 0.08	26.11 ± 0.12	25.99 ± 0.14	25.85 ± 0.10	25.00 ± 0.05
428351	10:00:58.48	01:49:55.97	25.27 ± 0.07	25.51 ± 0.12	25.26 ± 0.09	25.01 ± 0.04	25.07 ± 0.04
441697	09:57:39.01	01:50:40.05	26.02 ± 0.09	24.96 ± 0.05	24.89 ± 0.06	26.16 ± 0.21	24.30 ± 0.05
442053	09:58:32.63	01:50:43.59	25.95 ± 0.22	24.96 ± 0.12	25.08 ± 0.09	24.82 ± 0.04	24.54 ± 0.03
454766	10:00:57.43	01:51:27.89	26.01 ± 0.17	23.99 ± 0.04	23.85 ± 0.04	25.11 ± 0.04	24.32 ± 0.02
485056	10:00:17.89	01:53:14.39	25.99 ± 0.07	26.29 ± 0.13	27.24 ± 0.41	> 25.1	27.03 ± 0.19
545752	09:57:23.39	01:56:45.93	24.92 ± 0.03	24.89 ± 0.04	25.09 ± 0.07	25.60 ± 0.15	25.52 ± 0.09
564423	10:00:31.87	01:57:50.12	25.95 ± 0.07	25.40 ± 0.06	25.43 ± 0.08	26.18 ± 0.08	24.83 ± 0.02
631862	09:57:42.84	02:01:39.64	25.89 ± 0.08	25.59 ± 0.08	25.42 ± 0.09	25.27 ± 0.04	24.80 ± 0.03
720309	09:59:10.82	02:06:41.96	> 26.4	25.12 ± 0.05	24.88 ± 0.05	24.36 ± 0.02	24.06 ± 0.02
724872	10:02:52.10	02:06:57.91	25.07 ± 0.09	24.74 ± 0.09	25.45 ± 0.12	25.04 ± 0.04	24.71 ± 0.04
784810	10:01:47.48	02:10:15.43	25.72 ± 0.06	25.69 ± 0.08	25.82 ± 0.12	26.02 ± 0.09	25.16 ± 0.04
852845	09:58:50.94	02:13:55.09	26.01 ± 0.08	25.25 ± 0.05	25.32 ± 0.08	25.03 ± 0.03	24.30 ± 0.02
859061	10:00:19.59	02:14:13.28	26.29 ± 0.10	25.95 ± 0.10	26.14 ± 0.17	24.84 ± 0.03	24.88 ± 0.03
882958	09:58:46.60	02:15:31.33	25.78 ± 0.07	25.48 ± 0.07	25.89 ± 0.12	26.17 ± 0.11	25.03 ± 0.04
978062	09:57:47.90	02:20:43.55	25.07 ± 0.04	24.71 ± 0.03	24.72 ± 0.05	24.60 ± 0.03	24.20 ± 0.02
1055131	09:57:54.25	02:25:08.42	25.42 ± 0.04	25.57 ± 0.07	25.48 ± 0.09	25.10 ± 0.04	24.52 ± 0.03
1103149	09:57:54.69	02:27:54.95	25.81 ± 0.06	25.91 ± 0.09	25.86 ± 0.13	25.05 ± 0.03	24.92 ± 0.05
1151531	10:02:12.54	02:30:45.84	25.03 ± 0.03	25.15 ± 0.05	25.82 ± 0.13	24.91 ± 0.03	24.13 ± 0.02
1209618	10:00:47.53	02:34:04.50	25.85 ± 0.07	25.66 ± 0.08	26.48 ± 0.23	25.65 ± 0.06	25.19 ± 0.04
1212944	10:01:56.33	02:34:16.22	25.94 ± 0.08	26.22 ± 0.14	25.98 ± 0.15	26.13 ± 0.11	25.17 ± 0.04
1274544	09:58:12.23	02:37:52.34	25.09 ± 0.09	25.01 ± 0.11	24.87 ± 0.07	23.86 ± 0.01	23.50 ± 0.01
1297232	09:57:24.53	02:39:13.18	25.16 ± 0.04	25.08 ± 0.05	25.38 ± 0.08	25.03 ± 0.11	24.59 ± 0.10
1313521	09:57:35.64	02:40:12.09	25.86 ± 0.08	25.21 ± 0.06	25.21 ± 0.08	24.03 ± 0.03	23.66 ± 0.05
1346929	10:00:30.65	02:42:09.10	25.71 ± 0.07	25.36 ± 0.06	26.11 ± 0.17	25.26 ± 0.05	26.76 ± 0.20
1352064	09:57:32.07	02:42:25.56	25.67 ± 0.06	25.41 ± 0.07	25.39 ± 0.09	25.88 ± 0.20	24.42 ± 0.07
1356755[a]	09:57:25.45	02:42:41.22	26.32 ± 0.41	24.54 ± 0.11	24.56 ± 0.16	24.02 ± 0.04	> 23.6
1371152	10:00:15.97	02:43:32.91	26.24 ± 0.11	25.50 ± 0.07	25.50 ± 0.10	26.41 ± 0.17	25.74 ± 0.10
1409328	09:59:17.15	02:45:48.22	25.90 ± 0.10	25.50 ± 0.09	25.31 ± 0.11	25.30 ± 0.06	24.38 ± 0.03
1412106	09:57:21.36	02:45:57.47	25.30 ± 0.06	25.47 ± 0.09	26.12 ± 0.22	25.21 ± 0.11	25.29 ± 0.18

[a] This candidate is not set at high redshift with `the Farmer` photometry, so the photometry is from the CLASSIC catalog.

Table 4.2. – Physical parameters from `the Farmer` photometry for the selected $z > 7.5$ candidates. The columns give the median photometric redshifts, stellar masses, star formation rates, reduced χ^2 for the best-fit galaxy and stellar templates, extinctions, absolute UV magnitudes, identifiers in Stefanon et al. 2019 and Bowler et al. 2020, and blended flags.

ID	$z_{\rm phot}$	$\log(M_*)$ $[M_\odot]$	$\log({\rm SFR})$ $[M_\odot {\rm yr}^{-1}]$	$\chi^2_{\rm gal}$	$\chi^2_{\rm star}$	$E(B-V)$ [mag]	$M_{\rm FUV}$ [mag]	Anc.	Blended
234500	$8.20^{+0.43}_{-0.35}$	$10.43^{+0.16}_{-0.17}$	$2.26^{+0.19}_{-0.30}$	0.74	1.70	0.3	−21.46	...	
241443	$7.70^{+0.48}_{-0.18}$	$10.44^{+0.17}_{-0.18}$	$2.43^{+0.15}_{-0.33}$	1.18	1.80	0.3	−21.89	...	
295952	$8.99^{+0.44}_{-4.98}$	$8.62^{+0.14}_{-0.05}$	$1.28^{+0.08}_{-0.07}$	4.36	3.69	0.0	−21.54	...	
327551	$9.22^{+0.12}_{-0.12}$	$8.99^{+0.19}_{-0.06}$	$1.57^{+0.09}_{-0.07}$	1.43	1.74	0.0	−22.44	...	
336101	$7.51^{+0.09}_{-0.09}$	$10.21^{+0.12}_{-0.14}$	$1.88^{+0.11}_{-0.13}$	0.88	2.20	0.0	−21.50	213/Y3	
365776	$9.16^{+0.40}_{-1.23}$	$8.85^{+0.04}_{-0.04}$	$1.49^{+0.07}_{-0.07}$	3.70	2.90	0.0	−22.13	...	
403992	$8.52^{+0.31}_{-0.50}$	$9.86^{+0.15}_{-0.19}$	$1.47^{+0.34}_{-0.13}$	1.18	1.32	0.0	−21.24	266	
428351	$7.58^{+0.14}_{-0.11}$	$9.77^{+0.14}_{-0.15}$	$1.59^{+0.11}_{-0.15}$	1.07	2.01	0.1	−21.75	301/Y4	Y
441697	$9.51^{+0.11}_{-0.15}$	$9.74^{+0.19}_{-0.22}$	$1.50^{+0.08}_{-0.08}$	2.02	3.42	0.0	−22.45	...	
442053	$9.00^{+0.43}_{-1.38}$	$10.18^{+0.17}_{-0.20}$	$2.14^{+0.16}_{-0.27}$	0.79	1.23	0.3	−22.04	...	Y
454766	$9.79^{+0.07}_{-0.08}$	$9.58^{+0.21}_{-0.21}$	$1.90^{+0.09}_{-0.09}$	2.53	4.33	0.0	−23.40	...	
485056	$7.40^{+0.12}_{-0.13}$	$8.42^{+0.15}_{-0.15}$	$0.84^{+0.09}_{-0.10}$	1.61	1.40	0.0	−20.69	356	
545752	$7.56^{+0.05}_{-0.05}$	$9.21^{+0.17}_{-0.14}$	$1.43^{+0.08}_{-0.09}$	1.10	1.16	0.0	−22.15	...	
564423	$9.16^{+0.15}_{-0.17}$	$9.53^{+0.18}_{-0.20}$	$1.26^{+0.10}_{-0.09}$	1.53	2.65	0.0	−21.87	237/Y5	
631862	$8.51^{+0.46}_{-0.85}$	$10.03^{+0.16}_{-0.19}$	$1.91^{+0.13}_{-0.31}$	1.13	2.00	0.2	−21.48	...	
720309	$9.90^{+0.07}_{-7.03}$	$10.50^{+0.15}_{-0.16}$	$2.64^{+0.13}_{-0.32}$	1.67	2.33	0.3	−22.30	...	
724872	$8.13^{+0.52}_{-0.52}$	$9.88^{+0.14}_{-0.16}$	$1.67^{+0.13}_{-0.30}$	0.87	1.78	0.0	−22.16	...	
784810	$8.67^{+0.23}_{-0.35}$	$9.60^{+0.15}_{-0.20}$	$1.43^{+0.15}_{-0.33}$	1.13	2.04	0.0	−21.50	598/Y10	
852845	$9.16^{+0.17}_{-0.21}$	$10.34^{+0.17}_{-0.17}$	$2.09^{+0.10}_{-0.29}$	0.86	1.26	0.0	−21.98	...	
859061	$7.88^{+0.28}_{-0.16}$	$10.25^{+0.14}_{-0.15}$	$2.00^{+0.17}_{-0.30}$	1.14	2.18	0.0	−20.99	Y11	Y
882958	$8.70^{+0.30}_{-1.14}$	$9.58^{+0.15}_{-0.21}$	$1.26^{+0.30}_{-0.18}$	1.51	1.11	0.0	−21.62	...	Y
978062	$8.85^{+0.18}_{-0.36}$	$10.26^{+0.14}_{-0.18}$	$1.94^{+0.39}_{-0.10}$	1.04	2.77	0.1	−22.51	762/Y1	
1055131	$8.36^{+0.28}_{-0.35}$	$10.11^{+0.12}_{-0.15}$	$1.66^{+0.36}_{-0.14}$	0.67	2.27	0.0	−21.76	839	
1103149	$7.78^{+0.32}_{-0.16}$	$10.08^{+0.13}_{-0.15}$	$1.77^{+0.12}_{-0.24}$	0.52	1.64	0.0	−21.26	879	
1151531	$8.34^{+0.25}_{-0.36}$	$10.23^{+0.07}_{-0.14}$	$1.63^{+0.13}_{-0.39}$	1.01	2.15	0.0	−21.98	914/Y2	
1209618	$8.39^{+0.33}_{-0.37}$	$9.81^{+0.14}_{-0.18}$	$1.45^{+0.15}_{-0.12}$	0.81	1.93	0.0	−21.31	Y8	
1212944	$8.60^{+0.27}_{-0.40}$	$9.72^{+0.17}_{-0.21}$	$1.39^{+0.16}_{-0.15}$	0.96	1.03	0.0	−21.16	953/Y15	
1274544	$7.36^{+0.12}_{-0.12}$	$10.74^{+0.11}_{-0.13}$	$2.40^{+0.14}_{-0.31}$	1.37	3.01	0.2	−21.98	...	
1297232	$7.60^{+0.06}_{-0.07}$	$9.84^{+0.17}_{-0.19}$	$1.63^{+0.12}_{-0.34}$	0.95	1.40	0.0	−21.89	...	
1313521	$7.90^{+0.27}_{-0.21}$	$10.86^{+0.15}_{-0.16}$	$2.64^{+0.14}_{-0.38}$	0.81	2.22	0.3	−21.47	...	Y
1346929	$7.93^{+0.44}_{-0.17}$	$9.10^{+0.16}_{-0.17}$	$1.16^{+0.15}_{-0.10}$	2.75	2.67	0.1	−21.43	1032	
1352064	$8.87^{+0.21}_{-0.44}$	$9.91^{+0.21}_{-0.24}$	$1.65^{+0.12}_{-0.26}$	1.30	0.93	0.0	−21.87	...	
1356755[a]	$8.75^{+0.75}_{-6.56}$	$10.58^{+0.17}_{-0.22}$	$2.54^{+0.18}_{-0.26}$	0.27	0.53	0.3	−22.13	...	
1371152	$9.29^{+0.19}_{-0.21}$	$9.34^{+0.19}_{-0.22}$	$1.26^{+0.11}_{-0.09}$	0.79	1.59	0.0	−21.85	Y12	
1409328	$8.59^{+0.55}_{-1.27}$	$10.15^{+0.18}_{-0.19}$	$1.93^{+0.14}_{-0.23}$	0.83	0.69	0.0	−21.53	...	
1412106	$8.10^{+0.38}_{-0.28}$	$9.68^{+0.18}_{-0.22}$	$1.44^{+0.21}_{-0.28}$	0.66	2.45	0.0	−21.75	...	

[a] This candidate is not set at high redshift with `the Farmer` photometry, so the physical parameters are from the Classic catalog.

4.3.1. Unblended galaxy sample

We identify 18 new unblended candidates at $z > 7.5$ from the selection in both COSMOS2020 catalogs. Figures 4.2, 4.3 and 4.4 illustrate the observed photometry of these candidates, in addition to the best-fitted galaxy and stellar templates, for both the Classic and `the Farmer` catalogs. In the case the flux is smaller than the flux uncertainty, the photometry is replaced by a 3σ upper limit (only for clarity). Figures. 4.5 and 4.6 show stamp images centered on the candidate coordinates. In the optical and near-infrared bands, `the Farmer` photometry is usually within the Classic photometric uncertainties, which are systematically larger than `the Farmer` ones. This results in narrower redshift probability distributions for the `the Farmer` photometry. In the IRAC channels, the photometry from `IRACLEAN` and from `the Tractor` tend to be in correct agreement, even if not within the respective uncertainties.

We find three candidates with $z_{\rm phot} > 9.5$ according to `the Farmer` results. The candidate ID441697 is robustly detected in the J band, its photometric redshift with `the Farmer` is $z_{\rm phot} = 9.51$. In this case, the Classic photometric redshift $z_{\rm phot} = 9.1$ may suggest a lower redshift, nonetheless all the PDFz weight is at $z > 8$ in both catalogs. The two other candidates, ID454766 and ID720309, are both only detected in the H and K_s bands, and have both $z_{\rm phot} \sim 9.8$ for `the Farmer` photometry and $z_{\rm phot} \sim 9.6$ in the Classic catalog. In the case of candidate ID454766, the Classic PDFz indicates a secondary solution at $z = 4$ because of optical detections at 3σ in the r and i bands, although it is not clearly visible from the stamp images. In addition, the photometric uncertainties from `IRACLEAN` may be underestimated in this case, so that the constraints on the SED mostly come from the mid-infrared. Nevertheless, `the Farmer` photometry leads to a single-peaked redshift distribution, and gives similar weights to the near-infrared and mid-infrared bands.

We observe that magnitudes may present significant shifts between the two COSMOS2020 catalogs, even if the observed colors are equivalent. One of the main reasons is that `IRACLEAN` and `the Farmer` provide total fluxes, whereas fixed aperture fluxes are used for the high-resolution images in the Classic catalog. Hence, these aperture fluxes are rescaled using aperture-to-total corrections applied to all the bands, and computed from the weighted mean difference between fixed aperture and pseudo-total fluxes (using Kron apertures) from `SExtractor`. The candidates ID454766 and ID720309 at $z_{\rm phot} > 9.5$ both present overestimated pseudo-total fluxes, leading to aperture-to-total corrections reaching 0.8 mag. As a consequence, the $K_s - {\rm ch1}$ colors may be bluer than expected for these objects. In addition, the candidate ID454766 is the brightest galaxy of the sample, with an absolute UV magnitude of $M_{\rm UV} \sim -23.4$ mag (in both catalogs). There is no clear explanation for such large differences between the aperture and pseudo-total magnitudes in the near-infrared bands, which are mainly contributing to the aperture-to-total corrections. In addition, these candidates are detected at 2σ in multiple HSC optical bands in the CLASSIC catalog even though it is not detectable by eye in the images, whereas `the Farmer` photometry is more consistent with zero fluxes. In these cases, the optical pseudo-total magnitudes are ill-defined, resulting in noisy aperture-to-total corrections. As a consequence, the estimated physical properties such as stellar mass and absolute magnitudes may be biased in the CLASSIC catalog for these two sources. For this reason, we prefer to rely on `the Farmer` magnitudes and colors to estimate physical parameters.

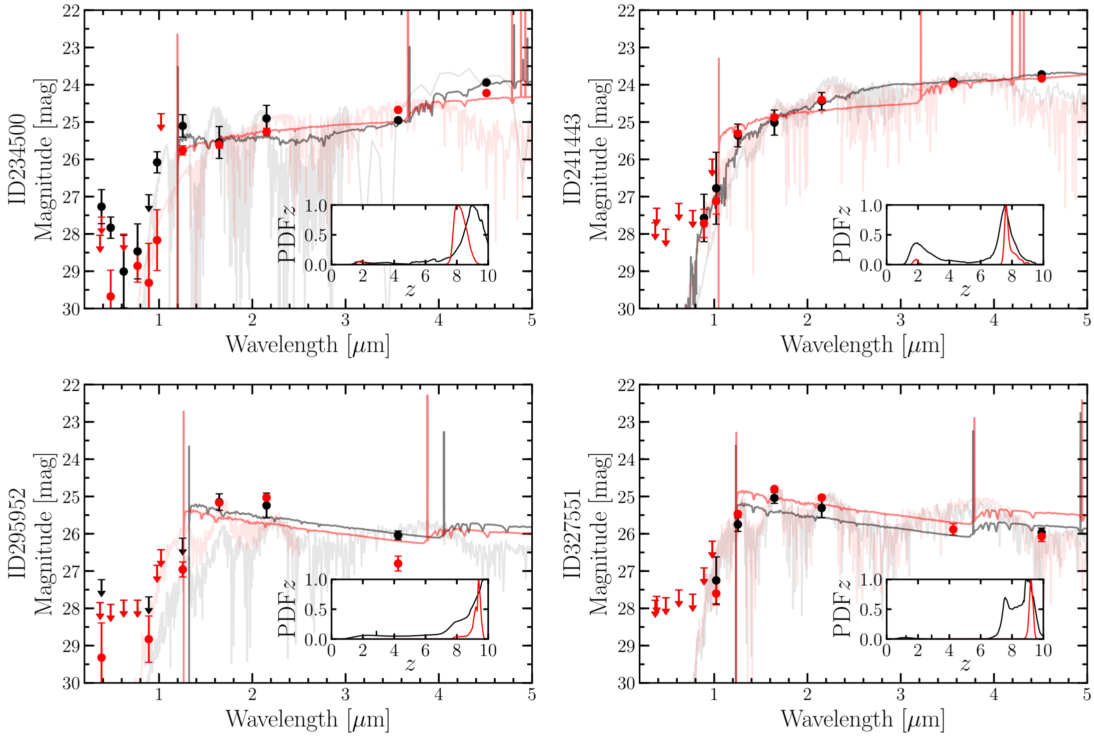

Figure 4.2. – Observed photometry and best fitting templates for the new unblended $z > 7.5$ candidates in the COSMOS field. The black (red, respectively) markers and lines are for the CLASSIC (`the Farmer`) catalog. The photometry is replaced by the 3σ upper limit in the case of non-detection at 1σ. The bright lines show the best-fitting galaxy templates. The faint lines show the best-fitting stellar templates. The inset plots show the redshift probability distributions.

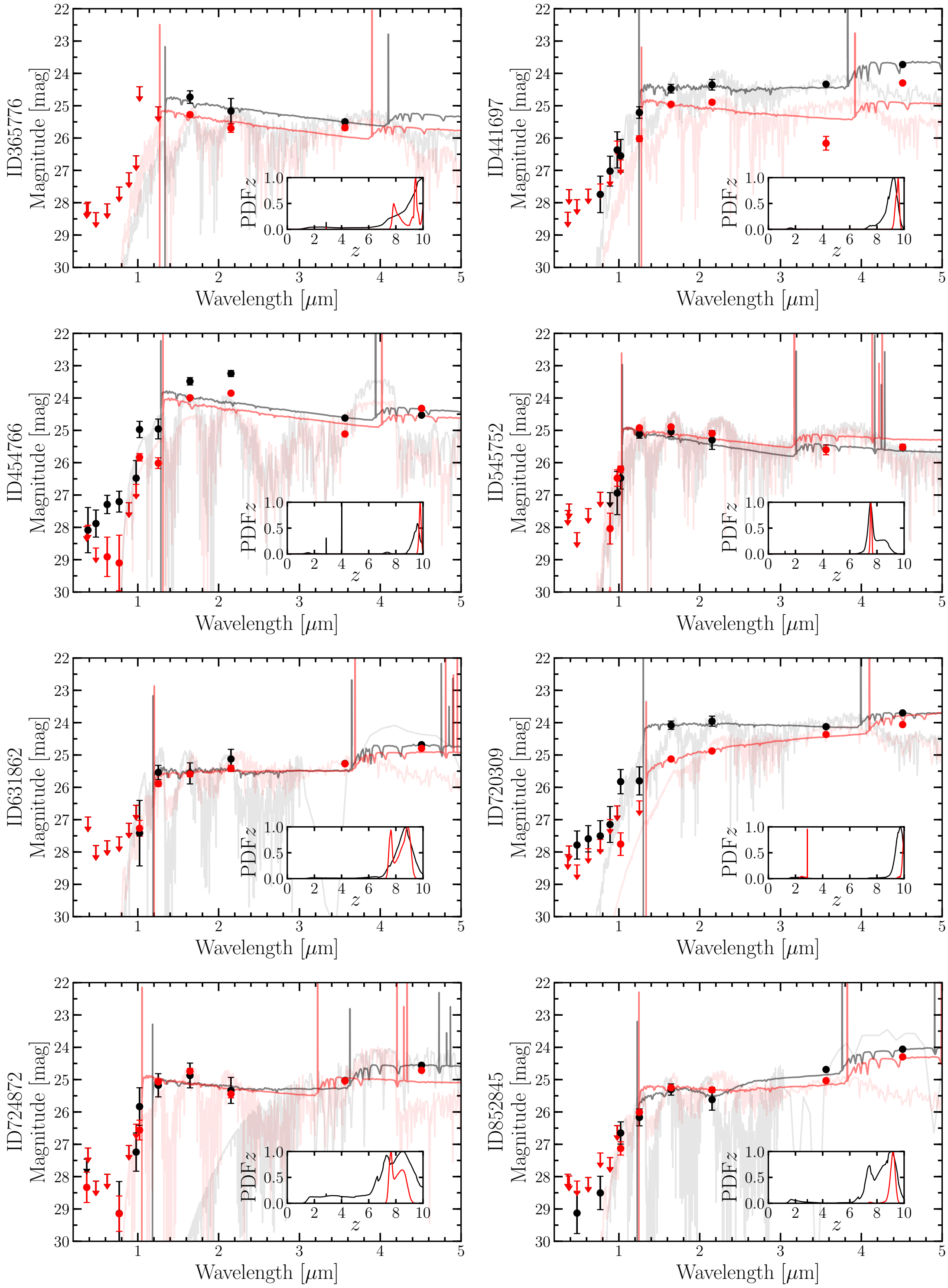

Figure 4.3. – Continued

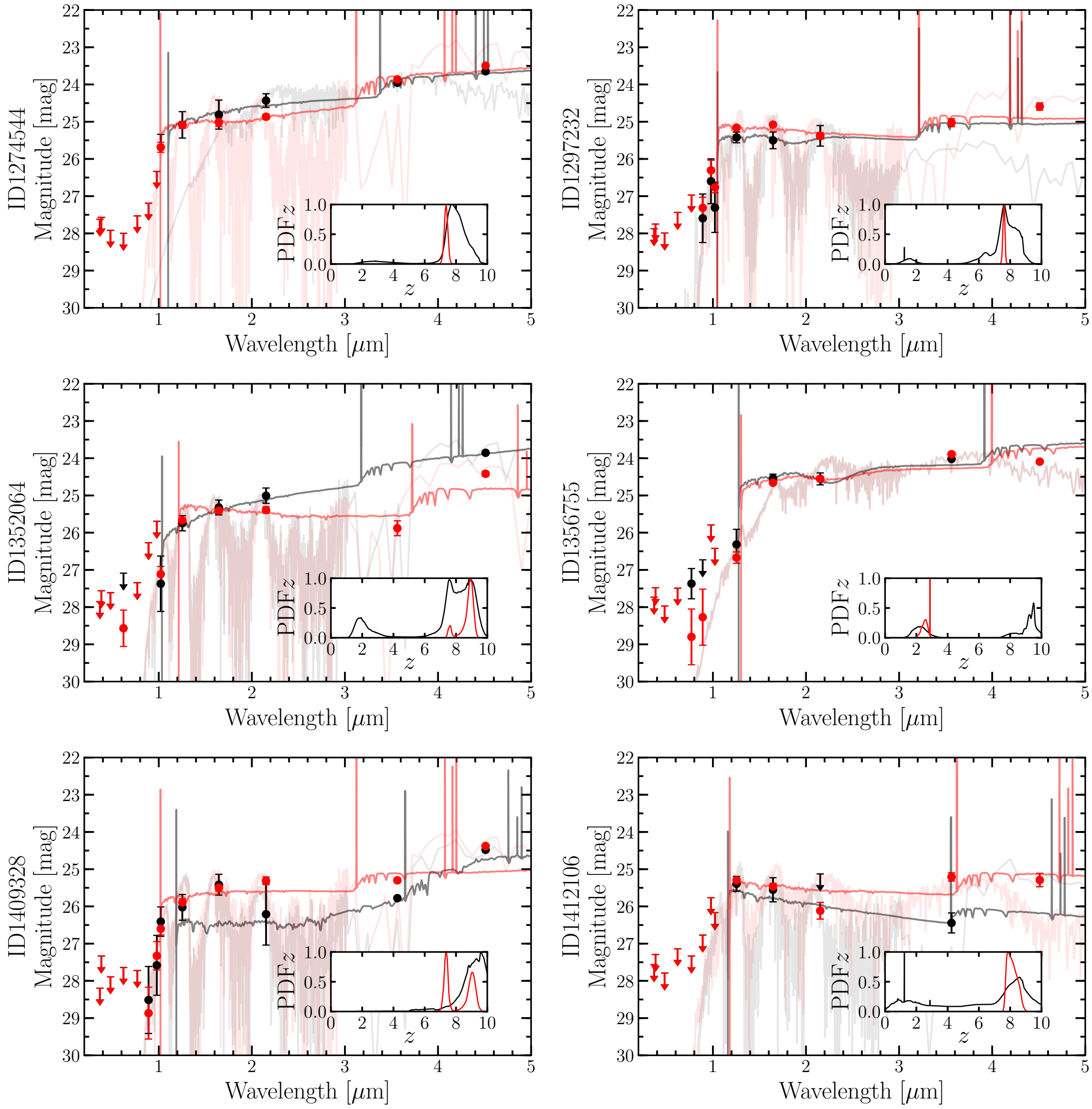

Figure 4.4. – Continued

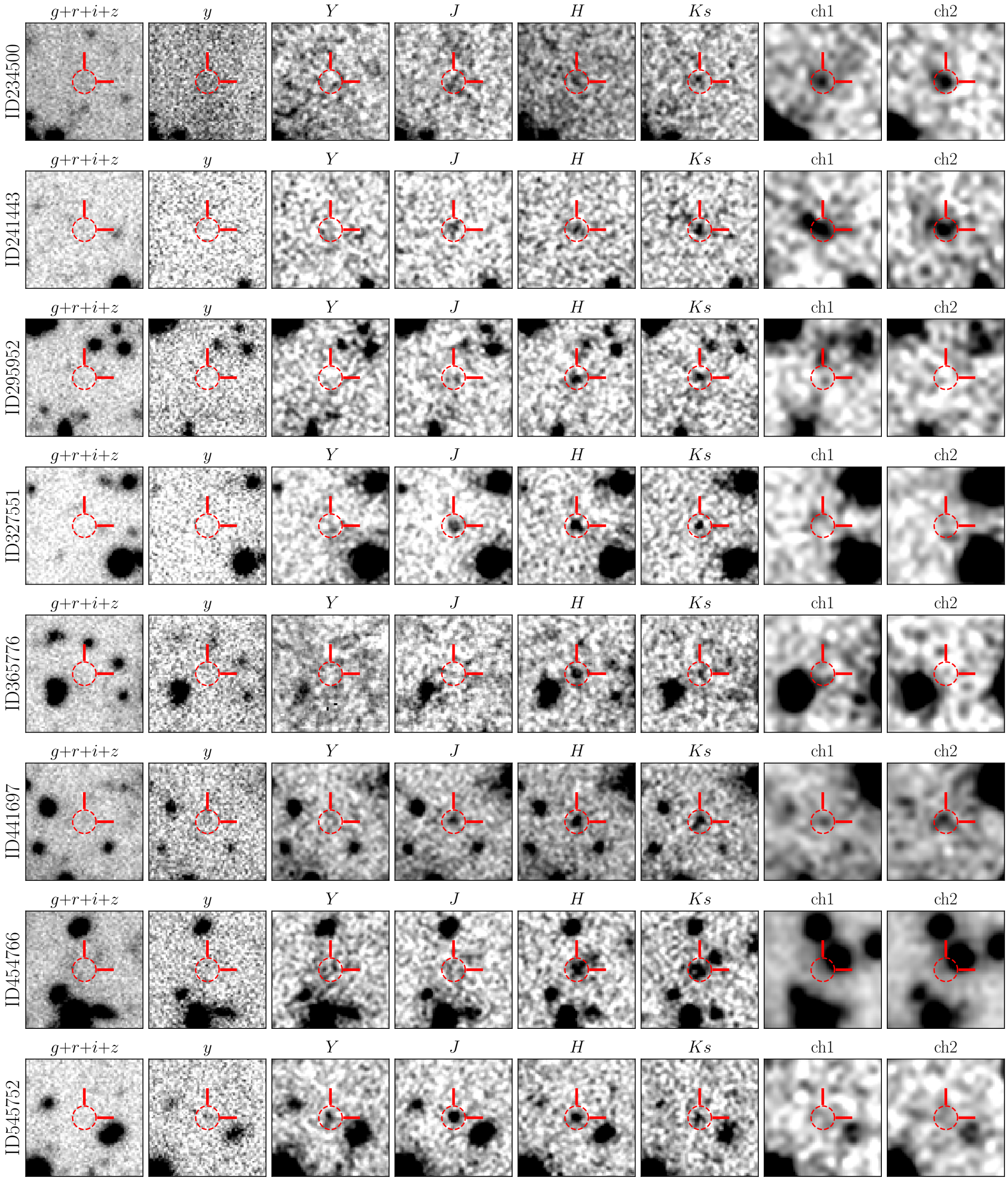

Figure 4.5. – Stamp images of the $z > 7.5$ new unblended candidates in the COSMOS field. Each candidate appears in one row of stamps. The stamps are 10″ wide, oriented with North to the top and East to the left. The stamps are saturated beyond the range $[-1, 4]\sigma$, where σ is the 3σ clipped standard deviation of the pixel values in the stamp. The red circles indicate 2″ diameter apertures. The optical *griz* stamps are stacked for conciseness.

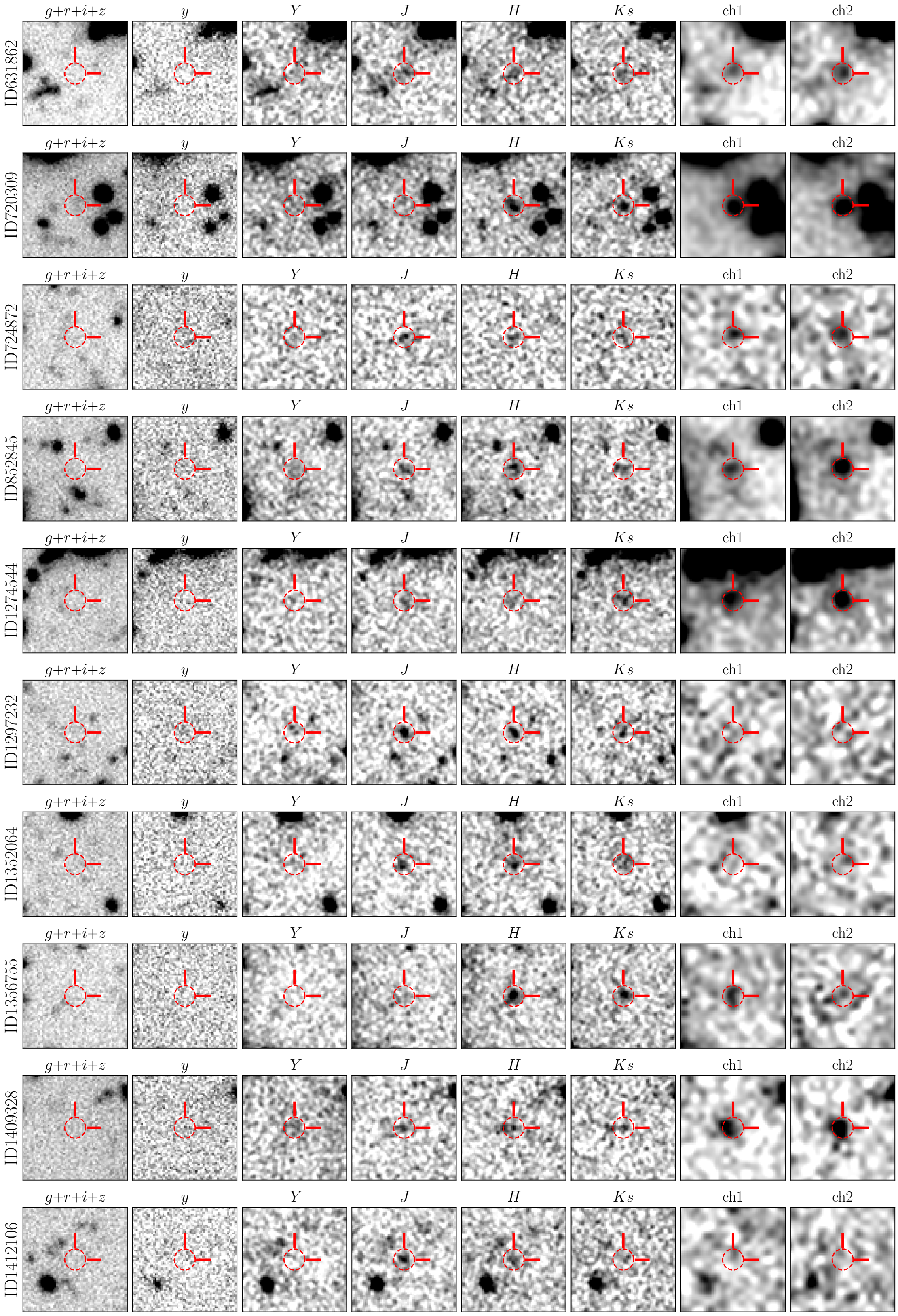

Figure 4.6. – Continued

4.3.2. Blended galaxy sample

In the case of high-redshift galaxies blended with nearby sources, the Classic aperture photometry may be contaminated. Low-redshift sources are far more numerous than high-redshift galaxies, so it is highly probable that the nearby sources are at low redshift, and potentially detected in the optical. As a result, the estimated photometric redshifts may disfavor the high-redshift solution, because of the optical flux glowing from the blended neighbors. The aperture-to-total flux correction applied to the Classic photometry do not correct for this effect, since this scaling only affects magnitudes and not colors. It is precisely in these cases that `the Farmer` photometry is expected to be more reliable than the Classic aperture photometry. We note that the IRAC photometry extracted with `IRACLEAN` can accurately handle blended sources, so that the Classic optical and near-infrared photometry are the only concerned. In the case of these blended candidates, the star-galaxy separation relies on the best-fit template χ^2 from `the Farmer` catalog. We reject two blended candidates for this reason.

We identify three new high-redshift candidates which are blended with nearby sources from the selection with `the Farmer` catalog. The observed photometry and best-fitted galaxy templates of these candidates are represented in Fig. 4.7, and the stamp images are shown in Fig. 4.8. The Classic photometry and posterior redshift distributions are also indicated. Based on aperture photometry, all of these candidates present a 3σ detection in at least one HSC optical band. The Classic redshift probability distributions peak at $z \sim 2$ for all of the candidates, although one of them presents a secondary $z > 7$ solution. In contrast, the majority of the PDFz weights are located at $z > 7$ with `the Farmer` catalog. The observed magnitude range of these candidates is $25.0 < H < 25.5$ mag. These results highlight the importance of `the Farmer` photometry to identify candidates which are clearly detectable in the images, but rejected using aperture photometry.

The candidate ID882958 presents a diffuse emission in the g-band image and not in the other optical bands. This leads to a significant detection (6σ) in `the Farmer` catalog. In contrast, the surface brightness profiles in the J, H and K_s-band images appear fairly concentrated. This may be simply due to noise fluctuations, leading to a local maximum at the coordinates of the candidates. At the detection limit, `the Farmer` may fit this local maximum and the estimated signal-to-noise may be significant. In this case, we do not reject the candidates despite the significant optical detection.

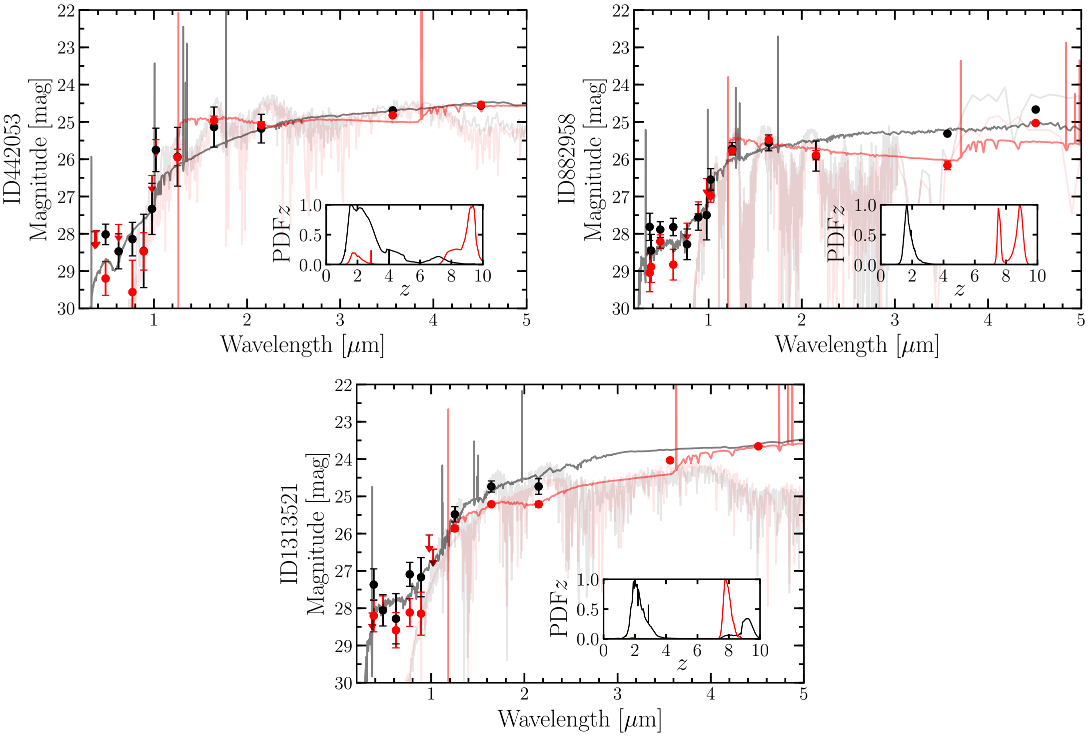

Figure 4.7. – Same as Fig. 4.2 for the new blended $z > 7.5$ galaxy candidates.

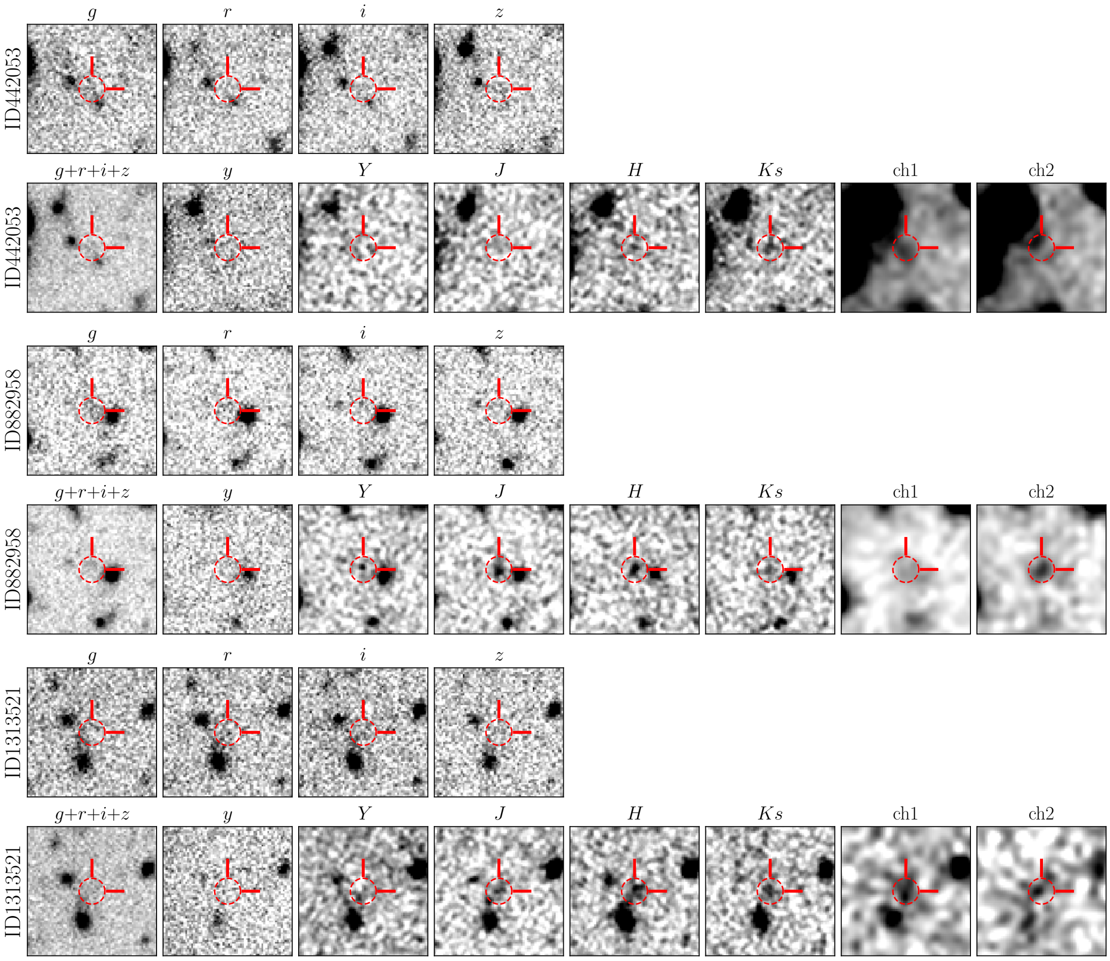

Figure 4.8. – Same as Fig. 4.5 for the new blended $z > 7.5$ galaxy candidates.

4.3.3. Comparison with the literature

We describe in this section the galaxy candidates at $z > 7$ which were previously identified by Stefanon et al. 2019 and Bowler et al. 2020 in the COSMOS field. The data sets, selection methods and galaxy samples from these papers are described here. Stefanon et al. 2019 (see also Stefanon et al. 2017) used the near-infrared broad and narrow bands from UltraVISTA DR3, all the available CFHT/MegaCam, Subaru/Suprime-Cam and HSC optical bands in the optical and *Spitzer*/IRAC channels 1 to 4 in the mid-infrared. In complement, this study also benefited of *HST*/WFC3 coverage from the Drift And SHift mosaic (DASH; Momcheva et al. 2016; Mowla et al. 2019), with an improved spatial resolution. Stefanon et al. 2019 identified 10 candidates at $z \sim 8$ and 6 candidates at $z \sim 9$, including one which may be three distinct sources. All these candidates have an absolute UV magnitude above $M_{\rm UV} > -22.5$ mag.

The most recent study in the COSMOS field from Bowler et al. 2020 included a combined analysis of COSMOS and the *XMM-Newton* - Large Scale Structure (XMM-LSS) field, for a total area of 6 deg^2. The authors used the latest UltraVISTA DR4 data (broad bands only) and the *Spitzer*/IRAC channel 1 and 2 images from SPLASH, SEDS, and SMUVS in the infrared. The optical data consisted of the CFHT/MegaCam u^*, g, r, i, z broad bands from CFHTLS, and the HSC-SSP DR1 g, r, i, z, y broad bands. The additional Suprime-Cam z' band, deeper than the HSC/z band in that data release, was also used. Bowler et al. 2020 identified 27 Lyman break galaxies at $7.5 < z < 9.1$, including 14 candidates at $z \sim 8$ and 2 candidates at $z \sim 9$ in the COSMOS field. The brightest candidate has an absolute UV magnitude of $M_{\rm UV} = -23$ mag at $z \sim 9$, and all the other candidates are fainter than $M_{\rm UV} = -22.5$ mag. Among these candidates, 7 were already identified by Stefanon et al. 2019. After a detection in combined $J + H$ and $H + K_s$ images, the selection was based on photometric redshifts. The majority of the candidates were detected in the IRAC images, resulting in robust photometric redshifts. The brown dwarf/galaxy separation was also performed based on IRAC photometry. In the selection of high-redshift galaxies, the authors rejected precedent candidates from Stefanon et al. 2019 which were detected at 2σ in the Suprime-Cam/z' band.

Confirmed candidates

Among the 25 distinct candidates previously identified, we confirm 15 of them to be at high redshift. This represents 12 of the 16 candidates selected by Bowler et al. 2020 in the COSMOS field, and 10 of the 16 candidates from Stefanon et al. 2019, including 3 only selected in that paper. The identifiers from Stefanon et al. 2019 and Bowler et al. 2020 are indicated in Table 4.2. In the following, we use the identifiers from Stefanon et al. 2019 (starting with the letter Y) for the candidates selected in that paper only, and the identifiers from Bowler et al. 2020 (between three or four digits) otherwise. The photometry of the 15 confirmed candidates is represented in Fig. 4.9 and 4.10, and the corresponding stamp images are shown in Fig. 4.11 and 4.12. The majority of these candidates presents single-peaked redshift probability distributions located at $z > 7$. In addition, these candidates are all classified as galaxies in both COSMOS2020 catalogs, except the candidates 266 (ID403992) in the Classic catalog and the candidates 356 (ID485056) and 1032 (ID1346929) with `the Farmer` photometry.

The candidates 301 (ID428351) and Y11 (ID859061) are blended with nearby sources and present significant non-zero aperture fluxes in the optical. This was the reason for the candidate Y11 to be rejected from the selection of Bowler et al. 2020. Using the Classic catalog, the photometric redshifts are $z_{\rm phot} \sim 2$ for both sources. In contrast, these candidates are undetected in the optical with `the Farmer` catalog, leading to $z_{\rm phot} \sim 8$. Similarly to the new blended candidates, only the photometry with `the Farmer` is considered for these sources. For the candidate 301, we note that the smaller 1.8″ diameter apertures used in Bowler et al. 2020 may have limited the impact of the nearby source on the optical photometry.

The estimated redshifts and absolute UV magnitudes are in excellent agreement with those from Stefanon et al. 2019 and Bowler et al. 2020. We find that the absolute magnitudes from `the Farmer` are systematically shallower in the case of blended candidates, which is expected since the template-fitting photometry separates the fluxes from nearby sources. In contrast, we also find shallower magnitudes with `the Farmer` for the two candidates 356 (ID485056) and 879 (ID1103149), which do not clearly present close neighbors. Nevertheless, internal structures may be observed in the stamp images, and the Classic magnitudes are in fact in better agreement with Bowler et al. 2020. This situation may be due to the simple symmetric templates used to estimate the photometry in `the Farmer`, which may miss a fraction of the total flux. Still, we keep `the Farmer` results for these candidates in the following.

The candidate 762 (ID978062) is particularly bright, with an H-band magnitude of 24.5 mag. Its relatively broad PDFz, with a FWHM larger than 1, results from the Lyman break located between the Y and the J band. The resulting photometric redshift is higher ($z = 8.85$ instead of 8.19) than in Bowler et al. 2020, and the absolute magnitude brighter ($M_{\mathrm{UV}} = -22.51$ mag instead of -22.36 mag).

The candidate Y8 (ID1209618) presents a problematic `IRACLEAN` photometry with an extremely low channel 1 flux, which is not the case in `the Farmer` catalog. In addition, the `IRACLEAN` photometric uncertainties in both channels 1 and 2 are much smaller than in the near-infrared bands for the Classic catalog, so that the main constraint on the SED is an unexpectedly red mid-infrared color. The best-fit galaxy template from `LePhare` is still at $z > 8$, in agreement with the photometric redshift estimated with `the Farmer`.

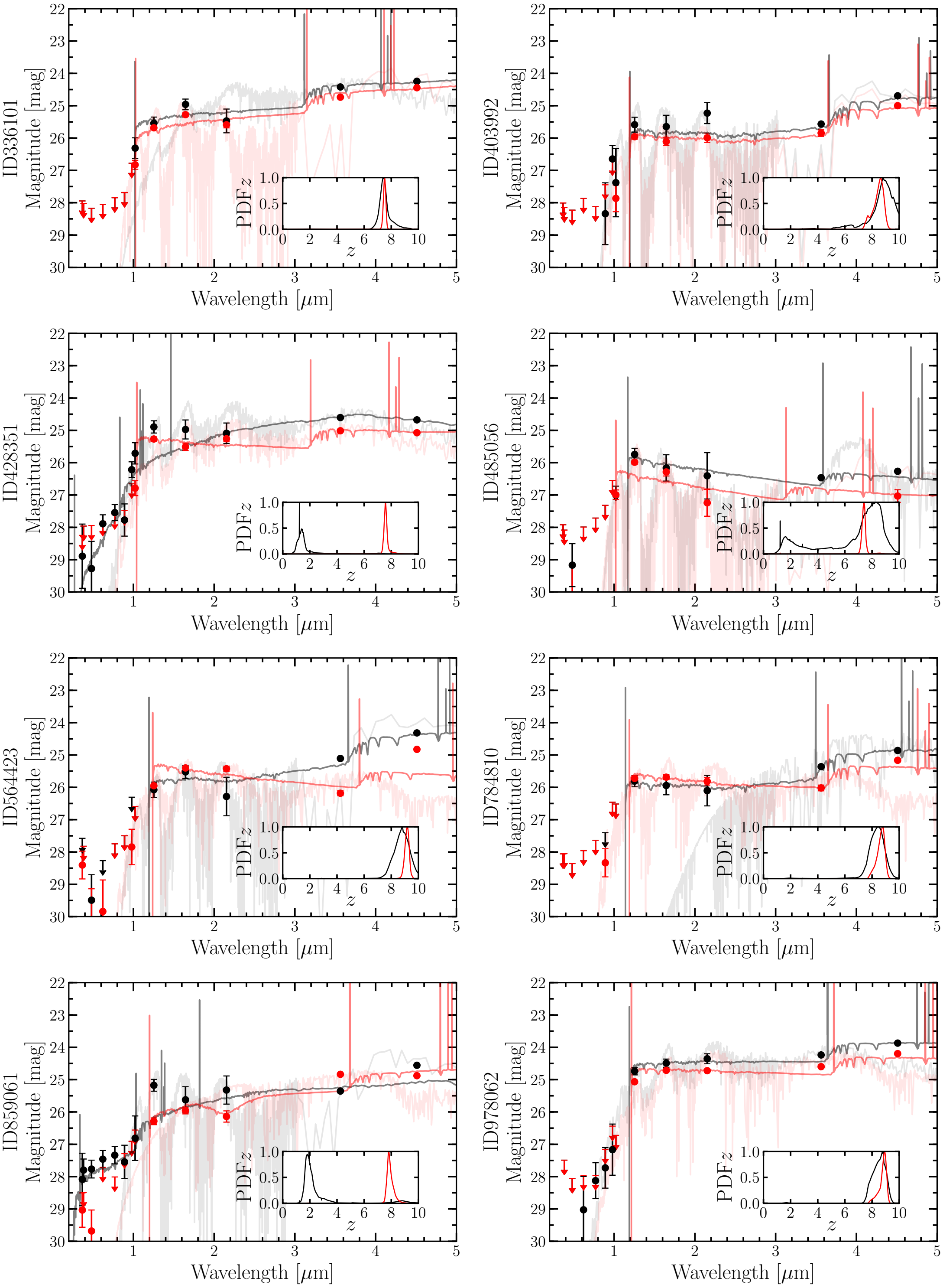

Figure 4.9. – Same as Fig. 4.2 for the $z > 7.5$ candidates from Stefanon et al. 2019 and Bowler et al. 2020 which are confirmed in the COSMOS2020 catalog.

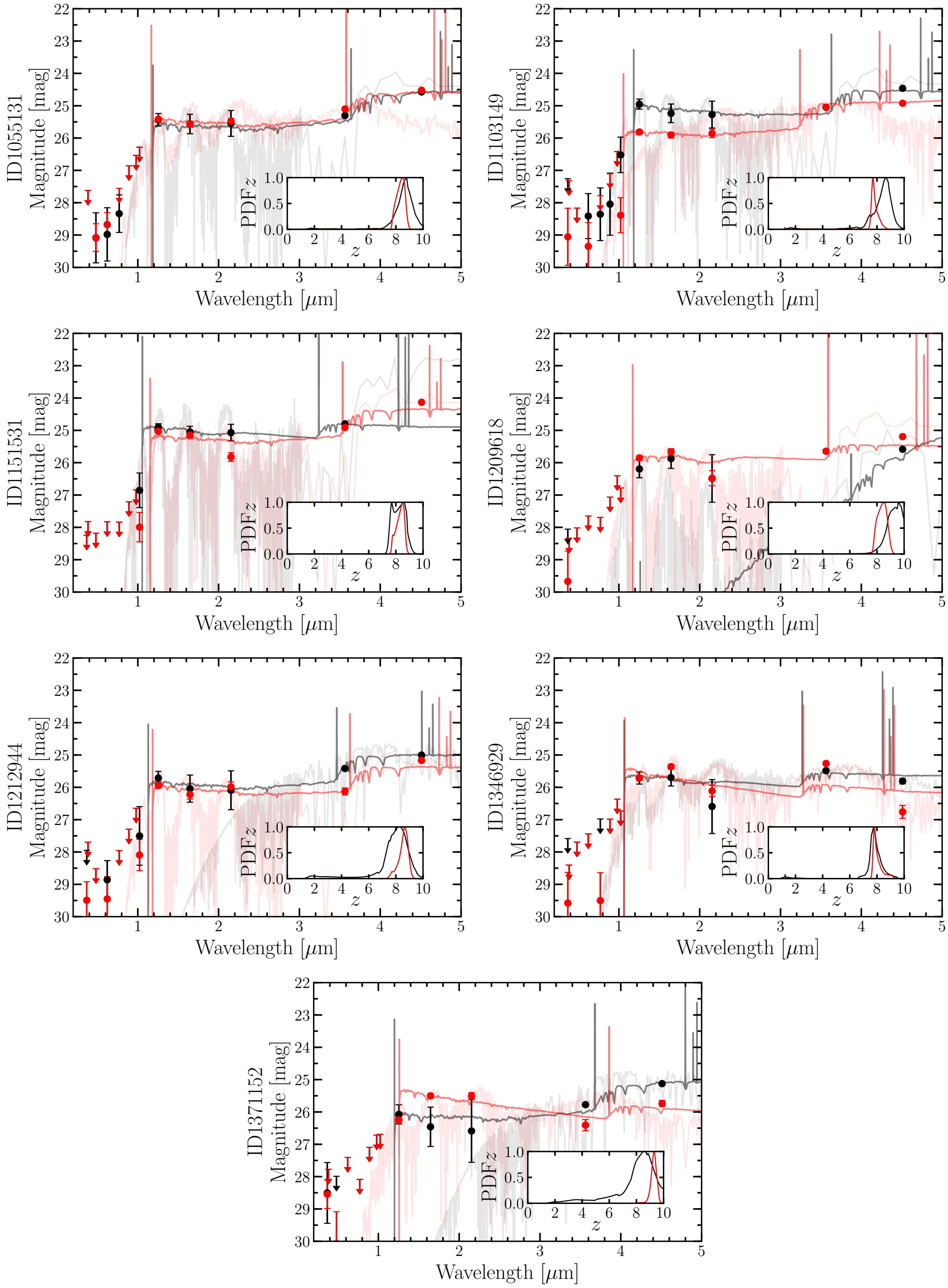

Figure 4.10. – Continued.

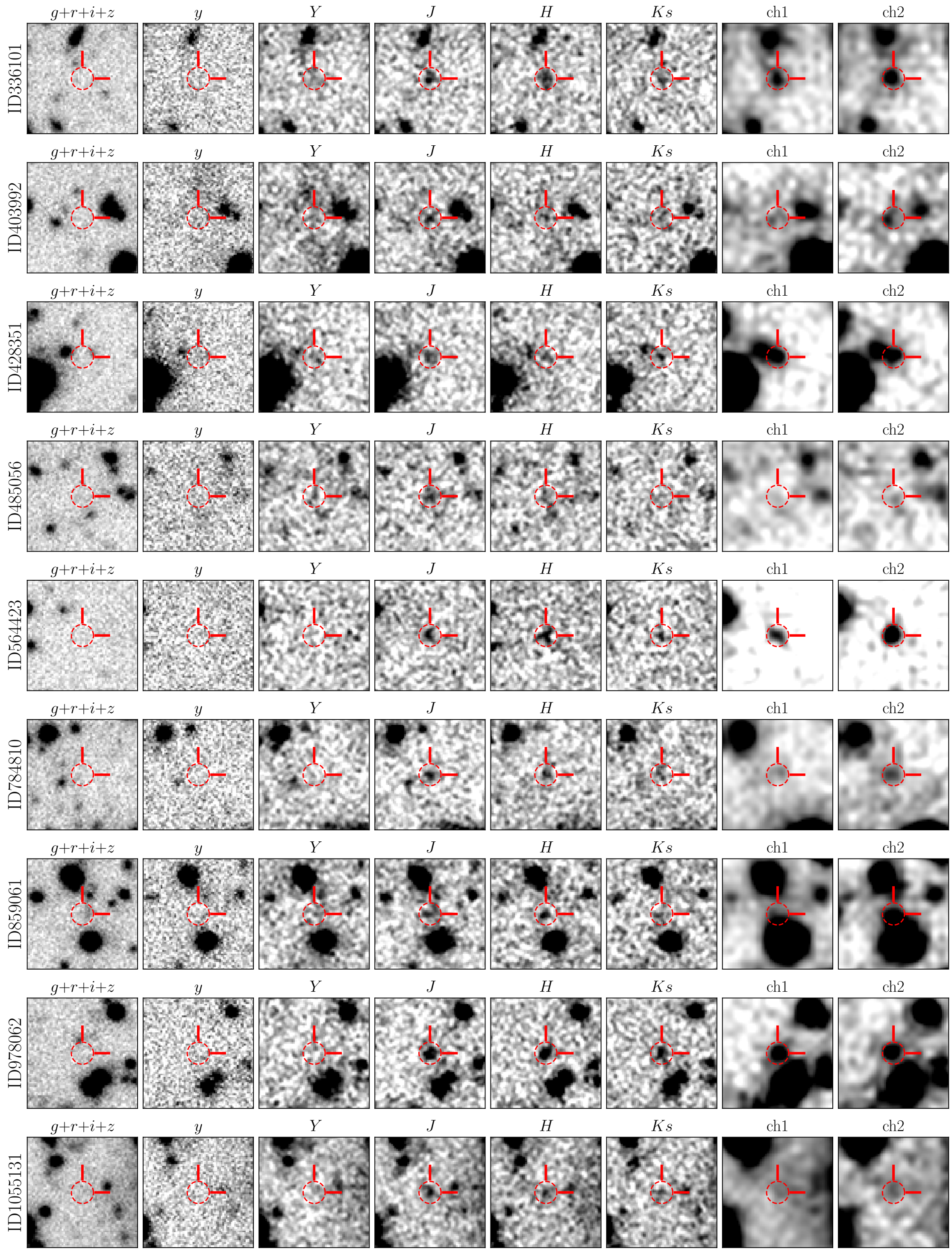

Figure 4.11. – Same as Fig. 4.5 for the $z > 7.5$ candidates from Stefanon et al. 2019 and Bowler et al. 2020 which are confirmed in the COSMOS2020 catalog.

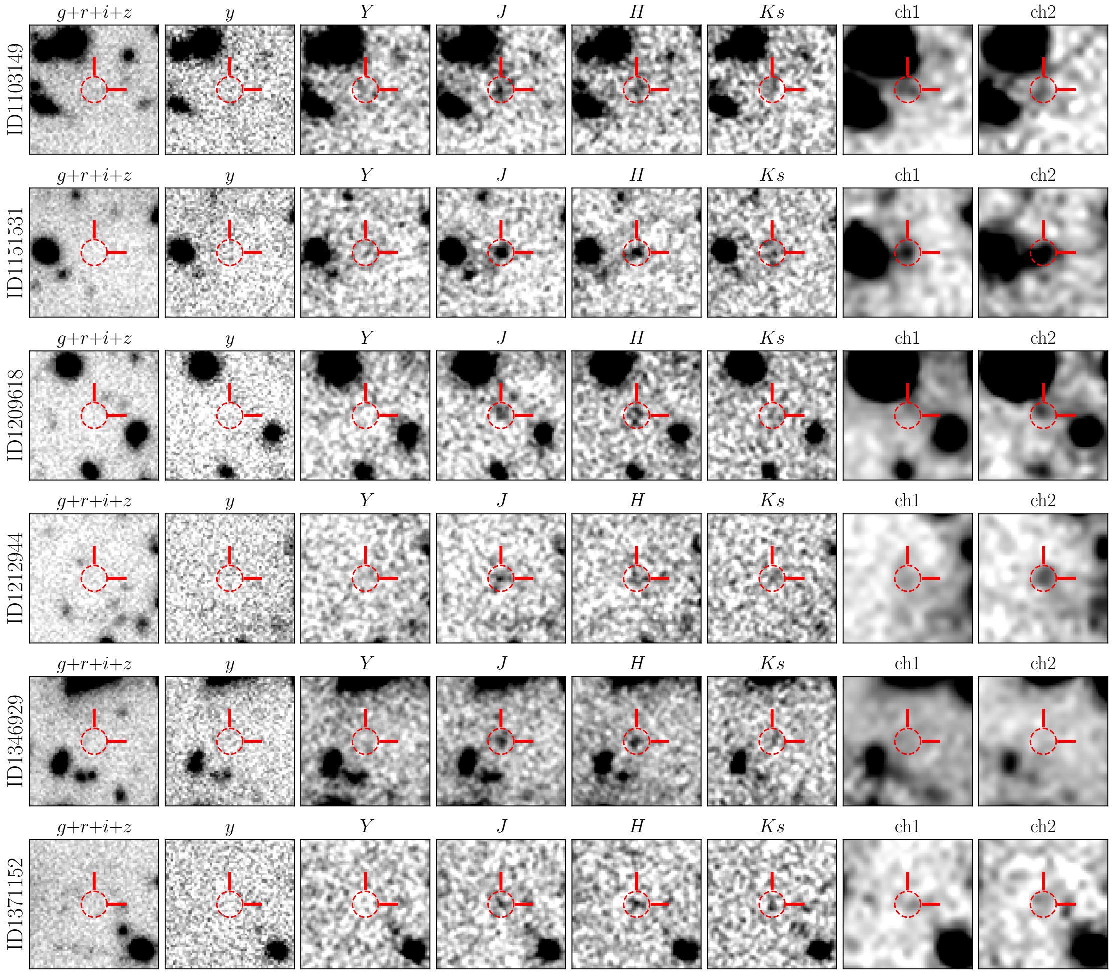

Figure 4.12. – Continued.

Rejected candidates

We now describe the 10 candidates from Stefanon et al. 2019 and Bowler et al. 2020 which were not selected in this work. For four of these candidates (Y6, Y13, 919, 1212), the estimated redshift probability distributions present two major peaks, including strong low-redshift solutions. In addition, the candidates Y6 and Y13 are detected at more than 2σ in the y and z bands, respectively, and were already rejected in the Bowler et al. 2020 galaxy sample. For these reasons, these candidates are not included in the present sample. The candidate 1212 is the brightest high-redshift galaxy identified in the COSMOS field in Bowler et al. 2020, with a photometric redshift of $z = 9.1$ and an absolute UV magnitude of $M_{\rm UV} = -23$. For this candidate, both the Classic and `the Farmer` catalogs present a 3σ detection in the r band, although it is not clear from the stamp image. As a consequence, it is not kept in the present selection, even though it remains an interesting candidate.

The combined image used to perform the detection does not recover six of the ancillary candidates (Y7, Y9, Y14, Y15, 634, 1043). Figure 4.13 indicates the stamp images in multiple broad bands at the corresponding coordinates. The candidate Y7 is clearly visible in the combined detection image, however it is not identified as a distinct object because of the two large and bright nearby sources (Bowler et al. 2020 arrived to the same conclusion). All the other undetected candidates are barely visible by eye in the J, H, channel 1 and 2 images. This necessarily limits the precision of any photometric redshift estimate. For this reason, we did not attempt to estimate the photometry or the physical parameters of these candidates.

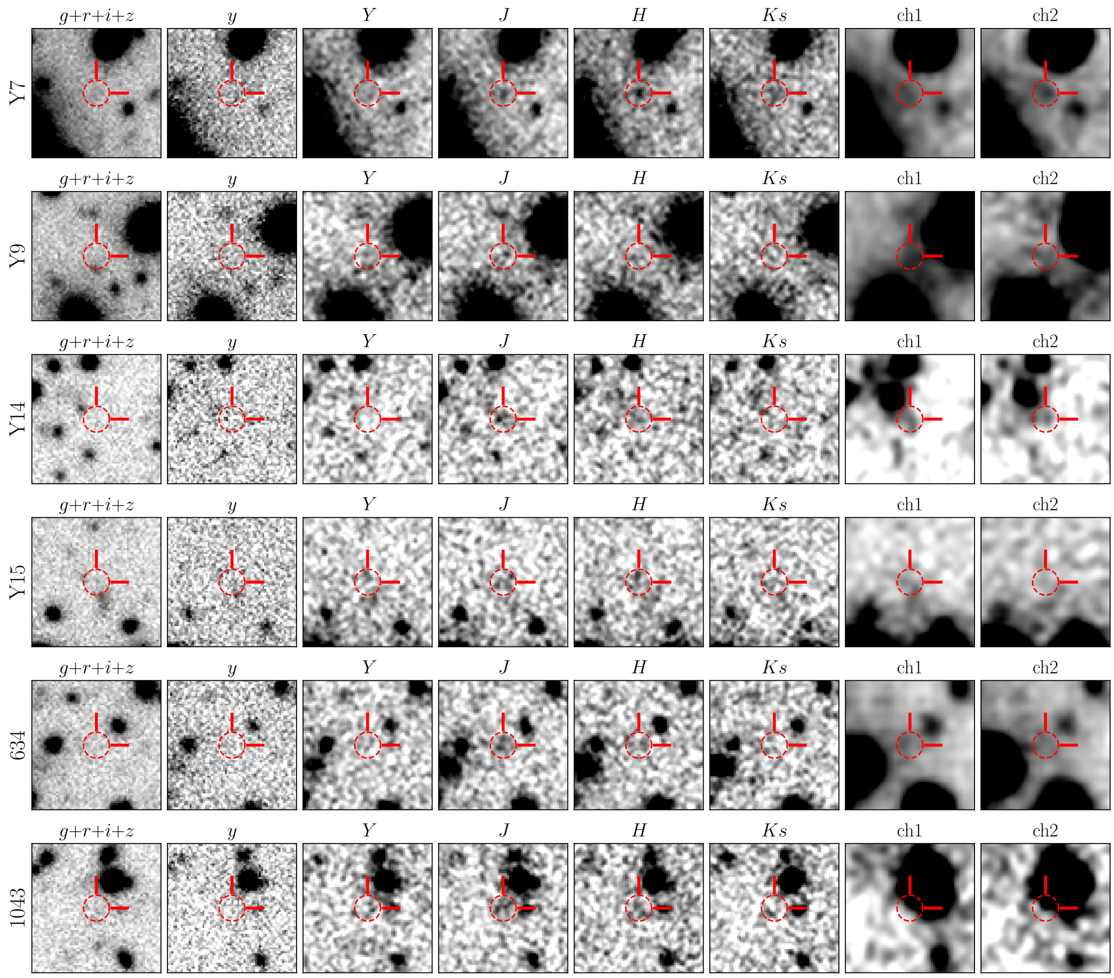

Figure 4.13. – Same as Fig. 4.5 for the $z > 7.5$ candidates from Stefanon et al. 2019 and Bowler et al. 2020 which are undetected in the COSMOS2020 detection image.

4.3.4. Lensing magnification

The high-redshift galaxy sample may be subject to gravitational lensing, and in particular lensing magnification, from massive, low-redshift galaxies. While gravitational lensing preserves surface brightness, the apparent solid angle of the background source may increase, leading to an increased apparent flux. Magnification from gravitational lensing may strongly affect the detection of rare galaxies at $z > 6$. (Mason et al. 2015; Barone-Nugent et al. 2015; Roberts-Borsani et al. 2016; Stefanon et al. 2019).

We investigate the impact of lensing magnification on the selected galaxy candidates. Lens galaxies are modelled as singular isothermal spheres (SIS), in which the spatial distribution of mass ρ is parametrized as:

$$\rho(r) = \frac{\sigma_v^2}{2\pi G r^2}, \tag{4.1}$$

where r is the radial distance from the center and σ_v is the velocity dispersion of stars. Stellar velocity dispersion scales with the mass of dark matter inside the galaxy, related to the strength of the gravitational lens. In this case, the Einstein radius of the lens θ_E can be computed as (e.g., Bartelmann et al. 2001):

$$\theta_E = 4\pi \left(\frac{\sigma_v}{c}\right)^2 \frac{D_{\mathrm{LS}}}{D_{\mathrm{S}}}, \tag{4.2}$$

where c is the speed of light, D_{LS} and D_{S} are the angular diameter distances between the lens and the source, and between the observer and the source, respectively. The lensing magnification μ can be written as:

$$\mu = \frac{\theta}{\theta - \theta_E}, \tag{4.3}$$

where θ is the angular separation between the lens and the source in the image plane, namely the observed angular separation.

Stellar velocity dispersion may be estimated from photometry through the Faber-Jackson relation (Faber et al. 1976), linking the intrinsic luminosity of an object to its velocity dispersion. Such relations can be calibrated using spectroscopic samples of galaxies, providing secure redshifts and velocity dispersion estimates. We use the Faber–Jackson relation from Barone-Nugent et al. 2015, based on the B-band absolute magnitude M_B and calibrated using early-type galaxies with redshifts spanning $0 < z < 1.6$. This relation can be written as:

$$\log_{10}\left(\frac{\sigma_v}{200\,\mathrm{km\,s^{-1}}}\right) = \frac{-0.4 M_B - b\log_{10}(1+z) - \log_{10}(m)}{3.9}, \tag{4.4}$$

with $b = 0.7 \pm 0.3$ and $m = (2.3 \pm 0.2) \times 10^8$. In this relation, the redshift evolution reflects the evolution of the mass-to-light ratio with cosmic time. The velocity dispersion uncertainties are dominated by the intrinsic scatter in the Faber-Jackson, estimated at $46\,\mathrm{km\,s^{-1}}$. We checked that these velocity dispersion estimates are consistent with Faber-Jackson relation from Bernardi et al. 2003 using i-band absolute magnitudes.

For each of the selected galaxy candidates, we search for massive low-redshift galaxies within a $20''$ radius. About 90 % of the lensing affecting galaxies at $z \sim 8$ comes from galaxies at redshift $z_L < 3.5$ (Mason et al. 2015). Photometric redshifts and absolute magnitudes in the rest-frame Suprime-Cam/B are taken from `the Farmer` catalog. We restrict the lens selection to galaxies with a velocity dispersion of at least $\sigma_v = 200\,\mathrm{km\,s^{-1}}$, because the spectroscopic samples used to calibrate the Faber-Jackson relation become incomplete at lower values (Barone-Nugent et al. 2015). In addition, we only include lenses with a magnification of $\mu \geq 1.1$. For galaxies with multiple lenses, the cumulative magnification is computed as the product of individual magnifications.

We find that 14 of the selected galaxy candidates are magnified with $\mu \geq 1.1$, including 6 galaxies with $\mu \geq 1.2$. This includes 5 already identified candidates from Stefanon et al. 2019 and Bowler et al. 2020. However, we find no evidence of strongly lensed galaxies with multiple images with large magnifications. The coordinates and the estimated magnification from each of the lens galaxies are listed in Table 4.3. We note that lenses leading to $\mu \geq 1.1$ are identified up to a $15''$ angular distance. The strongest magnification occurs for the candidate ID441697, with a cumulative magnification of $\Pi\mu = 2.36$ from five nearby lenses, representing a flux boost of 0.9 mag. The main contribution comes from the $z = 0.50$ galaxy located within $4.6''$ and with a $\sigma_v = 231\,\mathrm{km\,s^{-1}}$ velocity dispersion, leading to a $\mu = 1.37$ magnification. The candidate Y8 (ID1209618) presents a nearby $z = 1.26$ galaxy at a $4.4''$ distance with a velocity dispersion of $\sigma_v = 215\,\mathrm{km\,s^{-1}}$, which gives a $\mu = 1.21$ magnification. This candidate was already identified as magnified by Stefanon et al. 2019. In that paper, the estimated velocity dispersion is about $40\,\mathrm{km\,s^{-1}}$ higher and the angular separation $0.3''$ smaller, resulting in a higher magnification $\mu = 1.39$. Three other candidates (Y1, Y10, Y12) from Stefanon et al. 2019 are also moderately magnified, with $1.1 < \mu < 1.2$.

Consequently, the selected galaxy candidates at $z > 7.5$ are significantly affected by weak lensing magnification, although there is no evidence of strong lenses. We note that the velocity dispersion lower limit of $\sigma_v = 200\,\mathrm{km\,s^{-1}}$ significantly restricts the number of lens galaxies, so that the reported total magnifications may be underestimated. This will need to be further investigated with more precise velocity dispersion estimates at fainter luminosities.

4.3.5. Spectroscopic confirmation proposals

The newly identified high-redshift galaxies in the COSMOS field are potential targets for spectroscopic observation programs. This step is necessary to validate the candidates selected from broad-band imaging. Up to now, four observing

Table 4.3. – Coordinates and physical parameters of the galaxy lenses affecting the selected $z > 7.5$ candidates. The columns indicate the candidate identifier, cumulative magnification, lens coordinates, angular separation between the lens and the candidate, lens photometric redshift, stellar mass, stellar velocity dispersion and magnification.

ID	$\Pi\mu$	R.A. [J2000]	Dec. [J2000]	θ [arcsec]	$z_{\rm phot}$	$\log(M_*)$ [$M_\odot$]	σ_v [km s^{-1}]	μ
327551	1.21 ± 0.11	09:57:47.85	01:43:58.26	4.6	$1.27^{+0.01}_{-0.01}$	$10.14^{+0.05}_{-0.04}$	219	1.21 ± 0.11
441697	2.36 ± 0.80	09:57:38.92	01:50:31.66	8.5	$1.99^{+0.01}_{-0.01}$	$10.70^{+0.04}_{-0.03}$	335	1.20 ± 0.07
		09:57:39.27	01:50:37.69	4.6	$0.50^{+0.01}_{-0.01}$	$10.91^{+0.03}_{-0.04}$	231	1.37 ± 0.20
		09:57:38.22	01:50:33.38	13.7	$1.35^{+0.01}_{-0.01}$	$11.45^{+0.03}_{-0.03}$	293	1.11 ± 0.04
		09:57:38.62	01:50:43.51	6.8	$1.71^{+0.03}_{-0.06}$	$11.59^{+0.04}_{-0.03}$	262	1.17 ± 0.07
		09:57:39.20	01:50:28.70	11.7	$0.49^{+0.01}_{-0.01}$	$11.00^{+0.03}_{-0.04}$	216	1.10 ± 0.05
442053	1.33 ± 0.18	09:58:33.03	01:50:42.75	6.0	$1.50^{+0.03}_{-0.04}$	$10.97^{+0.52}_{-0.05}$	218	1.14 ± 0.07
		09:58:32.80	01:50:46.76	4.0	$1.74^{+0.04}_{-0.04}$	$10.89^{+0.06}_{-0.06}$	207	1.17 ± 0.09
545752	1.13 ± 0.07	09:57:23.71	01:56:40.06	7.5	$0.57^{+0.03}_{-0.03}$	$10.32^{+0.08}_{-0.06}$	201	1.13 ± 0.07
784810	1.16 ± 0.07	10:01:47.28	02:10:08.33	7.7	$1.00^{+0.01}_{-0.02}$	$10.50^{+0.03}_{-0.03}$	239	1.16 ± 0.07
978062	1.16 ± 0.08	09:57:47.84	02:20:40.47	3.2	$2.98^{+0.07}_{-2.83}$	$10.09^{+0.06}_{-0.07}$	224	1.16 ± 0.08
1055131	1.13 ± 0.06	09:57:54.61	02:25:05.19	6.3	$1.19^{+0.01}_{-0.01}$	$10.02^{+0.05}_{-0.04}$	204	1.13 ± 0.06
1209618	1.21 ± 0.11	10:00:47.67	02:34:08.38	4.4	$1.26^{+0.02}_{-0.02}$	$11.15^{+0.03}_{-0.03}$	215	1.21 ± 0.11
1212944	1.20 ± 0.07	10:01:55.37	02:34:12.31	14.9	$0.56^{+0.01}_{-0.01}$	$11.60^{+0.03}_{-0.03}$	337	1.20 ± 0.07
1274544	1.15 ± 0.08	09:58:12.09	02:37:58.61	6.6	$0.74^{+0.02}_{-0.01}$	$11.02^{+0.05}_{-0.04}$	209	1.15 ± 0.08
1313521	1.19 ± 0.10	09:57:35.69	02:40:09.94	2.3	$3.01^{+0.05}_{-0.12}$	$10.12^{+0.06}_{-0.06}$	208	1.19 ± 0.10
1356755	1.10 ± 0.05	09:57:26.03	02:42:47.05	10.5	$0.43^{+0.01}_{-0.02}$	$11.00^{+0.03}_{-0.03}$	202	1.10 ± 0.05
1371152	1.11 ± 0.05	10:00:15.72	02:43:29.37	5.1	$2.95^{+0.02}_{-0.02}$	$10.15^{+0.06}_{-0.06}$	237	1.11 ± 0.05
1412106	1.25 ± 0.10	09:57:20.95	02:45:47.34	11.8	$1.38^{+0.03}_{-0.03}$	$10.93^{+0.05}_{-0.05}$	287	1.12 ± 0.04
		09:57:20.83	02:46:01.44	9.0	$1.17^{+0.01}_{-0.02}$	$11.28^{+0.05}_{-0.06}$	231	1.11 ± 0.05

[a] The magnification uncertainties are computed from the propagated intrinsic scatter in the velocity dispersion estimates from the Faber-Jackson relation.

proposals have been submitted to confirm the redshift of promising new candidates. Firstly, one program for the Northern extended millimeter array (NOEMA) spectroscopy aims to confirm the candidate ID1356755 with 2 mm observations (P.Is.: F. Valentino, M. Béthermin). This frequency targets the [CII] emission line, at a rest-frame wavelength of 158 μm, an star formation indicator unaffected by dust absorption (contrarily to optical and near-infrared observations). The selected candidate is one of the brightest in our sample, with $H \sim 24.5$ mag and $K_s \sim 24.5$ mag. Secondly, a program for the multi-object spectrometer for infrared exploration (MOSFIRE), at the Keck Observatory, proposes to observe three candidates, including ID1356755 and the candidate 762 from Bowler et al. 2020 using J-band spectroscopy (P.I.: B. Mobasher). This proposal was however rejected. Thirdly, an *HST*/WFC3 program, including near-infrared G141 grism spectroscopy and F140W imaging, also targets the candidate ID1356755 (P.I.: F. Valentino). This proposal was also rejected.

Finally, small *JWST* proposal for NIRSpec integral field unit (IFU) spectroscopy for the candidates ID441697, ID564423 (237), ID852845 (Y11), ID978062 (762), and ID1356755. These ultra-luminous galaxies are the most secure candidates at $9 < z < 10$ according to the two photometric catalogs with both the `LePhare` and `EAZY` photometric redshifts. This program will provide spatially-resolved spectroscopy to measure the UV and optical continuum and their associated emission lines. In particular, the Lyα break should be detected well enough to derive a redshift, and strong oxygen lines are also expected. Multiple galaxy candidates at $z \sim 7$ (Bowler et al. 2014) and $z \sim 9$ (Stefanon et al. 2019) were extended and even multi-component merger looking systems. The NIRSpec IFU will resolve these possible mergers.

4.4. Galaxy luminosity function

In this section, I use the results of the search for $z > 7.5$ star-forming galaxies to determine the bright end of the UV luminosity function. The absolute UV magnitudes are computed with `LePhare` using the GALEX far-UV filter, with a central wavelength of 1526 Å and a full-width at half maximum of 224 Å, and are listed in Table 4.2. We use the physical parameters estimated from `the Farmer` photometry. This is necessary because of the blended candidates not included in the Classic selection (Sect. 4.3.2). In addition, the overestimated aperture-to-total corrections for the candidates ID454766, ID720309 (discussed in Sect 4.3.1), may lead to overly bright magnitudes. Nonetheless, we use the Classic photometry for the candidate ID1356755 which is set to low redshift with `the Farmer` (Sect. 4.3.1). Since the photometric redshift estimates mainly rely on near-infrared broad-band imaging, the redshift probability distributions are relatively broad in the interval $7 < z < 10$, and so are the photometric redshift uncertainties. Yet, we split the selected galaxy sample into three redshift bins, centered at $z = 8, 9, 10$ with a fixed $\Delta z = 1$ width. As a result, the candidates with photometric redshifts at the limit between two adjacent bins may be scattered in one bin or the other.

4.4.1. Binned luminosity function

The binned luminosity function is calculated using the $V_{\rm max}$ estimator (Schmidt 1968). This estimator is non-parametric, although the number and the width of the bins are set, and implicitly assumes a uniform spatial distribution of galaxies. The number density in a given magnitude bin depends on the maximum volume $V_{\rm max}$ each galaxy could have been selected in. This volume, for a given galaxy i, is computed as:

$$V_{{\rm max},i} = \int_\Omega \int_{z_{{\rm min},i}}^{z_{{\rm max},i}} \frac{dV}{d\Omega dz} d\Omega dz, \tag{4.5}$$

where $z_{{\rm min},i}$ and $z_{{\rm max},i}$ are the lower and upper redshift limits within a galaxy i can be included in the sample, and dV is the differential comoving volume (Sect. 1.5.1).

The maximum comoving volume is defined as the shell between the limits of the redshift bins, with the 1.404 deg^2 of the HSC-masked UltraVISTA area. The maximum redshifts $z_{\max,i}$ are the redshifts for which the luminosity distance equals $D_L(z_{\rm phot})$, times the square root of the ratio between the H-band flux and the flux limit, set to $H = 25.6$ mag. This expression comes from the fact that the luminosity distance is inversely proportional to the square root of the observed flux (Sect. 1.1.3). Thus, the luminosity function ϕ can be expressed as:

$$\phi(M)\Delta M = \sum_{i=1}^{N(M)} \frac{1}{V_{\max,i}}, \tag{4.6}$$

where $N(M)$ is the number of galaxies in the magnitude bin centered at M and of width ΔM. The associated Poisson uncertainties σ_ϕ are computed as (Marshall 1985):

$$\sigma_\phi(M)\Delta M = \sqrt{\sum_{i=1}^{N(M)} \frac{1}{V_{\max,i}^2}}. \tag{4.7}$$

The total uncertainties are computed as the quadratic sum of the Poisson errors and cosmic variance errors, estimated following Trenti et al. 2008 (see Appendix A for more details). Since the galaxy samples become highly incomplete at faint magnitudes, the LFs are computed brightward of $M_{\rm UV} = -21.5$ mag. Bowler et al. 2020 estimated from source injection simulations that the high-redshift galaxy samples become more than 50% incomplete at $M_{\rm UV} > -21.4$ mag in the UltraVISTA DR4 images. We have not computed the completeness yet, although the galaxies with $M_{\rm UV} < -22$ mag are not expected to be severely affected by incompleteness.

The galaxy UV luminosity functions at $z = 8, 9, 10$ estimated from the selected galaxy candidates are represented in Fig. 4.14 and tabulated in Table 4.4. The results from McLure et al. 2013; Finkelstein et al. 2015; Bouwens et al. 2015b; Bouwens et al. 2019; Oesch et al. 2013; Oesch et al. 2018; McLeod et al. 2016; Morishita et al. 2018; Stefanon et al. 2019; Bowler et al. 2020 are shown for comparison. We use magnitude intervals with a 0.5 mag width, except for the brightest magnitude bin at $z = 10$ with a 1 mag width. We put an upper limit at 1σ in the magnitude bins with no galaxies. Cosmic variance represents about 14 % of the Poisson uncertainties at $M_{\rm UV} < -23$ mag, 20 % at $M_{\rm UV} = -22.75$ mag, and 30 % at $M_{\rm UV} = -22.25$ mag. We observe a clear decline of the number densities from $M_{\rm UV} = -23$ to -21.5 mag at $z = 8 - 9$. There is no clear evolution of the number densities from $z = 8$ to $z = 9$, with an equivalent number of candidates at $M_{\rm UV} > -22.5$ mag in both redshift bins.

Lensing magnification significantly affects the observed number densities in the brightest magnitude bins at $M_{\rm UV} < -22.5$ mag. In the $z = 9$ galaxy sample, the candidate ID978062 presents a magnification of $\mu = 1.16$ with an observed magnitude of $M_{\rm UV} = -22.51$ mag. Consequently, the unlensed UV magnitude

Table 4.4. – Galaxy luminosity functions derived from the $z > 7.5$ candidates. The columns indicate redshifts, comoving volumes, central absolute magnitudes, magnitude bin widths, number of selected galaxies and comoving number densities.

z	V	$M_{\rm UV}$	$\Delta M_{\rm UV}$	N	ϕ
	[10^6 Mpc^3]	[mag]	[mag]		[10^{-6} mag^{-1}Mpc^{-3}]
8	9.90	-22.75	0.5	0	< 0.20
		-22.25	0.5	2	0.40 ± 0.29
		-21.75	0.5	8	1.96 ± 0.80
9	8.97	-22.75	0.5	1	0.22 ± 0.23
		-22.25	0.5	4	0.89 ± 0.46
		-21.75	0.5	7	1.94 ± 0.81
10	8.17	-23.00	1.0	1	0.12 ± 0.12
		-22.25	0.5	2	0.49 ± 0.35

of this object is located in the fainter magnitude bin. Similarly, the candidate ID441697 at $z = 10$, with a cumulative magnification of $\mu = 2.36$, becomes fainter than $M_{\rm UV} = -22$ after removing the effect of lensing.

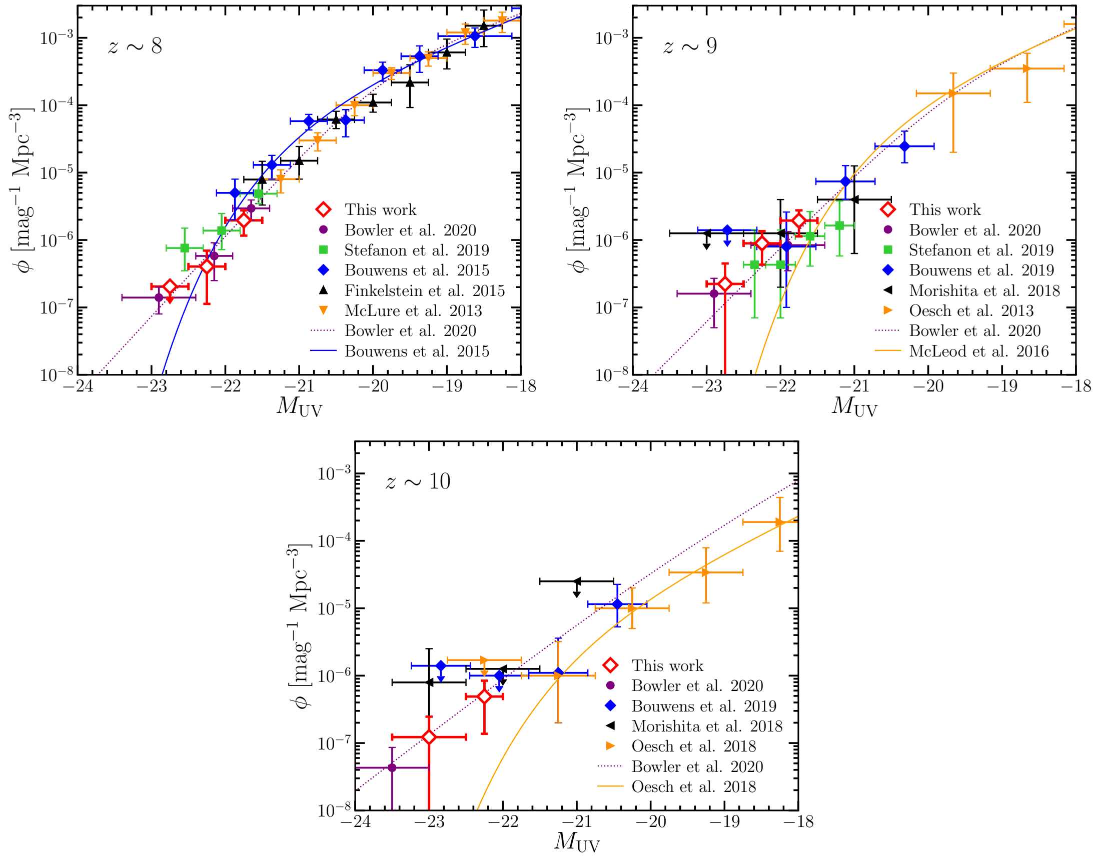

Figure 4.14. – Galaxy UV luminosity functions at $z = 8$ (*top left*), $z = 9$ (*top right*) and $z = 10$ (*bottom*). The red markers are the number densities from the galaxy sample presented in this work (uncorrected for incompleteness). The other markers and lines represent results from the literature. The upper limits are at 1σ.

4.4.2. Comparison with the literature

The calculated UVLFs are in good agreement with results from the literature, in particular at $M_{\rm UV} < -22$ mag. This argues in favor of the completeness of the galaxy sample in the bright magnitude bins. The most direct comparison is with Bowler et al. 2020, who used the same near-infrared images and similar optical and mid-infrared data (see Sect 4.3.3). There are 12 galaxy candidates among the 16 from Bowler et al. 2020 in common in the two selection. However, the authors analyzed about 6 deg^2 of imaging data from both the COSMOS and the XMM-LSS fields, sampling larger comoving volumes than in this work.

All the candidates from Bowler et al. 2020 at $z < 8.5$ and $M_{\rm UV} < -22.5$ mag are identified outside of the COSMOS field. This is the reason for the additional constraint on the bright end of the UVLF compared to our results. Nonetheless, the number densities at $M_{\rm UV} > -22.5$ mag are in excellent agreement with Bowler et al. 2020 and a factor of two lower than Stefanon et al. 2019.

At redshift $z \sim 9$, the constraint from Bowler et al. 2020 in the $M_{\rm UV} < -22.5$ mag bin entirely comes from the candidate 1212 in the COSMOS field, which was rejected in the present galaxy selection (see Sect. 4.3.3). In contrast, we find that the candidate 762 (ID978062) has a higher photometric redshift ($z = 8.85$ instead of 8.19) and slightly brighter absolute magnitude ($M_{\rm UV} = -22.51$ mag instead of -22.36 mag) than in Bowler et al. 2020. This candidate leads to the observed number density at $M_{\rm UV} < -22.5$ mag, also in agreement with the results from Bowler et al. 2020.

At redshift $z \sim 10$, the number densities computed from the three candidates selected in this work are in excellent agreement with the double-power-law evolution from Bowler et al. 2020. The candidate XMM3-3085 from Bowler et al. 2020, identified in the XMM field with a photometric redshift of $z_{\rm phot} = 10.8 \pm 1.0$, is extremely bright with an absolute magnitude of $M_{\rm UV} = -23.7$ mag and $H = 23.9$ mag. It is the brightest $z > 7$ galaxy candidate ever found in the literature, although spectroscopic confirmation is still required. The $z \sim 10$ candidate 2140+0241–303 from Morishita et al. 2018 has an *HST*/F160W flux of 24.4 mag and an absolute magnitude of $M_{\rm UV} = -22.6$ mag. The authors used the brightest of reionizing galaxies (BoRG[z9]) survey, including *HST* optical and near-infrared imaging in five broad bands over 370 arcmin^2, in addition to IRAC channel 1 imaging. The resulting number density from that paper is an order of magnitude brighter than our results at $M_{\rm UV} < -22.5$ mag.

4.5. Discussion

The shape of the observed galaxy UV luminosity function, in particular the bright end, depends on multiple physical and observational effects. At first, the attenuation by dust directly affects the visibility of the bright high-redshift galaxies. The mean dust content is generally expected to decrease with increasing redshift (e.g., Bouwens et al. 2016), because of the low metallicity of young stars in galaxies. Hence, the mean dust attenuation at $z > 9$ is often assumed to be zero (e.g., Bouwens et al. 2015b), so that the bright-end of the UVLF is expected to only reflect the recent star-formation in the galaxy population.

The presence of AGNs in the selected galaxy sample may affect the estimated galaxy UVLF at the bright end. High-redshift AGNs have Lyman alpha break features similar to star-forming galaxies without an AGN component. At intermediate redshift $4 < z < 6$, the contribution from faint AGNs dominates the number densities at $M_{\rm UV} < -23$ mag, whereas it becomes negligible at $M_{\rm UV} > -22$ mag (Ono et al. 2018). At higher redshift $z > 6$, the number density of faint AGNs is still unclear. The evolution of the quasar spatial density is often parametrized as $\rho(z) \propto 10^{k(z-z_0)}$, with $k \simeq -0.47$ from $z = 3.5$ to $z = 5$ (Fan et al. 2001) and $k \simeq -0.72$ from $z = 5$ to $z = 6$ (Jiang et al. 2016). Recently, Wang et al.

2019 measured a consistent value $k \simeq -0.78$ from $z = 6$ to $z = 6.7$. With this accelerated redshift evolution, high-redshift AGNs are sufficiently rare to have a negligible impact on the galaxy number density at $M_{\rm UV} = -23$ mag. The faint-end slope of the quasar UV luminosity function is nonetheless poorly constrained at high-redshift (Matsuoka et al. 2019). Hence, the non-stellar emission from potential AGNs can not be rejected for the brightest galaxy candidates at $z > 7$.

Because of gravitational lensing, the bright-end of the luminosity function is expected to be skewed through magnification bias (Turner et al. 1984) at very high redshifts, particularly for steep luminosity functions (Mason et al. 2015). This bias is entirely caused by the foreground galaxies at low redshift, and leads to two effects on the observed luminosity function. Firstly, the observed absolute magnitudes of lensed galaxies are brighter than in the intrinsic galaxy population. In a flux-limited sample, this increases the observed number densities at the faint end. Secondly, the magnification field decreases the intrinsic solid angle of the survey compared to the observed solid angle, leading to lower galaxy number densities in the image plane than in the source plane. In this work, we do not attempt to quantify this second effect. As discussed in Sect. 4.3.4, we find no evidence of strong lensing in the selected galaxy sample, although candidates are still affected by multiple weak lenses leading to significant cumulative magnifications. This leads to larger observed number densities at the very bright end, as discussed in Sect. 4.4.1. Thus, magnification bias partly explains the shape of the observed bright end of the luminosity function at the probed magnitudes.

In addition, the uncertainties in the absolute UV magnitudes may affect the bright-end through the Eddington bias (Eddington 1913). Because of the slope of the luminosity function, there are statistically more faint galaxies scattered into the brighter bins than the reverse, resulting in a flattened slope. This only concerns statistical uncertainties, related to the photometry and photometric redshifts, and not systematic uncertainties, such as the galaxy templates (stellar synthesis models, initial mass function) used to estimate absolute magnitudes. In the selected galaxy sample, photometric redshift uncertainties can be relatively large, leading to large uncertainties once propagated to absolute magnitudes. The Eddington bias is also stronger for steep luminosity functions. Nonetheless, this bias may be limited by using large magnitude bins.

4.6. Summary

Using both the Classic and `the Farmer` COSMOS2020 catalogs, I searched for high-redshift galaxies in the epoch of reionization. I identified 36 bright galaxy candidates at redshift $z > 7.5$ with $H < 25.6$ mag in the COSMOS field, including the majority of the candidates from Bowler et al. 2020. This selected sample of galaxies covers the absolute UV magnitude range of $-23.4 < M_{\rm UV} < -21$ mag. In order to confirm the redshift of newly identified candidates, proposals for spectroscopic observations were submitted. I used this sample of galaxies to construct the galaxy UV luminosity function at $z = 8$, $z = 9$ and $z = 10$. In the future, the deep imaging surveys with the next generation of telescopes, such as the *JWST* and *Euclid*, will bring new insights about high-redshift galaxies, with a much larger number of detections.

This study of the high-redshift galaxies in the COSMOS field highlighted some of the limitations of commonly used source extraction methods. Aperture photometry may be contaminated in the case of blended sources, in particular in the optical bands. Hence, blended high-redshift galaxies may be rejected because of underestimated photometric redshifts. With model-fitting photometry, such as with `the Farmer`, the emission from each of the nearby sources can be separated, leading to more accurate deblending. The resulting sample of high-redshift galaxies is therefore more complete. Nonetheless, the photometry of sources presenting internal structure may not be correctly fitted with simple symmetric surface brightness models. This aspect still needs to be improved in the future. In conclusion, this search for rare high-redshift galaxies strongly benefited from the availability of the two COSMOS2020 photometric catalogs. It offered the unique opportunity to exploit the advantages from both extraction methods, in order to select a robust sample of galaxies.

Conclusion

In this thesis, I studied the reionization of the Universe through the statistical analysis of galaxies at redshift $z > 6$, based on deep near-infrared imaging. The apparent properties of the high-redshift galaxy population can be used to describe the ionizing photon budget in the Universe, related to the fraction of neutral hydrogen in the inter-galactic medium. I investigated both pencil-beam and wide-field surveys to have a complete description of both the faint and bright galaxies. Thereby, I contributed to the preparation of the future surveys with the *James Webb* space telescope (*JWST*) and *Euclid*.

In preparation for the deep pencil-beam imaging surveys with *JWST*, I produced a prospective analysis of the faint high-redshift galaxies to be observed. I conducted extensive end-to-end simulations, from the generation of realistic mock images to the computation of the galaxy luminosity function, in order to evaluate the performance of these observing programs. In combination with the existing optical imaging from *HST*, I predicted that tens of high-redshift galaxies will be identified at $z \geq 8$ in the first *JWST* programs, with minimal contamination from brown dwarfs. Moreover, I robustly quantified the completeness and purity of the selected galaxy samples.

To search for rare, bright high-redshift galaxies, I processed the latest imaging data in the COSMOS field. This includes the infrared data from UltraVISTA and the *Spitzer* images from the Cosmic Dawn survey, in addition to the optical images from the Subaru Hyper Suprime-Cam. I have contributed greatly to the preparation of COSMOS2020, a new reference photometric catalog, providing the aperture photometry from optical and near-infrared high-resolution images. In addition to aperture photometry, the collaboration constructed a second catalog based on model-fitting to properly handle source deblending. These catalogs include more than 800 000 sources over the 1.5 $\deg^2$ area of the UltraVISTA survey. This work will be extremely useful for the scientific community, and notably for the *Euclid* space mission.

With the two COSMOS2020 photometric catalogs, I searched for galaxy during the epoch of reionization of the Universe. I identified 21 new galaxy candidates with photometric redshifts at $z > 7.5$. The combined analysis of the aperture and model-fitting photometry permitted robust galaxy samples to be selected, in particular in the case of blended galaxies contaminated by nearby sources. With this sample of high-redshift galaxies, I provided updated constraints on the bright end of the galaxy UV luminosity function at $z = 8$, $z = 9$ and $z = 10$.

Perspectives

Limitations of actual methods

The statistical description of the high-redshift galaxies, and more generally of the high-redshift Universe, remains limited by the actual understanding of these objects. Counting the number of galaxies to compute luminosity functions still relies on purity and completeness estimates, from simulations of sources injected into the images. With these simulations come an important amount of necessary assumptions, about the galaxy emission and morphology at high redshift, as well as the integrated effect of the foreground Universe along the line of sight. Early galaxies being mostly irregular with multiple components (e.g., Ribeiro et al. 2016), the characterization of galaxy morphology, and so the accurate simulations of these objects, remains challenging. In addition, low-redshift galaxies and stars contaminating the high-redshift samples also need to be depicted, so that a full view of the known Universe is actually required. As deeper observations with higher resolutions will be conducted, the knowledge of the galaxy observed emission and morphology from imaging and spectroscopy will increase as well.

Future deeper surveys will detect an increased number of high-redshift galaxies, as well as cold brown dwarfs. In fact, future samples of galaxies at high redshift may be even more severely contaminated by cold brown dwarfs. Hence, the improvements in the galactic model and the physical properties of these objects, in particular for type T and Y stars, will also benefit galaxy selections.

Future missions and telescopes

During the current decade, the next generation of telescopes will open a new window on the study of cosmic reionization. In the optical and near-infrared, the deep imaging surveys with larger telescopes and more sensitive detectors will significantly increase the number of galaxies identified at $z > 6$, improving the statistical description of these sources. Major advances will also come from the other observational probes for reionization.

In space, the future imaging surveys with the *JWST* and *Euclid* were already discussed in this thesis. Population III stars might be detectable for the first time with the *JWST*, in gravitationally lensed galaxies (Zackrisson et al. 2012; Rydberg et al. 2013). The rarest and brightest high-redshift galaxies will be observed with *Euclid*, as well as quasars, enabling the study the black hole coevolution (Euclid Collaboration et al. 2019). In addition, the Roman space telescope, formerly the wide-field infrared survey telescope (WFIRST; Spergel et al. 2013), will be launched to space in 2025. Its primary mirror is similar in size to the one on-board *HST*, but with a hundred times larger field of view. With the High Latitude Survey (HLS), Roman will observe $2\,200\,\mathrm{deg}^2$ of the sky up to a depth of $26.6\,\mathrm{mag}$ (5σ) in four near-infrared bands, considerably increasing the cosmological volume probed at $z > 8$ (Waters et al. 2016).

On the ground, future improvements in the instrumentation will provide larger collective area, in addition to enhanced adaptive optics. The optical telescope of the Rubin Observatory in Chile, with its legacy survey of space and time (LSST; Ivezić et al. 2019), will have a 8.4 m diameter primary mirror. With its first light in 2021, this instrument will observe 20 000 deg^2 of the southern sky using its wide-field optical imager (3.5 deg) in six filters from the near-ultraviolet to near-infrared ($0.3 - 1\,\mu$m). There are planned synergies with *Euclid*, notably in the Euclid Deep Field South (EDFS) to provide complementary optical imaging. Moreover, the first extremely large telescopes, namely the optical and near-infrared reflecting telescopes with at least 20-m primary mirror, will be operational during this decade. This includes the European extremely large telescope (E-ELT) in Chile, with its 39.3 m diameter primary mirror and its first light expected in 2025. The multi-adaptive optics imaging camera for deep observations (MICADO; Davies et al. 2018) will provide diffraction-limited near-infrared images ($0.8 - 2.4\,\mu$m), achieving sensitivities similar to *JWST* with a spatial resolution six times thinner (Fig. 4.15). Similarly, the thirty meter telescope (TMT) in Hawaii will have a 30 m diameter primary mirror and observe in wavelengths from UV to mid-infrared. Starting in 2026, its first light instruments include the infrared imaging spectrometer (IRIS), able to provide integral field spectroscopy with the smallest angular resolution ever achieved in the near-infrared (up to 0.004″).

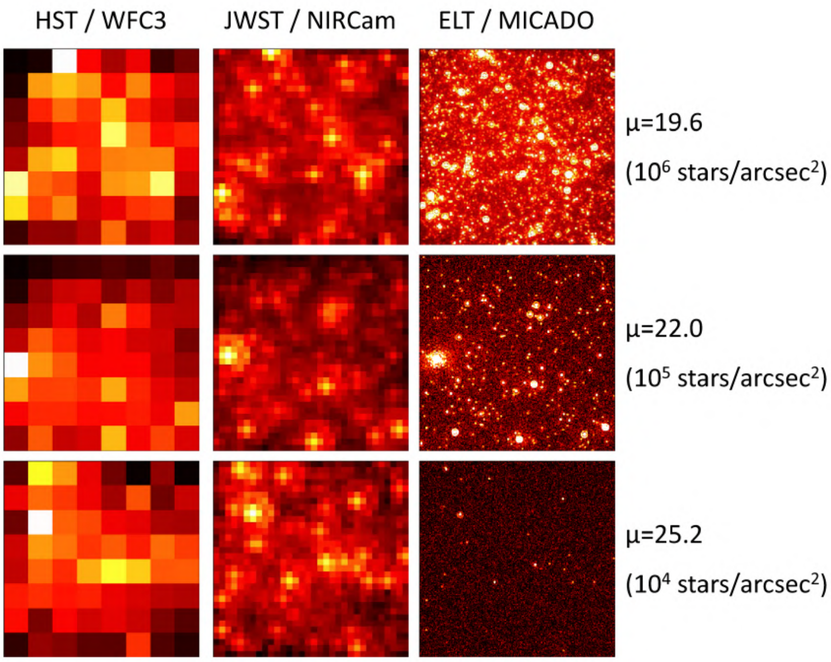

Figure 4.15. – Simulated images of crowded stellar fields at the indicated surface brightnesses μ (in mag/arcsec^2), for *HST*, *JWST*, and MICADO on E-ELT. These images are simulated with SimCADO. Source: Davies et al. 2018

In the longer wavelength range, the radio telescope SKA will provide the first direct measurement of cosmic reionization, through the spatial distribution of the neutral hydrogen 21 cm line (Koopmans et al. 2015). It will probe the whole reionization process from the birth of the first stars to the complete ionization of the IGM. Furthermore, the observation of transient objects at high redshift will be possible with SVOM in 2022, with an average of a hundred GRB observed per year (Wei et al. 2016). The origin and the environment of these events will be explored, as well as the illuminated structures along the line of sight.

List of publications

1. **Kauffmann, O. B.**, Le Fèvre, O., Ilbert, O., Chevallard, J., Williams, C. C., Curtis-Lake, E., Colina, L., Pérez-González, P. G., Pye, J. P., Caputi, K. I., 2020, “Simulating JWST deep extragalactic imaging surveys and physical parameter recovery”, published in A&A, 640, A67
2. Weaver, J. R., **Kauffmann, O. B.**, Ilbert, O., McCracken, H. J., Moneti, A., Toft, S., Brammer, G., Shuntov, M., Davidzon, I., Hsieh, B. C., Laigle, C., Anastasiou, A., Jespersen, C. K., Vinther, J., Capak, P., Casey, C. M., Milvang-Jensen, B., Mobasher, B., Sanders, D. B., Arnouts, S., Aussel, H., Dunlop, J. S., Faisst, A., Franx, M., Furtak, L. J., Fynbo, J. P. U., Greve, T., Gwyn, S., Kartaltepe, J. S., Kashino, D., Kokorev, V., Le Fèvre, O., Lilly, S., Masters, D., Magdis, G., Mehta, V., Peng, Y., Riechers, D. A., Salvato, M., Sawicki, M., Scarlata, C., Scoville, N., Shirley, R., Sneppen, A., Smolčić, V., Steinhardt, C., Stern, D., Tanaka, M., Taniguchi, Y., Teplitz, H. I., Vaccari, M., Wang, W.-H., Zalesky, L., Zamorani, G., “COSMOS2020: A panchromatic view of the Universe to z$\sim$10 from two complementary catalogs”, submitted to ApJS
3. Euclid collaboration, Moneti, A., McCracken, H. J., Shuntov, M., **Kauffmann, O. B.**, Weaver, J. R., Ilbert, O., Capak, P. L., Scarlata, C., Toft, S., Teplitz, H., Chary, R., Stern, D., et al., “Euclid preparation: Cosmic Dawn Survey Spitzer observations of the Euclid deep fields and calibration fields”, in prep.

Bibliography

Aihara, H. et al. (Jan. 2018). "The Hyper Suprime-Cam SSP Survey: Overview and survey design". In: *Publications of the Astronomical Society of Japan* 70, S4. DOI: 10.1093/pasj/psx066 (cit. on pp. 46, 91).

Aihara, H. et al. (Dec. 2019). "Second data release of the Hyper Suprime-Cam Subaru Strategic Program". In: *Publications of the Astronomical Society of Japan* 71, p. 114. DOI: 10.1093/pasj/psz103 (cit. on pp. 7, 91).

Arnouts, S. et al. (Dec. 1999). "Measuring and modelling the redshift evolution of clustering: the Hubble Deep Field North". In: *MNRAS* 310, pp. 540–556. DOI: 10.1046/j.1365-8711.1999.02978.x (cit. on p. 49).

Arnouts, S. et al. (Jan. 2002). "Measuring the redshift evolution of clustering: the Hubble Deep Field South". In: *MNRAS* 329, pp. 355–366. DOI: 10.1046/j.1365-8711.2002.04988.x (cit. on pp. 6, 48).

Ashby, M. L. N. et al. (Aug. 2018). "Spitzer Matching Survey of the UltraVISTA Ultra-deep Stripes (SMUVS): Full-mission IRAC Mosaics and Catalogs". In: *ApJS* 237, p. 39. DOI: 10.3847/1538-4365/aad4fb (cit. on pp. 90, 95).

Baraffe, I. et al. (May 2015). "New evolutionary models for pre-main sequence and main sequence low-mass stars down to the hydrogen-burning limit". In: *A&A* 577, A42. DOI: 10.1051/0004-6361/201425481 (cit. on p. 5).

Barkana, R. et al. (July 2001). "In the beginning: the first sources of light and the reionization of the universe". In: *Physics Reports* 349, pp. 125–238. DOI: 10.1016/S0370-1573(01)00019-9 (cit. on pp. 4, 31, 32).

Barone-Nugent, R. L. et al. (June 2015). "The impact of strong gravitational lensing on observed Lyman-break galaxy numbers at $4 \leq z \leq 8$ in the GOODS and the XDF blank fields". In: *MNRAS* 450, pp. 1224–1236. DOI: 10.1093/mnras/stv633 (cit. on pp. 157, 158).

Bartelmann, M. et al. (Jan. 2001). "Weak gravitational lensing". In: *Physics Reports* 340, pp. 291–472. DOI: 10.1016/S0370-1573(00)00082-X (cit. on p. 157).

Bañados, E. et al. (Jan. 2018). "An 800-million-solar-mass black hole in a significantly neutral Universe at a redshift of 7.5". In: *Natur* 553, pp. 473–476. DOI: 10.1038/nature25180 (cit. on p. 40).

Becker, G. D. et al. (Jan. 2011). "Detection of extended He II reionization in the temperature evolution of the intergalactic medium". In: *MNRAS* 410, pp. 1096–1112. DOI: 10.1111/j.1365-2966.2010.17507.x (cit. on p. 35).

Becker, G. D. et al. (Dec. 2015). "Reionisation and High-Redshift Galaxies: The View from Quasar Absorption Lines". In: *PASA* 32, e045. DOI: 10.1017/pasa.2015.45 (cit. on p. 37).

Becker, R. H. et al. (Dec. 2001). “Evidence for Reionization at z~6: Detection of a Gunn-Peterson Trough in a z=6.28 Quasar”. In: *AJ* 122, pp. 2850–2857. DOI: 10.1086/324231 (cit. on p. 36).

Bernardi, M. et al. (Apr. 2003). “Early-type Galaxies in the Sloan Digital Sky Survey. II. Correlations between Observables”. In: *AJ* 125, pp. 1849–1865. DOI: 10.1086/374256 (cit. on p. 158).

Bertin, E. (July 2006). “Automatic Astrometric and Photometric Calibration with SCAMP”. In: 351. Conference Name: Astronomical Data Analysis Software and Systems XV, p. 112 (cit. on p. 92).

– (2009). “SkyMaker: astronomical image simulations made easy.” In: *Mem. S.A.It.* 80, p. 422 (cit. on pp. 5, 59).

– (Jan. 2013). “PSFEx: Point Spread Function Extractor”. In: *Astrophysics Source Code Library*, ascl:1301.001 (cit. on p. 96).

Bertin, E. et al. (June 1996). “SExtractor: Software for source extraction.” In: *A&AS* 117, pp. 393–404. DOI: 10.1051/aas:1996164 (cit. on p. 91).

Bertin, E. et al. (2002). “The TERAPIX Pipeline”. In: vol. 281, p. 228 (cit. on p. 92).

Bolton, J. S. et al. (Sept. 2011). “How neutral is the intergalactic medium surrounding the redshift z = 7.085 quasar ULAS J1120+0641?” In: *MNRAS* 416, pp. L70–L74. DOI: 10.1111/j.1745-3933.2011.01100.x (cit. on p. 37).

Bolton, J. S. et al. (Feb. 2012). “Improved measurements of the intergalactic medium temperature around quasars: possible evidence for the initial stages of He II reionization at $z \simeq 6$”. In: *MNRAS* 419, pp. 2880–2892. DOI: 10.1111/j.1365-2966.2011.19929.x (cit. on p. 35).

Bouwens, R. J. et al. (Oct. 2015a). “Reionization After Planck: The Derived Growth of the Cosmic Ionizing Emissivity Now Matches the Growth of the Galaxy UV Luminosity Density”. In: *ApJ* 811, p. 140. DOI: 10.1088/0004-637X/811/2/140 (cit. on pp. 36, 47).

Bouwens, R. J. et al. (Apr. 2015b). “UV Luminosity Functions at Redshifts $z \sim 4$ to $z \sim 10$: 10,000 Galaxies from HST Legacy Fields”. In: *ApJ* 803, p. 34. DOI: 10.1088/0004-637X/803/1/34 (cit. on pp. 41–43, 46, 161, 164).

Bouwens, R. J. et al. (Dec. 2016). “ALMA Spectroscopic Survey in the Hubble Ultra Deep Field: The Infrared Excess of UV-Selected z = 2-10 Galaxies as a Function of UV-Continuum Slope and Stellar Mass”. In: *ApJ* 833, p. 72. DOI: 10.3847/1538-4357/833/1/72 (cit. on p. 164).

Bouwens, R. J. et al. (July 2017). “The $z \sim 6$ Luminosity Function Fainter than -15 mag from the Hubble Frontier Fields: The Impact of Magnification Uncertainties”. en. In: *ApJ* 843.2, p. 129. DOI: 10.3847/1538-4357/aa70a4 (cit. on p. 41).

Bouwens, R. J. et al. (July 2019). “Newly Discovered Bright $z \sim$ 9-10 Galaxies and Improved Constraints on Their Prevalence Using the Full CANDELS Area”. In: *ApJ* 880, p. 25. DOI: 10.3847/1538-4357/ab24c5 (cit. on p. 161).

Bowler, R. A. A. et al. (May 2014). "The bright end of the galaxy luminosity function at z≃7: before the onset of mass quenching?" In: *MNRAS* 440, pp. 2810–2842. DOI: 10.1093/mnras/stu449 (cit. on pp. 134, 160).

Bowler, R. a. A. et al. (Sept. 2015). "The galaxy luminosity function at z≃ 6 and evidence for rapid evolution in the bright end from z≃ 7 to 5". en. In: *MNRAS* 452.2, pp. 1817–1840. DOI: 10.1093/mnras/stv1403 (cit. on pp. 9, 46, 134).

Bowler, R. A. A. et al. (Apr. 2020). "A lack of evolution in the very bright end of the galaxy luminosity function from z ≃ 8 to 10". In: *MNRAS* 493, pp. 2059–2084. DOI: 10.1093/mnras/staa313 (cit. on pp. 9, 10, 134, 137, 138, 140, 149–152, 154–156, 158, 159, 161, 163–165).

Bowman, J. D. et al. (Mar. 2008). "Toward Empirical Constraints on the Global Redshifted 21 cm Brightness Temperature During the Epoch of Reionization". In: *ApJ* 676, pp. 1–9. DOI: 10.1086/528675 (cit. on p. 39).

Bowman, J. D. et al. (Mar. 2018). "An absorption profile centred at 78 megahertz in the sky-averaged spectrum". In: *Natur* 555, pp. 67–70. DOI: 10.1038/nature25792 (cit. on p. 39).

Brammer, G. B. et al. (Oct. 2008). "EAZY: A Fast, Public Photometric Redshift Code". In: *ApJ* 686, pp. 1503–1513. DOI: 10.1086/591786 (cit. on pp. 8, 92).

Bruzual, G. et al. (Oct. 2003). "Stellar population synthesis at the resolution of 2003". en. In: *MNRAS* 344.4, p. 1000. DOI: 10.1046/j.1365-8711.2003.06897.x (cit. on p. 47).

Caballero, J. A. et al. (Sept. 2008). "Contamination by field late-M, L, and T dwarfs in deep surveys". In: *A&A* 488, pp. 181–190. DOI: 10.1051/0004-6361:200809520 (cit. on pp. 5, 51).

Chambers, L. et al. (Jan. 2019). "Preparing for JWST Commissioning, Calibration, and Science with the Multi-Instrument Ramp Generator (MIRAGE)". In: 233. Conference Name: American Astronomical Society Meeting Abstracts #233, p. 157.12 (cit. on p. 58).

Chornock, R. et al. (Sept. 2013). "GRB 130606A as a Probe of the Intergalactic Medium and the Interstellar Medium in a Star-forming Galaxy in the First Gyr after the Big Bang". In: *ApJ* 774, p. 26. DOI: 10.1088/0004-637X/774/1/26 (cit. on p. 38).

Cirasuolo, M. et al. (Sept. 2007). "The evolution of the near-infrared galaxy luminosity function and colour bimodality up to z ∼= 2 from the UKIDSS Ultra Deep Survey Early Data Release". In: *MNRAS* 380, pp. 585–595. DOI: 10.1111/j.1365-2966.2007.12038.x (cit. on p. 46).

Cropper, M. et al. (July 2016). "VIS: the visible imager for Euclid". In: 9904. Conference Name: Space Telescopes and Instrumentation 2016: Optical, Infrared, and Millimeter Wave ISBN: 9781510601871 Place: eprint: arXiv:1608.08603, 99040Q. DOI: 10.1117/12.2234739 (cit. on p. 88).

Cucchiara, A. et al. (July 2011). "A Photometric Redshift of z ∼ 9.4 for GRB 090429B". In: *ApJ* 736, p. 7. DOI: 10.1088/0004-637X/736/1/7 (cit. on p. 38).

Cunha, C. E. et al. (July 2009). “Estimating the redshift distribution of photometric galaxy samples - II. Applications and tests of a new method”. In: *MNRAS* 396, pp. 2379–2398. DOI: 10.1111/j.1365-2966.2009.14908.x (cit. on p. 89).

Cushing, M. C. et al. (Dec. 2011). “The Discovery of Y Dwarfs using Data from the Wide-field Infrared Survey Explorer (WISE)”. In: *ApJ* 743, p. 50. DOI: 10.1088/0004-637X/743/1/50 (cit. on p. 50).

Davies, R. et al. (July 2018). “The MICADO first light imager for the ELT: overview, operation, simulation”. In: 0702. Conference Name: Ground-based and Airborne Instrumentation for Astronomy VII ISBN: 9781510619579 Place: eprint: arXiv:1807.10003, 107021S. DOI: 10.1117/12.2311483 (cit. on p. 169).

Davis, M. et al. (May 2007). “The All-Wavelength Extended Groth Strip International Survey (AEGIS) Data Sets”. In: *ApJL* 660, pp. L1–L6. DOI: 10.1086/517931 (cit. on p. 46).

Dawson, W. A. et al. (Jan. 2016). “The Ellipticity Distribution of Ambiguously Blended Objects”. In: *ApJ* 816, p. 11. DOI: 10.3847/0004-637X/816/1/11 (cit. on pp. 5, 58).

Dyson, F. W. et al. (1920). “A Determination of the Deflection of Light by the Sun’s Gravitational Field, from Observations Made at the Total Eclipse of May 29, 1919”. In: *Philosophical Transactions of the Royal Society of London Series A* 220, pp. 291–333. DOI: 10.1098/rsta.1920.0009 (cit. on p. 25).

Eddington, A. S. (Mar. 1913). “On a formula for correcting statistics for the effects of a known error of observation”. In: *MNRAS* 73, pp. 359–360. DOI: 10.1093/mnras/73.5.359 (cit. on p. 165).

Einstein, A. (1915). “Zur allgemeinen Relativitätstheorie”. In: *Sitzungsberichte der Königlich Preußischen Akademie der Wissenschaften (Berlin), Seite 778-786.* (Cit. on p. 25).

Erben, T. et al. (Feb. 2001). “How accurately can we measure weak gravitational shear?” In: *A&A* 366, pp. 717–735. DOI: 10.1051/0004-6361:20010013 (cit. on p. 60).

Euclid Collaboration et al. (Nov. 2019). “Euclid preparation. V. Predicted yield of redshift $7 < z < 9$ quasars from the wide survey”. In: *A&A* 631, A85. DOI: 10.1051/0004-6361/201936427 (cit. on p. 168).

Faber, S. M. et al. (Mar. 1976). “Velocity dispersions and mass-to-light ratios for elliptical galaxies”. In: *ApJ* 204, pp. 668–683. DOI: 10.1086/154215 (cit. on p. 157).

Fan, X. et al. (Jan. 2001). “High-Redshift Quasars Found in Sloan Digital Sky Survey Commissioning Data. IV. Luminosity Function from the Fall Equatorial Stripe Sample”. In: *AJ* 121, pp. 54–65. DOI: 10.1086/318033 (cit. on p. 164).

Fan, X. et al. (July 2006). “Constraining the Evolution of the Ionizing Background and the Epoch of Reionization with z~6 Quasars. II. A Sample of 19 Quasars”. In: *AJ* 132, pp. 117–136. DOI: 10.1086/504836 (cit. on pp. 4, 37).

Finkelstein, S. L. (Aug. 2016). “Observational Searches for Star-Forming Galaxies at $z > 6$”. In: *PASA* 33, e037. DOI: 10.1017/pasa.2016.26 (cit. on p. 48).

Finkelstein, S. L. et al. (Sept. 2015). "The Evolution of the Galaxy Rest-frame Ultraviolet Luminosity Function over the First Two Billion Years". In: *ApJ* 810, p. 71. DOI: 10.1088/0004-637X/810/1/71 (cit. on pp. 46, 161).

Finkelstein, S. L. et al. (July 2019). "Conditions for Reionizing the Universe with a Low Galaxy Ionizing Photon Escape Fraction". In: *ApJ* 879, p. 36. DOI: 10.3847/1538-4357/ab1ea8 (cit. on pp. 4, 39, 45).

Fontana, A. et al. (Dec. 2010). "The Lack of Intense Lyα in Ultradeep Spectra of z = 7 Candidates in GOODS-S: Imprint of Reionization?" In: *ApJL* 725, pp. L205–L209. DOI: 10.1088/2041-8205/725/2/L205 (cit. on p. 37).

Gardner, J. P. et al. (June 2006). "Science with the James Webb space telescope". In: *Proc. SPIE* 6265. DOI: 10.1117/12.670492 (cit. on p. 55).

Giavalisco, M. (2002). "Lyman-Break Galaxies". In: *ARA&A* 40, pp. 579–641. DOI: 10.1146/annurev.astro.40.121301.111837 (cit. on p. 47).

Giavalisco, M. et al. (Jan. 2004). "The Great Observatories Origins Deep Survey: Initial Results from Optical and Near-Infrared Imaging". In: *ApJL* 600, pp. L93–L98. DOI: 10.1086/379232 (cit. on p. 46).

Gnedin, N. Y. (June 2000). "Cosmological Reionization by Stellar Sources". In: *ApJ* 535, pp. 530–554. DOI: 10.1086/308876 (cit. on pp. 4, 32).

Grogin, N. A. et al. (Dec. 2011). "CANDELS: The Cosmic Assembly Near-infrared Deep Extragalactic Legacy Survey". In: *ApJS* 197, p. 35. DOI: 10.1088/0067-0049/197/2/35 (cit. on p. 46).

Hayes, M. et al. (Feb. 2014). "The Lyman Alpha Reference Sample. II. Hubble Space Telescope Imaging Results, Integrated Properties, and Trends". In: *ApJ* 782, p. 6. DOI: 10.1088/0004-637X/782/1/6 (cit. on p. 38).

Hogg, D. W. et al. (Oct. 2002). "The K correction". In: *preprint* (cit. on p. 53).

Hsieh, B. et al. (Dec. 2012). "The Taiwan ECDFS Near-Infrared Survey: Ultra-deep J and KS Imaging in the Extended Chandra Deep Field-South". In: *ApJS* 203, p. 23. DOI: 10.1088/0067-0049/203/2/23 (cit. on p. 91).

Hubble, E. (Mar. 1929). "A Relation between Distance and Radial Velocity among Extra-Galactic Nebulae". In: *Proceedings of the National Academy of Science* 15, pp. 168–173. DOI: 10.1073/pnas.15.3.168 (cit. on p. 25).

Ilbert, O. et al. (Sept. 2005). "The VIMOS-VLT deep survey - Evolution of the galaxy luminosity function up to z = 2 in first epoch data". en. In: *A&A* 439.3, pp. 863–876. DOI: 10.1051/0004-6361:20041961 (cit. on p. 53).

Ilbert, O. et al. (Oct. 2006). "Accurate photometric redshifts for the CFHT legacy survey calibrated using the VIMOS VLT deep survey". In: *A&A* 457, pp. 841–856. DOI: 10.1051/0004-6361:20065138 (cit. on pp. 6, 48).

Illingworth, G. D. et al. (Oct. 2013). "THEHSTEXTREME DEEP FIELD (XDF): COMBINING ALL ACS AND WFC3/IR DATA ON THE HUDF REGION INTO THE DEEPEST FIELD EVER". en. In: *ApJS* 209.1, p. 6. DOI: 10.1088/0067-0049/209/1/6 (cit. on p. 46).

Ivezić, Ž. et al. (Mar. 2019). "LSST: From Science Drivers to Reference Design and Anticipated Data Products". In: *ApJ* 873, p. 111. DOI: 10.3847/1538-4357/ab042c (cit. on p. 169).

Jiang, L. et al. (Dec. 2016). "The Final SDSS High-redshift Quasar Sample of 52 Quasars at z>5.7". In: *ApJ* 833, p. 222. DOI: 10.3847/1538-4357/833/2/222 (cit. on p. 164).

Jouvel, S. et al. (Sept. 2009). "Designing future dark energy space missions. I. Building realistic galaxy spectro-photometric catalogs and their first applications". In: *A&A* 504, pp. 359–371. DOI: 10.1051/0004-6361/200911798 (cit. on p. 89).

Kauffmann, O. B. et al. (Aug. 2020). "Simulating JWST deep extragalactic imaging surveys and physical parameter recovery". In: *A&A* 640, A67. DOI: 10.1051/0004-6361/202037450 (cit. on p. 97).

Kirkpatrick, J. D. et al. (July 2012). "Further Defining Spectral Type "Y" and Exploring the Low-mass End of the Field Brown Dwarf Mass Function". In: *ApJ* 753, p. 156. DOI: 10.1088/0004-637X/753/2/156 (cit. on p. 50).

Koekemoer, A. M. et al. (Sept. 2007). "The COSMOS Survey: Hubble Space Telescope Advanced Camera for Surveys Observations and Data Processing". en. In: *ApJS* 172, p. 196. DOI: 10.1086/520086 (cit. on p. 90).

Koekemoer, A. M. et al. (Dec. 2011). "CANDELS: The Cosmic Assembly Near-infrared Deep Extragalactic Legacy Survey—The Hubble Space Telescope Observations, Imaging Data Products, and Mosaics". In: *ApJS* 197, p. 36. DOI: 10.1088/0067-0049/197/2/36 (cit. on p. 46).

Koopmans, L. et al. (Apr. 2015). "The Cosmic Dawn and Epoch of Reionisation with SKA". In: *Advancing Astrophysics with the Square Kilometre Array (AASKA14)*, p. 1 (cit. on pp. 39, 170).

Kramer, R. H. et al. (Apr. 2008). "The thickness of high-redshift quasar ionization fronts as a constraint on the ionizing spectral energy distribution". In: *MNRAS* 385, pp. 1561–1575. DOI: 10.1111/j.1365-2966.2008.12945.x (cit. on p. 31).

Kuhlen, M. et al. (June 2012). "Concordance models of reionization: implications for faint galaxies and escape fraction evolution". In: *MNRAS* 423, pp. 862–876. DOI: 10.1111/j.1365-2966.2012.20924.x (cit. on pp. 33, 34).

Laigle, C. et al. (June 2016). "The COSMOS2015 Catalog: Exploring the $1 < z < 6$ Universe with Half a Million Galaxies". In: *ApJS* 224, p. 24. DOI: 10.3847/0067-0049/224/2/24 (cit. on pp. 7, 88, 90–92, 95).

Lang, D. et al. (Apr. 2016). "The Tractor: Probabilistic astronomical source detection and measurement". In: *Astrophysics Source Code Library*, ascl:1604.008 (cit. on p. 91).

Laporte, N. et al. (Dec. 2017). "A Spectroscopic Search for AGN Activity in the Reionization Era". In: *ApJ* 851, p. 40. DOI: 10.3847/1538-4357/aa96a8 (cit. on p. 40).

Laureijs, R. et al. (Oct. 2011). "Euclid Definition Study Report". In: *preprint* arXiv:1110.3193 (cit. on p. 88).

Lawrence, A. et al. (Aug. 2007). "The UKIRT Infrared Deep Sky Survey (UKIDSS)". In: *MNRAS* 379, pp. 1599–1617. DOI: 10.1111/j.1365-2966.2007.12040.x (cit. on p. 46).
Le Fèvre, O. et al. (Apr. 2015). "The VIMOS Ultra-Deep Survey: ~10 000 galaxies with spectroscopic redshifts to study galaxy assembly at early epochs $2 < z \simeq 6$". In: *A&A* 576, A79. DOI: 10.1051/0004-6361/201423829 (cit. on pp. 46, 48, 49).
Leauthaud, A. et al. (Sept. 2007). "Weak Gravitational Lensing with COSMOS: Galaxy Selection and Shape Measurements". en. In: *ApJS* 172.1, p. 219. DOI: 10.1086/516598 (cit. on pp. 51, 96).
Lemaître, G. (Mar. 1931). "Expansion of the universe, The expanding universe". In: *MNRAS* 91, pp. 490–501. DOI: 10.1093/mnras/91.5.490 (cit. on p. 25).
Livermore, R. C. et al. (Feb. 2017). "Directly Observing the Galaxies Likely Responsible for Reionization". en. In: *ApJ* 835.2, p. 113. DOI: 10.3847/1538-4357/835/2/113 (cit. on p. 41).
Lorenzoni, S. et al. (June 2011). "Star-forming galaxies at z≈ 8-9 from Hubble Space Telescope/WFC3: implications for reionization". In: *MNRAS* 414, pp. 1455–1466. DOI: 10.1111/j.1365-2966.2011.18479.x (cit. on p. 50).
Lotz, J. M. et al. (Mar. 2017). "The Frontier Fields: Survey Design and Initial Results". In: *ApJ* 837, p. 97. DOI: 10.3847/1538-4357/837/1/97 (cit. on p. 46).
MacArthur, L. A. et al. (Jan. 2003). "Structure of Disk-dominated Galaxies. I. Bulge/Disk Parameters, Simulations, and Secular Evolution". In: *ApJ* 582, pp. 689–722. DOI: 10.1086/344506 (cit. on p. 61).
Maciaszek, T. et al. (July 2016). "Euclid Near Infrared Spectrometer and Photometer instrument concept and first test results obtained for different breadboards models at the end of phase C". In: 9904. Conference Name: Space Telescopes and Instrumentation 2016: Optical, Infrared, and Millimeter Wave ISBN: 9781510601871, 99040T. DOI: 10.1117/12.2232941 (cit. on p. 88).
Madau, P. et al. (Apr. 1999). "Radiative Transfer in a Clumpy Universe. III. The Natur of Cosmological Ionizing Sources". In: *ApJ* 514, pp. 648–659. DOI: 10.1086/306975 (cit. on pp. 32, 34).
Madau, P. et al. (Aug. 2014). "Cosmic Star-Formation History". en. In: *ARA&A* 52, p. 415. DOI: 10.1146/annurev-astro-081811-125615 (cit. on pp. 42, 44).
Maniyar, A. S. et al. (June 2018). "Star formation history from the cosmic infrared background anisotropies". In: *A&A* 614, A39. DOI: 10.1051/0004-6361/201732499 (cit. on p. 44).
Marshall, H. L. (Dec. 1985). "The evolution of optically selected quasars with Z less than 2.2 and B less than 20". In: *ApJ* 299, pp. 109–121. DOI: 10.1086/163685 (cit. on p. 161).
Mason, C. A. et al. (May 2015). "Correcting the $z \sim 8$ Galaxy Luminosity Function for Gravitational Lensing Magnification Bias". In: *ApJ* 805, p. 79. DOI: 10.1088/0004-637X/805/1/79 (cit. on pp. 41, 157, 158, 165).

Masters, D. C. et al. (June 2019). “The Complete Calibration of the Color-Redshift Relation (C3R2) Survey: Analysis and Data Release 2”. In: *ApJ* 877, p. 81. DOI: 10.3847/1538-4357/ab184d (cit. on p. 89).

Matsuoka, Y. et al. (Feb. 2019). “Discovery of the First Low-luminosity Quasar at z > 7”. In: *ApJL* 872, p. L2. DOI: 10.3847/2041-8213/ab0216 (cit. on p. 165).

McCracken, H. J. et al. (Aug. 2012). “UltraVISTA: a new ultra-deep near-infrared survey in COSMOS”. In: *A&A* 544, A156. DOI: 10.1051/0004-6361/201219507 (cit. on pp. 7, 46, 90).

McGreer, I. D. et al. (Feb. 2015). “Model-independent evidence in favour of an end to reionization by z ≈ 6”. In: *MNRAS* 447, pp. 499–505. DOI: 10.1093/mnras/stu2449 (cit. on p. 37).

McLeod, D. J. et al. (July 2016). “The z = 9-10 galaxy population in the Hubble Frontier Fields and CLASH surveys: the z = 9 luminosity function and further evidence for a smooth decline in ultraviolet luminosity density at z≥ 8”. en. In: *MNRAS* 459.4, pp. 3812–3824. DOI: 10.1093/mnras/stw904 (cit. on pp. 45, 46, 161).

McLure, R. J. et al. (July 2013). “A new multifield determination of the galaxy luminosity function at z = 7–9 incorporating the 2012 Hubble Ultra-Deep Field imaging”. en. In: *MNRAS* 432.4, pp. 2696–2716. DOI: 10.1093/mnras/stt627 (cit. on p. 161).

McQuinn, M. et al. (Dec. 2011). “On Lyman-limit Systems and the Evolution of the Intergalactic Ionizing Background”. In: *ApJ* 743, p. 82. DOI: 10.1088/0004-637X/743/1/82 (cit. on p. 32).

Meurer, G. R. et al. (Aug. 1999). “Dust Absorption and the Ultraviolet Luminosity Density at z ~ 3 as Calibrated by Local Starburst Galaxies”. In: *ApJ* 521, pp. 64–80. DOI: 10.1086/307523 (cit. on p. 43).

Miyazaki, S. (Aug. 2015). “New wide field camera for Subaru Telescope: Hyper Suprime-Cam”. In: *IAU General Assembly* 22, p. 2255916 (cit. on p. 46).

Moffat, A. F. J. (Dec. 1969). “A Theoretical Investigation of Focal Stellar Images in the Photographic Emulsion and Application to Photographic Photometry”. In: *A&A* 3, p. 455 (cit. on pp. 8, 96).

Momcheva, I. G. et al. (Aug. 2016). “The 3D-HST Survey: Hubble Space Telescope WFC3/G141 Grism Spectra, Redshifts, and Emission Line Measurements for ~ 100,000 Galaxies”. In: *ApJS* 225, p. 27. DOI: 10.3847/0067-0049/225/2/27 (cit. on p. 149).

Morishita, T. et al. (Nov. 2018). “The Bright-end Galaxy Candidates at z ∼ 9 from 79 Independent HST Fields”. In: *ApJ* 867, p. 150. DOI: 10.3847/1538-4357/aae68c (cit. on pp. 161, 164).

Moster, B. P. et al. (Apr. 2011). “A Cosmic Variance Cookbook”. In: *ApJ* 731, p. 113. DOI: 10.1088/0004-637X/731/2/113 (cit. on p. 41).

Mowla, L. A. et al. (July 2019). “COSMOS-DASH: The Evolution of the Galaxy Size-Mass Relation since z ∼ 3 from New Wide-field WFC3 Imaging Combined

with CANDELS/3D-HST". In: *ApJ* 880, p. 57. DOI: 10.3847/1538-4357/ab290a (cit. on p. 149).
Oesch, P. A. et al. (Aug. 2013). "Probing the Dawn of Galaxies at z ~ 9-12: New Constraints from HUDF12/XDF and CANDELS data". In: *ApJ* 773, p. 75. DOI: 10.1088/0004-637X/773/1/75 (cit. on p. 161).
Oesch, P. A. et al. (Mar. 2016). "A Remarkably Luminous Galaxy at z=11.1 Measured with Hubble Space Telescope Grism Spectroscopy". In: *ApJ* 819, p. 129. DOI: 10.3847/0004-637X/819/2/129 (cit. on p. 40).
Oesch, P. A. et al. (Mar. 2018). "The Dearth of z ~ 10 Galaxies in All HST Legacy Fields—The Rapid Evolution of the Galaxy Population in the First 500 Myr". In: *ApJ* 855, p. 105. DOI: 10.3847/1538-4357/aab03f (cit. on pp. 46, 161).
Oke, J. B. (Feb. 1974). "Absolute Spectral Energy Distributions for White Dwarfs". In: *ApJS* 27, p. 21. DOI: 10.1086/190287 (cit. on pp. 52, 134).
Oke, J. B. et al. (Oct. 1968). "Energy Distributions, K Corrections, and the Stebbins-Whitford Effect for Giant Elliptical Galaxies". In: *ApJ* 154, p. 21. DOI: 10.1086/149737 (cit. on p. 53).
Ono, Y. et al. (Jan. 2018). "Great Optically Luminous Dropout Research Using Subaru HSC (GOLDRUSH). I. UV luminosity functions at z $\sim$ 4-7 derived with the half-million dropouts on the 100 deg2 sky". In: *Publications of the Astronomical Society of Japan* 70, S10. DOI: 10.1093/pasj/psx103 (cit. on pp. 46, 164).
Osterbrock, D. E. (1989). "Astrophysics of gaseous nebulae and active galactic nuclei". In: *University Science Books* (cit. on pp. 31, 32).
Ouchi, M. et al. (June 2008). "The Subaru/XMM-Newton Deep Survey (SXDS). IV. Evolution of Lyα Emitters from z = 3.1 to 5.7 in the 1 deg2 Field: Luminosity Functions and AGN". In: *ApJS* 176, pp. 301–330. DOI: 10.1086/527673 (cit. on p. 38).
Ouchi, M. et al. (Dec. 2009). "Large Area Survey for z = 7 Galaxies in SDF and GOODS-N: Implications for Galaxy Formation and Cosmic Reionization". In: *ApJ* 706, pp. 1136–1151. DOI: 10.1088/0004-637X/706/2/1136 (cit. on p. 35).
Ouchi, M. et al. (Nov. 2010). "Statistics of 207 Lyα Emitters at a Redshift Near 7: Constraints on Reionization and Galaxy Formation Models". In: *ApJ* 723, pp. 869–894. DOI: 10.1088/0004-637X/723/1/869 (cit. on p. 38).
Patel, M. et al. (Mar. 2010). "The reanalysis of spectra of GRB 080913 to estimate the neutral fraction of the IGM at a redshift of 6.7". In: *A&A* 512, p. L3. DOI: 10.1051/0004-6361/200913876 (cit. on p. 38).
Pawlik, A. H. et al. (Apr. 2009). "Keeping the Universe ionized: photoheating and the clumping factor of the high-redshift intergalactic medium". In: *MNRAS* 394, pp. 1812–1824. DOI: 10.1111/j.1365-2966.2009.14486.x (cit. on p. 35).
Pecaut, M. J. et al. (Sept. 2013). "Intrinsic Colors, Temperatures, and Bolometric Corrections of Pre-main-sequence Stars". In: *ApJS* 208, p. 9. DOI: 10.1088/0067-0049/208/1/9 (cit. on pp. 5, 50).

Peebles, P. J. E. (1980). “The large-scale structure of the universe”. In: *Research supported by the National Science Foundation. Princeton, N.J., Princeton University Press, 1980. 435 p.* (Cit. on p. 186).

Peimbert, A. et al. (Oct. 2016). “The primordial helium abundance and the number of neutrino families”. In: *Revista Mexicana de Astronomia y Astrofisica* 52, pp. 419–424 (cit. on p. 35).

Pentericci, L. et al. (Dec. 2011). “Spectroscopic Confirmation of z ~ 7 Lyman Break Galaxies: Probing the Earliest Galaxies and the Epoch of Reionization”. In: *ApJ* 743, p. 132. DOI: 10.1088/0004-637X/743/2/132 (cit. on p. 37).

Pentericci, L. et al. (Oct. 2014). “New Observations of z ~ 7 Galaxies: Evidence for a Patchy Reionization”. In: *ApJ* 793, p. 113. DOI: 10.1088/0004-637X/793/2/113 (cit. on p. 37).

Penzias, A. A. et al. (July 1965). “A Measurement of Excess Antenna Temperature at 4080 Mc/s.” In: *ApJ* 142, pp. 419–421. DOI: 10.1086/148307 (cit. on p. 25).

Planck Collaboration et al. (July 2018). “Planck 2018 results. VI. Cosmological parameters”. en. In: *preprint* arXiv:1807.06209 (cit. on pp. 4, 29, 30, 39).

Pontoppidan, K. M. et al. (July 2016). “Pandeia: a multi-mission exposure time calculator for JWST and WFIRST”. In: *Proc. SPIE* 9910. DOI: 10.1117/12.2231768 (cit. on p. 59).

Press, W. H. et al. (Feb. 1974). “Formation of Galaxies and Clusters of Galaxies by Self-Similar Gravitational Condensation”. In: *ApJ* 187, pp. 425–438. DOI: 10.1086/152650 (cit. on p. 186).

Pritchard, J. R. et al. (Aug. 2012). “21 cm cosmology in the 21st century”. In: *Reports on Progress in Physics* 75, p. 086901. DOI: 10.1088/0034-4885/75/8/086901 (cit. on p. 38).

Reddy, N. A. et al. (Jan. 2018). “The HDUV Survey: A Revised Assessment of the Relationship between UV Slope and Dust Attenuation for High-redshift Galaxies”. In: *ApJ* 853, p. 56. DOI: 10.3847/1538-4357/aaa3e7 (cit. on p. 43).

Ribeiro, B. et al. (Sept. 2016). “Size evolution of star-forming galaxies with 2 <z < 4.5 in the VIMOS Ultra-Deep Survey”. en. In: *A&A* 593, A22. DOI: 10.1051/0004-6361/201628249 (cit. on p. 168).

Rieke, G. et al. (May 2019a). “JWST/MIRI Surveys in GOODS-S”. In: 51. Conference Name: Bulletin of the American Astronomical Society, p. 11 (cit. on p. 57).

Rieke, M. et al. (May 2019b). “JWST GTO/ERS Deep Surveys”. In: 51. Conference Name: Bulletin of the American Astronomical Society, p. 45 (cit. on p. 56).

Roberts-Borsani, G. W. et al. (June 2016). “z $\gtrsim$ 7 Galaxies with Red Spitzer/IRAC [3.6]-[4.5] Colors in the Full CANDELS Data Set: The Brightest-Known Galaxies at z ~ 7-9 and a Probable Spectroscopic Confirmation at z = 7.48”. In: *ApJ* 823, p. 143. DOI: 10.3847/0004-637X/823/2/143 (cit. on p. 157).

Robertson, B. E. et al. (Apr. 2015). “COSMIC REIONIZATION AND EARLY STAR-FORMING GALAXIES: A JOINT ANALYSIS OF NEW CONSTRAINTS

FROM PLANCK AND THEHUBBLE SPACE TELESCOPE". en. In: *ApJL* 802.2, p. L19. DOI: 10.1088/2041-8205/802/2/L19 (cit. on p. 35).
Rydberg, C. et al. (Mar. 2013). "Detection of isolated Population III stars with the James Webb Space Telescope". In: *MNRAS* 429, pp. 3658–3664. DOI: 10.1093/mnras/sts653 (cit. on p. 168).
Salpeter, E. E. (Jan. 1955). "The Luminosity Function and Stellar Evolution." In: *ApJ* 121, p. 161. DOI: 10.1086/145971 (cit. on pp. 42, 52).
Saumon, D. et al. (Dec. 2008). "The Evolution of L and T Dwarfs in Color-Magnitude Diagrams". In: *ApJ* 689, pp. 1327–1344. DOI: 10.1086/592734 (cit. on p. 97).
Sawicki, M. et al. (Nov. 2019). "The CFHT large area U-band deep survey (CLAUDS)". In: *MNRAS* 489, pp. 5202–5217. DOI: 10.1093/mnras/stz2522 (cit. on pp. 7, 90).
Schechter, P. (Jan. 1976). "An analytic expression for the luminosity function for galaxies." In: *ApJ* 203, pp. 297–306. DOI: 10.1086/154079 (cit. on p. 40).
Schenker, M. A. et al. (Nov. 2014). "Line-emitting Galaxies beyond a Redshift of 7: An Improved Method for Estimating the Evolving Neutrality of the Intergalactic Medium". In: *ApJ* 795, p. 20. DOI: 10.1088/0004-637X/795/1/20 (cit. on p. 37).
Schmidt, M. (Feb. 1968). "Space Distribution and Luminosity Functions of Quasi-Stellar Radio Sources". In: *ApJ* 151, p. 393. DOI: 10.1086/149446 (cit. on p. 160).
Schreiber, C. et al. (Jan. 2018). "Dust temperature and mid-to-total infrared color distributions for star-forming galaxies at $0 < z < 4$". en. In: *A&A* 609, A30. DOI: 10.1051/0004-6361/201731506 (cit. on p. 5).
Scoville, N. et al. (Sept. 2007). "The Cosmic Evolution Survey (COSMOS): Overview". en. In: *ApJS* 172.1, p. 1. DOI: 10.1086/516585 (cit. on pp. 7, 46, 88).
Secunda, A. et al. (Sept. 2020). "Delayed Photons from Binary Evolution Help Reionize the Universe". In: *ApJ* 901, p. 72. DOI: 10.3847/1538-4357/abaefa (cit. on p. 39).
Sheth, R. K. et al. (Sept. 1999). "Large-scale bias and the peak background split". In: *MNRAS* 308, pp. 119–126. DOI: 10.1046/j.1365-8711.1999.02692.x (cit. on p. 186).
Shull, J. M. et al. (Mar. 2012). "Critical Star Formation Rates for Reionization: Full Reionization Occurs at Redshift $z \approx 7$". In: *ApJ* 747, p. 100. DOI: 10.1088/0004-637X/747/2/100 (cit. on p. 35).
Spergel, D. et al. (May 2013). "Wide-Field InfraRed Survey Telescope-Astrophysics Focused Telescope Assets WFIRST-AFTA Final Report". In: *preprint* (cit. on p. 168).
Stark, D. P. et al. (Nov. 2010). "Keck spectroscopy of faint $3 < z < 7$ Lyman break galaxies - I. New constraints on cosmic reionization from the luminosity and redshift-dependent fraction of Lyman α emission". In: *MNRAS* 408, pp. 1628–1648. DOI: 10.1111/j.1365-2966.2010.17227.x (cit. on p. 37).

Stark, D. P. et al. (Feb. 2011). “Keck Spectroscopy of Faint 3>z>7 Lyman Break Galaxies: A High Fraction of Line Emitters at Redshift Six”. In: *ApJL* 728, p. L2. DOI: 10.1088/2041-8205/728/1/L2 (cit. on p. 37).

Stefanon, M. et al. (Dec. 2017). “HST Imaging of the Brightest z $\sim$ 8-9 Galaxies from UltraVISTA: The Extreme Bright End of the UV Luminosity Function”. In: *ApJ* 851, p. 43. DOI: 10.3847/1538-4357/aa9a40 (cit. on pp. 134, 149).

Stefanon, M. et al. (Sept. 2019). “The Brightest z $\gtrsim$ 8 Galaxies over the COSMOS UltraVISTA Field”. In: *ApJ* 883, p. 99. DOI: 10.3847/1538-4357/ab3792 (cit. on pp. 9, 134, 137, 138, 140, 149–152, 154–158, 160, 161, 164).

Steidel, C. C. et al. (May 1996). “Spectroscopic Confirmation of a Population of Normal Star-forming Galaxies at Redshiftsz$\greater$ 3”. en. In: *ApJ* 462.1, pp. L17–L21. DOI: 10.1088/1538-4357/462/1/L17 (cit. on p. 47).

Steigman, G. (Nov. 2007). “Primordial Nucleosynthesis in the Precision Cosmology Era”. In: *Annual Review of Nuclear and Particle Science* 57, pp. 463–491. DOI: 10.1146/annurev.nucl.56.080805.140437 (cit. on pp. 33, 35).

Steinhardt, C. L. et al. (Aug. 2014). “Star Formation at 4 < z < 6 from the Spitzer Large Area Survey with Hyper-Suprime-Cam (SPLASH)”. In: *ApJL* 791, p. L25. DOI: 10.1088/2041-8205/791/2/L25 (cit. on pp. 7, 90).

Sérsic, J. L. (1963). “Influence of the atmospheric and instrumental dispersion on the brightness distribution in a galaxy”. In: *BAAA* 6, p. 41 (cit. on p. 61).

Taniguchi, Y. et al. (Sept. 2007). “The Cosmic Evolution Survey (COSMOS): Subaru Observations of the HST Cosmos Field”. In: *ApJS* 172, pp. 9–28. DOI: 10.1086/516596 (cit. on pp. 7, 91).

Taniguchi, Y. et al. (Dec. 2015). “The Subaru COSMOS 20: Subaru optical imaging of the HST COSMOS field with 20 filters*”. In: *Publications of the Astronomical Society of Japan* 67, p. 104. DOI: 10.1093/pasj/psv106 (cit. on pp. 7, 91).

Thomas, R. et al. (Jan. 2017). “VIMOS Ultra-Deep Survey (VUDS): IGM transmission towards galaxies with 2.5 < z < 5.5 and the colour selection of high-redshift galaxies”. In: *A&A* 597, A88. DOI: 10.1051/0004-6361/201425342 (cit. on pp. 47, 48).

Tilvi, V. et al. (May 2013). “Discovery of Lyman Break Galaxies at z $\sim$ 7 from the zFourGE Survey”. In: *ApJ* 768, p. 56. DOI: 10.1088/0004-637X/768/1/56 (cit. on p. 49).

Totani, T. et al. (June 2006). “Implications for Cosmic Reionization from the Optical Afterglow Spectrum of the Gamma-Ray Burst 050904 at z = 6.3*”. In: *Publications of the Astronomical Society of Japan* 58, pp. 485–498. DOI: 10.1093/pasj/58.3.485 (cit. on p. 38).

Trenti, M. et al. (Apr. 2008). “Cosmic Variance and Its Effect on the Luminosity Function Determination in Deep High-z Surveys”. en. In: *ApJ* 676.2, p. 767. DOI: 10.1086/528674 (cit. on pp. 41, 161, 186).

Turner, E. L. et al. (Sept. 1984). “The statistics of gravitational lenses - The distributions of image angular separations and lens redshifts”. In: *ApJ* 284, pp. 1–22. DOI: 10.1086/162379 (cit. on p. 165).

Verhamme, A. et al. (Dec. 2006). "3D Lyα radiation transfer. I. Understanding Lyα line profile morphologies". In: *A&A* 460, pp. 397–413. DOI: 10.1051/0004-6361:20065554 (cit. on p. 38).
Verhamme, A. et al. (Nov. 2008). "3D Lyα radiation transfer. III. Constraints on gas and stellar properties of z ~ 3 Lyman break galaxies (LBG) and implications for high-z LBGs and Lyα emitters". In: *A&A* 491, pp. 89–111. DOI: 10.1051/0004-6361:200809648 (cit. on p. 38).
Wang, F. et al. (Oct. 2019). "Exploring Reionization-era Quasars. III. Discovery of 16 Quasars at $6.4 \leq z \leq 6.9$ with DESI Legacy Imaging Surveys and the UKIRT Hemisphere Survey and Quasar Luminosity Function at $z \sim 6.7$". In: *ApJ* 884, p. 30. DOI: 10.3847/1538-4357/ab2be5 (cit. on p. 164).
Waters, D. et al. (Dec. 2016). "Forecasts for the WFIRST High Latitude Survey using the BlueTides simulation". In: *MNRAS* 463, pp. 3520–3530. DOI: 10.1093/mnras/stw2000 (cit. on p. 168).
Wei, J. et al. (Oct. 2016). "The Deep and Transient Universe in the SVOM Era: New Challenges and Opportunities - Scientific prospects of the SVOM mission". In: *preprint* (cit. on pp. 38, 170).
Wilkins, S. M. et al. (Apr. 2013). "Interpreting the observed UV continuum slopes of high-redshift galaxies". In: *MNRAS* 430, pp. 2885–2890. DOI: 10.1093/mnras/stt096 (cit. on p. 43).
Williams, C. C. et al. (May 2018). "The JWST Extragalactic Mock Catalog: Modeling Galaxy Populations from the UV through the Near-IR over 13 Billion Years of Cosmic History". en. In: *ApJS* 236.2, p. 33. DOI: 10.3847/1538-4365/aabcbb (cit. on p. 5).
Willmer, Christopher N. A. et al. (2020). "Guitarra, a Simulator for the JWST/NIRCam". In: 352. Conference Name: Uncovering Early Galaxy Evolution in the ALMA and JWST Era, pp. 356–358. DOI: 10.1017/S1743921319008408 (cit. on p. 58).
Zackrisson, E. et al. (Dec. 2012). "Detecting gravitationally lensed Population III galaxies with the Hubble Space Telescope and the James Webb Space Telescope". In: *MNRAS* 427, pp. 2212–2223. DOI: 10.1111/j.1365-2966.2012.22078.x (cit. on p. 168).

Appendices

A. Cosmic variance calculator

In order to include the contribution of cosmic variance into the luminosity function estimates, I used the cosmic variance calculator from Trenti et al. 2008. The authors provided an interactive web page [1] to compute the cosmic variance given the details of the survey, catalog and the assumed cosmological parameters. Table .1 gives the list of the parameters involved in this computation. Unfortunately, the server hosting the calculator was no longer operational when I was predicting the observed luminosity function from the accepted *JWST* programs (see chapter 2). In addition, the web page did not allow the user to modify the assumed cosmology. Therefore, I translated the cosmic variance calculator from C to Python, based on the C code provided by Michele Trenti. With the recent reupload of the cosmic variance calculator web page, additional tests could be implemented to confirm the results from the Python calculator.

The cosmic variance calculator estimates the uncertainty on the galaxy number counts due to the large scale structure in the Universe. In Trenti et al. 2008, cosmic variance is computed by first integrating the dark matter two-points correlation function $\xi(r)$ over the cosmological (comoving) volume V of the survey, to obtain the dark matter uncertainty $\sigma_{\rm DM}$ as:

$$\sigma^2_{\rm DM} = \frac{\int_V \int_V \xi(|r_1 - r_2|) d^3r_1 d^3r_2}{\int_V \int_V d^3r_1 d^3r_2}. \qquad (.1)$$

The integrated volume is computed using the the survey area and axis ratio, and the cosmological parameters to estimate radial comoving distances. The dark matter two point-correlation function describes the probability that a dark matter halo will be found within a given distance from another halo in a random location (Peebles 1980). It is computed from the Fourier transform of the dark matter power spectrum $P(k)$, which can be estimated from linear perturbation theory using the abundance parameters Ω_i, the spectral index n_s and the root-mean-square matter fluctuation σ_8, by convention averaged over a sphere of radius $8\,{\rm Mpc}/h$.

Secondly, the dark matter uncertainty is multiplied by the average bias b of the galaxy sample to compute the galaxy uncertainty $\sigma_{\rm CV}$ as:

$$\sigma^2_{\rm CV} = b^2 \sigma^2_{\rm DM}. \qquad (.2)$$

The minimum halo mass $M_{\rm min}$, required to match the number density of halos hosting the survey population, is computed given the intrinsic number of objects in the survey (so the completeness) and the halo filling factor. The galaxy bias, averaged over halo masses $M_h > M_{\rm min}$, is then estimated using the Press-Schechter (Press et al. 1974) or the Sheth-Tormen (Sheth et al. 1999) formalism. These

1. https://www.ph.unimelb.edu.au/~mtrenti/cvc/CosmicVariance.html

mathematical models describe the mass distribution of matter haloes in the Universe. While the Press-Schechter formalism relies on the spherical gravitational collapse of the mass density fluctuations, Sheth and Tormen considered ellipsoidal collapse.

The cosmic variance uncertainty needs to be added in quadrature to the Poisson uncertainty related to the observed galaxy number count. Since the completeness estimates also have an associated error, it should also be propagated into the total uncertainties.

Table .1. – List of the cosmic variance calculator parameters.

Name	Default	Type	Description
h	0.7	float	Hubble expansion rate parameter
Ω_m	0.26	float	Matter abundance parameter
Ω_b	0.0469	float	Baryonic matter abundance parameter
Ω_Λ	0.74	float	Dark energy abundance parameter
σ_8	0.9	float	Root-mean-square matter fluctuation averaged over a sphere of radius $8\,\mathrm{Mpc}/h$
n_s	1	float	Scalar spectral index
Bias	1	bool	Bias (0:Press-Schechter, 1:Sheth-Tormen)
SurveyAreaX		float	Geometry of the survey [arcmin]
SurveyAreaY		float	
z_{mean}		float	Center of the redshift interval
Δz		float	Width of the redshift interval
N		int	Number of galaxies
C	1	float	Completeness
HaloOff	1	float	Halo filling factor

B. Article: Euclid preparation: Cosmic Dawn Survey *Spitzer* observations of the Euclid deep fields and calibration fields

Astronomy & Astrophysics manuscript no. output
January 13, 2021

Euclid preparation: Cosmic Dawn Survey

Spitzer observations of the *Euclid* deep fields and calibration fields

Euclid collaboration, Andrea Moneti[1], H. J. McCracken[1], Marko Shuntov[1], Olivier Kauffmann[2], John R. Weaver[5,6], Oliver Ilbert[2], Peter L. Capak[3], Claudia Scarlata[4], Sune Toft[5,6], Harry Teplitz[3], Ranga-Ram Chary[3], and Dan Stern[7] ...

[1] Institut d'Astrophysique de Paris, UMR 7095, CNRS, and Sorbonne Université, 98 bis boulevard Arago, 75014 Paris, France
[2] Aix Marseille Univ, CNRS, LAM, Laboratoire d'Astrophysique de Marseille, Marseille, France
[3] Infrared Processing and Analysis Center, California Institute of Technology, 1200 East California Boulevard, Pasadena, CA 91125, USA
[4] Minnesota Institute for Astrophysics, University of Minnesota, 116 Church St SE, Minneapolis, MN 55455, USA
[5] Cosmic Dawn Center (DAWN)
[6] Niels Bohr Institute, University of Copenhagen, Jagtvej 128, 2200 Copenhagen, Denmark
[7] Jet Propulsion Laboratory, California Institute of Technology 4800 Oak Grove Drive Pasadena, CA 91109, USA

Released on TBD / Accepted date: TBD

ABSTRACT

We present a new infrared survey covering the three *Euclid* deep fields and four other *Euclid* calibration fields using *Spitzer*'s IRAC camera. We have combined these new observations with all relevant IRAC archival data of these fields in order to produce the deepest possible mosaics of these regions. In total, these observations represent nearly 11 % of the total *Spitzer* mission time. The resulting mosaics cover approximately 71.5 $\deg^2$ in the 3.6 and 4.5 μm bands, and approximately 21.8 $\deg^2$ in the 5.8 and 8 μm bands, they reach down to at least 24 AB magnitude in the 3.6 μm band, are tied to the Gaia astrometric reference system, with a typical astrometric uncertainty of $\lesssim 0\farcs15$, and the photometric calibration is in excellent agreement with WISE satellite data. We have extracted source number counts from the 3.6 μm channel, and they are in excellent agreement with previously existing determinations. Given that the *Spitzer* Space Telescope has now been decommissioned these mosaics are likely to be the definitive reduction of these IRAC data, and thus this survey represents an essential step in assembling multi-wavelength data on the *Euclid* deep fields which are set to become some of the premier fields for extragalactic astronomy in the 2020s.

Key words. cosmology: observations — cosmology: large scale structure of universe — cosmology: dark matter — galaxies: formation — galaxies: evolution — surveys

1. Introduction

The *Euclid* mission will survey 15 000 $\deg^2$ of the extragalactic sky to investigate the nature of dark energy and dark matter and to study the formation and evolution of galaxies (Laureijs et al. 2011). To this end *Euclid* will obtain high resolution imaging of a billion galaxies in a broad optical filter to measure their shapes and in three near-infrared (NIR) filters to measure their colours. It will also obtain NIR spectroscopy of about thirty million of these galaxies to measure abundances and redshifts. Additionally, photometric redshifts will be determined by combining the *Euclid* data with optical photometry from external surveys.

To reach the required precision on cosmological parameters and satisfy the stringent mission requirements on spectroscopic purity and shape noise bias, *Euclid* must also obtain observations 40 times deeper than the main survey over regions covering at least 40 $\deg^2$. To this end, three 'deep' fields have been selected by the *Euclid* consortium, as described in detail by Scaramella et al. (in preparation): the *Euclid* deep field north (EDF-N), a circular, 10 $\deg^2$ region centred on the well-studied north Ecliptic pole; the *Euclid* deep field Fornax (EDF-F), also circular and of 10 $\deg^2$, centred on the Chandra deep field south and including the GOODS-S (Giavalisco et al. 2004) and the Hubble Ultra Deep Field (Beckwith et al. 2006); and the *Euclid* deep field south (EDF-S), a pill-shaped area of 20 $\deg^2$ with no previous dedicated observations. In addition to the three deep fields *Euclid* will observe several fields for the calibration of photometric redshifts (photo-z); these fields also need to be observed to a level 25 times deeper than the main survey. These additional regions are centred on some of the best studied extragalactic survey fields that already have extensive spectroscopic data: (1) the COSMOS field (2.4 $\deg^2$), (2) the Extended Groth Strip (EGS, 0.5 $\deg^2$), (3) the Hubble Deep Field North (HDFN, 0.5 $\deg^2$, also GOODS-N),and (4) the XMM-Large Scale Structure survey field, which includes the Subaru XMM Deep Survey field (SXDS, 2.4 $\deg^2$), and VIMOS VLT Deep Survey (VVDS, 0.5 $\deg^2$).

While the primary objective of these deep fields is the survey calibration, they also provide an unprecedented dataset to study galaxies to faint magnitudes and high redshifts. The survey efficiency of *Euclid* in the NIR bands is orders of magnitudes greater than that of ground-based telescopes (e.g., VISTA). The *Euclid* deep fields alone will be 30 times larger and one magnitude deeper than the latest UltraVISTA data release covering the COSMOS field, and will reach a depth of 26 mag in the Y, J, H filters (5-σ). This NIR photometry will be associated with more than one million spectra, to a line flux limit similar to 3D-HST (Brammer et al. 2012) over an area 200 times larger. By combining blue and red grism ($0.92 < \lambda < 1.85$ μm), as well as numerous grism orientations, the deep fields will represent the best spectroscopic coverage produced by *Euclid*. Such spectroscopic dataset will be unique for the reconstruction of the galaxy environment at cosmic noon and for measuring the star formation rate from the Hα emission line intensity.

The deep and wide NIR data from Euclid are also ideal for detecting significant numbers of high redshift ($7 < z < 10$) galaxies, as the Lyman break is redshifted out of the optical into the NIR. However, in order to distinguish galaxy candidates from stars (primarily brown dwarfs), faint Balmer–break galaxies, and dusty star-forming galaxies at lower redshifts which all can have similar NIR magnitudes and colours, deep optical and mid-infrared (MIR) data are needed (Bouwens et al. 2019; Bridge et al. 2019; Bowler et al. 2020).

The "Cosmic Dawn Survey" (Toft et al, in prep) aims to obtain uniform, multi-wavelength imaging data for all the Euclid deep and calibration fields, to limits matching the Euclid data for characterisation of high redshift galaxies. The optical data will be provided by the Hawaii-Two-0 Subaru telescope/Hype-SuprimeCam (HSC) survey (McPartland et al, in prep.) for the EDF-N and EDF-F and likely by the Vera C. Rubin Observatory for EDF-S and EDF-F. For the COSMOS and SXDS fields optical data are provided by the Subaru HSC Strategic program (HSC-SSP Aihara et al. 2011).

In this paper, we present the *Spitzer* Space Telescope (Werner et al. 2004) component of the 'Cosmic Dawn survey', which covers the three *Euclid* deep fields and parts of the calibration fields. Most of the data were acquired with *Spitzer*'s IRAC camera (Fazio et al. 2004) at 3.6 and 4.5 µm during the last few years of operation as part of two major programs: The *Euclid*/WFIRST *Spitzer* legacy survey (SLS, 5286h, PI:Capak) covering the EDF-N and EDF-F fields, and the EDF-S survey (687h, PI:Scarlata). Together with the new data we have also reprocessed all relevant archival *Spitzer* data, thus including data obtained during the cryogenic mission, including data at 5.8 and 8.0 µm, in order to produce the deepest possible MIR images (mosaics) of these fields. A major improvement of our processing is that our pipeline ties the astrometry to the Gaia reference system which, given its higher precision, will greatly facilitate cross-identification with other data, which will of course also have to be tied to Gaia.

In addition to being essential for the identification of high redshift galaxies, MIR data are crucial to reveal the stellar mass content of the high-redshift Universe. The *Euclid* data alone are not sufficient to characterise the stellar masses at $z > 3.5$, as the Balmer break is redshifted out of the reddest band of the Near Infrared Spectrometer and Photometer. Without MIR data, the interpretation of spectral energy distributions (SEDs) would rely on rest-frame ultraviolet emission which is strongly affected by dust attenuation and dominated by stellar light of new-born stars. Therefore, integrated quantities like the stellar mass would be highly unreliable (Bell & de Jong 2001). Moreover, photometric redshifts would be prone to catastrophic failures, created by a mis-indentification between the Lyman and Balmer breaks (e.g. Le Fèvre et al. 2015; Kauffmann et al. 2020). In summary, *Spitzer*/IRAC data are crucial for identifying the most distant objects (e.g. Bridge et al. 2019), for improving the accuracy of their photometric redshifts and for deriving their physical properties such as stellar masses, dust content, age and star-formation rate from population synthesis models (e.g. Pérez-González et al. 2008; Caputi et al. 2015; Davidzon et al. 2017). The build-up of stellar mass, especially when confronted with the amount of matter residing in dark matter halos at high redshifts can be a highly discriminating test for galaxy formation models (Legrand et al. 2019). Extrapolation of recent work in the COSMOS field (Bowler et al. 2020) suggests that hundreds of the rarest, brightest $z > 7$ galaxies are expected to be discovered in the *Euclid* deep fields. These provide unique constraints on cosmic reionisation, as the brightest galaxies form in the highest density regions of the Universe which are expected to the sites of the first generation of stars and galaxies, and thus of reionisation bubbles (Trac et al. 2008).

The structure of this paper is as follows: Section 2 describes the observations; Section 3 presents our data processing techniques; and Section 4 compares our results to previous ones.

2. Observations

All observations described here were made with the IRAC camera. In brief, IRAC is a four-channel array camera on the *Spitzer* Space Telescope, observing simultaneously four fields slightly separated on the sky at 3.6, 4.5, 5.8, and 8.0 µm, known as channels 1–4, respectively. *Spitzer* science observations began in August 2003 but observations in channels 3 and 4 ceased once the on-board cryogen was exhausted (May 15, 2009). During the following "warm mission" phase, channels 1 and 2 continued to operate until the end of operations in January 2020, albeit with different performance. The earliest observations presented here were obtained in September 2003, and the latest ones in January 2020. Figure 1 shows histograms of the integration time accumulated in bins of 30 days over the observing period. These observations account for almost 1.5 million frames and an integration time of 34 000 hr, all channels combined. Also, these observations account for a total on-target time, omitting overheads, of just over 15 600 hr, or nearly 1.8 yr, which is almost 11 % of the *Spitzer* mission time.

Table 2 gives, for each field and for each channel, the number of frames (Data Collection Events or DCEs in IRAC terminology) used to produce the mosaics, which can be lower than the number of frames downloaded, as some were discarded (see Sect. 3), together with the total observing time. For channels 1 and 2, on the left side of the table, the information is subdivided into the cryogenic part and the warm part of the mission.

3. Processing

3.1. Pre-processing and calibration

Processing begins with the *Level 1* data products generated by the Spitzer Science Center via their "Basic Calibrated Data" pipeline, which were downloaded from the NASA/IPAC Infrare Science Archive (IRSA[1]). They have had all well-understood instrumental signatures removed, have been flux-calibrated in units of MJy sr^{-1}, and are delivered with an uncertainty image and a mask image; they are described in detail in the IRAC Instrument Handbook[2]. More precisely, we begin from the "corrected basic calibration data" products, which have file extensions `.cbcd` for the image, `.cbunc` for the uncertainty, and `.bimsk` for the mask. The files are grouped by AORs (Astronomical Observation Request), namely sets of a few to several hundred DCEs obtained sequentially. All frames are 256×256 pixels, the pixels are 1.″2 wide, and the image file header contains the photometric solution and an initial astrometric solution.

The processing is done field by field. A first pass over the files is used to check the headers for completeness and to discard a few incomplete AORs, which accounts for most of the

[1] `https://irsa.ipac.caltech.edu`

[2] `https://irsa.ipac.caltech.edu/data/SPITZER/docs/irac/iracinstrumenthandbook/home`

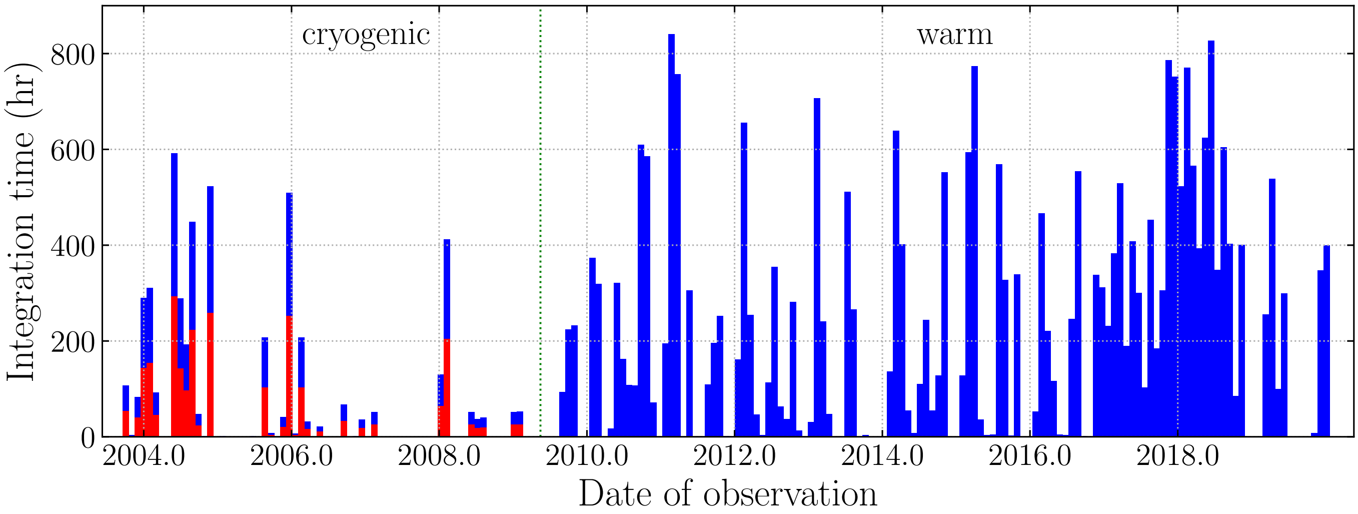

Fig. 1. Histogram of the exposure time of the analysed here (thus including the few discarded observations) using bins of 30 days. In red are the observations in channels 3 and 4, in blue those in channels 1 and 2; the vertical dotted line at 2009.37 indicates the end of the cryogenic mission.

Table 1. Valid observations

Field	Ch	cryo		warm		total		Ch	total	
		Num	Time	Num	Time	Num	Time		Num	Time
EDF-N	1	5859	52	113521	2380	119380	2432	3	5856	52
EDF-N	2	5857	52	113204	2467	119061	2519	4	7667	50
EDF-F	1	14299	363	105781	2672	120080	3035	3	14301	363
EDF-F	2	14299	363	105779	2764	120078	3127	4	29686	352
EDF-S	1	n/a	n/a	21982	534	21982	534	3	n/a	n/a
EDF-S	2	n/a	n/a	21982	552	21982	552	4	n/a	n/a
COSMOS	1	7014	185	191072	4886	198086	5071	3	7011	185
COSMOS	2	7013	185	191031	5052	198044	5237	4	13894	179
EGS	1	4673	192	44101	551	48774	743	3	4672	192
EGS	2	4673	192	44101	569	48774	761	4	14535	186
HDFN	1	6253	298	36485	930	42738	1228	3	6252	298
HDFN	2	6253	298	36485	962	42738	1260	4	22496	288
XMM	1	10264	154	98027	2410	108291	2564	3	10265	154
XMM	2	10265	154	98030	2495	108295	2649	4	14321	151

Notes. Here 'Num' is the number of frames used, and 'Time' is the integration time, in hours, they contribute. The left part of the table is for channels 1 & 2, split between cryogenic and warm mission, the right part is for channels 3 & 4 which were used during the cryogenic mission only.

differences in the number of frames listed in Table 2 between channels 1 and 2, or 3 and 4. This is followed by the correction of the "first frame" bias effect[3]. Next, the positions and magnitudes of WISE (Wright et al. 2010) and Gaia DR2 (Gaia Collaboration et al. 2018) sources falling within the field are downloaded. The Gaia sources are first 'moved' to their location at the time of the observations using the Gaia proper motions. Next they are identified on the IRAC images, their observed fluxes and positions determined using the `APEX` software (the point-source extractor in `MOPEX`[4]) in forced-photometry mode, and are used to determine a new astrometric correction. Some 30—40 Gaia sources are normally found in each frame, most of which are usable in channels 1 and 2, while only a few are detected in the long wavelength channels 3 and 4, but that is still easily sufficient to determine the astrometric solution.

An attempt was made to subtract bright stars in order to recover faint sources in their wings. A model star built from the template PSFs described in the IRAC Instrument Handbook (see Figure 4.7 there) is scaled to the median measured flux of the star and subtracted. This subtraction is done on the individual

[3] irsa.ipac.caltech.edu/data/SPITZER/docs/irac/iracinstrumenthandbook/37/

[4] https://irsa.ipac.caltech.edu/data/SPITZER/docs/dataanalysistools/tools/mopex/

frames before stacking them, and different templates are available for the cryogenic and the warm missions. While this procedure worked quite well for moderately bright stars (which are of course the vast majority and which represent only a small loss in area), it introduced significant artefacts around the (few) very bright stars. These artefacts included diffraction spikes corrected only out to a certain distance (out to where the template extends beyond the frame), other edge effects, and the subtraction of the core of bright galaxies. For these reasons the bright-star subtraction was not performed in the end.

3.2. Stacking and image combination

In the next step we compute a stacked median image for all frames within an AOR which corrects for persistence in the detectors and also for residual first-frame pattern that introduces structure in the background. In parallel, a background map is also created by iteratively clipping objects and masking them, and finally these backgrounds are subtracted from each frame. The final processing consists of resampling the background-subtracted frames onto a common grid with a scale of $0\farcs6\,\mathrm{pix}^{-1}$, i.e., half the instrument pixel size, that covers all data in all channels and which is the same in all channels. The resampled frames are then combined (or stacked) using `MOPEX` software to produce the final images (mosaics) while rejecting outliers and excluding masked regions. The stacking pipeline also produces the following ancillary characterisation images: (1) an uncertainty image determined from the standard deviation of the data contributing to each pixel, (2) a coverage map giving the number of frames contributing to each pixel, and (3) an exposure time map giving the total exposure time per pixel.

3.3. Products

As an example of the data quality, Figure 2 shows a zoomed section of the EDF-F mosaic in the four channels near the region of maximum coverage. We do not provide here figures of the full mosaics as they would be physically too small to show anything useful other than the overall coverage.

In Appendix B we present maps of the integration time per pixel for channels 1 and 3 of all the fields. Since channel 2 is observed together with channel 1, and similarly for channels 4 and 3, the paired channels have very similar coverage, albeit slightly shifted in position. The $10\,\mathrm{deg}^2$ circular area of EDF-N and EDF-F and the $20\,\mathrm{deg}^2$ pill-shaped area of EDF-S are easily seen on those figures. Also, and with the exception of EDF-S, for which there are only observations done specifically for this programme and no archival data, the integration time per pixel, and consequently the depth reached, is far from uniform. That variation of area covered as a function of exposure time for channels 1 and 3 and for all fields is shown graphically in Figure 3: which presents a cumulative histogram of the area covered vs. exposure time. The left-hand side of each curve thus gives the total area covered for that field, and these areas are also listed in Table 2. EDF-S is the most uniformly observed field and it covers the largest area, but it is also the shallowest, with only 0.1 hr per pixel on average. EDF-F and EDF-N show the planned coverage of $10\,\mathrm{deg}^2$ with about 1 hour of exposure time, with the second showing heavier coverage of some zones. The other fields were covered by many observing programs with different interests and which covered specific areas with different depth, and the combination of those programs with our own yields a curve with many plateaus. In the end there are a few small parts of the EDF-F and HDFN fields that have more than 100 hrs of exposure time.

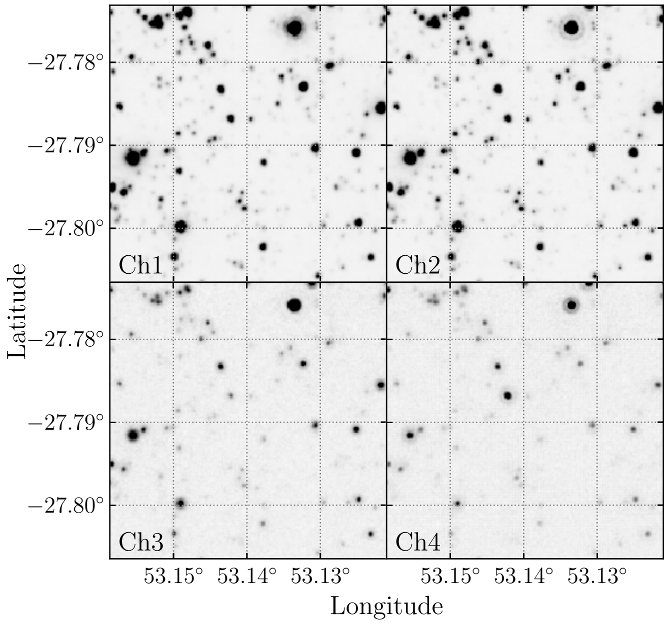

Fig. 2. Detail of EDF-F mosaic in the region near that of maximum exposure time, which here is the same for all four channels. Images are 200×200 pixels, or $2' \times 2'$. Display levels are $-\sigma$ to $+8\sigma$, where σ is the standard deviation of the sky pixels, which is $\sim 0.005\,\mathrm{MJy\,sr^{-1}}$ for channels 1 & 2, and $\sim 0.013\,\mathrm{MJy\,sr^{-1}}$ for channels 3 & 4.

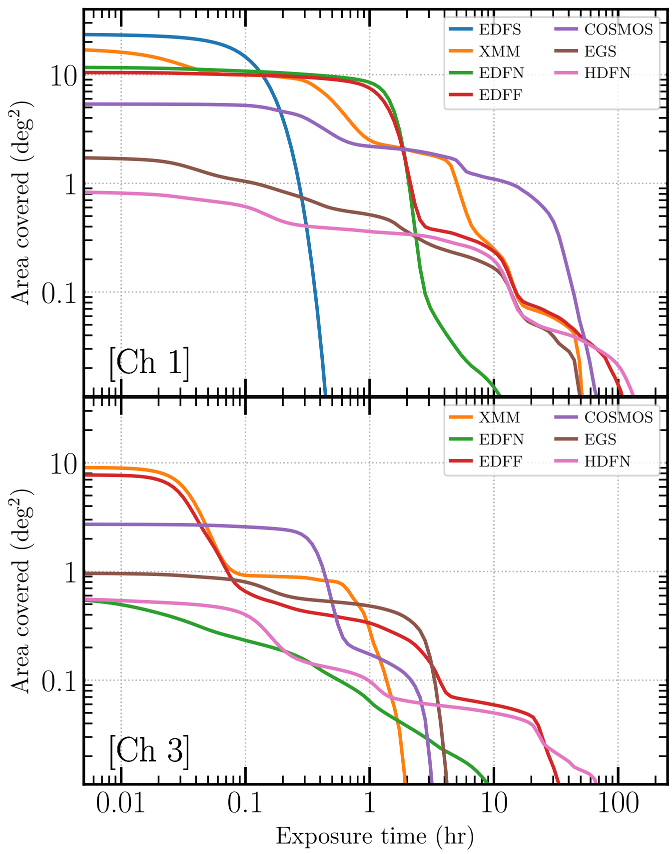

Fig. 3. Cumulative area coverage as a function of exposure time for channels 1 and 3, for all fields. The figures for channels 2 and 4 are similar to the ones above, as explained in the text.

Table 2. Location and area, in deg^2, covered in each field

Field	RA	Dec	ch1	ch2	ch3	ch4
EDF-N	$17^h 58^m$	66° 36′	11.74	11.54	0.61	0.62
EDF-F	$3^h 32^m$	−28° 12′	10.52	11.05	7.78	7.77
EDF-S	$4^h 5^m$	−48° 30′	23.60	23.14	–	–
COSMOS	$10^h 0^m$	2° 12′	5.37	5.46	2.72	2.72
EGS	$14^h 19^m$	52° 42′	1.76	1.80	0.97	0.98
HDFN	$12^h 37^m$	62° 24′	0.91	0.91	0.57	0.63
XMM	$2^h 27^m$	−4° 36′	17.54	17.48	9.09	9.10

3.4. Final sensitivities

We estimate the sensitivities of the stacked images by measuring the flux in circular 2″.5 diameter apertures randomly placed across each image after masking the regions with detected objects using the `SExtractor` segmentation map. The sensitivity is then computed as the standard deviation of these fluxes (3σ clipped). This procedure is done in 200×200 pixel cells (4 arcmin^2). Figure 4 shows the cumulative area covered as a function of sensitivity for the channel 1 mosaics. Note the similarity between this figure and the top panel of Figure 4 once the latter is rotated by 90 deg. The solid line shows our total depth, summed over all our survey fields. Previous results of other surveys from the literature are also shown for comparison. Generally, our measured sensitivities are consistent with literature measurements for surveys of equivalent exposure time.

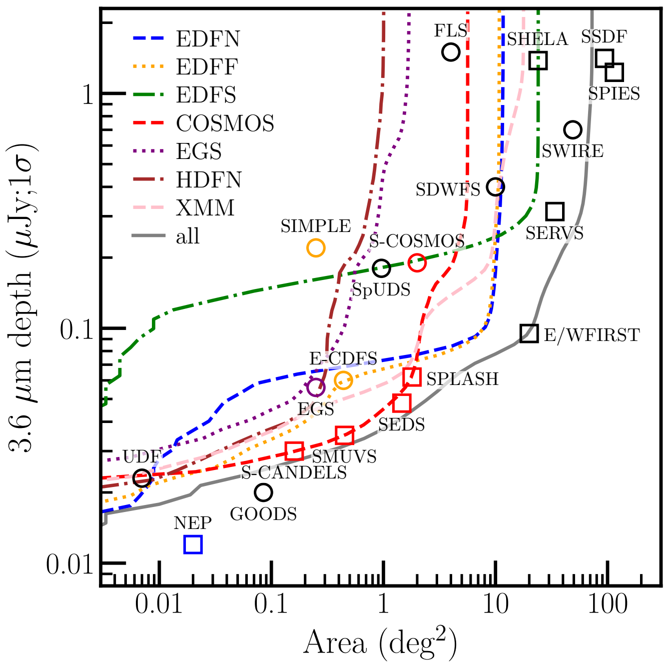

Fig. 4. Sensitivity of the *Spitzer*/IRAC channel 1 data as a function of cumulative area coverage. The coloured lines illustrates 1σ depths measured in empty 2″.5 diameter apertures in each field, and the grey solid line is the total depth summed over the fields. The data points indicate point-source sensitivities at 1σ compiled in Ashby et al. (2018). The circles and squares represent surveys executed during cryogenic and warm missions, respectively.

4. Validation and quality control

As part of our validation process we compare photometry and astrometry of sources in our stacks with reference catalogues and also extract number counts that can be compared to previous works.

4.1. Catalogue extraction

We begin by extracting source catalogues from the channels 1 and 2 of all fields using `SExtractor` (Bertin & Arnouts 1996). We adopt the usual approach of searching for objects that contain a minimum number of connected pixels above a specified noise threshold (in this case 2σ) and then measuring aperture magnitudes. In the case of our moderately deep IRAC data, where many sources are blended due to the large IRAC PSF, this approach is well known to miss a large number of faint sources. But those faint sources are of interest for our comparisons, and thus the catalogues extracted in this way are more than sufficient for our quality assessment purposes.

We extract two sets of catalogues for the validation of our data. For the first set we use `SExtractor` in ‘single image mode’, where source detection and photometry are done on the the flux image, while using the coverage map as a weight image. To account for its spatial variability, the global background is estimated on a grid with mesh size of 32×32 pixels, and the image is filtered with a 5×5 pixel Gaussian kernel with FWHM = 1″.5. For the photometry, fluxes are measured in circular apertures of 7″ diameter. To account for the fact that a source may reside in a region with a local background different from the global, the background for each source is computed locally in an annulus with a thickness of 32 pixels around its isophotal limits. The measured fluxes were converted to AB magnitude using a zero-point of 21.58, and the latter were converted to total magnitude using the aperture corrections given in the IRAC Instrument Handbook for the warm mission (−0.1164 and −0.1158 for channel 1 and channel 2 respectively). A list of relevant `SExtractor` parameters used for the catalogue extraction can be found in Table 3.

For the second set of catalogues, we use `SExtractor` in ‘dual image mode’ where object detection is done on the weighted sum of the channel 1 and channel 2 images:

$$D = \frac{W_{\rm ch1}\, I_{\rm ch1} + W_{\rm ch2}\, I_{\rm ch2}}{W_{\rm ch1} + W_{\rm ch2}}, \quad (1)$$

where D is the resulting detection image, $I_{\rm ch1}$ and $I_{\rm ch2}$ are the channel 1 and channel 2 flux images respectively, and $W_{\rm ch1}$ and $W_{\rm ch2}$ their corresponding weight images. Using the same detection image ensures that the same objects are measured in channels 1 and 2, and the measurement proper is done in the same way as for the first set.

4.2. Astrometric and photometric validation

We compare the positions of sources in each field with with the Gaia DR1 astrometric reference catalogue. Figure 5 shows the differences between reference and measured coordinates for EDF-N, as a representative field. The blue dashed line gives the size of the mosaic pixel (which is half the size of the instrument pixel). Similarly, for the same field, Figure 6 shows, for each coordinate, the difference between the reference and the measured value as a function of the coordinate. The fact that these plots are very flat indicates that there is no significant spatial variation

Table 3. `SExtractor` parameters used for detection and photometry.

Parameter name	Value
DETECT_MINAREA	5
DETECT_MAXAREA	1000000
THRESH_TYPE	RELATIVE
DETECT_THRESH	2
ANALYSIS_THRESH	2
FILTER_NAME	gauss_2.5_5x5.conv
DEBLEND_NTHRESH	32
DEBLEND_MINCONT	0.00001
BACK_SIZE	32
BACKPHOTO_THICK	32
BACK_FILTERSIZE	3
BACKPHOTO_TYPE	LOCAL
MAG_ZEROPOINT	21.58
PHOT_AUTOPARAMS	2.5,5.0
PIXEL_SCALE	0.60

in astrometric precision. Overall, therefore, the astrometry is accurate to 0.″15 RMS. These plots confirm that the astrometric solutions have been correctly applied to the individual images and that the combined images are free from residuals on a scale much smaller than an individual mosaic pixel, which is more than sufficient to measure precise infrared and optical-infrared colours.

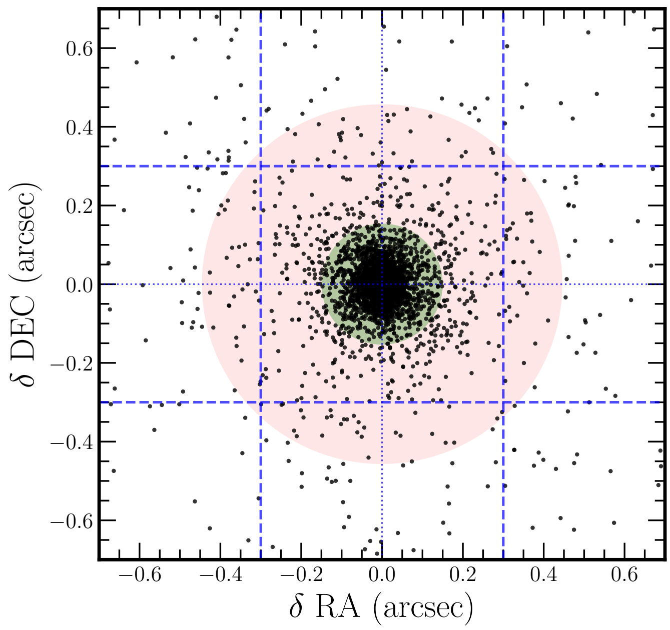

Fig. 5. The difference between the reference and the measured position, in arcseconds, of Gaia DR1 catalogue sources in the EDF-N channel 1 mosaic. The blue dashed lines indicate the size of one mosaic pixel. The shaded regions are ellipses containing 68 % and 99 % of all sources respectively. For clarity, only one in ten sources is plotted.

Finally, we perform a simple check on the photometric calibration of our mosaics. As described previously, individual images are photometrically calibrated by the Spitzer Science Center. Here we compare magnitudes of objects in our catalogues with those in the WISE survey. Because of the difference between the WISE W1 and IRAC channel 1 filter profiles, we select objects with $[3.6] - [4.5] \sim 0$. Figure 7 shows the magnitude difference for the EDF-N field, and the agreement is excellent.

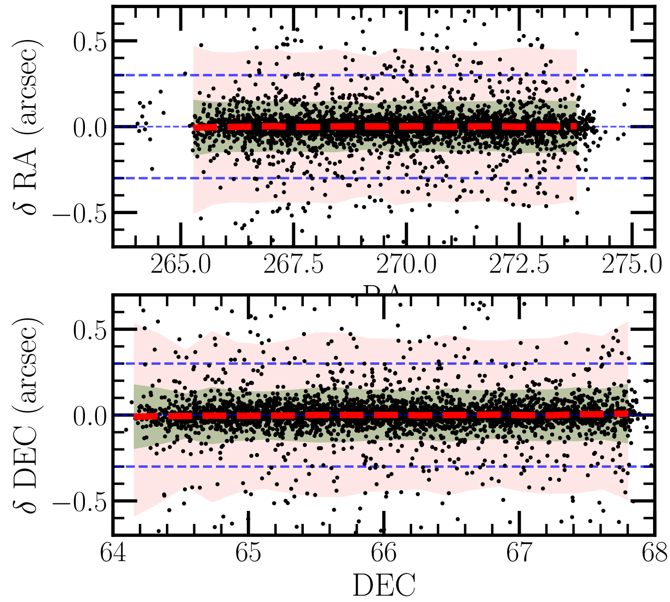

Fig. 6. The difference between the reference (Gaia) and the measured RA (top) and Dec (bottom) of sources in the EDF-N channel 1 mosaic as a function of the coordinate, in order to assess the spatial variation of the astrometric accuracy. The shaded areas indicate the regions containing 68 % and 99 % of all sources respectively. The RMS is around 0.″14 everywhere.

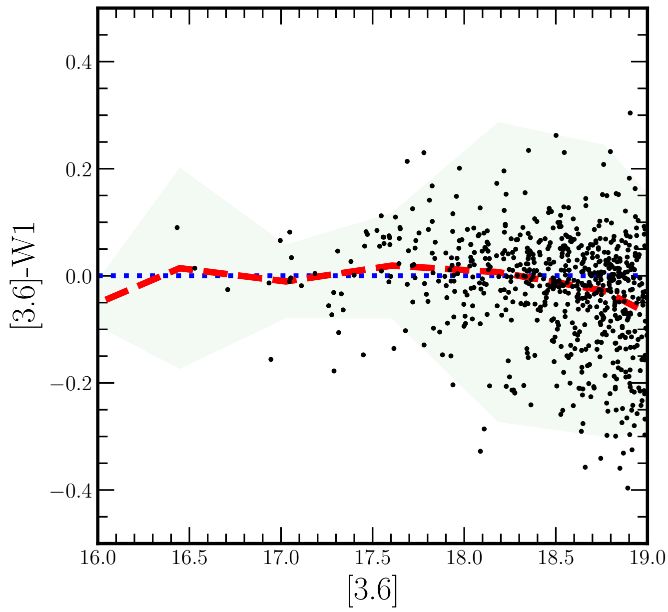

Fig. 7. Photometric comparison with the WISE survey. The magnitude measured in 7″ apertures for flat-spectrum objects ($[3.6] - [4.5] \sim 0$) is compared with W1 magnitudes in the ALLWISE survey. The shaded area represents the 68% confidence interval.

4.3. Magnitude number counts

We compute the differential number counts in channel 1 in each field using the corrected 7″ aperture magnitudes from catalogues extracted in 'single-image' mode. These are shown in Fig. 8, where the orange circles with uncertainties present our measurements and the lines show the number counts from the literature; the bottom-right panel shows the mean of all fields. We compare our number counts with those presented in Ashby et al. (2013) and with those computed using the new COSMOS2020 photometric catalogue (Weaver et al., in prep.), which we use as a reference.

There is a general agreement in the number counts in all the fields with Ashby et al. (2013) and COSMOS2020 for $16 < [3.6] < 22$. However, as our catalogues are based on aperture photometry, they become sensitive to object confusion at about 22 mag, meaning that we begin to miss sources fainter than that. In our comparison with the COSMOS2020 catalogue, we note that at the bright-end, the mosaics used to build the COSMOS2020 catalogues have had stars brighter than 16 mag removed, causing the deficit in bright sources observed at mag < 16. And at the faint end, the COSMOS2020 catalogue, which uses a high-resolution prior for the detection and a profile-fitting method for the measurement, is complete up to significantly fainter magnitudes.

EDF-N counts are slightly higher than the other fields at bright magnitudes. To investigate this difference we simulated a stellar catalogue 1 deg^2 centred on EDF-N using TRILEGAL (Girardi et al. 2005). Our count are in excellent agreement with this prediction. We also compared counts from ALLWISE (Wright et al. 2010) which overlap with EDF-N, shown in Fig. 9. The excellent agreement in both cases indicates that the difference with EDF-N and other fields is entirely due to the higher density of stellar sources consistent with the lower Galactic latitude of EDF-N.

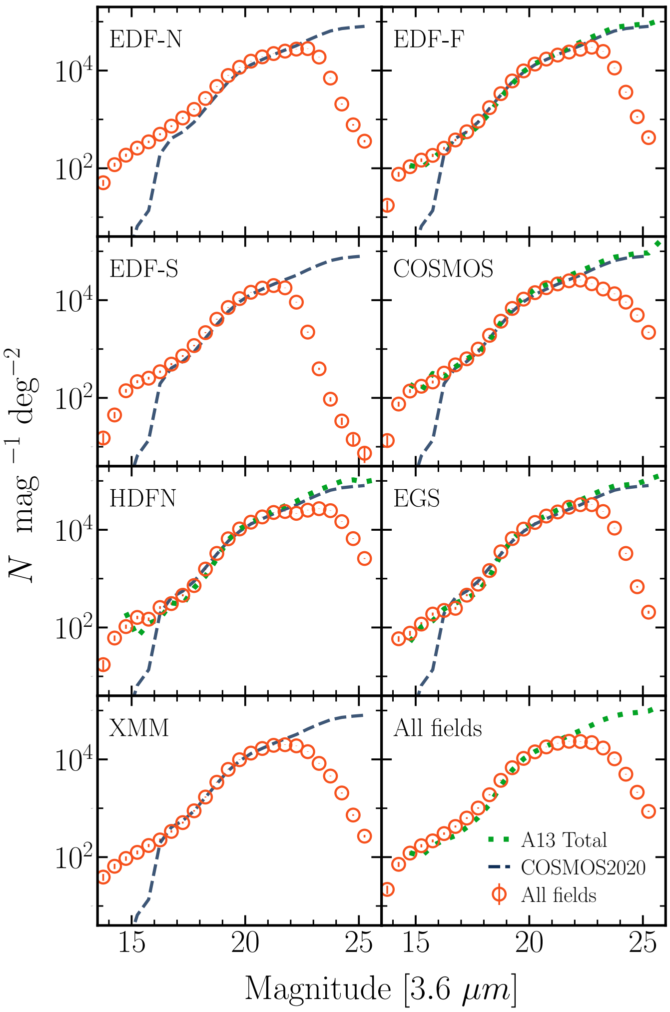

Fig. 8. Magnitude number counts in channel 1 (red circles) together with COSMOS2020 (long dashed lines) and Ashby et al. (2013) (A13) (short dotted green lines). The bottom right panel shows the mean of all fields compared to Ashby et al. (2013).

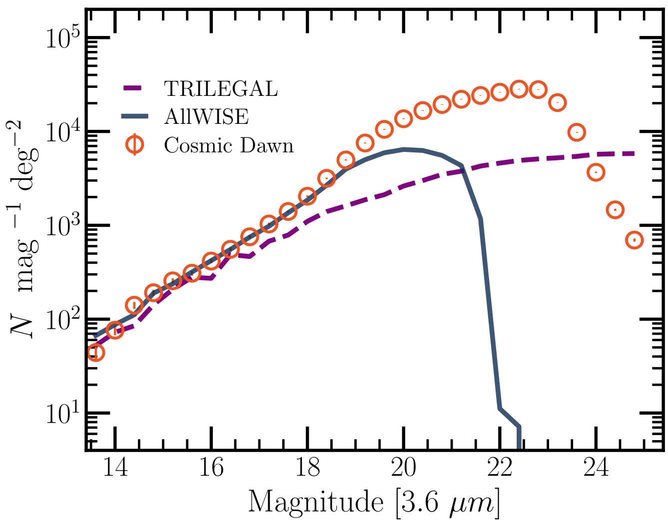

Fig. 9. Magnitude number counts in the EDF-N field compared to AllWISE and the predicted stellar number counts from TRILEGAL.

5. Summary

We presented the *Spitzer*/IRAC mid infrared component of the Cosmic Dawn Survey: an effort to complement Euclids deep field and calibration field observations with deep multi wavelength data to enable high redshift legacy science.

The survey consist of two major new programs covering the three *Euclid* deep fields (EDF-N, EDF-F and EDF-S) and a homogeneous reprocessing of all existing data in *Euclid*'s four calibration fields (COSMOS, XMM, EGS and HDFN). We have processed new data together with all existing archival data to produce mosaics of these fields covering a total of $\sim 71\,\mathrm{deg}^2$ in IRAC channels 1 and 2. Furthermore, the new mosaics are tied to the Gaia astrometric reference system, thus producing the definitive reduction of these data. The MIR data will be essential for a wide range of legacy science with Euclid, including better star/galaxy separation, more accurate photometric redshifts, determination of stellar masses of galaxies, and the construction of complete unbiased galaxy samples at z>2.

We validated our final products by comparing catalogues extracted from channel 1 and 2 to external catalogues. In all fields, comparing with Gaia, the residual astrometric uncertainty is less than $0\farcs15$ (1σ). Our photometric measurements are in excellent agreement with WISE photometry and our number counts are consistent with previous determinations.

The Cosmic Dawn Survey Spitzer survey presented here represents the first essential step in assembling the required multi-wavelength coverage in the *Euclid* deep fields which are set to become of the premiere fields in extragalactic astronomy in the coming decade. Since the Spitzer mission has been retired, and all available data in these fields have been processed with the latest reduction pipeline, the resulting mosaics will remain the deepest and widest MIR imaging survey for the foreseeable future, as no existing or approved future observatories are capable of obtaining such data. While JWST is more sensitive and has higher spatial resolution at these wavelengths, its mapping speed is too slow to cover comparable (degree scale) area. The Cosmic Dawn Survey Spitzer mosaics and associated products can be downloaded from the IRSA web site, Appendix A gives the details of the download site and the naming convention used. The community is encouraged to make use of them for their science.

In the context of the Cosmic Dawn Survey, several programs are currently underway to add data at other wavelengths to the *Euclid* deep fields and calibration fields. In particular deep optical data in the EDF-N and EDF-F are currently being obtained with the Subaru's Hyper-Suprime-Cam instrument as part of the Hawaii-Two-0 program (MacPartland et. al., in prep). These fields are also being targeted with high spatial resolution millimeter observations as part of the planned Large-scale Structure Survey with the Toltech Camera[5] on the Large Millimeter Telescope (LMT Pope et al. 2019). A deep U band survey is also underway with the CFHT (Zalesky et. al., in prep). EDF-S is being covered with K-band observations from the VISTA telescope (Nonino et. al., private communication), and planning is ongoing to obtain optical data with the Vera C. Rubin Observatory.

Acknowledgements. We thank the MOPEX support team for fixing issues that appeared when combining large numbers of files. This work is based on observations made with the *Spitzer* Space Telescope, which is operated by the Jet Propulsion Laboratory, California Institute of Technology under a contract with NASA, and has made use of the NASA/IPAC Infrared Science Archive, which is funded by the National Aeronautics and Space Administration and operated by the California Institute of Technology. This work has made use of data from the European Space Agency (ESA) mission Gaia (https://www.cosmos.esa.int/gaia), processed by the Gaia Data Processing and Analysis Consortium (DPAC, https://www.cosmos.esa.int/web/gaia/dpac/consortium). Funding for the DPAC has been provided by national institutions, in particular the institutions participating in the Gaia Multilateral Agreement. This publication makes use of data products from the Wide-field Infrared Survey Explorer, which is a joint project of the University of California, Los Angeles, and the Jet Propulsion Laboratory/California Institute of Technology, funded by the National Aeronautics and Space Administration. H.J.McC. acknowledges support from the PNCG. This work used the CANDIDE computer system at the IAP supported by grants from the PNCG and the DIM-ACAV and maintained by S. Rouberol. ST and JW acknowledge support from the European Research Council (ERC) Consolidator Grant funding scheme (project ConTExt, grant No. 648179) The Cosmic Dawn Center is funded by the Danish National Research Foundation under grant No. 140.

References

Aihara, H., Allende Prieto, C., An, D., et al. 2011, ApJS, 193, 29, doi: 10.1088/0067-0049/193/2/29

Ashby, M. L. N., Willner, S. P., Fazio, G. G., et al. 2013, The Astrophysical Journal, 769, 80, doi: 10.1088/0004-637X/769/1/80

Ashby, M. L. N., Caputi, K. I., Cowley, W., et al. 2018, The Astrophysical Journal Supplement Series, 237, 39, doi: 10.3847/1538-4365/aad4fb

Beckwith, S. V. W., Stiavelli, M., Koekemoer, A. M., et al. 2006, The Astronomical Journal, 132, 1729, doi: 10.1086/507302

Bell, E. F., & de Jong, R. S. 2001, ApJ, 550, 212, doi: 10.1086/319728

Bertin, E., & Arnouts, S. 1996, Astronomy and Astrophysics Supplement Series, 117, 393, doi: 10.1051/aas:1996164

Bouwens, R. J., Stefanon, M., Oesch, P. A., et al. 2019, ApJ, 880, 25, doi: 10.3847/1538-4357/ab24c5

Bowler, R. A. A., Jarvis, M. J., Dunlop, J. S., et al. 2020, MNRAS, 493, 2059, doi: 10.1093/mnras/staa313

Brammer, G. B., van Dokkum, P. G., Franx, M., et al. 2012, ApJS, 200, 13, doi: 10.1088/0067-0049/200/2/13

Bridge, J. S., Holwerda, B. W., Stefanon, M., et al. 2019, ApJ, 882, 42, doi: 10.3847/1538-4357/ab3213

Caputi, K. I., Ilbert, O., Laigle, C., et al. 2015, ApJ, 810, 73, doi: 10.1088/0004-637X/810/1/73

[5] http://toltec.astro.umass.edu/

Davidzon, I., Ilbert, O., Laigle, C., et al. 2017, Astronomy & Astrophysics, 605, A70, doi: 10.1051/0004-6361/201730419

Fazio, G. G., Hora, J. L., Allen, L. E., et al. 2004, The Astrophysical Journal Supplement Series, 154, 10, doi: 10.1086/422843

Gaia Collaboration, Brown, A. G. A., Vallenari, A., et al. 2018, Astronomy & Astrophysics, 616, A1, doi: 10.1051/0004-6361/201833051

Giavalisco, M., Ferguson, H. C., Koekemoer, A. M., et al. 2004, The Astrophysical Journal Letters, 600, L93, doi: 10.1086/379232

Girardi, L., Groenewegen, M. A. T., Hatziminaoglou, E., & da Costa, L. 2005, A&A, 436, 895, doi: 10.1051/0004-6361:20042352

Kauffmann, O. B., Le Fèvre, O., Ilbert, O., et al. 2020, A&A, 640, A67, doi: 10.1051/0004-6361/202037450

Laureijs, R., Amiaux, J., Arduini, S., et al. 2011, arXiv e-prints, 1110, arXiv:1110.3193. http://adsabs.harvard.edu/abs/2011arXiv1110.3193L

Le Fèvre, O., Tasca, L. A. M., Cassata, P., et al. 2015, A&A, 576, A79, doi: 10.1051/0004-6361/201423829

Legrand, L., McCracken, H. J., Davidzon, I., et al. 2019, Monthly Notices of the Royal Astronomical Society, 486, 5468, doi: 10.1093/mnras/stz1198

Pérez-González, P. G., Rieke, G. H., Villar, V., et al. 2008, ApJ, 675, 234, doi: 10.1086/523690

Pope, A., Aretxaga, I., Hughes, D., Wilson, G., & Yun, M. 2019, in American Astronomical Society Meeting Abstracts, Vol. 233, American Astronomical Society Meeting Abstracts #233, 363.20

Trac, H., Cen, R., & Loeb, A. 2008, ApJ, 689, L81, doi: 10.1086/595678

Werner, M. W., Roellig, T. L., Low, F. J., et al. 2004, The Astrophysical Journal Supplement Series, 154, 1, doi: 10.1086/422992

Wright, E. L., Eisenhardt, P. R. M., Mainzer, A. K., et al. 2010, The Astronomical Journal, 140, 1868, doi: 10.1088/0004-6256/140/6/1868

Appendix A: Delivered data products

The new mosaics and associated products can be obtained from the IRSA website at `https://irsa.ipac.caltech.edu/data/SPITZER/Cosmic_Dawn_Survey` (to be updated at publication time). The file naming convention is as follows:

```
CDS_{field}_ch{N}_{type}_v24.fits
```

where `field` is the field name, `N` is the channel number, and `type` is one of `ima` for the flux image, `cov` for the coverage in terms of number of frames used to build each pixel of the mosaic, `tim` for the exposure time in sec of the pixel, and `unc` for the uncertainty as determined from the standard deviation of the image pixels that contributed to the mosaic pixel. Also, table A gives the precise coordinates (of the tangent point), the reference pixel corresponding to that tangent point, and size, in pixels, of the mosaics. These values are the same for all channels of a field and for all the ancillary images. The pixel scale is $0\farcs60$ per pixel for all mosaics.

Appendix B: Coverage maps

Here we present the full set of pixel exposure time maps for channels 1 and 3; channels 2 and 4 are similar though slightly shifted in space. The colours span from nought to the 600 and 14 hr in channel 1 and 3, respectively, with a square root scaling, which was found to best show the different plateaus of exposure times. Thus red, yellow, green, light blue, dark blue, and violet correspond respectively to about 100%, 75%, 45%, 22%, 4%, and 0.1% of the maximum. The figures are all on the same physical scale (degrees of latitude per centimetre of paper) in order to show their relative sizes of the fields. The sometimes partial circular features as in the NE part of EDF-N and several partial ones in EGS are due to regions observed at many different times and thus at many different position angles.

Appendix C: PID numbers

Table C lists the Program-IDs (PIDs) of all the observations processed here. In bold the ones of the observing programmes that we planned for this work, the others are of the other observations that we reprocessed.

Table A.1. Data products information

Field	Longitude	Latitude	x-size	y-size	x-ref.pix	y-ref.pix
EDF-N	269.485804	66.590708	27410	30148	13705.55	15074.53
EDF-F	53.062008	–28.205431	23751	26204	11876.02	13102.29
EDF-S	61.301724	–48.496065	41676	33976	20838.59	16988.50
COSMOS	150.178292	2.220994	15440	17804	7720.46	8902.40
EGS	214.781187	52.720882	11278	13649	5639.32	6824.97
HDFN	189.405434	62.373754	11813	16979	5907.03	8489.78
XMM	34.101249	–4.598575	47583	25022	23791.97	12511.69

Notes. Longitude and Latitude are Ecliptic and J2000, for the image tangent point. These values are valid for all four channels of each field and for their ancillary images.

Table C.1. Spitzer Program IDs

Field	PIDs
EDFN	68 609 613 618–624 1101 1125 1188 1189 1191—1200 1317 1334 1600—1700 1910—1949 1951 1953–1961 1963–1983 2314 3286 3329 3672 10147 11161 **13153** 20466 30432 40385 60046 70062 70162 80109 80113 80243 80245 90209
EDFF	81 82 184 194 2313 11080 **13058** 20708 30866 40058 60022 61009 61052 70039 70145 70204 80217
EDFS	80039 **14235**
COSMOS	10159 11016 12103 13094 13104 14045 14081 14203 20070 40801 **50310** 61043 61060 70023 80057 80062 80134 80159 90042
EGS	8 10084 11065 11080 13118 20754 41023 60145 61042 80069 80156 80216 90180
HDFN	81 169 1304 10136 11004 11063 11080 11134 12095 13053 20218 30411 30476 40204 60122 60145 61040 61062 61063 70162 80215
XMM	181 3248 **10042** 11086 40021 60024 61041 61060 61061 70039 70062 80149 80156 80159 80218 90038 90175 90177

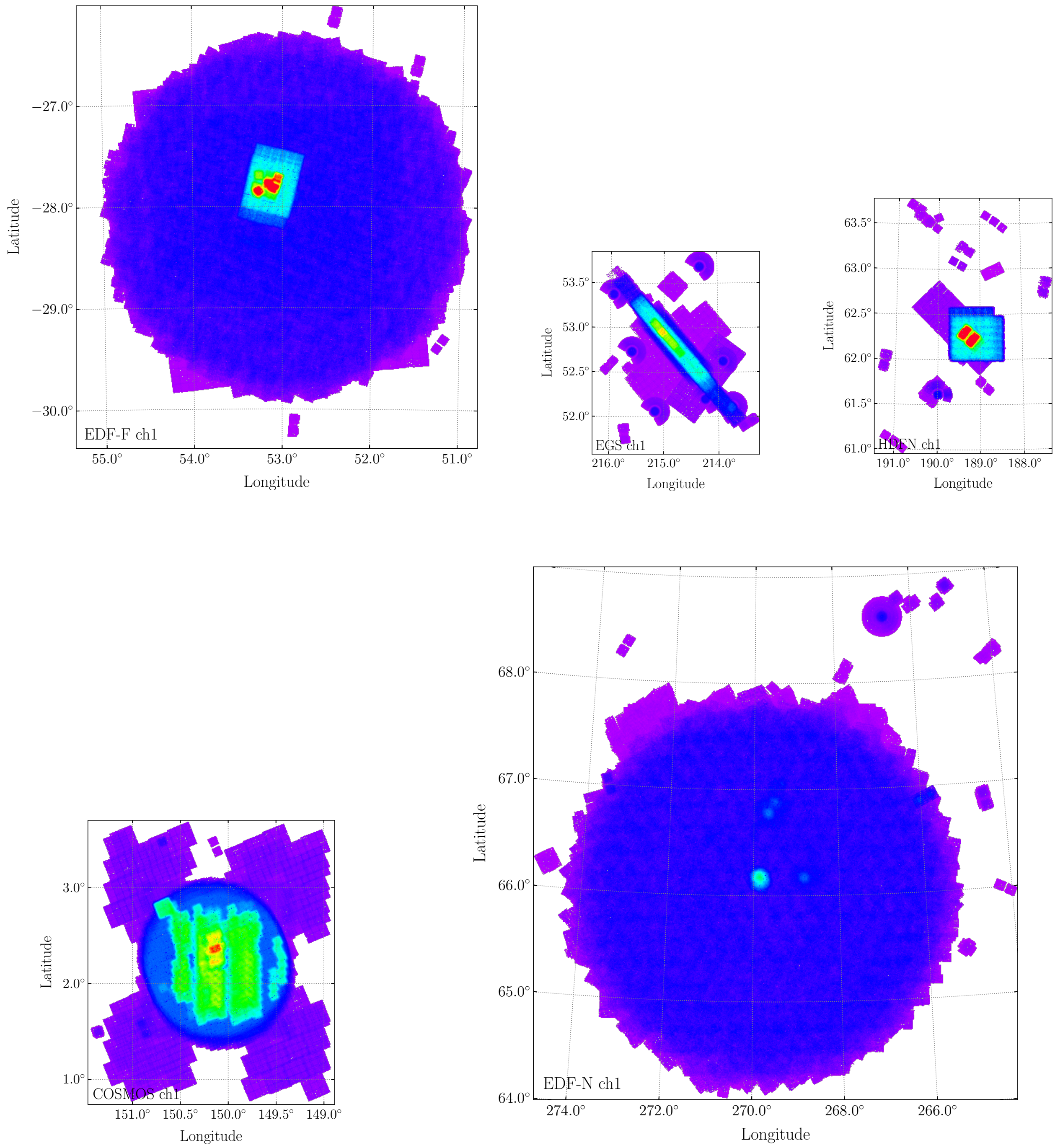

Fig. B.1. Field coverage maps, channel 1, part 1

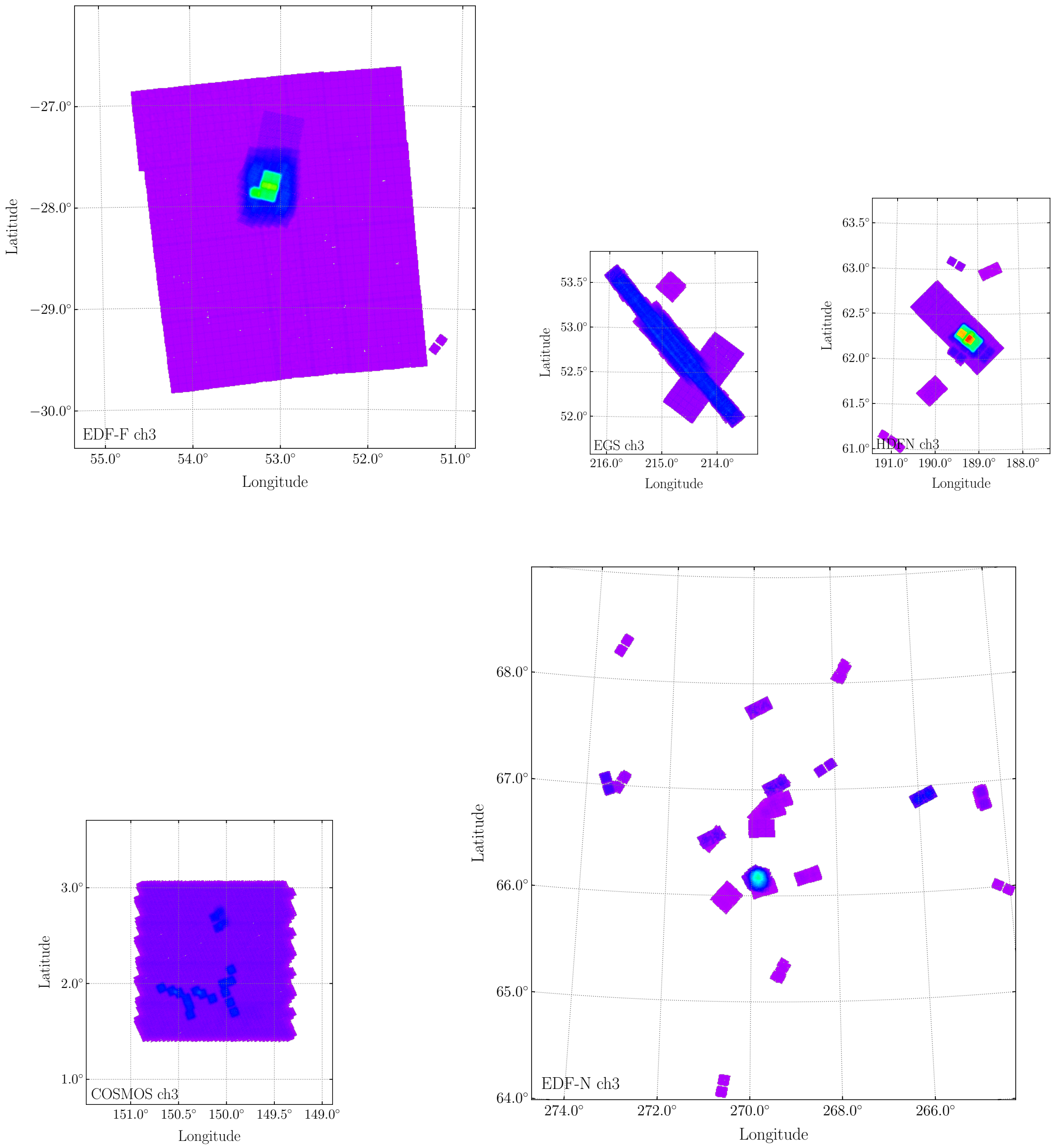

Fig. B.2. Field coverage maps, channel 3, part 1

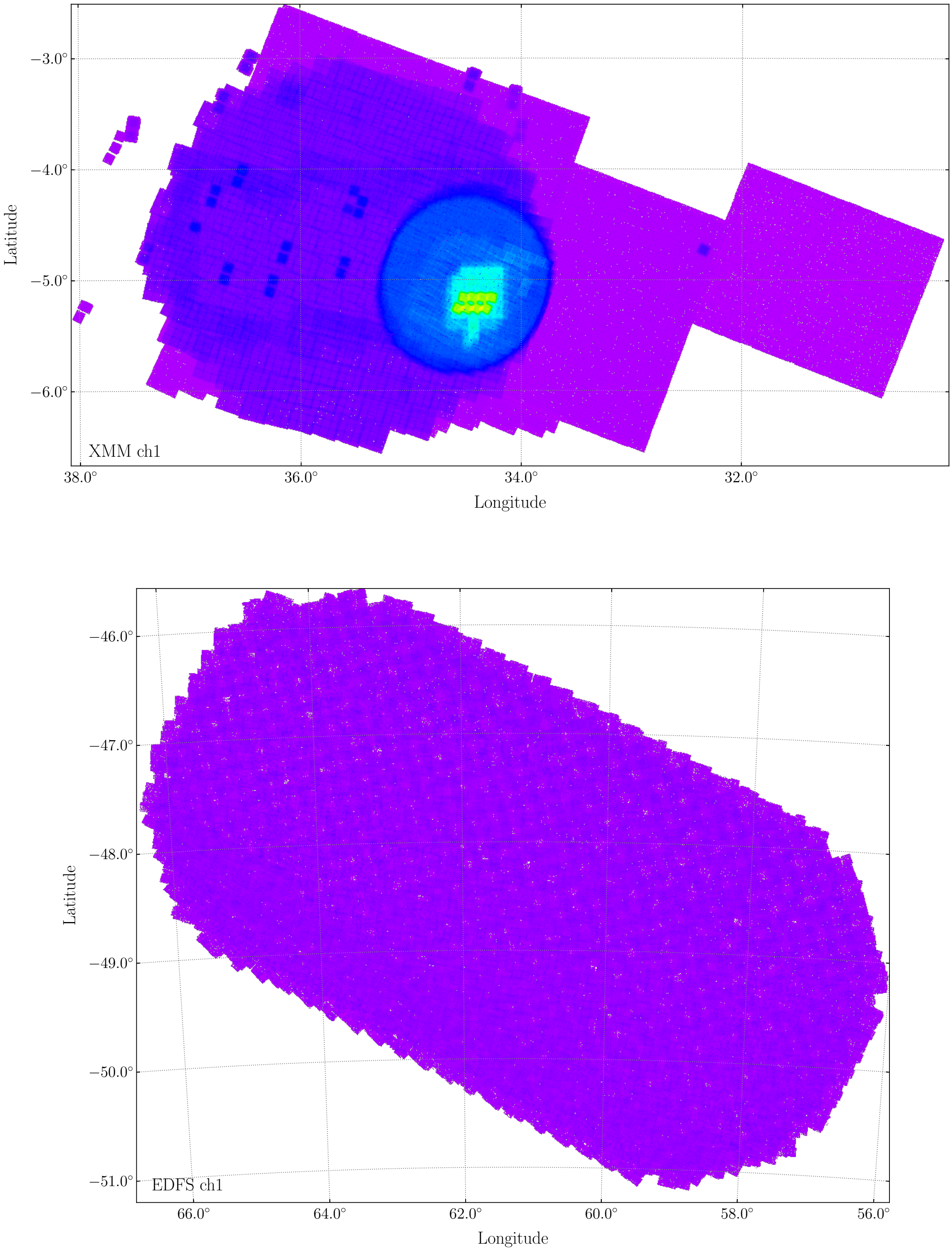

Fig. B.3. Field coverage maps, channel 1, part 2

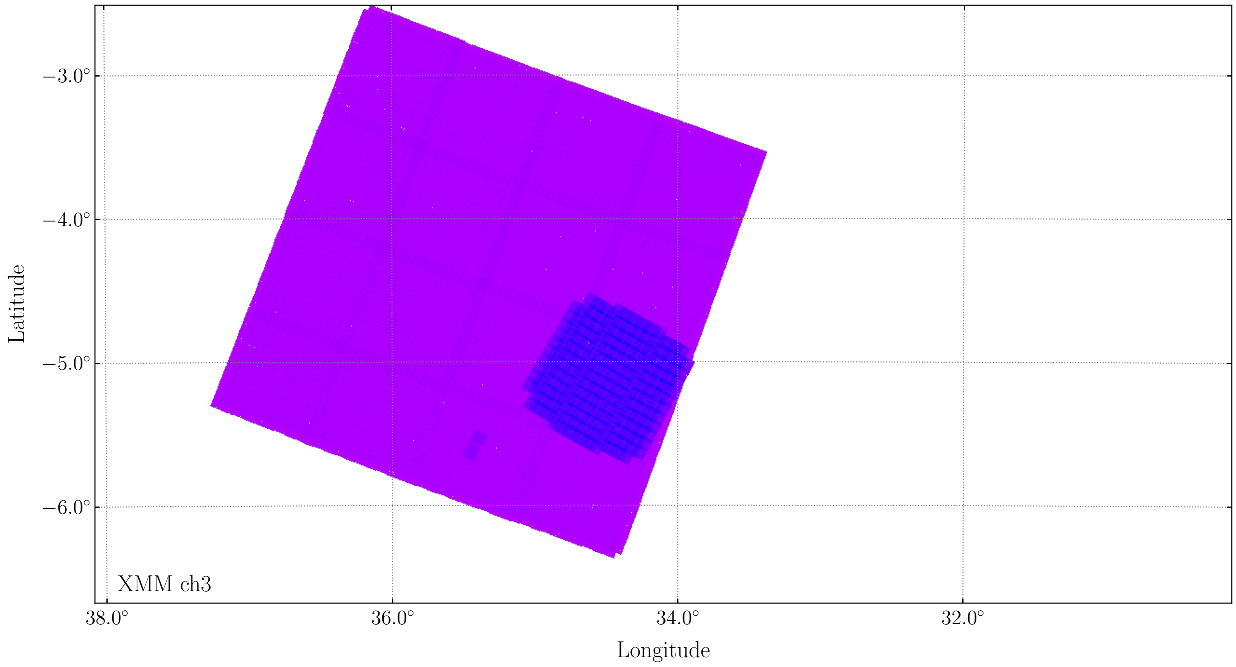

Fig. B.4. Field coverage maps, channel 3, part 2